

**Journal of
Mechanics of
Materials and Structures**

Volume 9, No. 1

January 2014



JOURNAL OF MECHANICS OF MATERIALS AND STRUCTURES

msp.org/jomms

Founded by Charles R. Steele and Marie-Louise Steele

EDITORIAL BOARD

ADAIR R. AGUIAR University of São Paulo at São Carlos, Brazil
KATIA BERTOLDI Harvard University, USA
DAVIDE BIGONI University of Trento, Italy
IWONA JASLUK University of Illinois at Urbana-Champaign, USA
THOMAS J. PENCE Michigan State University, USA
YASUhide SHINDO Tohoku University, Japan
DAVID STEIGMANN University of California at Berkeley

ADVISORY BOARD

J. P. CARTER University of Sydney, Australia
R. M. CHRISTENSEN Stanford University, USA
G. M. L. GLADWELL University of Waterloo, Canada
D. H. HODGES Georgia Institute of Technology, USA
J. HUTCHINSON Harvard University, USA
C. HWU National Cheng Kung University, Taiwan
B. L. KARIHALOO University of Wales, UK
Y. Y. KIM Seoul National University, Republic of Korea
Z. MROZ Academy of Science, Poland
D. PAMPLONA Universidade Católica do Rio de Janeiro, Brazil
M. B. RUBIN Technion, Haifa, Israel
A. N. SHUPIKOV Ukrainian Academy of Sciences, Ukraine
T. TARNAI University Budapest, Hungary
F. Y. M. WAN University of California, Irvine, USA
P. WRIGGERS Universität Hannover, Germany
W. YANG Tsinghua University, China
F. ZIEGLER Technische Universität Wien, Austria

PRODUCTION production@msp.org

SILVIO LEVY Scientific Editor


Cover photo: Ev Shafir

See msp.org/jomms for submission guidelines.

JoMMS (ISSN 1559-3959) at Mathematical Sciences Publishers, 798 Evans Hall #6840, c/o University of California, Berkeley, CA 94720-3840, is published in 10 issues a year. The subscription price for 2014 is US\$555/year for the electronic version, and \$710/year (+\$60, if shipping outside the US) for print and electronic. Subscriptions, requests for back issues, and changes of address should be sent to MSP.

JoMMS peer-review and production is managed by EditFLOW[®] from Mathematical Sciences Publishers.

PUBLISHED BY

 **mathematical sciences publishers**
nonprofit scientific publishing

<http://msp.org/>

© 2014 Mathematical Sciences Publishers

IMPROVED THERMOELASTIC COEFFICIENTS OF A NOVEL SHORT FUZZY FIBER-REINFORCED COMPOSITE WITH WAVY CARBON NANOTUBES

SHAILESH I. KUNDALWAL AND MANAS C. RAY

The elastic response of a novel short fuzzy fiber-reinforced composite (SFFRC) has recently been investigated by the authors (*Mech. Mater.* **53** (2012), 47–60). The distinctive feature of the construction of this novel SFFRC is that straight carbon nanotubes (CNTs) are radially grown on the circumferential surfaces of unidirectional short carbon fiber reinforcements. The waviness of CNTs is intrinsic to many manufacturing processes and plays an important role in the thermomechanical behavior of CNT-reinforced composites. However, the effect of the waviness of CNTs on the thermoelastic response of a SFFRC has yet to be investigated. Therefore, we investigate the effect of wavy CNTs on the thermoelastic properties of this SFFRC, revealing that the axial thermoelastic coefficients of the SFFRC significantly increase when the wavy CNTs are coplanar with the longitudinal plane of the carbon fibers for higher values of the waviness factor and wave frequency of the CNTs. The effective values of the thermal expansion coefficients of this SFFRC are also found to be sensitive to change in temperature.

A list of abbreviations and symbols can be found starting on page 21.

1. Introduction

Research on the synthesis of molecular carbon structures by an arc-discharge method for the evaporation of carbon led to the discovery of an extremely thin, needle-like graphitic carbon nanotube (CNT) [Iijima 1991]. Researchers probably thought that CNTs might be useful as nanoscale fibers for developing novel CNT-reinforced nanocomposites, and this conjecture motivated them to accurately study the physical properties (mechanical, thermal, and electrical) of CNTs. Numerous experimental and numerical studies revealed that the axial Young's modulus of CNTs is in the terapascal range [Treacy et al. 1996; Natsuki et al. 2004; Shen and Li 2004; Liu et al. 2005; Li and Guo 2008]. The quest for utilizing these exceptional mechanical properties of CNTs and their high aspect ratio led to the emergence of a new area of research on the development of CNT-reinforced nanocomposites [Odegard et al. 2003; Ashrafi and Hubert 2006; Seidel and Lagoudas 2006; Esteva and Spanos 2009; Ray and Batra 2009; Meguid et al. 2010; Khondaker and Keng 2012].

As nanoscale graphite structures, CNTs are of great interest not only for their mechanical properties but also for their thermal properties. For example, in several studies [Bandow 1997; Yosida 2000; Maniwa et al. 2001] the coefficients of thermal expansion (CTEs) of CNTs and their bundles are determined by using X-ray diffraction techniques. Bandow [1997] found that the CTE in the radial direction of multiwalled CNTs (MWCNTs) is almost the same as the CTE of graphite. Yosida [2000] and Maniwa

Keywords: short fuzzy fiber composite, wavy CNTs, micromechanics, thermoelastic coefficients.

et al. [2001] estimated the CTEs of single-walled CNT (SWCNT) bundles. Their results indicate that CNT bundles have a negative CTE at low temperatures and a positive CTE at high temperatures. Raravikar et al. [2002] estimated the CTEs of armchair (5, 5) and (10, 10) SWCNTs by using a molecular dynamics simulation (MDS) and found that the CTE of the CNT in the radial direction is less than that in the axial direction. Jiang et al. [2004] presented an analytical method to determine the CTEs of SWCNTs based on the interatomic potential and the local harmonic model. They found that all CTEs of SWCNTs are negative at low and room temperatures, and become positive at high temperatures. Kwon et al. [2004] performed a MDS and reported that the axial and radial CTEs of CNTs are nonlinear functions of change in temperature. Kirtania and Chakraborty [2009] presented a finite element (FE) analysis to estimate the CTEs of SWCNTs and demonstrated that the CTEs of SWCNTs increase uniformly with increase in the diameter of the SWCNT. The nonequilibrium Green's function method was employed by Jiang et al. [2009] to investigate the CTEs of SWCNTs and graphene. They found that the axial CTE is positive in the whole temperature range while the radial CTE is negative at low temperatures. Alamusi et al. [2012] investigated the axial CTEs of SWCNTs and MWCNTs by using a MDS, considering the effects of temperature and CNT diameter. For all CNTs, the obtained results revealed that axial CTEs are negative within a wide low-temperature range and positive in a high temperature range, and the temperature range for negative axial CTEs narrows as the diameter of the CNT decreases. Extensive research has also been carried out concerning the prediction of the CTEs of CNT-reinforced composites [Pipes and Hubert 2003; Kirtania and Chakraborty 2009]. In these studies, the results indicate that the addition of CNTs into the matrix causes significant improvement in the thermoelastic response of the CNT-reinforced composite as compared to that of the base composite.

It has been reported in many experimental studies [Shaffer and Windle 1999; Qian et al. 2000; Zhang et al. 2008; Yamamoto et al. 2009; Tsai et al. 2011] that CNTs are actually curved cylindrical tubes. The use of long CNTs in CNT-reinforced nanocomposites has revealed that CNT curvature significantly reduces the effective properties of the CNT-reinforced composite [Fisher et al. 2002; Berhan et al. 2004; Shi et al. 2004; Anumandla and Gibson 2006]. The effect of CNT curvature on the polymer matrix nanocomposite stiffness has been investigated by Pantano and Cappello [2008]. They concluded that in the presence of weak bonding, enhancement of the nanocomposite stiffness can be achieved through the bending energy of CNTs rather than through their axial stiffness. Li and Chou [2009] studied the failure of CNT/polymer matrix composites by using a micromechanics model and conducting FE simulations. They found that CNT waviness tends to reduce the elastic modulus and tensile strength of the nanocomposite but increases its ultimate strain. Farsadi et al. [2013] developed a three-dimensional FE model to investigate the influence of the waviness of the CNTs on the elastic moduli of a CNT-reinforced composite.

In addition to the waviness of CNTs, significant technical and manufacturing challenges have hindered the development of large-scale CNT-enhanced structures [Ajayan and Tour 2007; Schulte and Windle 2007]. Alignment, dispersion, and adhesion of CNTs in polymer matrices are vital for structural composite applications [Thostenson et al. 2001; Ajayan and Tour 2007; Schulte and Windle 2007]. More success can be achieved in improving the transverse multifunctional properties of hybrid CNT-reinforced composites by growing short CNTs on the circumferential surfaces of advanced fibers [Bower et al. 2000; Veedu et al. 2006; Qiu et al. 2007; Garcia et al. 2008]. For example, Veedu et al. [2006] developed a multifunctional composite in which CNTs are grown on the circumferential surfaces of the fibers and found that the presence of CNTs on the surfaces of the fibers reduces the effective CTE

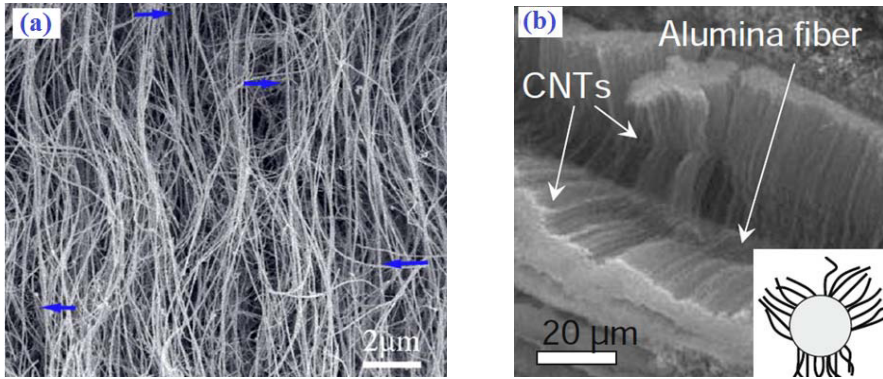


Figure 1. Left: SEM image of vertically aligned curved CNTs (adapted with permission from [Zhang et al. 2008]). Right: SEM image of aligned CNTs grown on alumina fiber (adapted with permission from [Yamamoto et al. 2009]).

of the multifunctional composite up to 62% compared to that of the base composite (that is, without CNTs). Qiu et al. [2007] developed a multifunctional composite through an effective infiltration-based vacuum-assisted resin transfer moulding process. Their study indicated that the effective CTE of the multifunctional composite was reduced up to 25.2% compared with that of the composite without CNTs. A fiber coated with radially grown CNTs on its circumferential surface is called a “fuzzy fiber” [Garcia et al. 2008; Yamamoto et al. 2009; Chatzigeorgiou et al. 2012], and the resulting composite may be called a fuzzy fiber-reinforced composite (FFRC). Chatzigeorgiou et al. [2012] estimated the thermoelastic properties of fuzzy fiber composites in which a carbon fiber is coated with radially aligned straight CNTs by employing the asymptotic expansion homogenization method. They reported that the radial CTE of the fuzzy fiber composite is one order of magnitude less than its axial CTE. Recently, the elastic properties and the load transfer characteristics of a novel short fuzzy fiber-reinforced composite (SFFRC) have been extensively studied in [Kundalwal and Ray 2012; Kundalwal 2013].

Scanning electron microscopy (SEM) images analyzed in [Zhang et al. 2008] and [Yamamoto et al. 2009] are shown in Figure 1. They show clearly that CNTs remain highly curved when they are grown on the surfaces of advanced fibers. It is hypothesized that their affinity to becoming curved is due to their high aspect ratio and associated low bending stiffness. Since the addition of CNTs in hybrid CNT-reinforced composites influences the thermoelastic properties of the hybrid nanocomposites, the waviness of the CNTs may also affect the effective thermoelastic response of the SFFRC. However, the thermoelastic response of such a hybrid nanocomposite, being composed of short fuzzy fiber reinforcements coated with wavy CNTs, has not yet been investigated. Therefore, in this study we have endeavored to investigate the effect of waviness of CNTs on the effective thermoelastic properties of a SFFRC.

The outline is as follows: Section 2 briefly describes the architecture of the SFFRC containing wavy CNTs coplanar with either of the two mutually orthogonal planes. Section 3 presents the development of the Mori–Tanaka (MT) models for estimating the effective thermoelastic properties of the SFFRC and its constituent phases. In Section 4, numerical results are presented. Finally, Section 5 delineates the conclusions drawn from this study.

2. Architecture of a novel SFFRC

The top part of [Figure 2](#) represents a lamina of a SFFRC in which the short fuzzy fibers are uniformly reinforced in the polymer matrix. Its in-plane cross section is illustrated in [Figure 2](#), bottom. The short fuzzy fiber coated with sinusoidally wavy CNTs [[Fisher et al. 2002](#); [Berhan et al. 2004](#); [Anumandla and Gibson 2006](#); [Pantano and Cappello 2008](#); [Zhang et al. 2008](#); [Tsai et al. 2011](#); [Farsadi et al. 2013](#)] reinforced in the polymer matrix can be viewed as a circular cylindrical short composite fuzzy fiber (SCFF), as illustrated in [Figure 3](#). The SCFFs are assumed to be uniformly dispersed over the volume of a lamina of the SFFRC in such a way that the three orthogonal principal material coordinate axes (1-2-3) exist in the composite as shown in [Figure 2](#), top. The architecture of the representative volume element

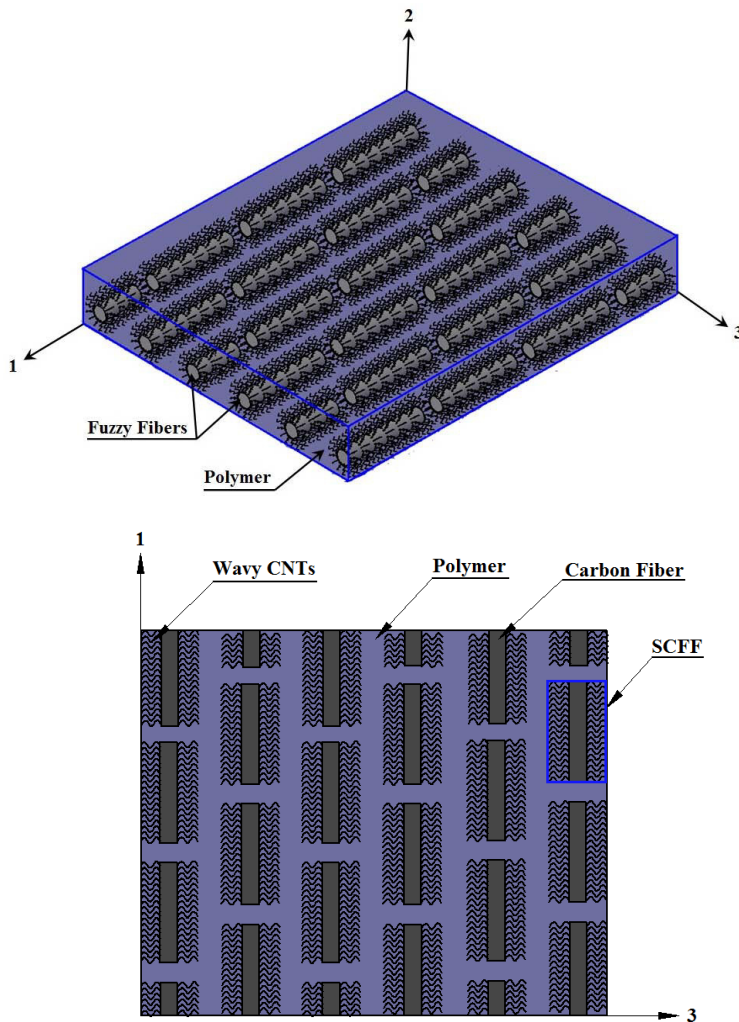


Figure 2. Top: schematic diagram of a lamina made of the SFFRC containing wavy CNTs. Bottom: In-plane cross section of the SFFRC lamina. (Wavy CNTs are coplanar with the longitudinal plane of the carbon fiber.)

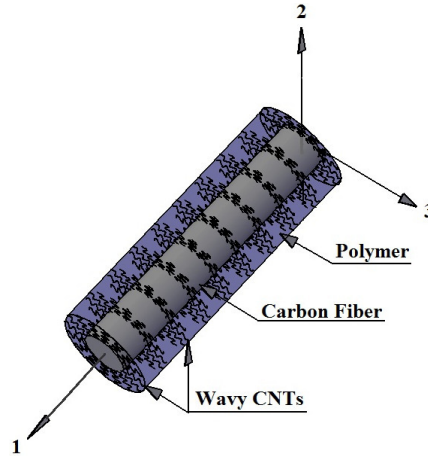


Figure 3. Fuzzy fiber coated with wavy CNTs reinforced in the polymer matrix (wavy CNTs are coplanar with the transverse plane of the carbon fiber).

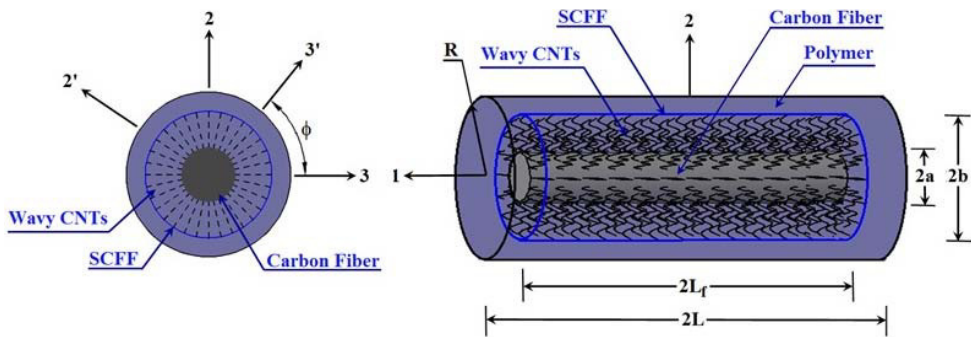


Figure 4. Architecture of the RVE of the SFFRC in which the SCFF is embedded in the polymer material.

(RVE) of the SFFRC in which the SCFF embedded in the polymer material is schematically illustrated in Figure 4. The orientation of the plane of the wavy CNTs radially grown on the circumferential surface of the carbon fiber is an important issue because the planar orientations of the wavy CNTs may influence the thermoelastic properties of the SFFRC; this issue needs to be carefully addressed. Two possible planar orientations of the wavy CNTs are considered herein. The wavy CNTs are coplanar with either the longitudinal (that is, the 1-3 or 1'-3') or the transverse (that is, the 2-3 or 2'-3') plane of the carbon fiber, as shown in Figures 2 and 3, respectively. Investigation of the effect of all other planar orientations of the wavy CNTs is beyond the scope of the present study.

3. Modeling of the effective thermoelastic properties of a novel SFFRC and its constituent phases

This section deals with the procedures of employing the MT model to predict the effective thermoelastic properties of the SFFRC and its constituent phases. The various steps involved in the computation of the effective thermoelastic properties of the SFFRC are outlined as follows.

- The first step in modeling the SFFRC is to determine the effective thermoelastic properties of a polymer matrix nanocomposite (PMNC) containing wavy CNTs coplanar with either the longitudinal (that is, the 1-3 or 1'-3') or the transverse (that is, the 2-3 or 2'-3') plane of the carbon fiber.
- Subsequently, considering the PMNC material as the matrix phase and the short carbon fibers as the reinforcement, the effective thermoelastic properties of the SCFF can be computed.
- Finally, using the effective thermoelastic properties of the SCFF and the polymer matrix, the effective thermoelastic properties of the SFFRC can be obtained.

3.1. Effective thermoelastic properties of the PMNC. From the constructional features of the SCFF, it may be seen that the carbon fiber is wrapped by a lamina of PMNC material, as illustrated in Figure 5. The average effective thermoelastic properties of the annular portion of the PMNC material surrounding the carbon fiber can be approximated by estimating the effective thermoelastic properties of the unwound lamina containing wavy CNTs. Hence, the effective elastic coefficient matrix $[\bar{C}^{NC}]$ and the effective thermal expansion coefficient vector $\{\bar{\alpha}^{NC}\}$ of the unwound lamina containing wavy CNTs are to be estimated a priori. Subsequently, appropriate transformations and homogenization procedures can be

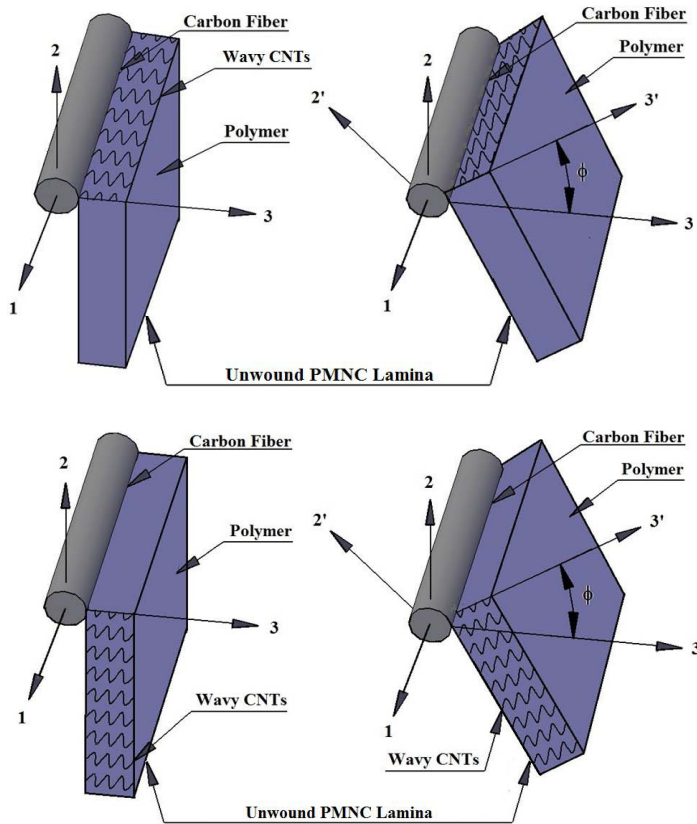


Figure 5. Unwound lamina of PMNC containing wavy CNTs coplanar with the longitudinal (top) or transverse (bottom) plane of the carbon fiber.

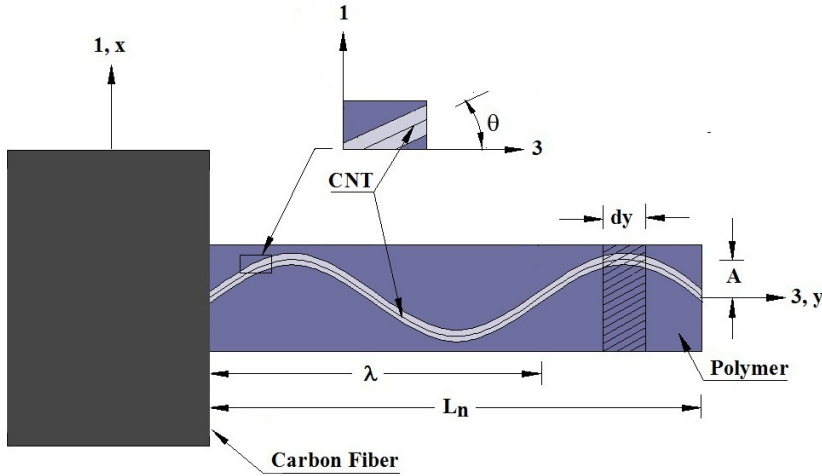


Figure 6. RVE of unwound PMNC material containing a wavy CNT coplanar with the longitudinal (that is, 1-3) plane of the carbon fiber (adapted with permission from [Kundalwal and Ray 2013]).

carried out on $[\bar{C}^{NC}]$ and $\{\bar{\alpha}^{NC}\}$ to determine the effective thermoelastic properties of the annular portion of PMNC surrounding the carbon fiber.

Wavy CNTs coplanar with the longitudinal plane of the carbon fiber. We first consider the wavy CNTs to be coplanar with the longitudinal plane (the 1-3 or 1'-3' plane) of the carbon fiber, as shown in Figures 2 and 4, while computing the thermoelastic properties of the PMNC. An appropriate RVE of unwound PMNC material containing a wavy CNT can be considered to investigate the thermoelastic properties of the unwound PMNC material. Such an RVE is schematically illustrated in Figure 6. The RVE shown in Figure 6 can be divided into infinitesimally thin slices of thickness dy and each slice can be treated as an off-axis unidirectional lamina in which the CNT axis makes an angle θ with the radial direction. The CNT waviness is assumed to be sinusoidal in the longitudinal plane of the carbon fiber and is defined by

$$x = A \sin(\omega y), \quad \omega = n\pi/L_n, \quad (1)$$

in which A and L_n are the amplitude of the CNT wave and the linear distance between the CNT ends, respectively, and n represents the number of CNT waves. The running length, L_{nr} , of the CNT is given by

$$L_{nr} = \int_0^{L_n} \sqrt{1 + A^2 \omega^2 \cos^2(\omega y)} dy, \quad (2)$$

where the angle θ shown in Figure 6 is given by

$$\tan \theta = dx/dy = A\omega \cos(\omega y). \quad (3)$$

The effective thermoelastic properties at any point of any slice of the unwound lamina of PMNC containing sinusoidally wavy CNTs where the CNT axis makes an angle θ with the radial direction (3 or 3') can be approximated by transforming the effective thermoelastic properties of the unwound lamina of PMNC containing straight CNTs. Hence, in what follows the MT model for predicting the effective

thermoelastic properties of the unwound lamina of PMNC with straight CNTs will be presented first. Due to difficulties in the atomistic modeling of CNTs inside the polymer matrix environment, researchers have considered CNTs as equivalent solid fibers for estimating the effective thermoelastic properties of CNT-reinforced composites [Fisher et al. 2002; Pipes and Hubert 2003; Berhan et al. 2004; Anumandla and Gibson 2006; Pantano and Cappello 2008; Tsai et al. 2011; Farsadi et al. 2013]. Thus, considering CNTs as solid fibers, the MT model [Mori and Tanaka 1973] can be utilized to estimate the effective elastic coefficient matrix $[C^{nc}]$ of the unwound lamina of PMNC with straight CNTs [Benveniste 1987]:

$$[C^{nc}] = [C^p] + v_n([C^n] - [C^p])([\tilde{A}_1][v_p[I] + v_n[\tilde{A}_1]]^{-1}), \quad (4)$$

in which

$$[\tilde{A}_1] = [I] + [S^n]([C^p])^{-1}([C^n] - [C^p])^{-1},$$

where v_n and v_p represent the volume fractions of the CNT fiber and polymer material, respectively, present in the RVE of the PMNC. The square matrix $[S^n]$ represents the Eshelby tensor for the cylindrical CNT. The elements of the Eshelby tensor $[S^n]$ for the cylindrical CNT reinforcement in the isotropic polymer matrix are explicitly written as [Qiu and Weng 1990]

$$[S^n] = \begin{bmatrix} S_{1111}^n & S_{1122}^n & S_{1133}^n & 0 & 0 & 0 \\ S_{2211}^n & S_{2222}^n & S_{2233}^n & 0 & 0 & 0 \\ S_{3311}^n & S_{3322}^n & S_{3333}^n & 0 & 0 & 0 \\ 0 & 0 & 0 & S_{2323}^n & 0 & 0 \\ 0 & 0 & 0 & 0 & S_{1313}^n & 0 \\ 0 & 0 & 0 & 0 & 0 & S_{1212}^n \end{bmatrix}, \quad (5)$$

in which

$$\begin{aligned} S_{1111}^n &= S_{2222}^n = \frac{5 - 4\nu^p}{8(1 - \nu^p)}, & S_{3333}^n &= 0, & S_{1122}^n &= S_{2211}^n = \frac{4\nu^p - 1}{8(1 - \nu^p)}, \\ S_{1133}^n &= S_{2233}^n = \frac{\nu^p}{2(1 - \nu^p)}, & S_{3311}^n &= S_{3322}^n = 0, & S_{1313}^n &= S_{2323}^n = 1/4, & S_{1212}^n &= \frac{3 - 4\nu^p}{8(1 - \nu^p)}, \end{aligned}$$

where ν^p denotes the Poisson's ratio of the polymer matrix.

Using the effective elastic coefficient matrix $[C^{nc}]$, the effective thermal expansion coefficient vector $\{\alpha^{nc}\}$ for unwound PMNC with straight CNTs can be derived in the form of [Laws 1973] as

$$\{\alpha^{nc}\} = \{\alpha^n\} + ([C^{nc}]^{-1} - [C^n]^{-1})([C^n]^{-1} - [C^p]^{-1})^{-1}(\{\alpha^n\} - \{\alpha^p\}), \quad (6)$$

where $\{\alpha^n\}$ and $\{\alpha^p\}$ are the thermal expansion coefficient vectors of the CNT fiber and the polymer material, respectively. The effective elastic coefficient matrix $[C^{NC}]$ and the effective thermal expansion coefficient vector $\{\alpha^{NC}\}$ at any point of any slice of the unwound lamina of PMNC where the CNT is inclined at an angle θ with the 3 ($3'$)-axis can be derived by employing the appropriate transformations:

$$[C^{NC}] = [T_1]^{-T}[C^{nc}][T_1]^{-1}, \quad \{\alpha^{NC}\} = [T_1]^{-T}\{\alpha^{nc}\}, \quad (7)$$

in which

$$[T_1] = \begin{bmatrix} k^2 & 0 & l^2 & 0 & kl & 0 \\ 0 & 1 & 0 & 0 & 0 & 0 \\ l^2 & 0 & k^2 & 0 & -kl & 0 \\ 0 & 0 & 0 & k & 0 & -l \\ -2kl & 0 & 2kl & 0 & k^2 - l^2 & -n \\ 0 & 0 & 0 & l & 0 & k \end{bmatrix},$$

with

$$k = \cos \theta = [1 + \{n\pi A/L_n \cos(n\pi y/L_n)\}^2]^{-1/2}$$

and

$$l = \sin \theta = n\pi A/L_n \cos(n\pi y/L_n) [1 + \{n\pi A/L_n \cos(n\pi y/L_n)\}^2]^{-1/2}.$$

Subsequently, the average effective elastic coefficient matrix $[\bar{C}^{\text{NC}}]$ and the thermal expansion coefficient vector $\{\bar{\alpha}^{\text{nc}}\}$ of the lamina of unwound PMNC material containing wavy CNTs can be obtained by averaging the transformed elastic coefficients (C_{ij}^{NC}) and the thermal expansion coefficients (α_{ij}^{NC}) over the linear distance between the CNT ends as [Hsiao and Daniel 1996]

$$[\bar{C}^{\text{NC}}] = \frac{1}{L_n} \int_0^{L_n} [C^{\text{NC}}] dy, \quad \{\bar{\alpha}^{\text{NC}}\} = \frac{1}{L_n} \int_0^{L_n} \{\alpha^{\text{NC}}\} dy. \quad (8)$$

When the carbon fiber is viewed to be wrapped by such an unwound lamina of PMNC, the matrix $[\bar{C}^{\text{NC}}]$ and the vector $\{\bar{\alpha}^{\text{NC}}\}$ as given by (8) also provide the effective properties at a point located in the PMNC with respect to the 1'-2'-3' coordinate system, where the wavy CNT is grown at an orientation angle ϕ with the 3-axis in the 2-3 plane as shown in Figures 4 and 5. Hence, at any point in the PMNC surrounding the carbon fiber, the effective elastic coefficient matrix $[\bar{C}^{\text{PMNC}}]$ and the effective thermal expansion coefficient vector $\{\bar{\alpha}^{\text{PMNC}}\}$ of the PMNC with respect to the 1-2-3 coordinate system turn out to be dependent on the CNT orientation angle ϕ and can be determined by the following transformations:

$$[\bar{C}^{\text{PMNC}}] = [T]^{-T} [\bar{C}^{\text{NC}}] [T]^{-1}, \quad \{\bar{\alpha}^{\text{PMNC}}\} = [T]^{-T} \{\bar{\alpha}^{\text{NC}}\}, \quad (9)$$

where

$$[T] = \begin{bmatrix} 1 & 0 & 0 & 0 & 0 & 0 \\ 0 & m^2 & n^2 & mn & 0 & 0 \\ 0 & n^2 & m^2 & -mn & 0 & 0 \\ 0 & -2mn & 2mn & m^2 - n^2 & 0 & 0 \\ 0 & 0 & 0 & 0 & m & -n \\ 0 & 0 & 0 & 0 & n & m \end{bmatrix}, \quad \text{with } m = \cos \phi \text{ and } n = \sin \phi.$$

From (9) it is obvious that the effective thermoelastic properties at any point in the PMNC surrounding the carbon fiber with respect to the principle material coordinate axes of the SFRC vary over the annular cross section of the PMNC phase of the RVE of the SCFF. However, without loss of generality, it may be considered that the volume average of these effective thermoelastic properties over the volume of the PMNC can be treated as the constant effective elastic coefficient matrix $[C^{\text{PMNC}}]$ and the constant effective thermal expansion coefficient vector $\{\alpha^{\text{PMNC}}\}$ of PMNC containing sinusoidally wavy CNTs

surrounding the carbon fiber with respect to the 1-2-3 coordinate axes of the SFFRC. These are given by

$$\begin{aligned} [C^{\text{PMNC}}] &= \frac{1}{\pi(b^2 - a^2)} \int_0^{2\pi} \int_a^b [\bar{C}^{\text{PMNC}}] r dr d\phi, \\ \{\alpha^{\text{PMNC}}\} &= \frac{1}{\pi(b^2 - a^2)} \int_0^{2\pi} \int_a^b \{\bar{\alpha}^{\text{PMNC}}\} r dr d\phi. \end{aligned} \quad (10)$$

Thus the effective constitutive relations for the PMNC material surrounding the carbon fiber with respect to the principle material coordinate (1-2-3) axes of the SFFRC can be expressed as

$$\{\sigma^{\text{PMNC}}\} = [C^{\text{PMNC}}](\{\epsilon^{\text{PMNC}}\} - \{\alpha^{\text{PMNC}}\} \Delta T), \quad (11)$$

in which ΔT represents the temperature deviation from a reference temperature.

Wavy CNTs coplanar with the transverse plane of the carbon fiber. Now the CNT waviness is assumed to be sinusoidal in the transverse plane (2-3 or 2'-3') of the carbon fiber, as shown in [Figure 3](#), and is characterized by

$$z = A \sin(\omega y), \quad \omega = n\pi/L_n, \quad (12)$$

in which the angle θ shown in [Figure 7](#) is given by

$$\tan \theta = dz/dy = A\omega \cos(\omega y). \quad (13)$$

The procedure of utilizing the MT model presented in [Section 3.1](#) for determining the effective thermoelastic properties of the unwound lamina of PMNC with straight CNTs can be utilized to estimate the effective thermoelastic properties of the unwound lamina of PMNC with wavy CNTs coplanar with the transverse plane of the carbon fiber. Once $[C^{nc}]$ and $\{\alpha^{nc}\}$ are computed by (4) and (6), respectively, the effective elastic coefficient matrix $[C^{\text{NC}}]$ and the effective thermal expansion coefficient vector $\{\alpha^{\text{NC}}\}$ at any point of any slice of the unwound lamina of PMNC where the CNT is inclined at an angle θ with the 3 (3')-axis can be derived by employing the appropriate transformations for the wavy CNTs coplanar with the transverse plane of the carbon fiber:

$$[C^{\text{NC}}] = [T_2]^{-T} [C^{nc}] [T_2]^{-1}, \quad \{\alpha^{\text{NC}}\} = [T_2]^{-T} \{\alpha^{nc}\}, \quad (14)$$

in which

$$[T_2] = \begin{bmatrix} 1 & 0 & 0 & 0 & 0 & 0 \\ 0 & k^2 & l^2 & kl & 0 & 0 \\ 0 & l^2 & k^2 & -kl & 0 & 0 \\ 0 & -2kl & 2kl & k^2 - l^2 & 0 & 0 \\ 0 & 0 & 0 & 0 & k & -l \\ 0 & 0 & 0 & 0 & l & k \end{bmatrix}.$$

Subsequently, (8) and (10) can be used to estimate the effective elastic coefficient matrix $[C^{\text{PMNC}}]$ and thermal expansion coefficient vector $\{\alpha^{\text{PMNC}}\}$ of the PMNC material surrounding the carbon fiber when the wavy CNTs are coplanar with the transverse plane of the carbon fiber.

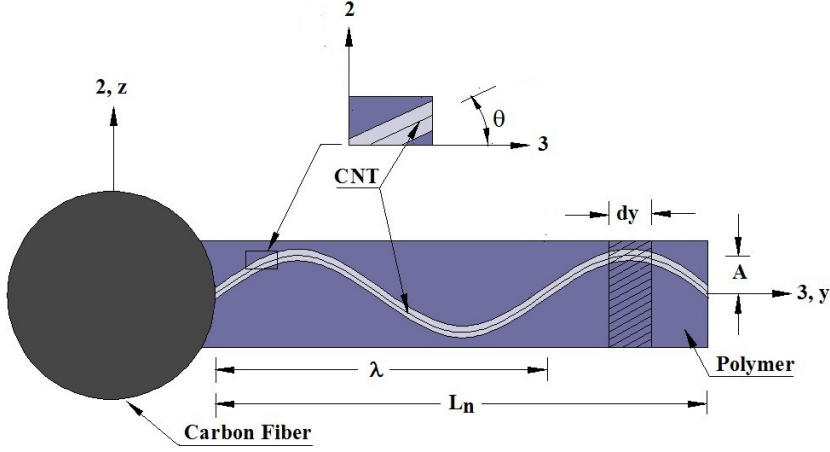


Figure 7. RVE of the unwound PMNC material containing a wavy CNT to be coplanar with the transverse plane (that is, 2-3 plane) of the carbon fiber (adapted with permission from [Kundalwal and Ray 2013]).

3.2. Effective thermoelastic properties of the SCFF. The second step in modeling the SCFF is to estimate the effective thermoelastic properties of the SCFF. Utilizing the effective elastic properties of PMNC containing wavy CNTs derived in the previous section as the matrix material properties and with the carbon fiber aligned along the 1-direction as the reinforcement, the MT model presented for the unwound PMNC can be augmented to derive the effective elastic coefficient matrix $[C^{SCFF}]$ of a lamina made of the SCFF:

$$[C^{SCFF}] = [C^{PMNC}] + \bar{v}_f ([C^f] - [C^{PMNC}]) ([\tilde{A}_2] [v_{PMNC} [I] + v_f [\tilde{A}_2]]^{-1}), \quad (15)$$

where

$$[\tilde{A}_2] = [I] + [S^f] ([C^{PMNC}])^{-1} ([C^f] - [C^{PMNC}])^{-1},$$

and where \bar{v}_f and v_{PMNC} are the volume fractions of the carbon fiber and PMNC, respectively, with respect to the volume of the RVE of the SCFF, and the Eshelby tensor, $[S^f]$, is determined based on the elastic properties of the PMNC and the shape of the carbon fiber. It should be noted that the PMNC material is transversely isotropic and, consequently, the Eshelby tensor [Li and Dunn 1998] corresponding to transversely isotropic material is utilized to compute the matrix $[S^f]$. The elements of the Eshelby tensor for the cylindrical carbon fiber embedded in the transversely isotropic PMNC material are explicitly given by [Li and Dunn 1998]:

$$[S^f] = \begin{bmatrix} S_{1111}^f & S_{1122}^f & S_{1133}^f & 0 & 0 & 0 \\ S_{2211}^f & S_{2222}^f & S_{2233}^f & 0 & 0 & 0 \\ S_{3311}^f & S_{3322}^f & S_{3333}^f & 0 & 0 & 0 \\ 0 & 0 & 0 & S_{2323}^f & 0 & 0 \\ 0 & 0 & 0 & 0 & S_{1313}^f & 0 \\ 0 & 0 & 0 & 0 & 0 & S_{1212}^f \end{bmatrix}, \quad (16)$$

in which

$$S_{1111}^f = S_{2222}^f = \frac{5C_{11}^{\text{PMNC}} + C_{12}^{\text{PMNC}}}{8C_{11}^{\text{PMNC}}}, \quad S_{1122}^f = S_{2211}^f = \frac{3C_{12}^{\text{PMNC}} - C_{11}^{\text{PMNC}}}{8C_{11}^{\text{PMNC}}}, \quad S_{1133}^f = S_{2233}^f = \frac{C_{13}^{\text{PMNC}}}{2C_{11}^{\text{PMNC}}},$$

$$S_{3311}^f = S_{3322}^f = 0, \quad S_{1313}^f = S_{2323}^f = 1/4, \quad S_{3333}^f = 0, \quad S_{1212}^f = \frac{3C_{11}^{\text{PMNC}} - C_{12}^{\text{PMNC}}}{8C_{11}^{\text{PMNC}}}.$$

Using the effective elastic coefficient matrix $[C^{\text{SCFF}}]$, the effective thermal expansion coefficient vector $\{\alpha^{\text{SCFF}}\}$ for the SCFF can be determined as follows [Laws 1973]:

$$\{\alpha^{\text{SCFF}}\} = \{\alpha^f\} + ([C^{\text{SCFF}}]^{-1} - [C^f]^{-1})([C^f]^{-1} - [C^{\text{PMNC}}]^{-1})^{-1}(\{\alpha^f\} - \{\alpha^{\text{PMNC}}\}), \quad (17)$$

where $[C^f]$ and $\{\alpha^f\}$ are the elastic coefficient matrix and thermal expansion coefficient vector of the carbon fiber, respectively.

3.3. Effective thermoelastic properties of the SFRC. Considering the SCFF as the cylindrical reinforcement embedded in the isotropic polymer matrix, the effective elastic properties $[C]$ of the SFRC can be determined by utilizing the MT model as follows:

$$[C] = [C^p] + v_{\text{SCFF}}([C^{\text{SCFF}}] - [C^p])([\tilde{A}_3][\bar{v}_p[I] + v_{\text{SCFF}}[\tilde{A}_3]]^{-1}), \quad (18)$$

in which

$$[\tilde{A}_3] = [I] + [S^{\text{SCFF}}]([C^p])^{-1}([C^{\text{SCFF}}] - [C^p])^{-1}$$

and where v_{SCFF} and \bar{v}_p are the volume fractions of the SCFF and polymer material, respectively, with respect to the volume of the RVE of the SFRC. The elements of the Eshelby tensor $[S^{\text{SCFF}}]$ for the cylindrical SCFF reinforcement in the isotropic polymer matrix are given by [Qiu and Weng 1990]

$$[S^{\text{SCFF}}] = \begin{bmatrix} S_{1111} & S_{1122} & S_{1133} & 0 & 0 & 0 \\ S_{2211} & S_{2222} & S_{2233} & 0 & 0 & 0 \\ S_{3311} & S_{3322} & S_{3333} & 0 & 0 & 0 \\ 0 & 0 & 0 & S_{2323} & 0 & 0 \\ 0 & 0 & 0 & 0 & S_{1313} & 0 \\ 0 & 0 & 0 & 0 & 0 & S_{1212} \end{bmatrix}, \quad (19)$$

in which

$$S_{1111} = 0, \quad S_{2222} = S_{3333} = \frac{5-4\nu^p}{8(1-\nu^p)}, \quad S_{2211} = S_{3311} = \frac{\nu^p}{2(1-\nu^p)},$$

$$S_{2233} = S_{3322} = \frac{4\nu^p-1}{8(1-\nu^p)}, \quad S_{1122} = S_{1133} = 0, \quad S_{1313} = S_{1212} = 1/4, \quad S_{2323} = \frac{3-4\nu^p}{8(1-\nu^p)}.$$

Finally, the effective thermal expansion coefficient vector $\{\alpha\}$ of the SFRC can be derived as [Laws 1973]

$$\{\alpha\} = \{\alpha^{\text{SCFF}}\} + ([C]^{-1} - [C^{\text{SCFF}}]^{-1})([C^{\text{SCFF}}]^{-1} - [C^p]^{-1})^{-1}(\{\alpha^{\text{SCFF}}\} - \{\alpha^p\}). \quad (20)$$

4. Results and discussion

In order to verify the validity of the MT model derived herein, the predictions of the MT model are first compared with the existing experimental and numerical results. Then the effective thermoelastic properties of the SFFRC containing wavy CNTs are determined by employing the MT model.

4.1. Comparison with experimental and numerical results. Recently, Kulkarni et al. [2010] experimentally and numerically investigated the elastic response of a nanoreinforced laminated composite (NRLC). The NRLC is made of CNT-reinforced polymer nanocomposite and carbon fiber. The cross sections of such NRLC are schematically shown in Figure 8. The geometry of the NRLC shown in Figure 8 is similar to that of the SCFF shown in Figure 3 if straight CNTs are considered. Thus, to confirm the modeling of the SCFF in the present study, we compare the results predicted by Kulkarni et al. [2010] for the NRLC with those predicted by the MT model for the SCFF with straight CNTs. It may be observed from Table 1 that the predicted value of the transverse Young's modulus (E_x) of the SCFF computed by the MT model matches closely with that of the experimental value predicted by Kulkarni et al. [2010]. The experimental value of E_x is lower than the theoretical prediction; this may be attributed to the fact that CNTs are not perfectly radially grown and straight, and hence the radial stiffening of the NRLC decreases [ibid.]. Further possible reasons for the disparity between the analytical and experimental results include lattice defects within CNTs [Ivanov et al. 2006; Yu et al. 2006] and the formation of voids in CNT-reinforced composites [Grunlan et al. 2006; Borca-Tasciuc et al. 2007]. Also, the value of E_x predicted by the MT model utilized herein is much closer to the experimental value than that of the numerical value predicted by Kulkarni et al. [2010]. This is attributed to the fact that the appropriate transformation and homogenization procedures given by (9) and (10) have been employed in the present study, whereas they did not consider such transformation and homogenization procedures in their numerical modeling. These comparisons are significant since the prediction of the transverse Young's modulus of the SCFF provides a critical check on the validity of the MT model. Thus it can be inferred from the comparisons shown in Table 1 that the MT model can be reasonably applied to predict the elastic properties of the SFFRC and its phases.

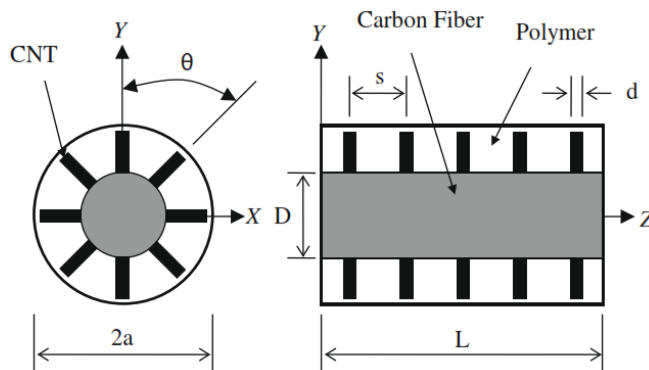


Figure 8. Transverse and longitudinal cross sections of the NRLC (adapted with permission from [Kulkarni et al. 2010]).

NRLC*			
	Numerical*	Experimental*	MT model
E_x (GPa)	13.93	10.02	11.91
ν_{xy}	0.34	–	0.38
ν_{zx}	0.16	–	0.18

Table 1. Comparisons of the effective engineering constants of NRLC, 2% CNT and 41% IM7 carbon fiber, with those of SCFF containing straight CNTs. E_x is the transverse Young's modulus of the NRLC, ν_{zx} and ν_{xy} are the axial and transverse Poisson's ratios of the NRLC, respectively, and * indicates data from [Kulkarni et al. 2010].

$w = A/\lambda$	E_{yy} (GPa)		E_{xx} (GPa)	
	FE Model [#]	MT	FE Model [#]	MT
0	18	17.800	4.577	4.448
0.005	17.920	17.790	4.574	4.448
0.010	17.780	17.800	4.570	4.446
0.015	17.690	17.750	4.566	4.445
0.020	17.570	17.720	4.563	4.442
0.025	17.480	17.680	4.561	4.440
0.030	17.130	17.630	4.559	4.435

Table 2. Comparisons of the engineering constants of unwound PMNC material with sinusoidally wavy CNTs, where [#] indicates data from [Farsadi et al. 2013], with $E^n = 1030$ GPa, $\nu^n = 0.063$, $E^p = 3.8$ GPa, $\nu^p = 0.4$, and CNT volume fraction $\nu_n = 0.014$; w is the waviness ratio, A and λ are the amplitude and the wavelength of the sinusoidally wavy CNT, E^n and E^p are the Young's moduli of the CNT and polymer matrix, respectively, E_{yy} and E_{xx} are the axial and transverse Young's moduli of unwound PMNC containing sinusoidally wavy CNTs, respectively, and ν^n and ν^p are the Poisson's ratios of the CNT and polymer matrix, respectively.

Next, the engineering constants of unwound PMNC containing sinusoidally wavy CNTs determined by the MT model are compared with those of the similar nanocomposite containing sinusoidally wavy CNTs studied by Farsadi et al. [2013]. Table 2 illustrates these comparisons. The two sets of results predicted by the FE and MT models are in excellent agreement, validating the MT model used in this study. The CTEs of unwound PMNC containing straight CNTs determined by the MT model are also compared with those of the similar CNT-reinforced composite studied by Kirtania and Chakraborty [2009], as shown in Table 3. For the effective values of CTEs of the CNT-reinforced composite, the two sets of results predicted by the FE and MT models are in excellent agreement, validating the MT model used here. It may also be observed from Tables 2 and 3 that the analytical MT model presented in this study requires much less computational time than the FE model. Thus one may use the analytical MT model for intuitive predictions of the effective thermoelastic properties of any novel advanced composites.

v_n	$\alpha_1 (\times 10^{-6} \text{ K}^{-1})$		$\alpha_2 (\times 10^{-6} \text{ K}^{-1})$	
	FE Model [§]	MT	FE Model [§]	MT
0.5	25.2030	24.4850	69.7540	69.9030
1	15.3020	15.0720	72.8670	72.8790
3	5.0978	5.1820	74.7155	74.5120
5.45	2.2670	2.2978	73.5434	73.1220
7.9	1.0643	1.1170	71.7165	71.1300
10.3	0.4253	0.4847	69.7879	69.0140
15.77	-0.3201	-0.2560	65.1728	64.0370

Table 3. Comparisons of the CTEs of unwound PMNC material with straight CNTs, where [§] indicates data from [Kirtania and Chakraborty 2009], with $E^n = 1000 \text{ GPa}$, $v^n = 0.2$, $E^p = 3.89 \text{ GPa}$, $v^p = 0.37$, $\alpha^n = -1.5 \times 10^{-6} \text{ K}^{-1}$, and $\alpha^p = 58 \times 10^{-6} \text{ K}^{-1}$; α_1 and α_2 are the axial and transverse CTEs of unwound PMNC with straight CNTs, respectively, and α^n and α^p are the CTEs of the CNT and polymer matrix, respectively.

4.2. Analytical modeling results. Armchair SWCNTs, carbon fiber, and polymer matrices are considered for evaluating the numerical results. Their material properties are taken from [Villeneuve et al. 1993; Peters 1998; Honjo 2007; Kwon et al. 2004; Shen and Li 2004] and are listed in Table 4. Since the investigations of earlier researchers [Yosida 2000; Maniwa et al. 2001; Jiang et al. 2004; Kwon et al. 2004; Jiang et al. 2009] have shown strong temperature dependence in the CTEs of CNTs, the variation in CTEs of the armchair (10, 10) CNT with temperature deviation is considered here. However, the elastic properties of CNTs, carbon fiber, and polymer are reported to be marginally dependent on the temperature deviation [Shen 2001]. Hence, the temperature dependence of the elastic properties of the constituent phases of the SFFRC is neglected. The relationships between the axial (α_3^n) and transverse (α_1^n) CTEs of the armchair (10, 10) CNT and the temperature deviation (ΔT) are given by [Kwon et al. 2004]:

$$\alpha_1^n = \alpha_2^n = 3.7601 \times 10^{-10} \Delta T^2 - 3.2189 \times 10^{-7} \Delta T - 3.2429 \times 10^{-8} \text{ K}^{-1}, \quad (21)$$

$$\alpha_3^n = 6.4851 \times 10^{-11} \Delta T^2 - 5.8038 \times 10^{-8} \Delta T + 9.0295 \times 10^{-8} \text{ K}^{-1}. \quad (22)$$

For the SFFRC, the hexagonal packing array of the SCFFs is considered for evaluating the numerical results. The maximum value of the CNT volume fraction in the SFFRC can be determined based on the

Material	C_{11}	C_{12}	C_{13}	C_{23}	C_{33}	C_{66}	α_1	α_2	
(10, 10) CNT ^a	288	254	87.8	87.8	1088	17	b	b	$d_n = 0.00136$
Carbon fiber ^{c,d}	236.4	10.6	10.6	10.7	24.8	25	1.1	6.8	$2a = 10$
Polymer ^e	4.09	1.55	1.55	1.55	4.09	1.27	66	66	

Table 4. Material properties of the constituent phases of the SFFRC, where ^a indicates data from [Shen and Li 2004], ^c [Honjo 2007], ^d [Villeneuve et al. 1993], and ^e [Peters 1998]. The values of α_1 and α_2 of the armchair (10, 10) CNT marked with ^b are from [Kwon et al. 2004] and are given in the text. Values of C are in units of GPa, α in 10^{-6} K^{-1} , and d_n and a in μm .

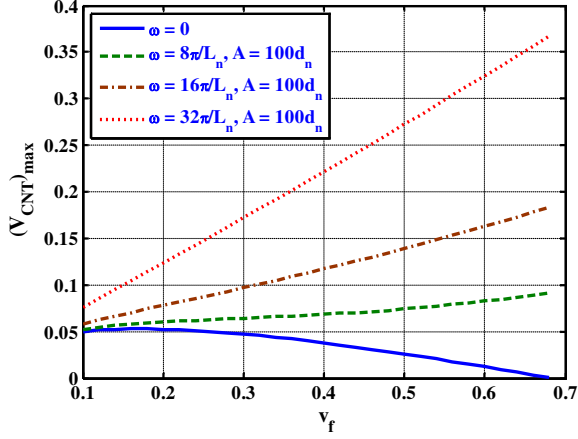


Figure 9. Variation of the maximum CNT volume fraction with the carbon fiber volume fraction in the SFFRC.

surface to surface distance at the roots of the two adjacent CNTs ($0.0017 \mu\text{m}$), the CNT diameter (d_n), and the running length of the sinusoidally wavy CNT (L_{nr}) as [Kundalwal and Ray 2013]

$$(V_{\text{CNT}})_{\text{max}} = \frac{\pi d_n^2 L_{nr}}{d(d_n + 0.0017)^2} v_f, \quad (23)$$

where d_n is the diameter of the CNT in μm . The derivation of (23) can be found in [Kundalwal and Ray 2013]. It is evident from (2) and (23) that an increase in the amplitude of the CNT increases the running length of the CNT which eventually increases the maximum CNT volume fraction $(V_{\text{CNT}})_{\text{max}}$ in the SFFRC. Figure 9 illustrates the variation of the maximum value of the CNT volume fraction in the SFFRC with the carbon fiber volume fraction (v_f) while the values of the wave frequency (ω) vary from $\omega = 8\pi/L_n$ to $\omega = 32\pi/L_n$. As expected, the maximum value of the CNT volume fraction in the SFFRC increases with the increase in the values of v_f and ω . To investigate the effect of wavy CNTs on the thermoelastic properties of the SFFRC, the value of ω is varied while keeping the value of v_f as 0.3, and adopting the following values of the other geometrical parameters of the RVE of the SFFRC:

- diameter of the armchair (10, 10) SWCNT $d_n = 0.00136 \mu\text{m}$ [Shen and Li 2004],
- radius of the carbon fiber $a = 5 \mu\text{m}$,
- radius of the RVE of the SFFRC $R = 8.2888 \mu\text{m}$,
- radius of the SCFF $b = 7.5353 \mu\text{m}$,
- half-length of the carbon fiber $L_f = 100 \mu\text{m}$,
- half-length of the RVE of the SFFRC $L = 110 \mu\text{m}$,
- length of the straight CNT $L_n = 2.5353 \mu\text{m}$,
- maximum amplitude of the wavy CNT $A = 100d_n \mu\text{m}$,
- maximum waviness factor $A/L_n = 0.0536 \mu\text{m}$.

First, the effective thermoelastic coefficients of the PMNC for different values of ω of the CNT are computed by employing the MT model. The estimated effective thermoelastic properties of the PMNC

are then used to compute the effective thermoelastic properties of a SCFF in which the carbon fiber is the reinforcement and the matrix phase is the PMNC material. However, for the sake of brevity, the effective thermoelastic properties of the PMNC and SCFF are not presented here. Unless otherwise mentioned, the two fixed values of ω ($\omega = 16\pi/L_n$ and $\omega = 32\pi/L_n$) are considered for evaluating the results.

Figure 10 illustrates the variation of the effective elastic coefficients C_{11} and C_{12} of the SF-FRC with waviness factor A/L_n . It may be observed from Figure 10(a) that the effective values of C_{11} of the SF-FRC are not affected by variations of the amplitude of the wavy CNTs in the 2-3 plane. When the wavy CNTs are coplanar with the 1-3 plane, increase in the values of A/L_n and ω significantly increases C_{11} . Figure 10(b) reveals that the waviness of the CNTs causes a significant increase in the value of C_{12} when the wavy CNTs are coplanar with the 1-3 plane. Figure 11 demonstrates the variation of the values of C_{13} and C_{55} of the SF-FRC with the waviness factor. Since the SF-FRC is transversely isotropic material, the values of C_{13} are found to be identical to those of C_{12} , as shown in Figures 10(b)

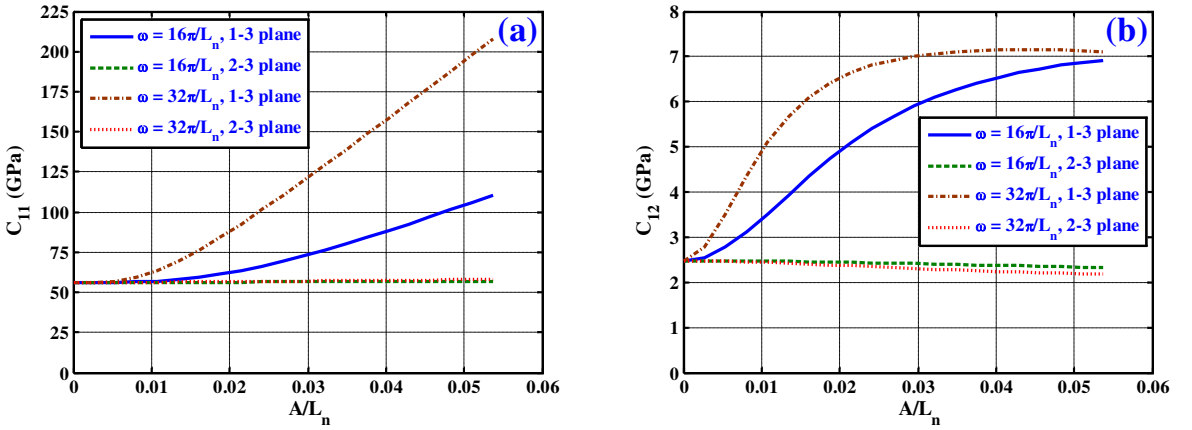


Figure 10. Variation of the effective elastic coefficients (a) C_{11} and (b) C_{12} of the SF-FRC with waviness factor ($v_f = 0.3$, $(V_{CNT})_{max}$).

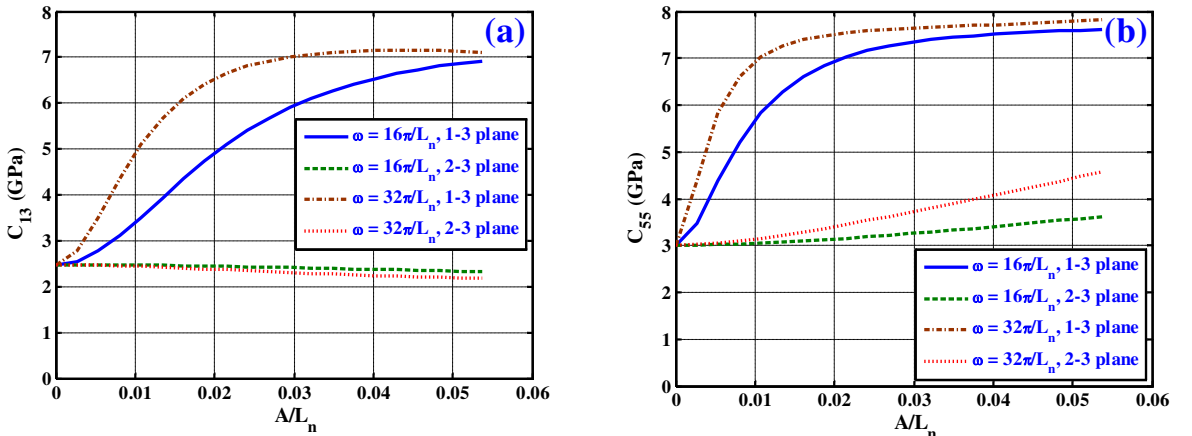


Figure 11. Variation of the effective elastic coefficients (a) C_{13} and (b) C_{55} of the SF-FRC with waviness factor ($v_f = 0.3$, $(V_{CNT})_{max}$).

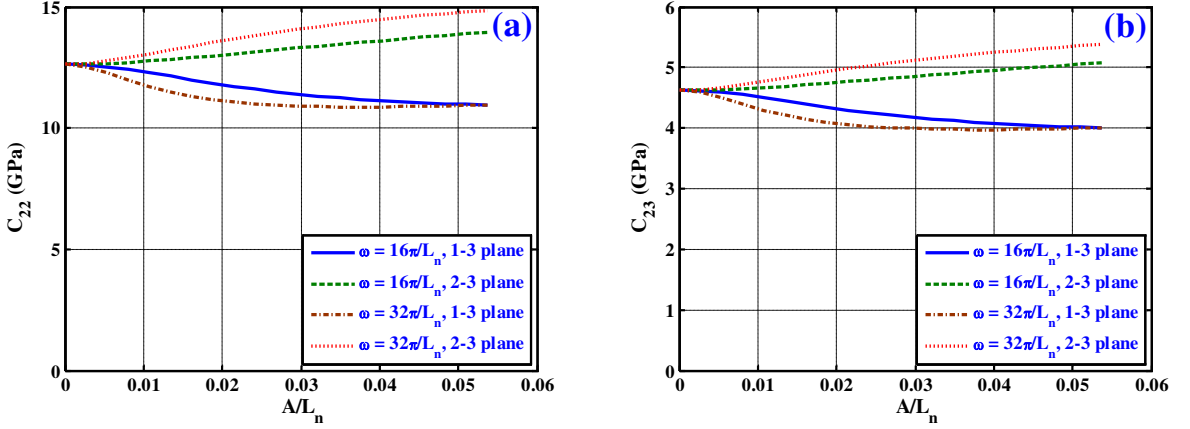


Figure 12. Variation of the effective elastic coefficients (a) C_{22} and (b) C_{23} of the SF-FRC with waviness factor ($v_f = 0.3$, $(V_{CNT})_{max}$).

and 11(a). It may be observed from Figure 11(b) that the value of C_{55} of the SFFRC initially increases significantly, and then stabilizes for higher values of A/L_n , when the wavy CNTs are coplanar with the 1-3 plane. Figure 12(a) reveals that increase in the value of A/L_n decreases C_{22} when the CNT waviness is coplanar with the 1-3 plane, whereas the value of C_{22} increases for higher values of A/L_n when the CNT waviness is coplanar with the 2-3 plane. A similar trend is obtained for the value of C_{23} , as shown in Figure 12(b). Although not presented here, the same is true for the effective elastic coefficient C_{44} .

It may be noted from Figures 10–12 that if the wavy CNTs are coplanar with the 1-3 plane then the axial elastic coefficients of the SFFRC are significantly improved over their values with straight CNTs ($\omega = 0$) for higher values of A/L_n and ω . When the wavy CNTs are coplanar with the longitudinal plane (1-3 or 1'-3' plane) of the carbon fiber, as shown in Figure 2, the amplitudes of the CNT waves becomes parallel to the 1-axis, which results in the aligning of the projections of parts of the CNT lengths with the 1-axis leading to axial stiffening of the PMNC. The greater the value of ω , the more such projections will occur, and hence the effective axial elastic coefficients (C_{11} , C_{12} , C_{13} , C_{55} , and C_{66}) of the SFFRC increase with an increase in the value of ω . On the other hand, if the wavy CNTs are coplanar with the transverse plane (2-3 or 2'-3' plane) of the carbon fiber, then the transverse elastic coefficients (C_{22} , C_{23} , C_{33} , and C_{44}) of the SFFRC increase from their values with straight CNTs ($\omega = 0$). The reverse is true when the wavy CNTs are coplanar with the 1-3 (1'-3') plane.

Figure 13 illustrates the variation in the axial (α_1) and transverse (α_2) CTEs of the SFFRC with the waviness factor. It may be observed from Figure 13(a) that the values of α_1 of the SFFRC are not affected by variations in the amplitude of the wavy CNTs in the 2-3 plane, whereas the value of α_1 initially increases and then significantly decreases for higher values of A/L_n and ω when the CNT waviness is coplanar with the 1-3 plane. It is also important to note from Figure 13(a) that the effective value of α_1 is zero for A/L_n and ω as 0.037 and $32\pi/L_n$, respectively, when the wavy CNTs are coplanar with the 1-3 plane. Figure 13(b) reveals that the waviness of the CNTs improves the effective values α_2 of the SFFRC when the wavy CNTs are coplanar with the 2-3 plane, compared to those of the SFFRC with straight CNTs ($\omega = 0$). Although not presented here, the computed effective values of α_3 are found to match identically with those of α_2 , corroborating the fact that the SFFRC is transversely isotropic material.

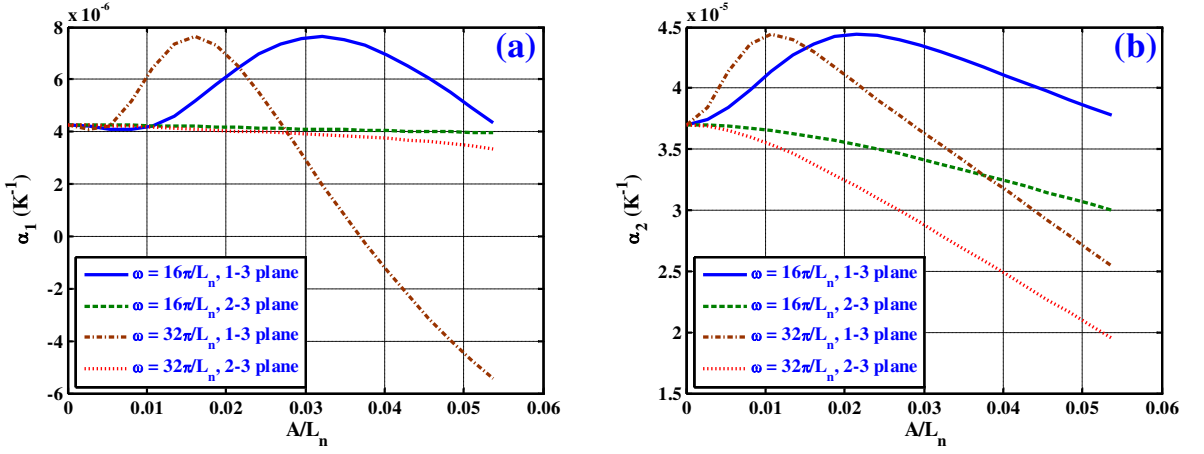


Figure 13. Variation of the effective (a) axial (α_1) and (b) transverse (α_2) CTEs of the FFRC with waviness factor ($\Delta T = 300 \text{ K}$, $v_f = 0.3$, $(V_{\text{CNT}})_{\text{max}}$).

Note from (20) that the CTEs of the SFFRC are dependent on the elastic coefficients of the SFFRC. Hence, with the increase in the value of A/L_n up to ~ 0.013 , the axial elastic coefficients of the unwound PMNC are increased which eventually influences the effective CTEs of the unwound PMNC when the CNT waviness is coplanar with the 1-3 plane. Therefore, the effective CTEs (α_1 , α_2 , and α_3) of the FFRC are initially increased for lower values of A/L_n . For $A/L_n \geq 0.013$, the effective CTEs (α_1 , α_2 , and α_3) of the SFFRC with wavy CNTs coplanar with the 1-3 plane start to decrease. This is attributed to the fact that the negative axial and transverse CTEs (α_1^n and α_2^n) of the radially grown wavy CNTs on the circumferential surfaces of the carbon fibers significantly suppress the positive CTE ($\alpha^p = 66 \times 10^{-6} \text{ K}^{-1}$) of the polymer matrix, which eventually lowers the effective values of α_1 of the SFFRC. This effect becomes more pronounced for higher values of A/L_n and ω because the CNT volume fraction in the SFFRC increases with A/L_n and ω , as depicted in Figure 9. From Figures 10–13 it is important to note that the axial thermoelastic coefficients significantly improve for higher values of A/L_n and ω when the CNT waviness is coplanar with the 1-3 plane. The effect of wavy CNTs coplanar with the 2-3 plane on the axial thermoelastic coefficients of the SFFRC is not as pronounced. On the other hand, marginal improvement in the transverse thermoelastic coefficients of the SFFRC is observed when the CNT waviness is coplanar with the 2-3 plane. Hence, for investigating the effect of temperature deviation on the effective thermal expansion coefficients of the SFFRC, the wavy CNTs are considered to be coplanar with the 1-3 plane when the values of ω and A are $32\pi/L_n$ and $0.136 \mu\text{m}$, respectively.

Practically, the carbon fiber volume fraction in short fiber composites can vary, typically from 0.2 to 0.6. Hence, to analyze the effect of temperature deviation on the effective thermal expansion coefficients of the SFFRC, the two discrete values of the carbon fiber volume fraction are considered, 0.25 and 0.55. Figure 14(a) and (b) illustrate the variation of the values of α_1 and α_2 of the SFFRC, respectively, with the temperature deviation for different values of the carbon fiber volume fraction. It is important to note from these figures that the effective values of CTEs of the SFFRC decrease with the increase in the temperature deviation for higher values of v_f and ω . It may also be observed that wavy CNTs coplanar with the 1-3 plane significantly improve the CTEs of the SFFRC over the values with straight CNTs

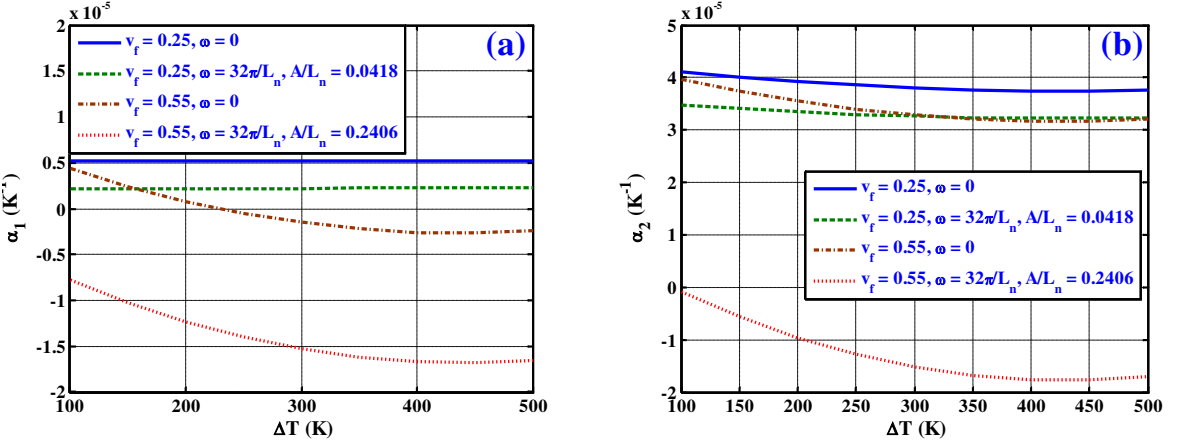


Figure 14. Variation of the effective (a) axial (α_1) and (b) transverse (α_2) CTEs of the SFFRC with temperature deviation when the wavy CNTs are coplanar with the longitudinal plane (that is, 1-3 plane) of the carbon fiber ($A = 0.136 \mu\text{m}$).

($\omega = 0$). This is attributed to the fact that as the values of v_f and ω increase the CNT volume fraction in the SFFRC increases, as shown in Figure 9, which eventually improves the values of the CTEs of the SFFRC. It is also seen from these two plots that the CTEs of the SFFRC can be modified by changing the values of A/L_n and ω according to the requirements of thermal management.

5. Conclusions

The effective thermoelastic properties of a novel short fuzzy fiber-reinforced composite (SFFRC) containing wavy carbon nanotubes (CNTs) have been investigated. An analytical micromechanics model based on the Mori–Tanaka model was utilized to predict the effective thermoelastic coefficients of this novel composite. The influence of the waviness of the CNTs on the thermoelastic coefficients of the SFFRC has been studied, considering sinusoidally wavy CNTs to be coplanar with either of two mutually orthogonal planes. The following main conclusions can be drawn from the investigations carried out here.

- (1) If the plane of the radially grown wavy CNTs is coplanar with the longitudinal plane of the carbon fiber then the axial effective thermoelastic coefficients of the SFFRC are significantly improved over those of the FFRC with either straight CNTs ($\omega = 0$) or wavy CNTs coplanar with the transverse plane of the carbon fiber.
- (2) When the CNT waviness is coplanar with the transverse plane of the carbon fiber, marginal improvement has been observed in the transverse effective thermoelastic coefficients of the SFFRC.
- (3) If the CNT waviness is coplanar with the longitudinal plane of the carbon fiber then the thermoelastic response of the SFFRC significantly improves with an increase in the temperature for higher values of the carbon fiber volume fraction, waviness factor, and wave frequency of the CNT.

Therefore, the SFFRC with sinusoidally wavy CNTs studied here may be used for advanced structures that require stringent constraints on dimensional stability.

List of abbreviations

CNT	Carbon nanotube	NRLC	Nanoreinforced laminated composite
CTE	Coefficient of thermal expansion	PMNC	Polymer matrix nanocomposite
CVD	Chemical vapor deposition	RVE	Representative volume element
FE	Finite element	SCFF	Short composite fuzzy fiber
MDS	Molecular dynamics simulation	SEM	Scanning electron microscopy
MT	Mori–Tanaka	SFFRC	Short fuzzy fiber-reinforced composite
MWCNT	Multiwalled carbon nanotube	SWCNT	Single-walled carbon nanotube

List of symbols

A	Amplitude of the CNT (μm)
$[\tilde{A}_1], [\tilde{A}_2], [\tilde{A}_3]$	Matrices of the strain concentration factors
a	Radius of the carbon fiber (μm)
b	Radius of the SCFF (μm)
$[\bar{C}^{\text{NC}}]$	Elastic coefficient matrix of the unwound PMNC containing wavy CNTs (GPa)
$[C^r]$	Elastic coefficient matrix of the r -th phase (GPa)
C_{ij}^r	Elastic coefficients of the r -th phase (GPa)
d_n	Diameter of the CNT (μm)
E^n and E^p	Young's moduli of the CNT and polymer matrix, respectively (GPa)
E_x	Transverse Young's modulus of the NRLC (GPa)
E_{yy} and E_{xx}	Axial and transverse Young's moduli of the unwound PMNC containing sinusoidally wavy CNTs, respectively (GPa)
$[I]$	Fourth-order identity matrix
L	Length of the RVE of the SFFRC (μm)
L_f	Half-length of the short carbon fiber embedded in the RVE of the SFFRC (μm)
L_n	Length of straight CNT (μm)
L_{nr}	Running length of sinusoidally wavy CNT (μm)
$(N_{\text{CNT}})_{\text{max}}$	Maximum number of radially grown aligned CNTs on the circumferential surface of the short carbon fiber
n	Number of waves of a sinusoidally wavy CNT along its axial direction
R	Radius of the RVE of the SFFRC (μm)
$[S^r]$	Eshelby tensor of the r -th domain
S_{ij}^r	Elements of the Eshelby tensor of the r -th domain
$[T], [T_1], [T_2]$	Transformation matrices
$(V_{\text{CNT}})_{\text{max}}$	Maximum volume fraction of the CNT in the SFFRC
v_{SCFF}	Volume fraction of the SCFF in the SFFRC
v_f	Volume fraction of the carbon fiber in the SFFRC
\bar{v}_f	Volume fraction of the carbon fiber in the SCFF
v_m	Volume fraction of the matrix in the composite
v_n	Volume fraction of the CNT in the PMNC/the CNT-reinforced nanocomposite

v_{PMNC}	Volume fraction of the PMNC in the SCFF
v_P	Volume fraction of the polymer in the PMNC
\bar{v}_P	Volume fraction of the polymer in the SFFRC
v_{SCFF}	Volume fraction of the SCFF in the SFFRC
$\{\alpha\}$	Thermal expansion coefficient vector of the SFFRC (K^{-1})
$\{\alpha^r\}$	Thermal expansion coefficient vector of the r -th phase (K^{-1})
α_i^r	Thermal expansion coefficients of the r -th phase (K^{-1})
ΔT	Temperature deviation from the reference temperature (K)
$\{\epsilon^r\}$	Strain vector of the r -th phase
λ	Wavelength of the CNT (nm)
ν^n and ν^P	Poisson's ratios of the CNT and polymer matrix, respectively
ν_{zx} and ν_{xy}	Axial and transverse Poisson's ratios of the unwound PMNC containing sinusoidally wavy CNTs, respectively
$\{\sigma^r\}$	Stress vector of the r -th phase (GPa)
ω	Wave frequency of the CNT (μm^{-1})

References

- [Ajayan and Tour 2007] P. M. Ajayan and J. M. Tour, “Material science: nanotube composites”, *Nature* **447** (2007), 1066–1068.
- [Alamusi et al. 2012] Alamusi, N. Hu, B. Jia, M. Arai, C. Yan, J. Li, Y. Liu, S. Atobe, and H. Fukunaga, “Prediction of thermal expansion properties of carbon nanotubes using molecular dynamics simulations”, **54** (2012), 249–254.
- [Anumandla and Gibson 2006] V. Anumandla and R. F. Gibson, “A comprehensive closed form micromechanics model for estimating the elastic modulus of nanotube-reinforced composites”, *Composites Part A: Applied Science and Manufacturing* **37**:12 (2006), 2178–2185.
- [Ashrafi and Hubert 2006] B. Ashrafi and P. Hubert, “Modeling the elastic properties of carbon nanotube array/polymer composites”, *Composites Science and Technology* **66**:3–4 (2006), 387–396.
- [Bandow 1997] S. Bandow, “Radial thermal expansion of purified multiwall carbon nanotubes measured by X-ray diffraction”, *Japanese Journal of Applied Physics* **36** (1997), L1403–L1405.
- [Benveniste 1987] Y. Benveniste, “A new approach to the application of Mori-Tanaka's theory in composite materials”, *Mechanics of Materials* **6**:2 (1987), 147–157.
- [Berhan et al. 2004] L. Berhan, Y. B. Yi, and A. M. Sastry, “Effect of nanorope waviness on the effective moduli of nanotube sheets”, *Journal of Applied Physics* **95**:9 (2004), 5027–5034.
- [Borca-Tasciuc et al. 2007] T. Borca-Tasciuc, M. Mazumdar, Y. Son, S. K. Pal, L. S. Schadler, and P. M. Ajayan, “Anisotropic thermal diffusivity characterization of aligned-carbon nanotube-polymer composites”, *Journal of Nanoscience and Nanotechnology* **7**:4–5 (2007), 1581–1588.
- [Bower et al. 2000] C. Bower, W. Zhu, S. Jin, and O. Zhou, “Plasma-induced alignment of carbon nanotubes”, *Applied Physics Letters* **77**:6 (2000), 830–832.
- [Chatzigeorgiou et al. 2012] G. Chatzigeorgiou, Y. Efendiev, N. Charalambakis, and D. C. Lagoudas, “Effective thermoelastic properties of composites with periodicity in cylindrical coordinates”, *International Journal of Solids and Structures* **49**:18 (2012), 2590–2603.
- [Esteva and Spanos 2009] M. Esteva and P. D. Spanos, “Effective elastic properties of nanotube reinforced composites with slightly weakened interfaces”, *Journal of Mechanics of Materials and Structures* **4**:5 (2009), 887–900.
- [Farsadi et al. 2013] M. Farsadi, A. Öchsner, and M. Rahmandoust, “Numerical investigation of composite materials reinforced with wavy carbon nanotubes”, *Journal of Composite Materials* **47**:11 (2013), 1425–1434.
- [Fisher et al. 2002] F. T. Fisher, R. D. Bradshaw, and L. C. Brinson, “Effects of nanotube waviness on the modulus of nanotube-reinforced polymers”, *Applied Physics Letters* **80**:24 (2002), 4647–4649.

- [Garcia et al. 2008] E. J. Garcia, B. L. Wardle, A. J. Hart, and N. Yamamoto, “Fabrication and multifunctional properties of a hybrid laminate with aligned carbon nanotubes grown *In Situ*”, *Composites Science and Technology* **68**:9 (2008), 2034–2041.
- [Grunlan et al. 2006] J. C. Grunlan, Y. Kim, S. Ziaee, X. Wei, B. Abdel-Magid, and K. Tao, “Thermal and mechanical behavior of carbon-nanotube-filled latex”, *Macromolecular Material Engineering* **291**:9 (2006), 1035–1043.
- [Honjo 2007] K. Honjo, “Thermal stresses and effective properties calculated for fiber composites using actual cylindrically-anisotropic properties of interfacial carbon coating”, *Carbon* **45**:4 (2007), 865–872.
- [Hsiao and Daniel 1996] H. M. Hsiao and I. M. Daniel, “Elastic properties of composites with fiber waviness”, *Composites Part A: Applied Science and Manufacturing* **27**:10 (1996), 931–941.
- [Iijima 1991] S. Iijima, “Helical microtubules of graphitic carbon”, *Nature* **354**:6348 (1991), 56–58.
- [Ivanov et al. 2006] I. Ivanov, A. Puzos, G. Eres, H. Wang, Z. Pan, H. Cui, R. Jin, J. Howe, and D. B. Geohegan, “Fast and highly anisotropic thermal transport through vertically aligned carbon nanotube arrays”, *Applied Physics Letters* **89**:22 (2006), Article ID #223110.
- [Jiang et al. 2004] H. Jiang, B. Liu, Y. Huang, and K. C. Hwang, “Thermal expansion of single wall carbon nanotubes”, *ASME Journal of Engineering Materials and Technology* **126**:3 (2004), 265–270.
- [Jiang et al. 2009] J.-W. Jiang, J.-S. Wang, and B. Li, “Thermal expansion in single-walled carbon nanotubes and graphene: nonequilibrium Green’s function approach”, *Phys. Rev. B* **80**:20 (2009), 205429.
- [Khondaker and Keng 2012] S. A. Khondaker and A. K. Keng, “A pull-out model for perfectly bonded carbon nanotube in polymer composites”, *Journal of Mechanics of Materials and Structures* **7**:8–9 (2012), 753–764.
- [Kirtania and Chakraborty 2009] S. Kirtania and D. Chakraborty, “Evaluation of thermoelastic properties of carbon nanotube-based composites using finite element method”, in *Proceedings of the International Conference on Mechanical Engineering AM-13*, Dhaka, Bangladesh, 2009.
- [Kulkarni et al. 2010] M. Kulkarni, D. Carnahan, K. Kulkarni, D. Qian, and J. L. Abot, “Elastic response of a carbon nanotube fiber reinforced polymeric composite: A numerical and experimental study”, *Composites Part B: Engineering* **41**:5 (2010), 414–421.
- [Kundalwal 2013] S. I. Kundalwal, *Micromechanical analysis of novel continuous and short fuzzy fiber reinforced composites*, Ph.D. thesis, Department of Mechanical Engineering, Indian Institute of Technology Kharagpur, 2013.
- [Kundalwal and Ray 2012] S. I. Kundalwal and M. C. Ray, “Effective properties of a novel composite reinforced with short carbon fibers and radially aligned carbon nanotubes”, *Mechanics of Materials* **53** (2012), 47–60.
- [Kundalwal and Ray 2013] S. I. Kundalwal and M. C. Ray, “Effect of carbon nanotube waviness on the elastic properties of the fuzzy fiber reinforced composites”, *ASME Journal of Applied Mechanics* **80**:2 (2013), 021010.
- [Kwon et al. 2004] Y.-K. Kwon, S. Berber, and D. Tománek, “Thermal contraction of carbon fullerenes and nanotubes”, *Physical Review Letters* **92**:1 (2004), 015901.
- [Laws 1973] N. Laws, “On the thermostatics of composite materials”, *Journal of the Mechanics and Physics of Solids* **21**:1 (1973), 9–17.
- [Li and Chou 2009] C. Li and T.-W. Chou, “Failure of carbon nanotube/polymer composites and the effect of nanotube waviness”, *Composites Part A: Applied Science and Manufacturing* **40**:10 (2009), 1580–1586.
- [Li and Dunn 1998] J. Y. Li and M. L. Dunn, “Anisotropic coupled-field inclusion and inhomogeneity problems”, *Philosophical Magazine A* **77**:5 (1998), 1341–1350.
- [Li and Guo 2008] H. Li and W. Guo, “Transversely isotropic elastic properties of single-walled carbon nanotubes by a rectangular beam model for the C-C bonds”, *Journal of Applied Physics* **103**:10 (2008), Article ID #103501.
- [Liu et al. 2005] J. Z. Liu, Q.-S. Zheng, L.-F. Wang, and Q. Jiang, “Mechanical properties of single-walled carbon nanotube bundles as bulk materials”, *Journal of the Mechanics and Physics of Solids* **53**:1 (2005), 123–142.
- [Maniwa et al. 2001] Y. Maniwa, R. Fujiwara, H. Kira, H. Tou, H. Kataura, S. Suzuki, Y. Achiba, E. Nishibori, M. Takata, M. Sakata, A. Fujiwara, and H. Suematsu, “Thermal expansion of single-walled carbon nanotube (SWNT) bundles: X-ray diffraction studies”, *Phys. Rev. B* **64**:24 (2001), 241402.
- [Meguid et al. 2010] S. A. Meguid, J. M. Wernik, and Z. Q. Cheng, “Atomistic-based continuum representation of the effective properties of nano-reinforced epoxies”, *International Journal of Solids and Structures* **47**:13 (2010), 1723–1736.

- [Mori and Tanaka 1973] T. Mori and K. Tanaka, “Average stress in matrix and average elastic energy of materials with misfitting inclusions”, *Acta Metallurgica* **21**:5 (1973), 571–574.
- [Natsuki et al. 2004] T. Natsuki, K. Tantrakarn, and M. Endo, “Prediction of elastic properties for single-walled carbon nanotubes”, *Carbon* **42**:1 (2004), 39–45.
- [Odegard et al. 2003] G. M. Odegard, T. S. Gates, K. E. Wise, C. Park, and E. J. Siochi, “Constitutive modeling of nanotube-reinforced polymer composites”, *Composites Science and Technology* **63**:11 (2003), 1671–1687.
- [Pantano and Cappello 2008] A. Pantano and F. Cappello, “Numerical model for composite material with polymer matrix reinforced by carbon nanotubes”, *Meccanica* **43**:2 (2008), 263–270.
- [Peters 1998] S. T. Peters, *Handbook of Composites*, Chapman and Hall, London, 1998.
- [Pipes and Hubert 2003] R. B. Pipes and P. Hubert, “Helical carbon nanotube arrays: thermal expansion”, *Composites Science and Technology* **63**:11 (2003), 1571–1579.
- [Qian et al. 2000] D. Qian, E. C. Dickey, R. Andrews, and T. Rantell, “Load transfer and deformation mechanisms in carbon nanotube-polystyrene composites”, *Applied Physics Letters* **76**:20 (2000), 2868–2870.
- [Qiu and Weng 1990] Y. P. Qiu and G. J. Weng, “On the application of Mori-Tanaka’s theory involving transversely isotropic spheroidal inclusions”, *Internat. J. Engrg. Sci.* **28**:11 (1990), 1121–1137.
- [Qiu et al. 2007] J. Qiu, C. Zhang, B. Wang, and R. Liang, “Carbon nanotube integrated multifunctional multiscale composites”, *Nanotechnology* **18**:27 (2007), 275708.
- [Raravikar et al. 2002] N. R. Raravikar, P. Koblinski, A. M. Rao, M. S. Dresselhaus, L. S. Schadler, and P. M. Ajayan, “Temperature dependence of radial breathing mode Raman frequency of single-walled carbon nanotubes”, *Phys. Rev. B* **66**:23 (2002), 235424.
- [Ray and Batra 2009] M. C. Ray and R. C. Batra, “Effective properties of carbon nanotube and piezoelectric fiber reinforced hybrid smart composites”, *ASME Journal of Applied Mechanics* **76**:3 (2009), 034503.
- [Schulte and Windle 2007] K. Schulte and A. H. Windle, “Editorial”, *Composites Science and Technology* **67**:5 (2007), 777.
- [Seidel and Lagoudas 2006] G. D. Seidel and D. C. Lagoudas, “Micromechanical analysis of the effective elastic properties of carbon nanotube reinforced composites”, *Mechanics of Materials* **38**:8–10 (2006), 884–907.
- [Shaffer and Windle 1999] M. S. P. Shaffer and A. H. Windle, “Fabrication and characterization of carbon nanotube/poly(vinyl alcohol) composites”, *Advanced Materials* **11**:11 (1999), 937–941.
- [Shen 2001] H.-S. Shen, “Hygrothermal effects on the postbuckling of shear deformable laminated plates”, *International Journal of Mechanical Sciences* **43**:5 (2001), 1259–1281.
- [Shen and Li 2004] L. Shen and J. Li, “Transversely isotropic elastic properties of single-walled carbon nanotubes”, *Physical Review B* **69**:4 (2004), 045414.
- [Shi et al. 2004] D.-L. Shi, X.-Q. Feng, Y. Y. Huang, K.-C. Hwang, and H. Gao, “The effect of nanotube waviness and agglomeration on the elastic property of carbon nanotube-reinforced composites”, *ASME Journal of Engineering Materials and Technology* **126**:3 (2004), 250–257.
- [Thostenson et al. 2001] E. T. Thostenson, Z. Ren, and T.-W. Chou, “Advances in the science and technology of carbon nanotubes and their composites: a review”, *Composites Science and Technology* **61**:13 (2001), 1899–1912.
- [Treacy et al. 1996] M. M. J. Treacy, T. W. Ebbesen, and J. M. Gibson, “Exceptionally high Young’s modulus observed for individual carbon nanotubes”, *Nature* **381**:6584 (1996), 678–680.
- [Tsai et al. 2011] C.-H. Tsai, C. Zhang, D. A. Jack, R. Liang, and B. Wang, “The effect of inclusion waviness and waviness distribution on elastic properties of fiber-reinforced composites”, *Composites Part B: Engineering* **42**:1 (2011), 62–70.
- [Veedu et al. 2006] V. P. Veedu, A. Cao, X. Li, K. Ma, C. Soldano, S. Kar, P. M. Ajayan, and M. N. Ghasemi-Nejhad, “Multi-functional composites using reinforced laminae with carbon-nanotube forests”, *Nature Materials* **5**:6 (2006), 457–462.
- [Villeneuve et al. 1993] J. F. Villeneuve, R. Naslain, R. Fourmeaux, and J. Sevely, “Longitudinal/radial thermal expansion and poisson ratio of some ceramic fibers as measured by transmission electron microscopy”, *Composites Science and Technology* **49**:1 (1993), 89–103.

- [Yamamoto et al. 2009] N. Yamamoto, A. J. Hart, E. J. Garcia, S. S. Wicks, H. M. Duong, A. H. Slocum, and B. L. Wardle, “High-yield growth and morphology control of aligned carbon nanotubes on ceramic fibers for multifunctional enhancement of structural composites”, *Carbon* **47**:3 (2009), 551–560.
- [Yosida 2000] Y. Yosida, “High-temperature shrinkage of single-walled carbon nanotube bundles up to 1600 K”, *Journal of Applied Physics* **87**:7 (2000), 3338–3341.
- [Yu et al. 2006] A. Yu, M. E. Itkis, E. Bekyarova, and R. C. Haddon, “Effect of single-walled carbon nanotube purity on the thermal conductivity of carbon nanotube-based composites”, *Applied Physics Letters* **89**:13 (2006), Article ID #133102.
- [Zhang et al. 2008] Q. Zhang, J.-Q. Huang, M.-Q. Zhao, W.-Z. Qian, Y. Wang, and F. Wei, “Radial growth of vertically aligned carbon nanotube arrays from ethylene on ceramic spheres”, *Carbon* **46**:8 (2008), 1152–1158.

Received 15 Mar 2013. Revised 27 Aug 2013. Accepted 27 Oct 2013.

SHAILESH I. KUNDALWAL: shail_kundal@yahoo.com

Department of Mechanical Engineering, Indian Institute of Technology, Kharagpur 721302, India

MANAS C. RAY: mcray@mech.iitkgp.ernet.in

Department of Mechanical Engineering, Indian Institute of Technology, Kharagpur 721302, India

MOMENT LYAPUNOV EXPONENTS AND STOCHASTIC STABILITY OF COUPLED VISCOELASTIC SYSTEMS DRIVEN BY WHITE NOISE

JIAN DENG, WEI-CHAU XIE AND MAHESH D. PANDEY

The moment and almost-sure stochastic stability of two-degree-of-freedom coupled viscoelastic systems, under parametric excitation of white noise, are investigated through moment Lyapunov exponents and Lyapunov exponents, respectively. The system of stochastic differential equations of motion is first decoupled by using the method of stochastic averaging for dynamic systems with small damping and weak excitations. Then a new scheme for determining the moment Lyapunov exponents is proposed for a coupled viscoelastic system. The largest Lyapunov exponent is calculated through its relation with moment Lyapunov exponent. The moment and almost-sure stability boundaries and critical excitation are obtained analytically. These analytical results are confirmed by numerical simulation. As an application example, the stochastic stability of flexural-torsional viscoelastic beam is studied. It is found that, under white noise excitation, the parameters of damping β and the viscoelastic intensity γ have stabilizing effects on the moment and almost-sure stability. However, viscosity parameter η plays a destabilizing role. The stability index decreases from positive to negative values with the increase of the amplitude of noise power spectrum, which suggests that the noise destabilize the system. These results are useful in engineering applications.

1. Introduction

Dynamic responses of many engineering structures are governed in general by an equation of motion of the form

$$\ddot{\mathbf{x}}(t) = \mathbf{f}(\mathbf{x}(t), \dot{\mathbf{x}}(t), \boldsymbol{\xi}(t)), \quad (1-1)$$

where the superscript dot denotes the derivative with respect to time, $\mathbf{x}(t)$ is the response vector, and $\boldsymbol{\xi}(t)$ is a vector of dynamic loadings. These dynamic loadings, such as those arising from earthquakes, wind, and blasting, can be characterized satisfactorily only by probabilistic models, which leads to the fact that (1-1) is actually a stochastic differential equation. Oseledec [1968] showed that for continuous dynamical systems, both deterministic and stochastic, there exist deterministic real numbers characterizing the average exponential rates of growth or decay of the solution for large time and called them Lyapunov exponents. The sample or almost sure stability of stochastic system (1-1) is governed by this Lyapunov exponent which is defined as (see [Xie 2006])

$$\lambda_{\mathbf{x}} = \lim_{t \rightarrow \infty} \frac{1}{t} \log \|\mathbf{x}\|, \quad (1-2)$$

where $\|\mathbf{x}\| = (\mathbf{x}^T \mathbf{x})^{1/2}$ is the Euclidean norm. If the largest Lyapunov exponent is negative, the trivial solution of system (1-1) is stable with probability 1; otherwise, it is unstable almost surely. Hence, the

Keywords: stochastic stability, moment Lyapunov exponents, white noise, viscoelasticity, coupled system.

vanishing of the largest Lyapunov exponent indicates the almost-sure stability boundaries in parameter space.

On the other hand, the stability of the p -th moment $E[\|\mathbf{x}\|^p]$ of the solution of system (1-1) is governed by the p -th moment Lyapunov exponent defined by (see [Xie 2006])

$$\Lambda_{\mathbf{x}}(p) = \lim_{t \rightarrow \infty} \frac{1}{t} \log E[\|\mathbf{x}\|^p], \quad (1-3)$$

where $E[\cdot]$ denotes the expected value. If $\Lambda_{\mathbf{x}}(p)$ is negative, then the p -th moment is stable; otherwise, it is unstable. Hence, the vanishing of the p -th moment Lyapunov exponent indicates the p -th moment stability boundaries in parameter space.

These stability properties of system (1-1) with stochastic differential equations are difficult to obtain exactly. The method of stochastic averaging, originally formulated in [Stratonovich 1963] and mathematically proved in [Khasminskii 1966], has been widely used to solve approximately stochastic differential equations containing a small parameter. Under certain conditions stochastic averaging can reduce the dimension of some problems, which greatly simplifies the solution [Xie 2006]. The popularity of stochastic averaging can be felt from the large number of papers in the literature, such as [Roberts and Spanos 1986; Ariaratnam 1996; Sri Namachchivaya and Ariaratnam 1987]. Larionov [1969] justified an averaging method in a rigorous manner for integrodifferential equations of both deterministic and stochastic systems.

For single-degree-of-freedom (SDOF) systems, Arnold et al. [1997] constructed an approximation for the moment Lyapunov exponents of a two-dimensional linear system driven by real or white noise, by using a perturbation approach. At the same time, asymptotic expansion series for the moment Lyapunov exponent and stability index are constructed and justified for the two-dimensional linear stochastic system [Khasminskii and Moshchuk 1998]. Xie [2006] systematically studied moment Lyapunov exponents, Lyapunov exponents, and the stability index of SDOF systems under various noise excitation in terms of the small fluctuation parameter. In the same book, Xie proposed a Monte Carlo simulation method for determining the moment Lyapunov exponents of stochastic systems. For two-degree-of-freedom (2DOF) coupled systems, Namachchivaya and van Roessel [2001] studied the moment Lyapunov exponents of two coupled elastic oscillators under real noise excitation, by using stochastic averaging method and asymptotic expansion method. More recently, in their serial papers, Kozic et al. [2012] investigated the Lyapunov exponent and moment Lyapunov exponents of 2DOF linear elastic systems subjected to a white noise parametric excitation.

The stability of elastic systems has been studied extensively [Bolotin 1964]. However, in engineering applications more and more viscoelastic materials, such as polymers and composite materials, are employed. For these materials, stress is not a function of instantaneous strain but depends on the past time history of strain and vice versa, which is quite different from linear elastic materials. In the case of a structural column, the viscoelastic property has a great impact on its dynamic behavior, particularly the dynamic stability [Potapov 1994]. When viscoelasticity is properly treated, the equation of motion becomes more complicated and turns out to be an integrodifferential equation rather than an ordinary differential equation as in the elastic case.

The deterministic dynamic stability of viscoelastic systems has been investigated by many authors [Ahmadi and Glocker 1983]. Ariaratnam was among the first who studied the stochastic almost-sure stability

of viscoelastic systems under wide band random fluctuations in the stiffness parameter [Ariaratnam 1993] and under bounded noise excitation [Ariaratnam 1996], by evaluating the largest Lyapunov exponent and the rotation number using the method of stochastic averaging. Abdelrahman [2002] systematically investigated stochastic stability of coupled systems and gyroscopic systems and extended Ariaratnam's method from SDOF to 2DOF systems, but still only the Lyapunov exponent was calculated. Sufficient conditions for almost-sure stability were obtained for both elastic and viscoelastic columns under the excitation of a random wide band stationary process using Lyapunov's direct method [Potapov 1994]. Later, Potapov [1997] described the behavior of stochastic viscoelastic systems by numerically evaluating Lyapunov exponents of linear integrodifferential equations.

It is known that the almost-sure stability cannot assure the moment stability. To have a complete picture of the dynamical stability of a stochastic system, it is important to study both the sample and moment stability and to determine both the Lyapunov exponents and the moment Lyapunov exponents, because moment Lyapunov exponents give not only the moment stability but also the almost-sure stability. Xie was the first to deal with the determination of small noise expansion of the moment Lyapunov exponent of a SDOF viscoelastic column under bounded noise excitation [Xie 2003]. Moment Lyapunov exponents of such a viscoelastic system under the excitation of a wide band noise was further investigated by using the averaging method of both first order and second order [Huang and Xie 2008].

The objective of this paper is to study the moment and almost sure stability of 2DOF coupled viscoelastic systems driven by white noise using the method of stochastic averaging. A new scheme for determining the moment Lyapunov exponents is presented for 2DOF coupled viscoelastic systems, which is an extension of [Ariaratnam et al. 1991] from elastic systems to viscoelastic and from almost-sure stability to moment stability characterized by moment Lyapunov exponents. This paper is also different from [Sri Namachchivaya and van Roessel 2001] where the Girsanov theorem and Feynman–Kac formula were used and viscoelasticity was not considered. Furthermore, this study carries out Monte Carlo simulation of moment Lyapunov exponents for coupled systems. This research is motivated by problems in the dynamic stability of viscoelastic systems subjected to stochastically fluctuating loads. Examples and numerical results are provided for illustration.

2. Formulation

Consider the coupled nongyroscopic stochastic system

$$\begin{aligned} \ddot{q}_1 + 2\varepsilon\beta_1 \dot{q}_1 + \omega_1^2(1 - \varepsilon\mathcal{H})q_1 + \varepsilon^{1/2}\omega_1(k_{11}q_1 + k_{12}q_2)\xi(t) &= 0, \\ \ddot{q}_2 + 2\varepsilon\beta_2 \dot{q}_2 + \omega_2^2(1 - \varepsilon\mathcal{H})q_2 + \varepsilon^{1/2}\omega_2(k_{21}q_1 + k_{22}q_2)\xi(t) &= 0, \end{aligned} \quad (2-1)$$

where q_1, q_2 are state coordinates, β_1, β_2 are damping coefficients, ω_1, ω_2 are natural frequencies, ε is a small parameter introduced to make the analysis more convenient. and the k_{ij} , $i, j = 1, 2$ are constants. We call k_{12} and k_{21} the coupling parameters; the case of $k_{12} = k_{21} = k$ is called symmetric coupling and that of $k_{12} = -k_{21} = k$ skew-symmetric coupling. \mathcal{H} is a linear viscoelastic operator given by

$$\mathcal{H}[\psi(t)] = \int_0^t \mathcal{H}(t-\tau)\psi(\tau) d\tau, \quad 0 \leq \int_0^\infty \mathcal{H}(\theta) d\theta < 1, \quad (2-2)$$

where $\mathcal{H}(\theta)$ is the relaxation kernel. $\xi(t)$ is the stochastic loads imposing on the system.

Equation (2-1) is a typical system of 2DOF coupled Stratonovich stochastic differential equations, which is extremely difficult to directly determine its stability property. The stochastic averaging method was often used to approximate the original Stratonovich stochastic system by an averaged Itô stochastic system, which is presumably easier to study, and infer properties of the dynamics of the original system by the understanding of the dynamics of the averaged system [Ariaratnam et al. 1991]. To apply the averaging method, one may first consider the unperturbed system, i.e., $\varepsilon = 0$ and $\xi(t) = 0$, which is of the form: $\ddot{q}_i + \omega_i^2 q_i = 0$, $i = 1, 2$. The stable solutions for the unperturbed system are found to be

$$q_i = a_i \cos \Phi_i, \quad \dot{q}_i = -\omega_i a_i \sin \Phi_i, \quad \Phi_i = \omega_i t + \phi_i, \quad i = 1, 2. \quad (2-3)$$

Then the method of variation of parameters is used. Differentiating the first equation of (2-3) and comparing with the second equation lead to

$$\dot{a}_i \cos \Phi_i - a_i \dot{\phi}_i \sin \Phi_i = 0. \quad (2-4)$$

Substituting (2-3) into (2-1) results in

$$\dot{a}_i \sin \Phi_i + a_i \dot{\phi}_i \cos \Phi_i = G_i, \quad (2-5)$$

where

$$G_i = -\varepsilon(2\beta_i \omega_i a_i \sin \Phi_i - \omega_i^2 \mathcal{H}[a_i \cos \Phi_i]) + \varepsilon^{1/2} \xi(t) \omega_i (k_{ii} a_i \cos \Phi_i + k_{ij} a_j \cos \Phi_j).$$

By solving (2-4) and (2-5), the equations in (2-1) can be written in amplitude, a_i , and phase, ϕ_i , as

$$\dot{a}_i = \varepsilon F_{a,i}^{(1)} + \varepsilon^{1/2} F_{a,i}^{(0)}, \quad \dot{\phi}_i = \varepsilon F_{\phi,i}^{(1)} + \varepsilon^{1/2} F_{\phi,i}^{(0)}, \quad (2-6)$$

where

$$\begin{aligned} F_{a,i}^{(0)} &= \xi(t) \left(\frac{1}{2} k_{ii} a_i \sin 2\Phi_i + \frac{1}{2} k_{ij} a_j \cos \Phi_j \sin \Phi_i \right), \\ F_{a,i}^{(1)} &= -\beta_i a_i + \beta_i a_i \cos 2\Phi_i - \sin \Phi_i \omega_i \tau_\varepsilon \mathcal{H}(a_i \cos \Phi_i), \\ F_{\phi,i}^{(0)} &= \xi(t) \left(k_{ii} \cos^2 \Phi_i + \frac{a_j}{a_i} k_{ij} \cos \Phi_i \cos \Phi_j \right), \\ F_{\phi,i}^{(1)} &= -\beta_i \sin 2\Phi_i - \frac{1}{a_i(t)} \cos \Phi_i \omega_i \tau_\varepsilon \mathcal{H}(a_i(s) \cos \Phi_i). \end{aligned} \quad (2-7)$$

If the correlation function $R(\tau)$ of the noise $\xi(t)$ decays sufficiently quickly to zero as τ increases, then the processes a_i and ϕ_i converge weakly on a time interval of order $1/\varepsilon$ to a Itô stochastic differential equation for the averaged amplitudes \bar{a}_i and phase angles $\bar{\phi}_i$, whose solutions provide a uniformly valid first-order approximation to the exact values

$$da_i = \varepsilon m_i^a dt + \varepsilon^{1/2} \sum_{j=1}^2 \sigma_{ij}^a dW_j^a, \quad i = 1, 2, \quad (2-8)$$

$$d\phi_i = \varepsilon m_i^\phi dt + \varepsilon^{1/2} \sum_{j=1}^2 \sigma_{ij}^\phi dW_j^\phi, \quad i = 1, 2, \quad (2-9)$$

where the overbar is dropped for simplicity of presentation and W_i^a, W_i^ϕ , $i = 1, 2$ are independent standard Wiener processes. The drift coefficients εm_i^a , εm_i^ϕ and the 2×2 diffusion matrices $\varepsilon \mathbf{b}^a = \varepsilon \boldsymbol{\sigma}^a (\boldsymbol{\sigma}^a)^T$, $\varepsilon \mathbf{b}^\phi = \varepsilon \boldsymbol{\sigma}^\phi (\boldsymbol{\sigma}^\phi)^T$, in which $\boldsymbol{\sigma}^a = [\sigma_{ij}^a]$, $\boldsymbol{\sigma}^\phi = [\sigma_{ij}^\phi]$, $\mathbf{b}^a = [b_{ij}^a]$, $\mathbf{b}^\phi = [b_{ij}^\phi]$, are given by

$$\begin{aligned}
 m_i^a &= \mathcal{M}_t \left\{ F_{a,i}^{(1)} + \int_{-\infty}^0 \mathbb{E} \left[\sum_{j=1}^2 \left(\frac{\partial F_{a,i}^{(0)}}{\partial a_j} F_{a,j\tau}^{(0)} + \frac{\partial F_{a,i}^{(0)}}{\partial \phi_j} F_{\phi,j\tau}^{(0)} \right) \right] d\tau \right\} \\
 &= a_i \left[-\beta_i - \omega_i \tau_\varepsilon \mathcal{M}_t (I_i^{sc}) + \frac{3}{16} k_{ii}^2 S_0 \right] + \frac{1}{8} \frac{a_j^2}{a_i} k_{ij}^2 S_0, \\
 m_i^\phi &= \mathcal{M}_t \left\{ F_{\phi,i}^{(1)} + \int_{-\infty}^0 \mathbb{E} \left[\sum_{j=1}^2 \left(\frac{\partial F_{\phi,i}^{(0)}}{\partial a_j} F_{\phi,j\tau}^{(0)} + \frac{\partial F_{\phi,i}^{(0)}}{\partial \phi_j} F_{\phi,j\tau}^{(0)} \right) \right] d\tau \right\} = -\omega_i \tau_\varepsilon \mathcal{M}_t (I_i^{cc}), \\
 b_{ii}^a &= \mathcal{M}_t \left\{ \int_{-\infty}^{\infty} \mathbb{E} [F_{a,i}^{(0)} F_{a,i\tau}^{(0)}] d\tau \right\} = \frac{1}{8} (k_{ii}^2 a_i^2 + 2k_{ij}^2 a_j^2) S_0, \\
 b_{ij}^a &= \mathcal{M}_t \left\{ \int_{-\infty}^{\infty} \mathbb{E} [F_{a,i}^{(0)} F_{a,j\tau}^{(0)}] d\tau \right\} = 0, \\
 b_{ii}^\phi &= \mathcal{M}_t \left\{ \int_{-\infty}^{\infty} \mathbb{E} [F_{\phi,i}^{(0)} F_{\phi,i\tau}^{(0)}] d\tau \right\} = \frac{3}{8} k_{ii}^2 S_0 + \frac{1}{4} \frac{a_j^2}{a_i^2} k_{ij}^2 S_0, \\
 b_{ij}^\phi &= \mathcal{M}_t \left\{ \int_{-\infty}^{\infty} \mathbb{E} [F_{\phi,i}^{(0)} F_{\phi,j\tau}^{(0)}] d\tau \right\} = \frac{1}{4} (k_{ii} k_{jj} + k_{ij} k_{ji}) S_0, \\
 I_i^{cc} &= \cos \Phi_i(t) \int_0^t \mathcal{H}(t-s) \cos \Phi_i(s) ds, \\
 I_i^{sc} &= \sin \Phi_i(t) \int_0^t \mathcal{H}(t-s) \cos \Phi_i(s) ds, \\
 F_{j\tau}^{(0)} &= F_j^{(0)}(a, \phi, \xi(t+\tau), t+\tau), \quad i, j = 1, 2,
 \end{aligned} \tag{2-10}$$

where the coupled oscillators are assumed to have noncommensurable frequencies, i.e., $\omega_1 \neq \omega_2$. A Gaussian white noise process is a weakly stationary process that is delta-correlated and has mean zero. This process is formally the derivative of the Wiener process given by $\xi(t) = \sqrt{S_0} \dot{W}(t)$, with constant cosine power spectral density $S(\omega) = S_0$ and sine power spectral density $\Psi(\omega) = 0$ over the entire frequency range.

The averaging operator is defined as

$$\mathcal{M}_t(\cdot) = \lim_{T \rightarrow \infty} \frac{1}{T} \int_t^{t+T} (\cdot) dt.$$

When applying the averaging operator, the integration is performed over explicitly appearing t only. The term containing viscoelastic operator is averaged according to the method given in [Larionov 1969]. Applying the transformation $s = t - \tau$ and changing the order of integration lead to

$$\begin{aligned}
\mathcal{M}_t \{I_i^{sc}\} &= \lim_{T \rightarrow \infty} \frac{1}{T} \int_{t=0}^T \int_{s=0}^t \mathcal{H}(t-s) \cos \Phi_i(s) \sin \Phi_i(t) ds dt \\
&= \lim_{T \rightarrow \infty} \frac{1}{T} \int_{t=0}^T \int_{\tau=0}^t \mathcal{H}(\tau) \sin \Phi_i(t) \cos \Phi_i(t-\tau) d\tau dt \\
&= \lim_{T \rightarrow \infty} \frac{1}{2T} \int_{\tau=0}^T \int_{t=\tau}^T \mathcal{H}(\tau) [\sin(2\omega_i t - \omega_i \tau + 2\bar{\varphi}) + \sin \omega_i \tau] dt d\tau \\
&= \frac{1}{2} \int_0^\infty \mathcal{H}(\tau) \sin \omega_i \tau d\tau = \frac{1}{2} \mathcal{H}^s(\omega_i).
\end{aligned} \tag{2-11}$$

Similarly, one obtains

$$\mathcal{M}_t \{I_i^{cc}\} = \frac{1}{2} \mathcal{H}^c(\omega_i), \tag{2-12}$$

where

$$\mathcal{H}^s(\omega) = \int_0^\infty \mathcal{H}(\tau) \sin \omega \tau d\tau, \quad \mathcal{H}^c(\omega) = \int_0^\infty \mathcal{H}(\tau) \cos \omega \tau d\tau \tag{2-13}$$

are the sine and cosine transformations of the viscoelastic kernel function $\mathcal{H}(t)$, respectively. The term

$$E_i = \beta_i + \omega_i \tau_\varepsilon \mathcal{M}_t \{I_i^{sc}\} = \beta_i + \frac{1}{2} \omega_i \tau_\varepsilon \frac{\omega_i \gamma}{\eta^2 + \omega_i^2}, \quad i = 1, 2, \tag{2-14}$$

may be called pseudodamping, because it plays the role of damping but includes viscoelasticity as well.

In this study, the viscoelastic kernel function is supposed to follow ordinary Maxwell model

$$\mathcal{H}(t) = \gamma e^{-\eta t}, \tag{2-15}$$

which can be used as an approximation to most linear viscoelastic behavior as closely as possible if enough number of Maxwell units are arranged in parallel. Its sine and cosine transformations in (2-13) are given by

$$\mathcal{H}^s(\omega) = \frac{\omega \gamma}{\eta^2 + \omega^2}, \quad \mathcal{H}^c(\omega) = \frac{\gamma \eta}{\eta^2 + \omega^2}. \tag{2-16}$$

It is of importance to note that both the averaged amplitude a_i and phase angle equations ϕ_i do not involve the phase angles and then the amplitude equations are advantageously decoupled from the phase angle equations. Hence, the averaged amplitude vector (a_1, a_2) is a two dimensional diffusion process.

3. Moment Lyapunov exponents and Lyapunov exponents

To obtain moment Lyapunov exponents from (2-8), one may transform the Itô stochastic differential equations for the amplitudes by using Khasminskii's transformation [1966]

$$r = \sqrt{a_1^2 + a_2^2}, \quad \varphi = \tan^{-1} \frac{a_2}{a_1}, \quad a_1 = r \cos \varphi, \quad a_2 = r \sin \varphi, \quad P = r^P, \tag{3-1}$$

and then the moment Lyapunov exponent is given by

$$\Lambda = \lim_{t \rightarrow \infty} \frac{1}{t} \log E[P]. \tag{3-2}$$

The Itô equations for P can be obtained using Itô's lemma [Xie 2006]:

$$dP = m_P(P, \varphi) dt + \sigma_{P1} dW_1 + \sigma_{P2} dW_2, \quad (3-3)$$

where

$$\sigma_{P1} = \varepsilon^{1/2} \left(\sigma_{11}^a \frac{\partial P}{\partial a_1} + \sigma_{21}^a \frac{\partial P}{\partial a_2} \right), \quad \sigma_{P2} = \varepsilon^{1/2} \left(\sigma_{12}^a \frac{\partial P}{\partial a_1} + \sigma_{22}^a \frac{\partial P}{\partial a_2} \right), \quad (3-4)$$

and

$$\begin{aligned} m_P(P, \varphi) &= \varepsilon \left\{ m_1^a \frac{\partial P}{\partial a_1} + m_2^a \frac{\partial P}{\partial a_2} + \frac{1}{2} \left[b_{11}^a \frac{\partial^2 P}{\partial a_1^2} + (b_{12}^a + b_{21}^a) \frac{\partial^2 P}{\partial a_1 \partial a_2} + b_{22}^a \frac{\partial^2 P}{\partial a_2^2} \right] \right\}, \\ &= \varepsilon p P \left\{ \frac{m_1^a}{\sqrt{a_1^2 + a_2^2}} \cos \varphi + \frac{m_2^a}{\sqrt{a_1^2 + a_2^2}} \sin \varphi + \frac{1}{2} \left[\frac{b_{11}^a}{a_1^2 + a_2^2} ((p-2) \cos^2 \varphi + 1) \right. \right. \\ &\quad \left. \left. + \frac{(b_{12}^a + b_{21}^a)}{2(a_1^2 + a_2^2)} (p-2) \sin 2\varphi + \frac{b_{22}^a}{a_1^2 + a_2^2} ((p-2) \sin^2 \varphi + 1) \right] \right\}. \end{aligned} \quad (3-5)$$

To determine the diffusion terms, one may use the replacement as

$$\Sigma_P dW = \sigma_{P1} dW_1 + \sigma_{P2} dW_2,$$

which yields the equation

$$\begin{aligned} \Sigma_P^2 &= \sigma_{P1}^2 + \sigma_{P2}^2 = \varepsilon \left\{ \sigma_{11}^a \frac{\partial P}{\partial a_1} + \sigma_{21}^a \frac{\partial P}{\partial a_2} \quad \sigma_{12}^a \frac{\partial P}{\partial a_1} + \sigma_{22}^a \frac{\partial P}{\partial a_2} \right\} \left\{ \sigma_{11}^a \frac{\partial P}{\partial a_1} + \sigma_{21}^a \frac{\partial P}{\partial a_2} \right\} \\ &= \varepsilon \left[((\sigma_{11}^a)^2 + (\sigma_{12}^a)^2) \left(\frac{\partial P}{\partial a_1} \right)^2 + 2(\sigma_{11}^a \sigma_{21}^a + \sigma_{12}^a \sigma_{22}^a) \frac{\partial P}{\partial a_1} \frac{\partial P}{\partial a_2} + ((\sigma_{21}^a)^2 + (\sigma_{22}^a)^2) \left(\frac{\partial P}{\partial a_2} \right)^2 \right] \\ &= \varepsilon \left[b_{11}^a \left(\frac{\partial P}{\partial a_1} \right)^2 + (b_{12}^a + b_{21}^a) \frac{\partial P}{\partial a_1} \frac{\partial P}{\partial a_2} + b_{22}^a \left(\frac{\partial P}{\partial a_2} \right)^2 \right]. \end{aligned} \quad (3-6)$$

Hence,

$$dP = m_P(P, \varphi) dt + \sigma_{P1} dW_1 + \sigma_{P2} dW_2 = m_P(P, \varphi) dt + \Sigma_P(P, \varphi) dW. \quad (3-7)$$

Similarly, one can obtain the Itô equations for φ ,

$$d\varphi = m_\varphi(\varphi) dt + \sigma_{\varphi1} dW_1 + \sigma_{\varphi2} dW_2 = m_\varphi(\varphi) dt + \Sigma_\varphi(\varphi) dW, \quad (3-8)$$

where

$$\sigma_{\varphi1} = \varepsilon^{1/2} \left(\sigma_{11}^a \frac{\partial \varphi}{\partial a_1} + \sigma_{21}^a \frac{\partial \varphi}{\partial a_2} \right), \quad \sigma_{\varphi2} = \varepsilon^{1/2} \left(\sigma_{12}^a \frac{\partial \varphi}{\partial a_1} + \sigma_{22}^a \frac{\partial \varphi}{\partial a_2} \right), \quad (3-9)$$

$$m_\varphi(\varphi) = \varepsilon \left\{ m_1^a \frac{\partial \varphi}{\partial a_1} + m_2^a \frac{\partial \varphi}{\partial a_2} + \frac{1}{2} \left[b_{11}^a \frac{\partial^2 \varphi}{\partial a_1^2} + (b_{12}^a + b_{21}^a) \frac{\partial^2 \varphi}{\partial a_1 \partial a_2} + b_{22}^a \frac{\partial^2 \varphi}{\partial a_2^2} \right] \right\}$$

$$= \varepsilon \left\{ -\frac{m_1^a}{\sqrt{a_1^2 + a_2^2}} \sin \varphi + \frac{m_2^a}{\sqrt{a_1^2 + a_2^2}} \cos \varphi + \frac{1}{2} \left[\frac{b_{11}^a}{a_1^2 + a_2^2} \sin 2\varphi - \frac{(b_{12}^a + b_{21}^a)}{a_1^2 + a_2^2} (2 \cos^2 \varphi - 1) - \frac{b_{22}^a}{a_1^2 + a_2^2} \sin 2\varphi \right] \right\}, \quad (3-10)$$

and

$$\begin{aligned} \Sigma_\varphi^2 &= \sigma_{\varphi_1}^2 + \sigma_{\varphi_2}^2 = \varepsilon \left[b_{11}^a \left(\frac{\partial \varphi}{\partial a_1} \right)^2 + (b_{12}^a + b_{21}^a) \frac{\partial \varphi}{\partial a_1} \frac{\partial \varphi}{\partial a_2} + b_{22}^a \left(\frac{\partial \varphi}{\partial a_2} \right)^2 \right] \\ &= \varepsilon \left[\frac{b_{11}^a}{a_1^2 + a_2^2} \sin^2 \varphi - \frac{(b_{12}^a + b_{21}^a)}{a_1^2 + a_2^2} \sin \varphi \cos \varphi + \frac{b_{22}^a}{a_1^2 + a_2^2} \cos^2 \varphi \right]. \end{aligned} \quad (3-11)$$

It is noted that the coefficients of the right-hand side terms of amplitude equations in (2-8), such as m_i^a , $i = 1, 2$, are homogeneous of degree one in a_1 and a_2 , which results in the fact that the diffusion term \mathbf{b}^a in (2-10) are homogeneous of degree two in a_1 and a_2 . Therefore, substituting $a_1 = r \cos \varphi$ and $a_2 = r \sin \varphi$ from (3-1) into (3-5), one finds that the drift $m_P(P, \varphi)$ and diffusion term $\Sigma_P(P, \varphi)$ are functions of P of degree one and φ . However, the drift $m_\varphi(\varphi)$ in (3-10) and diffusion term $\Sigma_\varphi(\varphi)$ in (3-11) are functions of φ only, which shows $P(t)$ in (3-7) and $\varphi(t)$ in (3-8) are coupled, although $\varphi(t)$ is itself a diffusion process.

To obtain the moment Lyapunov exponent, a linear stochastic transformation is adopted:

$$S = T(\varphi) P, \quad P = T^{-1}(\varphi) S, \quad 0 \leq \varphi < \pi,$$

from which one obtains

$$\frac{\partial S}{\partial P} = T(\varphi), \quad \frac{\partial S}{\partial \varphi} = T'_\varphi P, \quad \frac{\partial^2 S}{\partial P^2} = 0, \quad \frac{\partial^2 S}{\partial P \partial \varphi} = T'_\varphi, \quad \frac{\partial^2 S}{\partial^2 \varphi} = P T''_{\varphi\varphi}, \quad (3-12)$$

where T'_φ and $T''_{\varphi\varphi}$ denote the first and second derivative of $T(\varphi)$ with respect to φ , respectively.

The Itô equation for the transformed p -th norm process S can also be derived using Itô's Lemma

$$dS = m_S dt + \left(\sigma_{P1} \frac{\partial S}{\partial P} dW_1 + \sigma_{P2} \frac{\partial S}{\partial P} dW_2 + \sigma_{\varphi_1} \frac{\partial S}{\partial \varphi} dW_1 + \sigma_{\varphi_2} \frac{\partial S}{\partial \varphi} dW_2 \right). \quad (3-13)$$

The drift coefficient is given by

$$\begin{aligned} m_S &= m_P \frac{\partial S}{\partial P} + m_\varphi \frac{\partial S}{\partial \varphi} + \frac{1}{2} \left(b_{11}^S \frac{\partial^2 S}{\partial P^2} + (b_{12}^S + b_{21}^S) \frac{\partial^2 S}{\partial P \partial \varphi} + b_{22}^S \frac{\partial^2 S}{\partial \varphi^2} \right) \\ &= \frac{1}{2} P (\sigma_{\varphi_1}^2 + \sigma_{\varphi_2}^2) T''_{\varphi\varphi} + (m_\varphi P + \sigma_{P1} \sigma_{\varphi_1} + \sigma_{P2} \sigma_{\varphi_2}) T'_\varphi + m_P T, \end{aligned} \quad (3-14)$$

and the diffusion terms have the relation

$$\mathbf{b}^S = [\boldsymbol{\sigma}^S (\boldsymbol{\sigma}^S)^T], \quad \boldsymbol{\sigma}^S = \begin{bmatrix} \sigma_{P1} & \sigma_{P2} \\ \sigma_{\varphi_1} & \sigma_{\varphi_2} \end{bmatrix}. \quad (3-15)$$

Substituting σ_{P1}, σ_{P2} from (3-4) and $\sigma_{\varphi1}, \sigma_{\varphi2}$ from (3-9) into (3-15) lead to

$$\begin{aligned}
 b_{11}^S &= \sigma_{P1}^2 + \sigma_{P2}^2 = \Sigma_P^2, \quad b_{22}^S = \sigma_{\varphi1}^2 + \sigma_{\varphi2}^2 = \Sigma_\varphi^2, \\
 b_{12}^S &= b_{21}^S = \sigma_{P1}\sigma_{\varphi1} + \sigma_{P2}\sigma_{\varphi2} \\
 &= \varepsilon((\sigma_{11}^a)^2 + (\sigma_{12}^a)^2) \frac{\partial P}{\partial a_1} \frac{\partial \varphi}{\partial a_1} + \varepsilon(\sigma_{11}^a \sigma_{21}^a + \sigma_{12}^a \sigma_{22}^a) \left(\frac{\partial P}{\partial a_1} \frac{\partial \varphi}{\partial a_2} + \frac{\partial P}{\partial a_2} \frac{\partial \varphi}{\partial a_1} \right) + \varepsilon((\sigma_{21}^a)^2 + (\sigma_{22}^a)^2) \frac{\partial P}{\partial a_2} \frac{\partial \varphi}{\partial a_2} \\
 &= \varepsilon \left\{ b_{11}^a \frac{\partial P}{\partial a_1} \frac{\partial \varphi}{\partial a_1} + b_{12}^a \left(\frac{\partial P}{\partial a_1} \frac{\partial \varphi}{\partial a_2} + \frac{\partial P}{\partial a_2} \frac{\partial \varphi}{\partial a_1} \right) + b_{22}^a \frac{\partial P}{\partial a_2} \frac{\partial \varphi}{\partial a_2} \right\} \\
 &= \varepsilon P \left(-\frac{b_{11}^a}{a_1^2 + a_2^2} \cos \varphi \sin \varphi + \frac{b_{12}^a}{a_1^2 + a_2^2} (\cos^2 \varphi - \sin^2 \varphi) + \frac{b_{22}^a}{a_1^2 + a_2^2} \cos \varphi \sin \varphi \right). \quad (3-16)
 \end{aligned}$$

For bounded and nonsingular transformation $T(\varphi)$, both processes P and S are expected to have the same stability behavior. Therefore, $T(\varphi)$ is chosen so that the drift term of the Itô differential Equation (3-13) is independent of the phase process φ so that

$$dS = \varepsilon \Lambda S dt + \varepsilon^{1/2} (\sigma_{S1} dW_1 + \sigma_{S2} dW_2). \quad (3-17)$$

Comparing the drift terms of equations (3-13) and (3-17), one can find that such a transformation $T(\varphi)$ is given by the equation

$$\frac{1}{2} P (\sigma_{\varphi1}^2 + \sigma_{\varphi2}^2) T''_{\varphi\varphi} + (m_\varphi P + \sigma_{P1}\sigma_{\varphi1} + \sigma_{P2}\sigma_{\varphi2}) T'_\varphi + m_P T = \varepsilon \Lambda S, \quad 0 \leq \varphi < \pi, \quad (3-18)$$

in which $T(\varphi)$ is a periodic function in φ of period π . Equation (3-18) defines an eigenvalue problem of a second-order differential operator with Λ being the eigenvalue and $T(\varphi)$ the associated eigenfunction. Taking the expected value of both sides of (3-17), one can find that $E[\sigma_{S1} dW_1 + \sigma_{S2} dW_2] = 0$ [Xie 2006]. Hence, one obtains $E[S] = \varepsilon \Lambda E[S] dt$, from which the eigenvalue Λ is seen to be the Lyapunov exponent of the p -th moment of the system (2-1), that is, $\Lambda = \Lambda_{q(t)}(p)$. It is noted that both processes P and S have the same stability behavior.

Substituting (3-16) into (3-18) yields

$$\mathcal{L}(p)[T] = \frac{1}{P} \left(\frac{1}{2} \Sigma_\varphi^2 P T''_{\varphi\varphi} + [m_\varphi P + b_{12}^S] T'_\varphi + m_P T \right) = \varepsilon \Lambda T, \quad 0 \leq \varphi < \pi, \quad (3-19)$$

where Σ_φ^2 , m_φ , b_{12}^S , and m_P are given in (3-11), (3-10), (3-16), and (3-5), respectively. Substituting these equations into (3-19) yields

$$\mathcal{L}(p)[T] = \lambda_2 T''_{\varphi\varphi} + \lambda_1 T'_\varphi + \lambda_0 T = \Lambda T, \quad 0 \leq \varphi < \pi, \quad (3-20)$$

where

$$\lambda_2 = \frac{1}{2} \left[\frac{b_{11}^a}{a_1^2 + a_2^2} \sin^2 \varphi - \frac{(b_{12}^a + b_{21}^a)}{a_1^2 + a_2^2} \sin \varphi \cos \varphi + \frac{b_{22}^a}{a_1^2 + a_2^2} \cos^2 \varphi \right],$$

$$\lambda_1 = \left\{ \left[\frac{m_2^a \cos \varphi}{\sqrt{a_1^2 + a_2^2}} - \frac{m_1^a \sin \varphi}{\sqrt{a_1^2 + a_2^2}} + \frac{b_{11}^a \sin 2\varphi}{2(a_1^2 + a_2^2)} - \frac{(b_{12}^a + b_{21}^a)(2 \cos^2 \varphi - 1)}{2(a_1^2 + a_2^2)} - \frac{b_{22}^a \sin 2\varphi}{2(a_1^2 + a_2^2)} \right] \right. \\ \left. + p \left(-\frac{b_{11}^a}{a_1^2 + a_2^2} \cos \varphi \sin \varphi + \frac{b_{12}^a}{a_1^2 + a_2^2} (\cos^2 \varphi - \sin^2 \varphi) + \frac{b_{22}^a}{a_1^2 + a_2^2} \cos \varphi \sin \varphi \right) \right\},$$

$$\lambda_0 = p \left\{ \frac{m_1^a}{\sqrt{a_1^2 + a_2^2}} \cos \varphi + \frac{m_2^a}{\sqrt{a_1^2 + a_2^2}} \sin \varphi \right. \\ \left. + \frac{1}{2} \left(\frac{b_{11}^a}{a_1^2 + a_2^2} ((p-2) \cos^2 \varphi + 1) + \frac{b_{12}^a + b_{21}^a}{2(a_1^2 + a_2^2)} (p-2) \sin 2\varphi + \frac{b_{22}^a}{a_1^2 + a_2^2} ((p-2) \sin^2 \varphi + 1) \right) \right\}.$$

Substituting $a_1 = r \cos \varphi$, $a_2 = r \sin \varphi$ into these equations, one finds that the coefficients λ_0 , λ_1 , and λ_2 are functions of φ and p only. Solving Equation (3-20) yields the moment Lyapunov exponent Λ .

This idea was first applied in [Wedig 1988] to derive the eigenvalue problem for the moment Lyapunov exponent of a SDOF linear Itô stochastic system. This paper extends to 2DOF coupled systems and considered viscoelasticity.

Determination of moment Lyapunov exponents. It is found that the coefficients in (3-20) are periodic with period π , it is reasonable to consider a Fourier cosine series expansion of the eigenfunction $T(\varphi)$ in the form

$$T(\varphi) = \sum_{i=0}^K C_i \cos(2i\varphi). \quad (3-21)$$

Here only cosine functions are adopted because sometimes the eigenvalue problems in (3-20) contains $1/\sin(2\varphi)$. This Fourier expansion method is actually a method for solving partial differential equations and has been used in [Wedig 1988; Bolotin 1964; Sri Namachchivaya and van Roessel 2001], and elsewhere.

Substituting this expansion and $a_1 = r \cos \varphi$, $a_2 = r \sin \varphi$ into eigenvalue problem (3-20), multiplying both sides by $\cos(2j\varphi)$, $j = 0, 1, \dots, K$, and performing integration with respect to φ from 0 to $\pi/2$ yield a set of equations for the unknown coefficients C_i , $i = 0, 1, \dots, K$:

$$\sum_{i=0}^K a_{ij} C_i = \Lambda C_j, \quad j = 0, 1, 2, \dots, \quad (3-22)$$

where

$$a_{ij} = \frac{4}{\pi} \int_0^{\pi/2} \mathcal{L}(p) [\cos(2i\varphi)] \cos(2j\varphi) d\varphi, \quad j = 0, 1, \dots, K, \quad (3-23)$$

and

$$\int_0^{\pi/2} \cos(2i\varphi) \cos(2j\varphi) d\varphi = \begin{cases} \pi/4 & \text{if } i = j, \\ 0 & \text{if } i \neq j. \end{cases}$$

The eigenvalue can be obtained by solution of a polynomial equation as follows. Rearranging (3-22) leads to

$$\begin{bmatrix} a_{00} - \hat{\Lambda} & a_{01} & a_{02} & a_{03} & \cdots \\ a_{10} & a_{11} - \Lambda & a_{12} & a_{13} & \cdots \\ a_{20} & a_{21} & a_{22} - \Lambda & a_{23} & \cdots \\ a_{30} & a_{31} & a_{32} & a_{33} - \Lambda & \cdots \\ \cdots & \cdots & \cdots & \cdots & \ddots \end{bmatrix} \begin{Bmatrix} C_0 \\ C_1 \\ C_2 \\ C_3 \\ \cdots \end{Bmatrix} = \mathbf{0}. \quad (3-24)$$

The third-order submatrix is listed here. For convenience, Λ is inserted in a_{ij} .

$$\begin{aligned} a_{00} &= \frac{1}{128}(3k_{11}^2 + 3k_{22}^2 + 8k^2)S_0p^2 + \frac{1}{64}(5k_{11}^2S_0 + 5k_{22}^2S_0 + 24k^2S_0 - 32(E_1 + E_2))p - \Lambda, \\ a_{01} &= \frac{1}{64}(k_{11}^2 - k_{22}^2)S_0p^2 + \frac{1}{32}(k_{11}^2S_0 - k_{22}^2S_0 - 8(E_1 - E_2))p, \\ a_{02} &= \frac{1}{256}(k_{11}^2 + k_{22}^2 - 8k^2)S_0p^2 - \frac{1}{128}(k_{11}^2 + k_{22}^2 - 16k^2)S_0p, \\ a_{10} &= \frac{1}{64}(k_{11}^2 - k_{22}^2)S_0p^2 + \frac{1}{16}(k_{11}^2S_0 - k_{22}^2S_0 - 4(E_1 - E_2))p + \frac{1}{16}(k_{11}^2S_0 - k_{22}^2S_0 - 8(E_1 - E_2)), \\ a_{11} &= \frac{1}{512}(7k_{11}^2 + 7k_{22}^2 + 8k^2)S_0p^2 + \frac{1}{256}(11k_{11}^2S_0 + 11k_{22}^2S_0 + 40k^2S_0 - 64(E_1 + E_2))p \\ &\quad - \frac{1}{64}(k_{11}^2 + k_{22}^2 + 24k^2)S_0 - \frac{1}{2}\Lambda, \\ a_{12} &= \frac{1}{128}(k_{11}^2 - k_{22}^2)S_0p^2 - \frac{1}{8}(E_1 - E_2)p - \frac{1}{32}(k_{11}^2S_0 - k_{22}^2S_0 - 8(E_1 - E_2)), \\ a_{20} &= \frac{1}{256}(k_{11}^2 + k_{22}^2 - 8k^2)S_0p^2 + \frac{3}{128}(k_{11}^2 + k_{22}^2 - 8k^2)S_0p + \frac{1}{32}(k_{11}^2 + k_{22}^2 - 40k^2)S_0, \\ a_{21} &= \frac{1}{128}(k_{11}^2 - k_{22}^2)S_0p^2 + \frac{1}{64}(3k_{11}^2S_0 - 3k_{22}^2S_0 - 8(E_1 - E_2))p + \frac{1}{16}(k_{11}^2S_0 - k_{22}^2S_0 - 8(E_1 - E_2)), \\ a_{22} &= \frac{1}{256}(3k_{11}^2 + 3k_{22}^2 + 8k^2)S_0p^2 + \frac{1}{128}(5k_{11}^2S_0 + 5k_{22}^2S_0 + 24k^2S_0 - 32(E_1 + E_2))p \\ &\quad - \frac{1}{16}(k_{11}^2 + k_{22}^2 + 16k^2)S_0 - \frac{1}{2}\Lambda, \end{aligned} \quad (3-25)$$

where E_i is the pseudodamping defined in (2-14).

To have a nontrivial solution of the C_k , it is required that the determination of the coefficient matrix of (3-24) equal zero, from which the eigenvalue $\Lambda(p)$ can be obtained,

$$e_{K+1}^{(K)}[\Lambda^{(K)}]^{K+1} + e_K^{(K)}[\Lambda^{(K)}]^K + \cdots + e_1^{(K)}[\Lambda^{(K)}]^1 + e_0^{(K)} = 0, \quad (3-26)$$

where $\Lambda^{(K)}$ denotes the approximate moment Lyapunov exponent under the assumption that the expansion of eigenfunction $T(\varphi)$ is up to K -th order Fourier cosine series. The set of approximate eigenvalues obtained by this procedure converges to the corresponding true eigenvalues as $K \rightarrow \infty$. However, as shown in Figure 1, the approximate eigenvalues converges so quickly that the approximations almost coincide after the order $K \geq 1$. One may approximate the moment Lyapunov exponent of the system by

$$\Lambda_{q(t)}(p) \approx \Lambda^{(K)}(p). \quad (3-27)$$

Determination of Lyapunov exponents. The p -th moment Lyapunov exponent $\Lambda_{q(t)}(p)$ is a convex analytic function in p that passes through the origin and the slope at the origin is equal to the largest

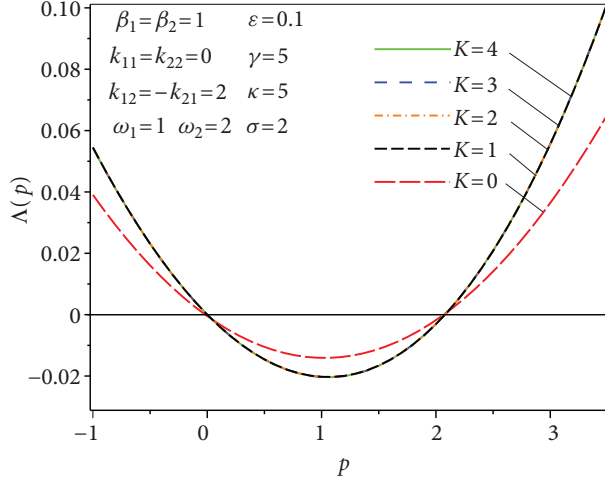


Figure 1. Moment Lyapunov exponents for various K -th order Fourier expansion.

Lyapunov exponent $\lambda_{q(t)}$, i.e.,

$$\lambda_{q(t)}(p) = \lim_{p \rightarrow 0} \frac{\Lambda^{(K)}(p)}{p} = - \lim_{p \rightarrow 0} \frac{e_0^{(K)}}{p e_1^{(K)}}, \quad (3-28)$$

which is obtained directly from (3-26).

For comparison, the largest Lyapunov exponent for system (2-8) can be directly derived from invariant probability density by solving a Fokker–Plank equation [Xie 2006].

(1) If $k_{11}^2 + k_{22}^2 > 4|k_{12}k_{21}|$, i.e., $\Delta_0 > 0$, we have

$$\lambda = \frac{1}{2} \left[(\lambda_1 + \lambda_2) + (\lambda_1 - \lambda_2) \coth \left(\frac{\lambda_1 - \lambda_2}{\sqrt{\Delta_0}} \alpha \right) \right], \quad (3-29)$$

where $\alpha = \cosh^{-1} \frac{Q}{4|k_{12}k_{21}|S_0}$.

(2) If $k_{11}^2 + k_{22}^2 < 4|k_{12}k_{21}|$, i.e., $\Delta_0 < 0$, we have

$$\lambda = \frac{1}{2} \left[(\lambda_1 + \lambda_2) + (\lambda_1 - \lambda_2) \coth \left(\frac{\lambda_1 - \lambda_2}{\sqrt{-\Delta_0}} \alpha \right) \right], \quad (3-30)$$

where $\alpha = \cos^{-1} \frac{Q}{4|k_{12}k_{21}|S_0}$.

(3) If $k_{11}^2 + k_{22}^2 = 4|k_{12}k_{21}|$, i.e., $\Delta_0 = 0$, we have

$$\lambda = \frac{1}{2} \left((\lambda_1 + \lambda_2) + (\lambda_1 - \lambda_2) \coth \frac{2(\lambda_1 - \lambda_2)}{|k_{12}k_{21}|S_0} \right). \quad (3-31)$$

The constants Q and Δ_0 are defined as

$$\begin{aligned} Q &= (k_{11}^2 + k_{22}^2 - 4k_{12}k_{21})S_0, & \Delta_0 &= \frac{1}{64}(Q^2 - 16k_{12}^2k_{21}^2S_0), \\ \lambda_1 &= -\beta_1 - \omega_1\tau_\varepsilon\mathcal{M}_t(I_1^{sc}) + \frac{1}{8}k_{11}^2S_0, & \lambda_2 &= -\beta_2 - \omega_2\tau_\varepsilon\mathcal{M}_t(I_2^{sc}) + \frac{1}{8}k_{22}^2S_0. \end{aligned} \quad (3-32)$$

4. Stability boundary

Moment Lyapunov exponents can be numerically determined from (3-26). When $K = 0$, the eigenfunction in (3-21) is $T(\varphi) = C_0$; then, from $a_{00} - \Lambda^{(0)} = 0$, the moment Lyapunov exponent is defined as

$$\Lambda_{q(t)}(p) \approx \Lambda^{(0)}(p) = \frac{1}{128}(3k_{11}^2 + 3k_{22}^2 + 8k^2)S_0p^2 + \frac{1}{64}[5k_{11}^2S_0 + 5k_{22}^2S_0 + 24k^2S_0 - 32(E_1 + E_2)]p. \quad (4-1)$$

If viscoelasticity is not considered, i.e., $\tau_\varepsilon = 0$ and $E_i = \beta_i$, then (4-1) reduces to the moment Lyapunov exponent for 2DOF linear systems subjected to white noise parametric excitation which was reported in Equation (3.19) in [Janevski et al. 2012], where the perturbation method was applied.

The moment stability boundary is then obtained as

$$(3k_{11}^2 + 3k_{22}^2 + 8k^2)S_0p + 2[5k_{11}^2S_0 + 5k_{22}^2S_0 + 24k^2S_0 - 32(E_1 + E_2)] = 0. \quad (4-2)$$

Again, if viscoelasticity and coupling parameter ($k = 0$) are not considered, (4-2) can be reduced to that obtained by other approximate methods such as asymptotic expansion of integrals and stochastic averaging; see Equation (40) of [Ariaratnam and Xie 1993].

The Lyapunov exponent is given by

$$\lambda^{(0)}(p) = \lim_{p \rightarrow 0} \frac{\Lambda^{(0)}(p)}{p} = \frac{1}{64}[5k_{11}^2S_0 + 5k_{22}^2S_0 + 24k^2S_0 - 32(E_1 + E_2)]. \quad (4-3)$$

The almost-sure stability region is found to be

$$5k_{11}^2S_0 + 5k_{22}^2S_0 + 24k^2S_0 - 32(E_1 + E_2) < 0. \quad (4-4)$$

From (4-2) and (4-4), the almost-sure and the moment stability boundary are both a straight line in the coordinates with E_1 and E_2 .

When $K = 1$, the eigenfunction is $T(\varphi) = C_0 + C_1 \cos 2\varphi$, the moment Lyapunov exponent can be solved from

$$\begin{vmatrix} a_{00} - \Lambda^{(1)} & a_{01} \\ a_{10} & a_{11} - \Lambda^{(1)} \end{vmatrix} = \mathbf{0}. \quad (4-5)$$

Expanding we get an equation, $(\Lambda^{(1)})^2 + e_1^{(1)}\Lambda^{(1)} + e_0^{(1)} = 0$, leading to an analytical expression for the

moment Lyapunov exponent. The coefficients for systems with white noise ($S(\omega) = S_0$) are given by

$$\begin{aligned}
e_1^{(1)} &= -\frac{1}{256}(13p^2 + 42p - 8)S_0(k_{11}^2 + k_{22}^2) - \frac{1}{64}(3p^2 + 22p - 56)S_0k^2 + p(E_1 + E_2), \\
e_0^{(1)} &= S_0^2(k_{11}^4 + k_{22}^4)\left(\frac{5}{32768}p^4 + \frac{5}{4096}p^3 + \frac{1}{8192}p^2 - \frac{13}{2048}p\right) \\
&\quad + S_0^2k_{11}^2k_{22}^2\left(\frac{37}{16384}p^4 + \frac{29}{2048}p^3 + \frac{97}{4096}p^2 + \frac{3}{1024}p\right) + S_0^2k^4\left(\frac{1}{2048}p^4 + \frac{1}{128}p^3 + \frac{1}{512}p^2 - \frac{21}{128}p\right) \\
&\quad + S_0^2(k_{11}^2 + k_{22}^2)k^2\left(\frac{5}{4096}p^4 + \frac{13}{1024}p^3 + \frac{7}{1024}p^2 - \frac{19}{256}p\right) \\
&\quad + S_0k_{11}^2\left[-\left(\frac{5}{512}E_1 + \frac{21}{512}E_2\right)p^3 - \left(\frac{5}{256}E_1 + \frac{37}{256}E_2\right)p^2 + \left(\frac{5}{64}E_1 - \frac{3}{64}E_2\right)p\right] \\
&\quad + S_0k_{22}^2\left[-\left(\frac{5}{512}E_2 + \frac{21}{512}E_1\right)p^3 - \left(\frac{5}{256}E_2 + \frac{37}{256}E_1\right)p^2 + \left(\frac{5}{64}E_2 - \frac{3}{64}E_1\right)p\right] \\
&\quad + S_0k^2(E_1 + E_2)\left(-\frac{3}{128}p^3 - \frac{11}{64}p^2 + \frac{7}{16}p\right) + \frac{1}{8}p^2(E_1^2 + E_2^2 + 6E_1E_2) - \frac{1}{4}p(E_1 - E_2)^2. \quad (4-6)
\end{aligned}$$

It can be found that on the condition of white noise, our case reduced to the results of [Janevski et al. 2012]. When $k_{11} = k_{22} = 0$, the moment Lyapunov exponent is given by

$$\begin{aligned}
\Lambda^{(1)}(p) &= \left(\frac{3}{128}p^2 + \frac{11}{64}p - \frac{7}{16}\right)k^2S_0 - \frac{1}{2}p(E_1 + E_2) \\
&\quad + \frac{1}{128}\left[(3136 + 224p + 116p^2 + 4p^3 + p^4)k^4S_0^2 + 2048p(p+2)(E_1 - E_2)^2\right]^{1/2}. \quad (4-7)
\end{aligned}$$

The moment stability boundary is then obtained as $\Lambda^{(1)}(p) = 0$. From this boundary, one can establish the relation between E_1 and E_2 , and the critical excitation S_0 , which will be shown in application part.

The corresponding largest Lyapunov exponents are

$$\lambda^{(1)}(p) = \frac{1}{112} \frac{21k^4S_0^2 - 56k^2S_0(E_1 + E_2) + 32(E_1 - E_2)^2}{k^2S_0}. \quad (4-8)$$

The almost-sure stability region is found to be

$$21k^4S_0^2 - 56k^2S_0(E_1 + E_2) + 32(E_1 - E_2)^2 < 0. \quad (4-9)$$

The analytical accurate results of Lyapunov exponents from (3-29) and numerical results from (3-28) are compared in Figure 2, left, which shows the two results almost overlap. Care should be taken that for $S(\omega) \rightarrow 0$, the numerical results may become unstable due to roundoff errors. Figure 2, left, illustrates that Lyapunov moments converge quickly with the increase of expansion order K . It is noted that although the results in Figure 2 overlap, the analytical expressions from (3-29) to (3-31) seem not to agree with the expression given in (4-8). This can be explained by the discrepancy between exact solutions and a sequence of approximations.

When $K = 2$, the eigenfunction is $T(\varphi) = C_0 + C_1 \cos 2\varphi + C_2 \cos 4\varphi$, and the moment Lyapunov exponent can be solved from

$$\begin{vmatrix} a_{00} - \Lambda^{(2)} & a_{01} & a_{02} \\ a_{10} & a_{11} - \Lambda^{(2)} & a_{12} \\ a_{20} & a_{21} & a_{22} - \Lambda^{(2)} \end{vmatrix} = \mathbf{0}. \quad (4-10)$$

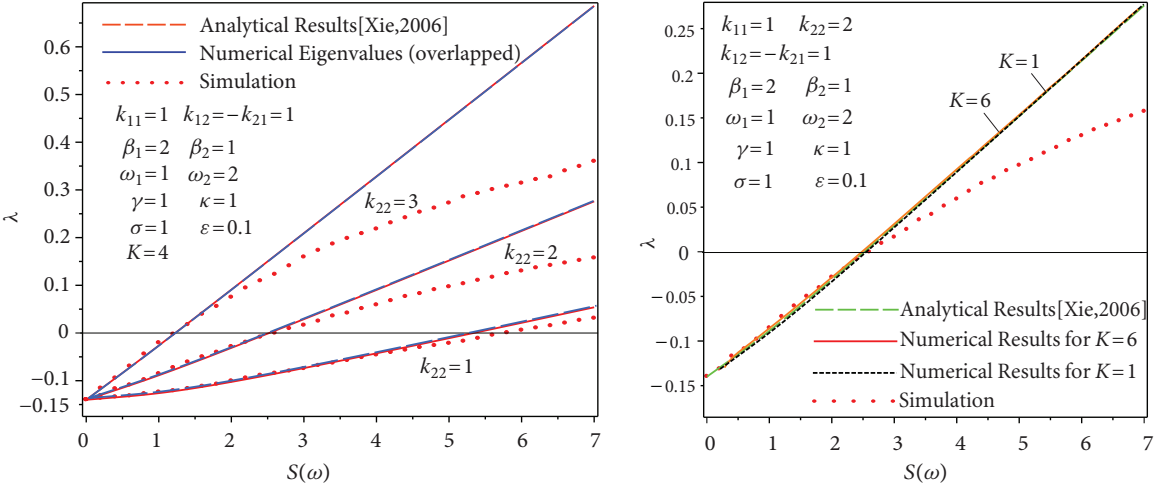


Figure 2. Comparisons of largest Lyapunov exponents for varying k_{22} (left) and varying K (right).

Expanding we get a cubic equation, $(\Lambda^{(2)})^3 + e_2^{(2)}(\Lambda^{(2)})^2 + e_1^{(2)}\Lambda^{(2)} + e_0^{(2)} = 0$. The coefficients for symmetric coupled systems with white noise ($S(\omega) = S_0$, $k_{12} = k_{21} = k$, and $k_{11} = k_{22} = 0$) are given by

$$\begin{aligned}
 e_2^{(2)} &= -\frac{1}{256}(13p^2 + \frac{17}{32}p - \frac{27}{8})S_0k^2 + \frac{3}{2}p(E_1 + E_2), \\
 e_1^{(2)} &= S_0^2k^4(\frac{3}{2048}p^4 + \frac{13}{512}p^3 - \frac{55}{512}p^2 - \frac{143}{128}p + \frac{35}{16}) - S_0k^2(E_1 + E_2)(\frac{5}{64}p^3 + \frac{17}{32}p^2 - \frac{27}{8}p) \\
 &\quad + (\frac{9}{16}E_1^2 + \frac{9}{16}E_2^2 + \frac{15}{8}E_1E_2)p^2 + (E_1 - E_2)^2(\frac{1}{2} - \frac{3}{8}p), \\
 e_0^{(2)} &= -S_0^3k^6(\frac{1}{131072}p^6 + \frac{15}{65536}p^5 - \frac{1}{32768}p^4 - \frac{427}{16384}p^3 + \frac{1}{1024}p^2 + \frac{357}{1024}p) \\
 &\quad + S_0^2k^4(E_1 + E_2)(\frac{3}{4096}p^5 + \frac{13}{1024}p^4 - \frac{55}{1024}p^3 - \frac{143}{256}p^2 + \frac{35}{32}p) \\
 &\quad + S_0k^2[-(\frac{5}{512}E_1^2 + \frac{5}{512}E_2^2 + \frac{15}{256}E_1E_2)p^4 - (\frac{9}{128}E_1^2 + \frac{9}{128}E_2^2 + \frac{25}{64}E_1E_2)p^3 \\
 &\quad + (\frac{89}{128}E_1^2 + \frac{89}{128}E_2^2 + \frac{127}{64}E_1E_2)p^2 - (\frac{33}{32}E_1^2 + \frac{33}{32}E_2^2 - \frac{33}{16}E_1E_2)p] \\
 &\quad + (\frac{1}{32}E_1^3 + \frac{1}{32}E_2^3 + \frac{15}{32}E_1^2E_2 + \frac{15}{32}E_1E_2^2)p^3 + (E_1^3 + E_2^3 - E_1^2E_2 - E_1E_2^2)(\frac{1}{4}p - \frac{3}{16}p^2). \quad (4-11)
 \end{aligned}$$

The analytical expression for moment Lyapunov exponent can then be obtained by solving this cubic equation. However, for $K \geq 3$, no explicit expressions can be presented, as quartic equation is involved.

The Lyapunov exponent for $K = 2$ is given by

$$\lambda^{(2)} = -\lim_{p \rightarrow 0} \frac{e_0^{(2)}}{pe_1^{(2)}} = \frac{1}{256} \frac{\lambda_N}{\lambda_D}, \quad (4-12)$$

where

$$\begin{aligned}
\lambda_N &= 22848S_0^3k^6 + (14480(k_{11}^2 + k_{22}^2)S_0 - 71680(E_1 + E_2))S_0^2k^4 \\
&+ \left\{ (2076k_{11}^4 + 2076k_{22}^4 - 72k_{11}^2k_{22}^2)S_0^2 \right. \\
&\quad \left. + ((10752k_{11}^2 - 23040k_{22}^2)E_2 + (10752k_{22}^2 - 23040k_{11}^2)E_1)S_0 + 67584(E_1 - E_2)^2 \right\} S_0k^2 \\
&+ (k_{11}^4k_{22}^2 + k_{11}^2k_{22}^4 + 75k_{11}^6 + 75k_{22}^6)S_0^3 \\
&+ ((512k_{22}^4 + 256k_{22}^2k_{22}^2 - 1280k_{11}^4)E_1 + (512k_{11}^4 + 256k_{22}^2k_{22}^2 - 1280k_{22}^4)E_2)S_0^2 \\
&+ ((7680k_{11}^2 - 512k_{22}^2)E_1^2 - 7168(k_{11}^2 + k_{22}^2)E_1E_2 + (7680k_{22}^2 - 512k_{11}^2)E_2^2)S_0 \\
&- 16384(E_1^3 + E_2^3 - E_1^2E_2 - E_1E_2^2), \\
\lambda_D &= 560S_0^2k^4 + 48(k_{11}^2 + k_{22}^2)S_0^2k^2 + (3k_{11}^4 + 3k_{22}^4 - 2k_{22}^2k_{22}^2)S_0^2 \\
&+ 32((k_{22}^2 - k_{11}^2)E_1 + (k_{11}^2 - k_{22}^2)E_2)S_0 + 128(E_1 - E_2)^2.
\end{aligned}$$

5. Stability index

The stability index is the nontrivial zero of the moment Lyapunov exponent. Hence, it can be determined as a root-finding problem such that $\Lambda_{q(t)}(\delta_{q(t)}) = 0$. When the order K of the Fourier expansion is 0, from (4-1), the stability index is given by

$$\delta_{q(t)} = 2 \frac{5k_{11}^2S_0 + 5k_{22}^2S_0 + 24k^2S_0 - 32(E_1 + E_2)}{3k_{11}^2S_0 + 3k_{22}^2S_0 + 8k^2S_0}. \quad (5-1)$$

When $K = 1$, the stability index is the nontrivial solution of $\Lambda^{(1)}(p) = 0$ from (4-7), which is hard to express analytically. Typical results of the stability index are shown in Figure 3. It is seen that the stability index decreases from positive to negative values with the increase of the amplitude of power spectrum, which suggests that the noise destabilizes the system. The larger the pseudodamping coefficient E_1 , the larger the stability index, and then the more stable the system.

6. Simulation

Monte Carlo simulation is applied to determine the p -th moment Lyapunov exponents and to check the accuracy of the approximate results from the stochastic averaging.

Suppose the excitation is approximated by a Gaussian white noise with spectral density $S(\omega) = \vartheta^2 =$ constant for all ω , and then $\xi(t) dt = \vartheta dW(t)$. Let

$$\begin{aligned}
x_1(t) &= q_1(t), & x_2(t) &= \dot{q}_1(t), & x_3(t) &= q_2(t), & x_4(t) &= \dot{q}_2(t), \\
x_5(t) &= \int_0^t \gamma e^{-\xi(t-s)} q_1(s) ds, & x_6(t) &= \int_0^t \gamma e^{-\xi(t-s)} q_2(s) ds.
\end{aligned} \quad (6-1)$$

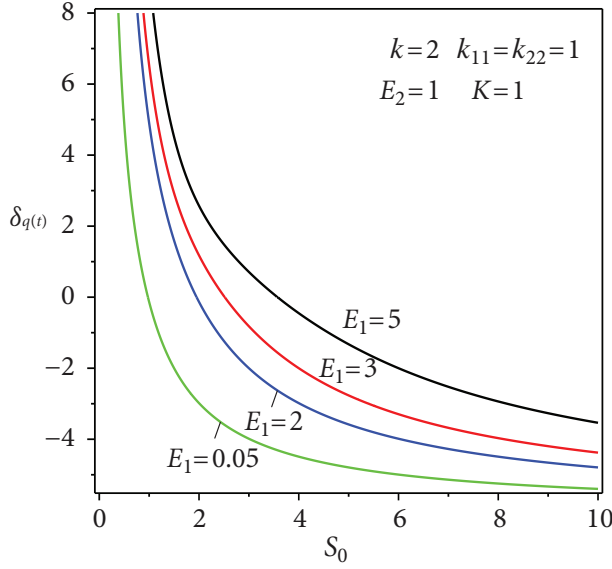


Figure 3. Stability index for system under white noise.

Equation (2-1) can be written as a six-dimensional system of Itô differential equations

$$d\mathbf{x} = \mathbf{A} \mathbf{x} dt + \mathbf{B} \mathbf{x} \vartheta dW, \quad (6-2)$$

where $\mathbf{x} = \{x_1, x_2, x_3, x_4, x_5, x_6\}^T$, and

$$\mathbf{A} = \begin{bmatrix} 0 & 1 & 0 & 0 & 0 & 0 \\ -\omega_1^2 & -2\varepsilon\beta_1 & 0 & 0 & -\varepsilon\omega_1^2 & 0 \\ 0 & 0 & 0 & 1 & 0 & 0 \\ 0 & 0 & -\omega_2^2 & -2\varepsilon\beta_2 & 0 & -\varepsilon\omega_2^2 \\ \gamma & 0 & 0 & 0 & -\zeta & 0 \\ 0 & 0 & \gamma & 0 & 0 & -\zeta \end{bmatrix}, \quad \mathbf{B} = \begin{bmatrix} 0 & 0 & 0 & 0 & 0 & 0 \\ -\varepsilon^{1/2}\omega_1 k_{11} & 0 & -\varepsilon^{1/2}\omega_1 k_{12} & 0 & 0 & 0 \\ 0 & 0 & 0 & 0 & 0 & 0 \\ -\varepsilon^{1/2}\omega_2 k_{21} & 0 & -\varepsilon^{1/2}\omega_2 k_{22} & 0 & 0 & 0 \\ 0 & 0 & 0 & 0 & 0 & 0 \\ 0 & 0 & 0 & 0 & 0 & 0 \end{bmatrix}. \quad (6-3)$$

Equation (6-2) is linear homogeneous. We apply the algorithm proposed in [Xie 2006; Wolf et al. 1985] to simulate the moment Lyapunov exponents and Lyapunov exponents. The norm for simulations is

$$\|\mathbf{x}(t)\| = \sqrt{\sum_{i=1}^6 x_i^2}.$$

The iteration equations are given by, using the explicit Euler scheme,

$$\begin{aligned} x_1^{k+1} &= x_1^k + x_2^k \cdot \Delta t, \\ x_2^{k+1} &= x_2^k + (-\omega_1^2 x_1^k - 2\varepsilon\beta_1 x_2^k + \varepsilon\omega_1^2 x_5^k) \Delta t - \varepsilon^{1/2}\omega_1 (k_{11} x_1^k + k_{12} x_3^k) \vartheta \cdot \Delta^k, \\ x_3^{k+1} &= x_3^k + x_4^k \cdot \Delta t, \\ x_4^{k+1} &= x_4^k + (-\omega_2^2 x_3^k - 2\varepsilon\beta_2 x_4^k + \varepsilon\omega_2^2 x_6^k) \Delta t - \varepsilon^{1/2}\omega_2 (k_{21} x_1^k + k_{22} x_3^k) \vartheta \cdot \Delta^k, \end{aligned}$$

$$x_5^{k+1} = x_5^k + (\gamma x_1^k - \zeta x_5^k) \Delta t, \quad \text{and} \quad x_6^{k+1} = x_6^k + (\gamma x_3^k - \zeta x_6^k) \Delta t,$$

where Δt is the time step and k denotes the k -th iteration.

The analytical and numerical Lyapunov exponents in Figure 2 are tangent lines of results from Monte Carlo simulation, which confirms the method of stochastic averaging is a valid first-order approximation method. In Monte Carlo simulation, the sample size for estimating the expected value is $N = 5000$, time step is $\Delta t = 0.0005$, and the number of iteration is 10^8 .

7. Application: flexural-torsional stability of a rectangular beam

As an application, the flexural-torsional stability of a simply supported, uniform, narrow, rectangular, viscoelastic beam of length L subjected to a stochastically varying concentrated load $P(t)$ acting at the center of the beam cross-section as shown in Figure 4 is considered. Both nonfollower and follower loading cases are studied.

For the elastic beam under dynamic loading, the flexural and torsional equations of motion are given by (see [Xie 2006])

$$\begin{aligned} EI_y \frac{\partial^4 u}{\partial z^4} + \frac{\partial^2 (M_x \psi)}{\partial z^2} - \frac{\partial^2 M_y}{\partial z^2} + m \frac{\partial^2 u}{\partial t^2} + D_u \frac{\partial u}{\partial t} &= 0, \\ -GJ \frac{\partial^2 \psi}{\partial z^2} + \frac{\partial M_x}{\partial z} \frac{\partial u}{\partial z} + M_x \frac{\partial^2 u}{\partial z^2} + \frac{\partial M_z}{\partial z} + mr^2 \frac{\partial^2 \psi}{\partial t^2} + D_\psi \frac{\partial \psi}{\partial t} &= 0, \end{aligned} \quad (7-1)$$

with boundary conditions

$$u(0, t) = u(L, t) = \frac{\partial^2 u(0, t)}{\partial z^2} = \frac{\partial^2 u(L, t)}{\partial z^2} = 0, \quad \psi(0, t) = \psi(L, t) = 0, \quad (7-2)$$

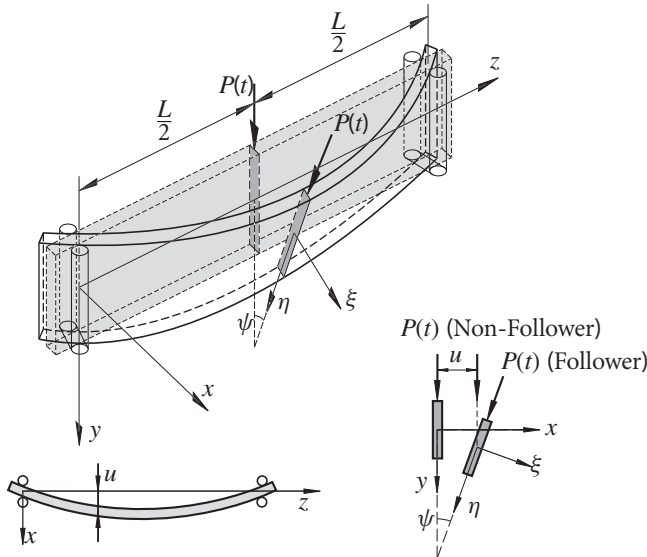


Figure 4. Flexural-torsional vibration of a rectangular beam.

where M_x , M_y , and M_z are the bending moments in the x , y , and z direction, respectively. $u(t)$ is the lateral deflection and $\psi(t)$ is the angle of twist. E is Young's modulus of elasticity and G is the shear modulus. I_y is the moment of inertia in the y direction. J is Saint-Venant's torsional constant. $E I_y$ is the flexural rigidity, GJ is the torsional rigidity, m is the mass per unit length of the beam, r is the polar radius of gyration of the cross section, D_ψ and D_u are the viscous damping coefficients in the ψ and u directions, respectively, t is time and z is the axial coordinate.

For a three-dimensional loading, the stress and strain tensors σ and ϵ are given by

$$\sigma = \sigma_I + s, \quad \epsilon = \epsilon_I + e, \quad (7-3)$$

where σ_I and ϵ_I are the stress and strain first invariants, which produce dilatation and no distortion, also called hydrostatic or volumetric tensor, and s and e are the stress and strain deviatoric components, which tend to distort the body. The deviatoric stress tensor can be obtained by subtracting the hydrostatic stress tensor from the stress tensor.

According to Boltzmann's superposition principle, a constitutive relation for a linear viscoelastic material under three-dimensional loading can be obtained by replacing the bulk modulus B and the shear modulus G by appropriate Volterra operators [Drozdov 1998]. Most natural and polymer materials exhibit a elastic dilatation whereas the shear deformation is viscoelastic. The bulk modulus is assumed to time-independent and then the viscoelastic constitutive relation is given by

$$\sigma_I = 3B\epsilon_I, \quad s = 2G(1 - \mathcal{H})e, \quad (7-4)$$

where κ is the bulk modulus, G is the shear modulus, and \mathcal{H} is the relaxation operator defined in (2-3) for Maxwell viscoelastic materials. Therefore, for problems with viscoelastic materials, one may simply replace the elastic moduli E and G in elastic problems by the Volterra operators $E(1 - \mathcal{H})$ and $G(1 - \mathcal{H})$, respectively. The governing equation for a viscoelastic deep beam can be obtained from (7-1) as

$$\begin{aligned} E I_y (1 - \mathcal{H}) \frac{\partial^4 u}{\partial z^4} + \frac{\partial^2 (M_x \psi)}{\partial z^2} - \frac{\partial^2 M_y}{\partial z^2} + m \frac{\partial^2 u}{\partial t^2} + D_u \frac{\partial u}{\partial t} = 0, \\ - GJ(1 - \mathcal{H}) \frac{\partial^2 \psi}{\partial z^2} + \frac{\partial M_x}{\partial z} \frac{\partial u}{\partial z} + M_x \frac{\partial^2 u}{\partial z^2} + \frac{\partial M_z}{\partial z} + m r^2 \frac{\partial^2 \psi}{\partial t^2} + D_\psi \frac{\partial \psi}{\partial t} = 0. \end{aligned} \quad (7-5)$$

These equations are partial stochastic differential equations and are difficult to solve. An approximate solution can be obtained by using Galerkin method. Seek solutions of the form

$$u(z, t) = q_1 \sin \frac{\pi z}{L}, \quad \psi(z, t) = q_2 \sin \frac{\pi z}{L}, \quad (7-6)$$

in which $q_1 = u_m = u(\frac{1}{2}L, t)$, $q_2 = \psi_m = \psi(\frac{1}{2}L, t)$. Substituting into (7-5), multiplying by $\sin(\pi z/L)$, and integrating with respect to z from 0 to L yields

$$\begin{aligned} \ddot{Q}_1 + 2\beta_1 \dot{Q}_1 + \omega_1^2 (1 - \mathcal{H}) Q_1 + \omega_1 k_{12} \xi(t) Q_2 = 0, \\ \ddot{Q}_2 + 2\beta_2 \dot{Q}_2 + \omega_2^2 (1 - \mathcal{H}) Q_2 + \omega_2 k_{21} \xi(t) Q_1 = 0, \end{aligned} \quad (7-7)$$

where

$$K = \sqrt{\frac{\omega_2(12 - \pi^2)}{\omega_1(4 + \pi^2)}}, \quad \beta_1 = \frac{D_u}{2m}, \quad \beta_2 = \frac{D_\psi}{2mr^2}, \quad \omega_1^2 = \left(\frac{\pi}{L}\right)^4 \frac{EI_y}{m}, \quad \omega_2^2 = \left(\frac{\pi}{L}\right)^2 \frac{GJ}{mr^2},$$

$$\xi(t) = \frac{P(t)}{P_{cr}}, \quad P_{cr} = \frac{4mrL|\omega_1^2 - \omega_2^2|}{[(12 - \pi^2)(4 + \pi^2)]^{1/2}}, \quad k_{12} = -k_{21} = \frac{|\omega_1^2 - \omega_2^2|}{2\sqrt{\omega_1\omega_2}} = k_F, \quad (7-8)$$

where β_1 and β_2 are reduced viscous damping coefficients, P_{cr} is the critical force for the simply supported narrow rectangular beam.

For nonfollower force case, the only difference is that $M_y = 0$ in (7-5). The equations of motion are of the same form of (7-7), but the parameters are different,

$$K = -\sqrt{\frac{\omega_2}{\omega_1}}, \quad 2\beta_1 = \frac{D_u}{m}, \quad 2\beta_2 = \frac{D_\psi}{mr^2}, \quad \omega_1^2 = \left(\frac{\pi}{L}\right)^4 \frac{EI_y}{m}, \quad \omega_2^2 = \left(\frac{\pi}{L}\right)^2 \frac{GJ}{mr^2},$$

$$\xi(t) = \frac{P(t)}{P_{cr}}, \quad P_{cr} = \frac{8mrL\omega_1\omega_2}{4 + \pi^2}, \quad k_{12} = k_{21} = \sqrt{\omega_1\omega_2} = k_N. \quad (7-9)$$

It is seen that (7-7) has the same form of (2-1), except that $k_{11} = k_{22} = 0$. By introducing the polar transformation and using the method of stochastic averaging, Equation (7-7) can be approximated in amplitude by the Itô stochastic differential equations in (2-8), where the drift and diffusion terms are given by

$$m_i^a = a_i[-\beta_i - \tau_\varepsilon \mathcal{M}_i(I_i^{sc})] + \frac{1}{8} \frac{a_j^2}{a_i} k_{ij}^2 S_0, \quad b_{ii}^a = \frac{1}{4} k_{ij}^2 a_j^2 S_0, \quad b_{ij}^a = 0. \quad (7-10)$$

Substituting (7-10) and $a_1 = r \cos \varphi$, $a_2 = r \sin \varphi$ into (3-20) yields the eigenvalue problem, from which moment Lyapunov exponents can be determined by solving (3-26).

Some analytical stability boundaries are discussed here. For nonfollower symmetric coupled systems under white noise excitation, the moment stability boundaries can be obtained from (4-1) for $K = 0$ and (4-7) for $K = 1$, and the almost-sure stability boundaries is from (4-3) for $K = 0$ and (4-9) for $K = 1$, which is shown in Figure 5, left. The moment stability boundaries are more conservative than the almost-sure boundary. With the moment order p increase, these moment boundaries become more and more conservative.

One can also obtain the critical amplitude of power spectral density of white noise excitation for the case $K = 1$ from (4-7) and (4-9), which is illustrated in Figure 5, right. The critical excitation increases with the pseudodamping coefficient, which confirms that damping and viscoelasticity would consume some energy of motion during vibration. Smaller amplitude of excitation (S_0) would destabilize the system in terms of higher-order moment stability, which suggests that stability region with higher-order moment is more conservative than that with lower-order moment stability. Almost-sure stability is the least conservative. Some numerical values for discrete points already shown in Figure 5, right, are listed in Table 1 for reference.

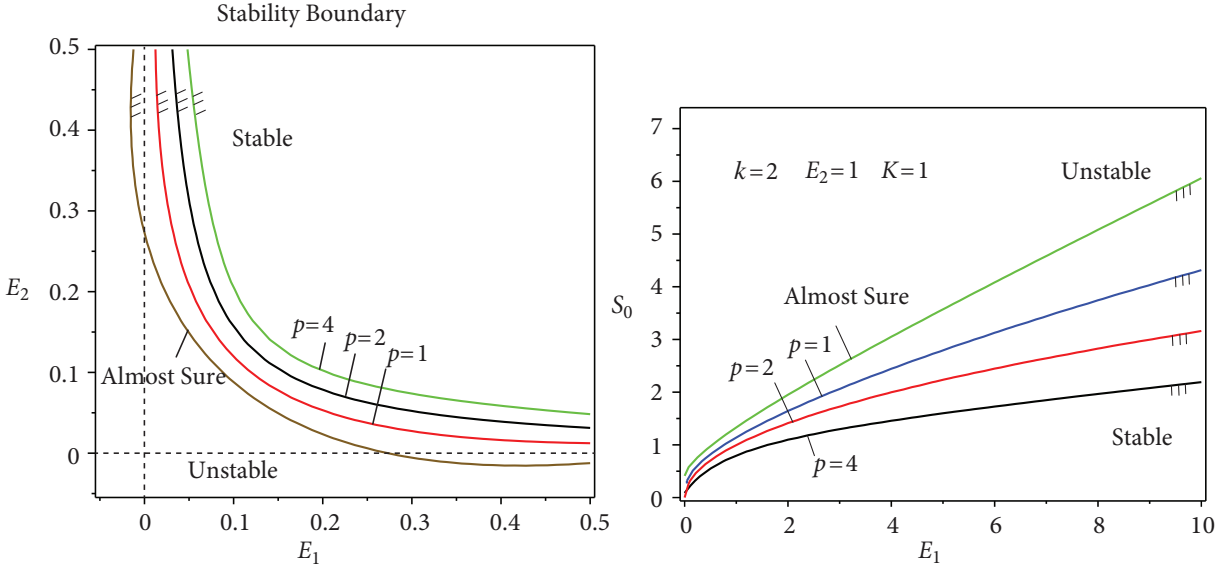


Figure 5. Left: Almost-sure and p -th moment stability boundaries. Right: Critical excitation and pseudodamping.

E_1	$p = 0$	$p = 1$	$p = 2$	$p = 4$
0	0.6667	0.2857	0.2500	0.2000
2	2.0000	0.8571	0.7500	0.6000
4	3.3333	1.4286	1.2500	1.0000
6	4.6667	2.0000	1.7500	1.4000
8	6.0000	2.5714	2.2500	1.8000
10	7.3333	3.1429	2.7500	2.2000

E_1	$p = 0$	$p = 1$	$p = 2$	$p = 4$
0	0.4593	0.2500	-	0.1000
2	1.9512	1.6443	1.4142	1.1000
4	3.0526	2.4459	2.0000	1.4600
6	4.0836	3.1290	2.4495	1.7286
8	5.0816	3.7463	2.8284	1.9667
10	6.0605	4.3184	3.1623	2.1909

Table 1. Critical excitations S_0 for the cases $K = 0$ (left) and $K = 1$ (right).

8. Discussion

Figure 6, top, shows that with the increase of β , the slope of the moment curves at the original point change from negative to positive, which suggests the beam’s status from instability to stability and so damping plays a stabilizing role in flexural-torsional analysis of the beam under white noise excitation.

Figure 6, bottom, shows that the viscoelastic intensity γ has a stabilizing effect (left panel) but η plays a destabilizing effect on systems under white noise (right panel). With an increase of γ , the stability index also increases, which means the stability region for $p > 0$ becomes wider, so the viscoelasticity help stabilization. However, the decrease of η means the relaxation time increase, the stability region for $p > 0$ also becomes wider, which shows smaller η or larger relaxation time helps to stabilize the system. The effect of stabilization is prominent only when η is small. As η exceeds 10, large increase of η produces very small effect on stabilization.

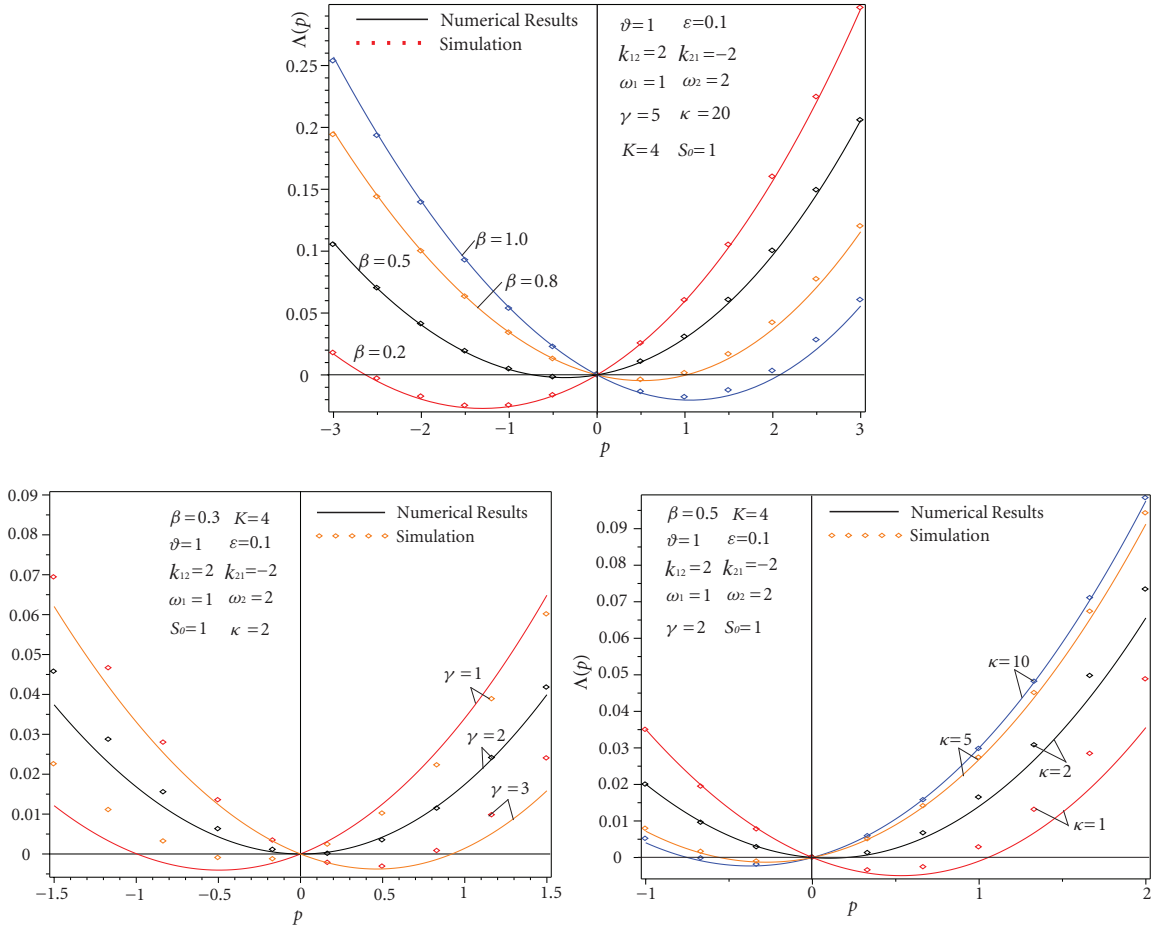


Figure 6. Effect of damping (top), viscosity γ (bottom left), and viscosity η (bottom right) on moment Lyapunov exponents.

9. Conclusions

The stochastic stability of coupled viscoelastic systems described by Stratonovich stochastic integro-differential equations of 2DOF was investigated. The system was parametrically excited by white noise of small intensity with small damping. The Stratonovich equations of motion were first decoupled into two-dimensional Itô stochastic differential equations, by making use of the method of stochastic averaging for the nonviscoelastic terms and the method of Larionov for viscoelastic terms. An elegant scheme for determining the moment Lyapunov exponents was presented by only using Khasminskii and Wedig's mathematical transformations from the decoupled Itô equations. The moment Lyapunov exponents and Lyapunov exponents are compared well to the Monte Carlo simulation results and other analytical expressions from the literature.

As an application, the flexural-torsional stability of a simply supported rectangular viscoelastic beam subjected to a stochastically varying concentrated load acting at the center of the beam cross-section is considered. The moment and almost-sure stability boundaries and the critical amplitude of power spectral

density are obtained. It is found that, under white noise excitation, the parameters of damping β and the viscoelastic intensity γ have stabilizing effects on the moment and almost-sure stability. However, viscosity parameter η plays a destabilizing role. The stability index decreases from positive to negative values with the increase of the amplitude of power spectrum, which suggests that the noise destabilize the system. These results are useful in engineering applications.

Acknowledgement

The research for this paper was supported, in part, by the Natural Sciences and Engineering Research Council of Canada.

References

- [Abdelrahman 2002] N. M. Abdelrahman, *Stochastic stability of viscoelastic dynamical systems*, University of Waterloo, Waterloo, Canada, 2002.
- [Ahmadi and Glocker 1983] G. Ahmadi and P. G. Glocker, “Dynamic stability of a Kelvin-viscoelastic column”, *J. Engineering Mech.* **109**:4 (1983), 990–999.
- [Ariaratnam 1993] S. T. Ariaratnam, “Stochastic stability of linear viscoelastic systems”, *Prob. Engin. Mech.* **8**:3-4 (1993), 153–155.
- [Ariaratnam 1996] S. T. Ariaratnam, “Stochastic stability of viscoelastic systems under bounded noise excitation”, pp. 11–18 in *Advances in nonlinear stochastic mechanics* (Trondheim, 1995), Solid Mech. Appl. **47**, Kluwer, Dordrecht, 1996.
- [Ariaratnam and Xie 1993] S. T. Ariaratnam and W. C. Xie, “Lyapunov exponents and stochastic stability of two-dimensional parametrically excited random systems”, *Trans. ASME J. Appl. Mech.* **60**:3 (1993), 677–682.
- [Ariaratnam et al. 1991] S. T. Ariaratnam, D. S. F. Tam, and W. C. Xie, “Lyapunov exponents and stochastic stability of coupled linear systems under white noise excitation”, *Probabilistic Engineering Mechanics* **6**:2 (1991), 51–56.
- [Arnold et al. 1997] L. Arnold, M. M. Doyle, and N. Sri Namachchivaya, “Small noise expansion of moment Lyapunov exponents for two-dimensional systems”, *Dynam. Stability Systems* **12**:3 (1997), 187–211.
- [Bolotin 1964] V. V. Bolotin, *The dynamic stability of elastic systems*, Holden-Day, San Francisco, 1964.
- [Drozdo 1998] A. D. Drozdov, *Viscoelastic structures: mechanics of growth and aging*, Academic Press, San Diego, 1998.
- [Huang and Xie 2008] Q. Huang and W. C. Xie, “Stability of SDOF linear viscoelastic system under the excitation of wide-band noise”, *J. Appl. Mech. (ASME)* **75**:2 (2008), id 021012.
- [Janevski et al. 2012] G. Janevski, P. Kozic, and R. Pavlovic, “Moment Lyapunov exponents and stochastic stability of a thin-walled beam subjected to eccentric axial loads”, *J. Theor. Appl. Mech.* **50**:1 (2012), 61–83.
- [Khasminskii 1966] R. Z. Khasminskii, “A limit theorem for solutions of differential equations with a random right hand part”, *Teor. Veroyatnost. i Primenen* **11** (1966), 444–462. In Russian; translated in *Theor. Probab. Appl.* **11** (1966), 390–406.
- [Khasminskii and Moshchuk 1998] R. Khasminskii and N. Moshchuk, “Moment Lyapunov exponent and stability index for linear conservative system with small random perturbation”, *SIAM J. Appl. Math.* **58**:1 (1998), 245–256.
- [Larionov 1969] G. S. Larionov, “Investigation of the vibration of relaxing systems by the averaging method”, *Mech. Polymers* **5** (1969), 714–720.
- [Oseledec 1968] V. I. Oseledec, “A multiplicative ergodic theorem: Lyapunov characteristic number for dynamical systems”, *Trudy Moskov. Mat. Obšč.* **19** (1968), 179–210. In Russian; translated in *Trans. Moscow Math. Soc.* **19** (1968), pp. 197–231.
- [Potapov 1994] V. D. Potapov, “On almost sure stability of a viscoelastic column under random loading”, *J. Sound Vib.* **173** (1994), 301–308.
- [Potapov 1997] V. D. Potapov, “Numerical method for investigation of stability of stochastic integro-differential equations”, *Appl. Numer. Math.* **24**:2-3 (1997), 191–201.

- [Roberts and Spanos 1986] J. B. Roberts and P.-T. D. Spanos, “Stochastic averaging: an approximate method of solving random vibration problems”, *Internat. J. Non-Linear Mech.* **21**:2 (1986), 111–134.
- [Sri Namachchivaya and Ariaratnam 1987] N. Sri Namachchivaya and S. T. Ariaratnam, “Periodically perturbed Hopf bifurcation”, *SIAM J. Appl. Math.* **47**:1 (1987), 15–39.
- [Sri Namachchivaya and van Roessel 2001] N. Sri Namachchivaya and H. J. van Roessel, “Moment Lyapunov exponent and stochastic stability of two coupled oscillators driven by real noise”, *Trans. ASME J. Appl. Mech.* **68**:6 (2001), 903–914.
- [Stratonovich 1963] R. L. Stratonovich, *Topics in the theory of random noise, I: General theory of random processes; nonlinear transformations of signals and noise*, Gordon and Breach, New York, 1963.
- [Wedig 1988] W. Wedig, “Lyapunov exponent of stochastic systems and related bifurcation problems”, pp. 315–317 in *Stochastic structural dynamics: progress in theory and applications*, edited by S. T. Ariaratnam et al., Elsevier Applied Science, London, 1988.
- [Wolf et al. 1985] A. Wolf, J. B. Swift, H. L. Swinney, and J. A. Vastano, “Determining Lyapunov exponents from a time series”, *Phys. D* **16**:3 (1985), 285–317.
- [Xie 2003] W.-C. Xie, “Moment Lyapunov exponents of a two-dimensional system under bounded noise parametric excitation”, *J. Sound Vibration* **263**:3 (2003), 593–616.
- [Xie 2006] W.-C. Xie, *Dynamic stability of structures*, Cambridge University Press, 2006.

Received 14 Apr 2013. Revised 26 Dec 2013. Accepted 11 Feb 2014.

JIAN DENG: j7deng@uwaterloo.ca

Department of Civil Engineering, Lakehead University, Thunder Bay, ON P7B 5E1, Canada

WEI-CHAU XIE: xie@uwaterloo.ca

Department of Civil and Environmental Engineering, University of Waterloo, Waterloo, ON N2L 3G1, Canada

MAHESH D. PANDEY: mdpandey@uwaterloo.ca

Department of Civil and Environmental Engineering, University of Waterloo, Waterloo, ON N2L 3G1, Canada

COMBINED EFFECTS OF INTERSTITIAL AND LAPLACE PRESSURE IN HOT ISOSTATIC PRESSING OF CYLINDRICAL SPECIMENS

LAURA GALUPPI AND LUCA DESERI

Sintering of precompacted metallic and ceramic micro and nanopowders is a complex problem influenced by several factors. We quantify the influence of both local capillary stresses acting at the surface of one pore or particle (usually referred to as Laplace pressure) and the gas pressure in pores during sintering of precompacted metallic (micro/nano)powdered cylinders. The latter influences only the third phase of sintering, that is, the phase in which the porosity is closed.

The isostatic pressing loading mode, which also covers the case of free sintering, is considered. Whereas the Laplace pressure is demonstrated to have a beneficial effect on sintering, the gas pressure acts against the reduction of the porosity, causing an increase in sintering time. This contribution could reach the sum of the stress due to loading and the interstitial pressure, thereby preventing the desired porosity to be reached.

For the sake of illustration, a specific aluminum-zinc-magnesium-copper alloy is examined in this paper. The purpose is to estimate the effects of sintering time and residual porosity and to determine thresholds under which the contributions described above are negligible. In order to determine the effects of Laplace and gas pressure in pores on the stability of the process, a high-order perturbation analysis has been performed.

1. Introduction

In recent decades, powder technology has become one of the most important technological processes for the production of metallic and ceramics components. Free sintering, hot isostatic pressing (HIP), and hot forging are different ways to realize a key phase in which the primary mechanical properties of the final material are obtained. In order to be able to predict the final structure of a body undergoing such a process, it is crucial to define an analytical theory of sintering allowing one to follow the evolution of the mechanical properties of the material (determined by this structure) during sintering, and to get the final features of the compound at the end of this process.

The foundations of the analytical study of sintering processes were laid down in the 70s (see, for example, [Skorohod 1972; Ashby 1974; Coleman and Beere 1975]) and many studies gave important new results in the 90s [Duva and Crow 1992; Cocks 1994; Olevsky and Molinari 2000]. In recent years, several papers have improved knowledge of sintering processes. This has been done both from analytical (see, among others, [Olevsky et al. 2006; Maximenko et al. 2012; Wakai 2013]) and experimental (see, for example, [Guillon et al. 2008; Sankar et al. 2011]) points of view; the latter is usually focused on new materials and techniques. An innovative sintering technique, widely developed and used in recent years,

Keywords: sintering, powder technology, nanopowders, hot isostatic pressing, interstitial and Laplace pressure, ceramic compaction, metallic powder compaction .

is spark plasma sintering (SPS), in which materials are compacted and condensed to higher densities. Systems designed for SPS use direct current pulses to create spark energy between the particles of the material. This technology achieves rapid fusing between particles and, unlike other sintering processes that are solely involved in metalworking, SPS can be applied to ceramics, composite materials, and nanostructures. The compaction of samples can be achieved in a relatively short time period, making SPS a very promising technique for elaborate nanostructured materials. Several studies have recently been performed on this technique [Munir et al. 2006; Schwarz et al. 2012; Wolff et al. 2012].

The present work is focused on modeling the evolution of material properties during sintering of axisymmetric samples. It is a natural extension of [Olevsky and Molinari 2006], dealing with an analysis of the kinetics and stability of porous axially symmetric bodies undergoing sintering under different loading modes. In that paper, in addition to an extensive review of the available literature, both about modeling of sintered materials obtained by compacted powders (see, for example, [Bigoni and Piccolroaz 2004; Piccolroaz et al. 2006a; 2006b]) and constitutive equations for porous media, the problem is solved for the cases in which both the interstitial stress (due to the pressure exerted by the gas in the pores) and the Laplace pressure (due to the surface tension at the interfaces between matrix and pores) are negligible compared with the external loading. The strategy introduced in [Olevsky and Molinari 2006] appears to be the most effective among the possibilities for predicting the kinetics of bodies undergoing sintering (even for the simple geometry mentioned above). More modern formulations dealing with multiscale mechanics may also be conceived to deliver more accurate micromechanics-based approaches to sintering (see, for example, [Deseri and Owen 2003; 2010; 2013; Paola and Zingales 2011; 2012; Dal Corso and Deseri 2013; Deseri et al. 2013; Paola et al. 2013], among many others).

Even though sintering is an inhomogeneous process, not only due to the inhomogeneity of the properties of the powder particles but also to internal stresses that can arise either from external constraints, differential densification [Green et al. 2008], or particle rearrangement during sintering [Wakai et al. 2007; Lee et al. 2012], in this work only the average state of the stress is considered. This is motivated by the observation, pointed out in [Olevsky and Molinari 2006], that the assumption of homogeneous plane stress through a sample is reasonable even in the case of a nonuniform cross-section (see, for example, [Hutchinson et al. 1978] for tensile tests). Incidentally, this is equivalent to assuming that specimens undergo constant states of (plane) stresses corresponding to the average of the actual stress fields. The approach suggested by the assumptions above has the advantage of capturing the essentials of both kinetics and stability, avoiding searching for the solutions of complicated (initial) boundary value problems. Nevertheless, in [Olevsky and Molinari 2006], this strategy has been employed only for cases in which the effect of the Laplace pressure is negligible with respect to the applied stresses. Hence it needs to be extended to the case of moderate stresses in comparison with the interstitial gas pressure.

Here we consider ideal processes where stresses are kept constant, unlike in [Olevsky and Molinari 2006], where, instead, a fictitious external load replaces the role of the stress.

This paper is outlined as follows. In Section 2, the theory of sintering introduced in [Olevsky 1998; Olevsky and Molinari 2006] is essentially summarized and specialized for the case of isostatic pressing processes, emphasizing the role of the Laplace pressure and the gas pressure in pores. In Section 2.3, the two most-used ways to get the relationship between the porosity (defined as the ratio of the volume of pores and the total volume of the sintered material) and the Laplace pressure (also called the *sintering*

stress) are revisited; furthermore, the model for obtaining such a pressure based on the microscopic dissipation is shown to be compatible with the incompressibility of the matrix if and only if the material is nonlinearly viscous. Analogously, in [Section 2.4](#) a practical way to account for the interstitial stress (that is, the gas pressure in pores) is proposed.

In [Section 3](#), the effect of the Laplace pressure on the evolution of the porosity in sintering processes entailing isostatic pressing is studied. An accurate comparison among different models of the normalized shear and bulk moduli of the material and between the two different expressions for the sintering is performed. In [Section 3.1](#), two issues are investigated. First of all, thresholds on stresses caused by external loads are determined, under which the influence of the interstitial pressure cannot be neglected. Such thresholds may be strongly influenced by the strain rate sensitivity of the material and the average radius of the particles; this feature may have a stronger impact for nanostructured powders. Furthermore, the discrepancy between the values of the residual porosity is evaluated by neglecting or accounting for the Laplace pressure in sintering processes of a given time-duration. In [Section 4](#), an analogous analysis is performed regarding the effect of gas pressure in pores in isostatic pressing sintering processes. In performing such analysis, two cases may arise through a comparison between the stress caused by external loading and Laplace pressure (sintering driving) and gas pressure in pores (opposing the reduction of the porosity). In particular, the occurrence of equality between such values can be reached at a definite (critical) porosity, which remains constant at a limit value. It is clear that, if this value is greater than the desired porosity at the end of the process, this cannot be obtained.

Finally, in [Section 5](#), the stability of the process, namely of the solution of the problem in terms of the time evolution of the porosity obtained in [Section 2](#), is performed in two steps along the lines traced in [\[Olevsky and Molinari 2006\]](#). A lower-order analysis is performed in [Section 5.1](#), where perturbations on the porosity alone are considered. In [Sections 5.2](#) and [5.3](#), a higher-order analysis is performed by perturbing, together with the porosity, the reference value of the Laplace pressure and the gas pressure in pores; this more refined analysis shows that the effect of the latter is to reduce the stability of the process. The [Appendix](#) is devoted to analyzing free sintering processes. In particular, since no external stress is applied, it is crucial to examine to what extent different ways of evaluating the Laplace pressure may influence the outcome in terms of the evolution of the porosity. Hence, a parametric analysis in terms of the given temperature is performed to estimate the sintering time for a prescribed target residual porosity.

2. Theory of sintering and kinetics of porosity

The sintering process is classically divided into three phases [\[Swinkels and Ashby 1981; Swinkels et al. 1983; Cocks 1994\]](#):

- A first stage in which the particles are brought into contact and necks grow at the particle contacts; in this phase, the material may be modeled as an aggregate of individual particles with little contact. For crystalline materials, this phase involves diffusion of vacancies in the crystal lattice, whereas noncrystalline materials sinter by viscous flow [\[Scherer 2001\]](#).
- An intermediate second stage in which the material can be idealized as a porous material with connected porosity.
- A third and final phase in which, usually for relative density (that is, as will be discussed in the sequel, the ratio between the volume of the matrix and the total volume of the sintered material)

greater than 90% [Coleman and Beere 1975], i.e., for porosity less than 10%, in which the pores are isolated and spherical. In the sequel, this value of the porosity will be denoted by θ_c , called the closure porosity.

It is important to note that in the second phase the pores can be considered quasispherical [Ashby 1974].

The mechanical response of a porous body with nonlinear-viscous behavior (stages 2 and 3) is strongly influenced by the presence of pores (see, for example, [Wakai 2013]) and is described by a rheological constitutive relation, namely:

$$\sigma_{ij} = \frac{\sigma(w)}{w} [\varphi \dot{\varepsilon}'_{ij} + \psi \dot{\varepsilon} \delta_{ij}] + p_L \delta_{ij} - p_I \delta_{ij}, \quad (1)$$

interrelating the components of the stress σ_{ij} and the strain rate $\dot{\varepsilon}_{ij}$ [Olevsky 1998]. The quantity p_L represents the Laplace pressure, while the term p_I represents the gas pressure in the pores. Obviously, $p_I = 0$ during the first and second phases, since the porosity is open. Here, $\dot{\varepsilon}'_{ij}$ denotes the ij -th component of the deviatoric strain rate tensor; w is the effective equivalent strain rate, defined as

$$w = \frac{1}{\sqrt{1-\theta}} \sqrt{\varphi \dot{\gamma}^2 + \psi \dot{\varepsilon}^2}, \quad (2)$$

where

$$\dot{\varepsilon} = \dot{\varepsilon}_{ii} \quad (3)$$

measures the local shrinking rate (whenever the sintering process entails a volume reduction), and

$$\dot{\gamma} = \sqrt{\dot{\varepsilon}'_{ij} \dot{\varepsilon}'_{ij}} \quad (4)$$

measures the local rate of change in shape. Here and subsequently, index notation with Einstein summation convention is adopted.

The quantity p_L represents the interstitial pressure produced by the gas contained in the pores; in the sequel we will refer to p_L as either the ‘‘Laplace pressure’’ or the ‘‘sintering stress’’ (see [Olevsky 1998; Olevsky and Molinari 2000; 2006]).

For further developments, it is convenient to introduce the stress quantities p and τ directly related to shrinking and change in shape, respectively:

$$p = \frac{1}{3} \text{tr} \sigma = \frac{\sigma(w)}{w} \psi \dot{\varepsilon} + p_L - p_I, \quad (5)$$

$$\tau = \sqrt{\sigma'_{ij} \sigma'_{ij}} = \frac{\sigma(w)}{w} \varphi \dot{\gamma}, \quad (6)$$

where σ'_{ij} denotes the ij -th component of of the deviatoric stress tensor. The quantities φ , ψ , p_L , and p_I and their dependence upon the porosity will be treated in Sections 2.2, 2.3, and 2.4.

Let us consider a cylindrical axisymmetric specimen, subject to an external load. The porosity θ , defined as the ratio between the pore volume and the total volume [Olevsky and Molinari 2006], is supposed to be constant throughout the sample. This is equivalent to considering the spatial average of the porosity.

From now on, we shall consider average stress distributions of the following form:

$$[\sigma_{ij}] = \begin{bmatrix} \sigma_r & 0 & 0 \\ 0 & \sigma_r & 0 \\ 0 & 0 & \sigma_z \end{bmatrix}, \quad (7)$$

where z denotes the direction of the axis of the sample and r is any radial direction. Furthermore, in the sequel, the corresponding average strain rate tensor will be considered. Here, $\dot{\epsilon}_z$ and $\dot{\epsilon}_r$ denote the axial and radial strain rates, respectively. Hence, $\dot{\epsilon}$ and $\dot{\gamma}$ turn out to be

$$\dot{\epsilon} = \dot{\epsilon}_z + 2\dot{\epsilon}_r, \quad \dot{\gamma} = \sqrt{\frac{2}{3}}|\dot{\epsilon}_z - \dot{\epsilon}_r|. \quad (8)$$

Following [Olevsky and Molinari 2006], one can introduce a loading mode parameter n^* defined by

$$n^* = \frac{\tau}{p} = \frac{(\sigma(w)/w)\dot{\gamma}}{(\sigma(w)/w)\dot{\epsilon} + p_l - p_I} \quad (9)$$

Similar to the loading mode parameter, it is useful to define a *strain rate mode parameter* n as

$$n = \frac{\varphi\dot{\gamma}}{\psi\dot{\epsilon}}. \quad (10)$$

The parameter n assumes the following values for the corresponding loading modes:

- (1) $n = 0$ for isostatic pressing,
- (2) $n \rightarrow \infty$ for pure shear ($p = 0$),
- (3) $n = -\sqrt{6}$ for “free” forging,
- (4) $n = \sqrt{6}$ for drawing, and
- (5) $n = \sqrt{\frac{2}{3}} \operatorname{sgn}(\dot{\epsilon}_z)\varphi/\psi$ for constrained forging.

In the sequel, we will consider cases 1, 3, and 5 only.

We refer to “free” forging as the loading mode represented in Figure 1a, a transverse compressive force acting at the top and bottom faces of the sample with no lateral confinement. Hence, the case of constrained forging, shown in Figure 1b, is nothing but an axial compression of the sample in a rigid die.

From (1), (8), and (10), the following relation can be obtained:

$$\sigma_z = \frac{\sigma(w)}{w}\psi\dot{\epsilon}\left[1 + \sqrt{\frac{2}{3}}n \operatorname{sgn}(\dot{\epsilon}_z - \dot{\epsilon}_r)\right] + p_L - p_I; \quad (11)$$

the dependence of the effective equivalent stress $\sigma(w)$ on the effective equivalent strain rate w determines the constitutive behavior of a porous material.

Following [Ashby 1990], a power-law mechanism for the deformation is assumed:

$$\frac{\sigma(w)}{\sigma_0} = A\left(\frac{w}{\dot{\epsilon}_0}\right)^m, \quad (12)$$

where A and m are material constants (A is temperature dependent, $0 < m < 1$), and σ_0 and $\dot{\epsilon}_0$ are the reference stress and reference strain rate, respectively. The two limiting cases corresponding to ideal plasticity and linear viscosity are given by $m = 0$ and $m = 1$, respectively.

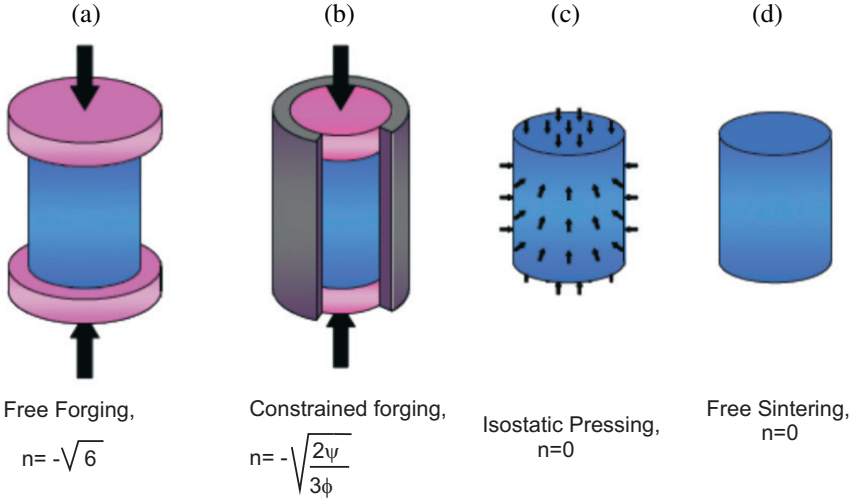


Figure 1. Different loading modes.

Equations (12) and (2) can be used to obtain an explicit expression for the ratio between the effective equivalent stress $\sigma(w)$ and the effective equivalent strain rate w in terms of the porosity, the normalized shear and bulk moduli, the loading mode, and the shrinking rate:

$$\frac{\sigma(w)}{w} = \frac{\sigma_0 A}{\dot{\epsilon}_0^m} w^{m-1} = \frac{\sigma_0 A}{\dot{\epsilon}_0^m} |\dot{\epsilon}|^{m-1} \left[\frac{\psi}{1-\theta} \left(\frac{\psi}{\phi} n^2 + 1 \right) \right]^{(m-1)/2}. \quad (13)$$

This paper is mainly devoted to studying the influence of both the Laplace pressure and the gas pressure in pores on the overall stress; for this reason, it is essential to monitor the magnitude $|\sigma_z - p_L + p_I|$, which can be regarded as a “driving force” of the sintering process, for each analyzed loading mode.

To this end, by substituting expression (13) into (11) the following relation can be obtained:

$$\sigma_z - p_L + p_I = \frac{A\sigma_0}{\dot{\epsilon}_0^m} |\dot{\epsilon}|^m \left[\frac{\psi}{1-\theta} \left(\frac{\psi}{\phi} n^2 + 1 \right) \right]^{(m-1)/2} \left[1 + \sqrt{\frac{2}{3}} n \operatorname{sgn}(\dot{\epsilon}_z - \dot{\epsilon}_r) \right]^{-1/m}. \quad (14)$$

In order to achieve an analytical expression for the evolution of the material behavior during the sintering process, it is necessary now to introduce the porosity θ , defined as the ratio of the volume of pores and the total volume. By denoting the total volume of the sintered material as V_{tot} and the volumes of the matrix pores as V_{matrix} and $V_{\text{pores}} = V_{\text{tot}} - V_{\text{matrix}}$, respectively, the relative density can be written as:

$$\rho = \frac{V_{\text{matrix}}}{V_{\text{tot}}}. \quad (15)$$

The porosity reads:

$$\theta = \frac{V_{\text{pores}}}{V_{\text{tot}}} = 1 - \rho. \quad (16)$$

Because of mass continuity and the assumed incompressibility of the matrix (the shrinkage is only due to the change of the porosity) [Olevsky 1998], the evolution law for the porosity is given by

$$\dot{\epsilon} = \frac{\dot{\theta}}{1-\theta}. \quad (17)$$

Taking into account expression (17) and recalling that the shrinkage is $\dot{\epsilon} < 0$ and thus $\dot{\theta} < 0$, the relationship (14) leads to the following evolution equation for the porosity:

$$\begin{aligned} \dot{\theta} = \text{sgn}(\dot{\theta})[\text{sgn}(\dot{\theta})(\sigma_z - p_L + p_I)]^{1/m} \frac{\dot{\epsilon}_0}{(A\sigma_0)^{1/m}} \\ \times \left[\frac{\psi}{1-\theta} \left(\frac{\varphi}{\psi} n^2 + 1 \right) \right]^{(1-m)/2m} \left[\psi \left(1 + \sqrt{\frac{2}{3}} n \text{sgn}(\dot{\epsilon}_z - \dot{\epsilon}_r) \right) \right]^{-1/m} (1-\theta), \end{aligned} \quad (18)$$

which accounts for the contribution of the Laplace pressure and the gas pressure in the pores. The analogue of (18) neglecting such contributions was obtained in [Olevsky and Molinari 2006, Equation 15].

2.1. Evolution law for porosity for isostatic pressing processes. For the case of isostatic pressing, $\sigma_z = \sigma_r$; in the sequel their common value will be denoted by σ . Here the loading mode parameter n is zero and the process entails a monotonic decrease of the porosity, that is, $\dot{\theta} < 0$; hence, relation (18) reduces to the following expression:

$$\dot{\theta} = -[-(\sigma - p_L + p_I)]^{1/m} \frac{\dot{\epsilon}_0}{(A\sigma_0)^{1/m}} (1-\theta)^{(3m-1)/2m} \psi^{-(1+m)/2m}. \quad (19)$$

Obviously, since $\dot{\gamma} = 0$, the normalized shear modulus φ has no influence on the process. The normalized bulk modulus ψ is a known function of the porosity θ ; for such a function, here and subsequently, we shall use the expressions given in Section 2.2. For this case, the models of [Ponte Castañeda 1991; Sofronis and McMeeking 1992] give the same behavior. This is because of the expression of the normalized bulk modulus ψ , which is indeed the same for both models.

Equation (19) may be normalized by using the dimensionless specific time defined as

$$\tau_L = \left[\frac{p_{L0}}{\sigma_0 A} \right]^{1/m} \dot{\epsilon}_0, \quad (20)$$

where p_{L0} is the reference value of the Laplace pressure, dependent on the surface tension and on the characteristic radius of the particles; it will be discussed in Section 2.3. Consequently, the evolution law for the porosity (19) can be rewritten as

$$\frac{\partial \theta}{\partial \tau_L} = -(1-\theta)^{(3m-1)/2m} [-(\sigma - p_L + p_I)]^{1/m} \psi^{-(1+m)/2m}. \quad (21)$$

For future use, it is useful to introduce a dimensionless pressure parameter, called the specific external pressure (SEP):

$$\text{SEP} = \sigma/\alpha/r_0, \quad (22)$$

where α denotes the surface tension and r_0 the average radius of the particles (for further explanation, see Section 2.3).

2.2. Dependence of the normalized shear and bulk moduli on porosity. In the literature there are several studies relating to the determination of the normalized bulk and shear moduli. In particular we will use four different models:

- The Skorohod model [Skorohod 1972]:

$$\varphi = (1 - \theta)^2, \quad \psi = \frac{2}{3} \frac{(1 - \theta)^3}{\theta}.$$

- The Ponte Castañeda–Duva–Crow model [Ponte Castañeda 1991; Duva and Crow 1992]:

$$\varphi = \frac{(1 - \theta)^{2/(1+m)}}{1 + \frac{2}{3}\theta}, \quad \psi = \frac{2}{3} \left(\frac{1 - \theta^m}{m\theta^m} \right)^{2/(m+1)}.$$

- The McMeeking–Sofronis model [Sofronis and McMeeking 1992]:

$$\varphi = \left(\frac{1 - \theta}{1 + \theta} \right)^{2/(1+m)}, \quad \psi = \frac{2}{3} \left(\frac{1 - \theta^m}{m\theta^m} \right)^{2/(m+1)}.$$

- The Cocks model [Cocks 1994]:

$$\varphi = \frac{(1 - \theta)^{2/(1+m)}}{1 + \frac{2}{3}\theta}, \quad \psi = \frac{m + 1}{3} \frac{(1 + \theta)(1 - \theta)^{2/(m+1)}}{\theta}.$$

In Figures 2 and 3 moduli ψ and φ , respectively, are plotted as functions of porosity for different values of the parameter m . The Skorohod model accounts for linear-viscous incompressible material with voids only; indeed, the moduli ψ and φ are independent from the parameter m .

2.3. Dependence of the Laplace pressure on porosity. The effective Laplace pressure p_L is the result of the collective action of local capillary stresses in a porous material. A variety of approaches can be found in the literature. We will consider two possible derivations of the expression for the Laplace pressure.

(1) *Sintering stress derived by using a stochastic approach.* This derivation was employed by Skorohod [1972], who obtained p_L by calculating the surface free energy per unit mass with respect to the specific volume of the porous material by assuming spherical particles. The achieved result may be stated as follows:

$$p_L = p_{L0}(1 - \theta)^2 = \frac{3\alpha}{r_0}(1 - \theta)^2, \quad (23)$$

where α is the surface tension and r_0 is the characteristic radius of the particles.

(2) *Sintering stress derived by averaging the dissipation.* Here we summarize results shown in [Olevsky and Molinari 2000, Appendix A.2.2] about the derivation of an expression for the Laplace pressure. A hollowed sphere is considered as a schematic for a pore (see Figure 4); at its surface, namely for $r = R_1$ (where r denotes the radial coordinate), the pressure $p_{L0} = 2\alpha/r_0$ is applied, whereas the external boundary ($r = R_2$) is stress free.

The porosity is then determined by the volume fraction:

$$\theta = \left(\frac{R_1}{R_2} \right)^3. \quad (24)$$

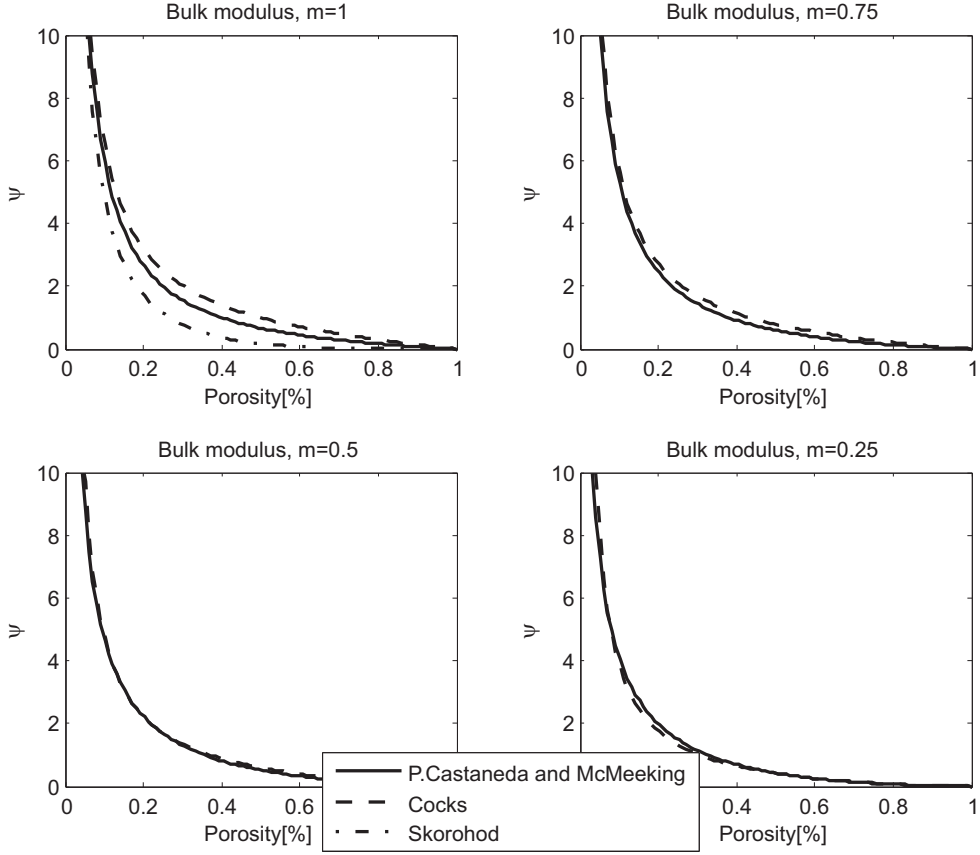


Figure 2. Normalized bulk modulus ψ as a function of porosity, for different values of the strain rate sensitivity, m .

The introduction of standard compatibility conditions into the constitutive relation (1) yields the radial and circumferential stresses as functions of the unknown radial velocity $V_r(r)$ (and of p_L and p_I). Finally, the stress balance (in the radial direction) allows for determining

$$V_r(r) = -\frac{p_{L0} R_1^3 R_2^3}{2(A\sigma_0/\dot{\epsilon}_0^m)\varphi(R_2^3 - R_1^3)r^2}, \quad (25)$$

for $m = 1$, namely in the case of linearly viscous behavior.

Henceforth, the effective equivalent strain rate w (see (2)) appearing in (1) is relevant for the expression of the dissipation potential proposed in [Olevsky 1998, Equation (26)], that is,

$$D = \frac{A\sigma_0/(\dot{\epsilon}_0^{-1/m})}{m+1}(1-\theta)w^{m+1}. \quad (26)$$

Through this expression, the dissipation of the matrix and its average on the volume of the hollowed sphere may be deduced. Additionally, the dissipation of the effective porous material, subject to free sintering, is evaluated; its connection with the volume-averaged dissipation through Hill's identity [Olevsky

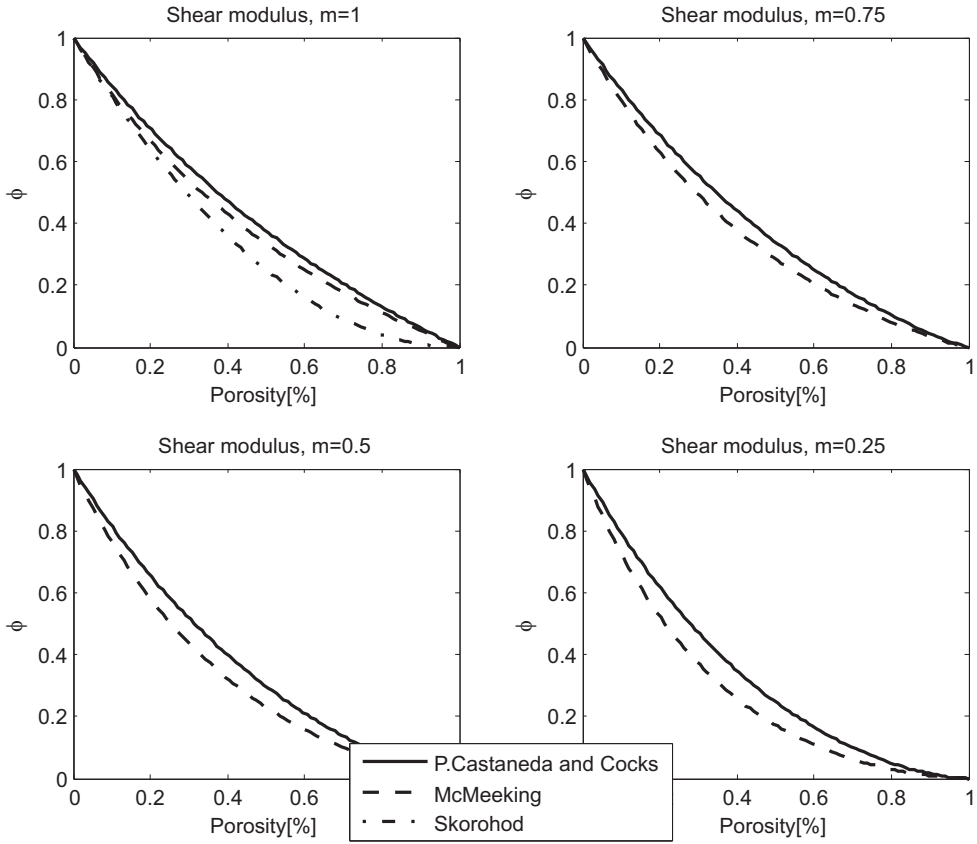


Figure 3. Normalized shear modulus ϕ as a function of porosity, for different values of the strain rate sensitivity, m .

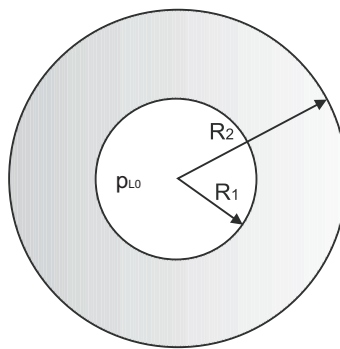


Figure 4. A representative element of the porous medium.

and Molinari 2000, Equation A29] allows for determining the following expression for the Laplace pressure:

$$p_L = \frac{2\alpha}{r_0} \sqrt{\frac{3}{2} \psi(\theta) \frac{\theta}{1-\theta}}. \quad (27)$$

The latter can be particularized to obtain the sintering stress associated with the models cited above; in particular,

- $p_L = \frac{2\alpha}{r_0}(1 - \theta)$ for the Skorohod model,
- $p_L = \frac{2\alpha}{r_0}$ for the Castañeda and McMeeking models, and
- $p_L = \frac{2\alpha}{r_0}\sqrt{1 + \theta}$ for the Cocks model.

Figure 5 shows the dependence of the Laplace pressure on the porosity θ . The stochastic approach, yielding relation (23), gives a parabolic trend for the Laplace pressure. This is increasing when the porosity decreases and is independent of the value of the parameter m , so that p_L does not depend upon the material behavior. In particular, the values of pressure calculated through (27) are compatible enough with the ones obtained from (23) in the porosity range of interest for common sintered components (see the blown-up inset in Figure 5).

2.4. Gas pressure in pores and its dependence upon porosity. During the sintering process, the porosity becomes isolated and the final stage of sintering starts at a relative density $\rho = 90\%$, that is, at the closure porosity $\theta_c = 0.1$. At this time, the gas pressure in the pores is equal to the external pressure; as the relative density ρ increases, the gas pressure in the closed pores also increases. The more natural way to

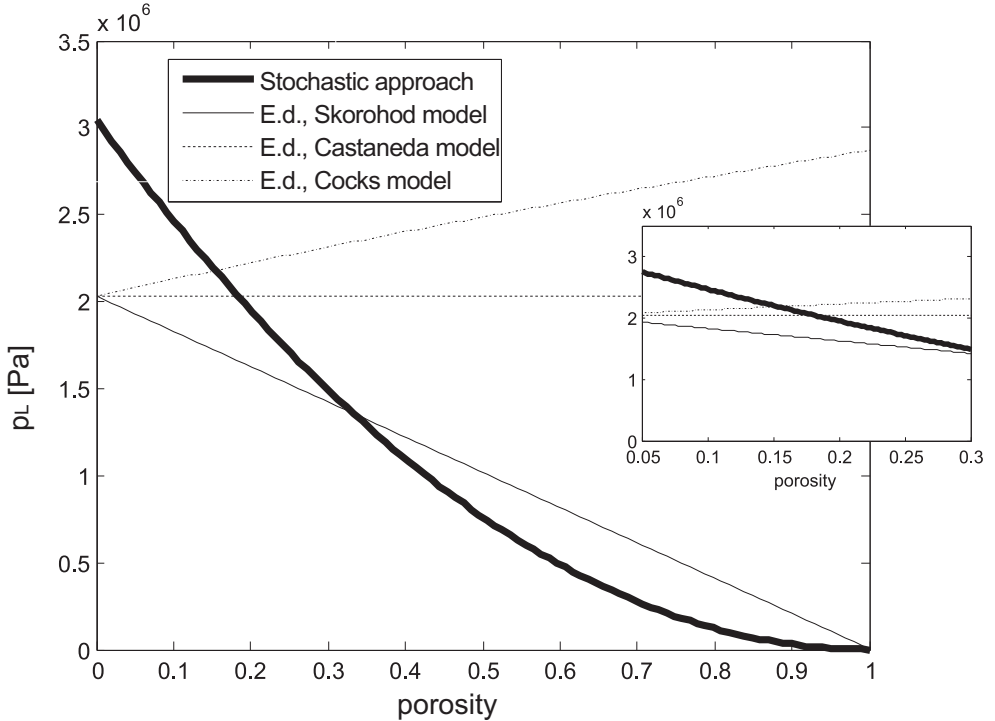


Figure 5. The Laplace pressure as a function of porosity.

account for such a phenomenon is through the ideal gas law [Arzt et al. 1983; Wilkinson 1988], that is, $(p_I + p_{\text{atm}})V_{\text{pores}} = \text{const.}$, where p_I is the gas pressure in the pores and p_{atm} the atmospheric pressure.

Recalling that, thanks to the incompressibility of the matrix, $V_{\text{matrix}} = \text{const.}$ during the process, from the ideal gas law it follows that the quantity $(p_I + p_{\text{atm}})(1 - \rho)/\rho = (p_I + p_{\text{atm}})V_{\text{pores}}/V_{\text{matrix}}$ remains constant. Recalling (16), the relationship can be rewritten as:

$$(p_I + p_{\text{atm}})\frac{\theta}{1-\theta} = \text{const.} = (p_0 + p_{\text{atm}})\frac{\theta_c}{1-\theta_c}, \quad (28)$$

where p_0 is the external pressure (that is, the gas pressure in the pores when the porosity closes). Thus, the evolution of the pressure in the pores during the sintering process is given by

$$p_I = \begin{cases} 0, & \text{if } \theta > \theta_c, \\ (p_0 + p_{\text{atm}})\frac{\theta_c}{\theta} \frac{1-\theta}{1-\theta_c} - p_{\text{atm}}, & \text{if } \theta < \theta_c. \end{cases} \quad (29)$$

In the case of isostatic pressing, the external pressure is equal to the applied stress $|\sigma|$.

The effects of the Laplace pressure p_L and the gas pressure in the pores p_I are investigated in Sections 3 and 4, respectively.

3. Effect of the Laplace pressure on sintering processes entailing isostatic pressing

In this section, the effect of the Laplace pressure on sintering processes entailing isostatic pressing is studied. To be precise, processes entailing, as the driving force, only the stress due to the external load are compared to processes in which the Laplace pressure is taken into account.

Figure 6 shows the time evolution of the porosity during an isostatic pressing process that reduces the porosity from 30% to 5%, obtained by using the Castañeda–Duva–Crow model for $\text{SEP} = 10$, in two cases:

- Accounting for the interstitial pressure p_L (the continuous line), and the driving force of the process is $\sigma - p_L$.
- Neglecting the Laplace pressure (the dashed line), and the driving force is only the stress due to the external load, σ .

The latter describes the approximation adopted in [Olevsky and Molinari 2006]. Indeed, since $|\sigma - p_L| > |\sigma|$, the time decay of the porosity would be lower than in reality. Nevertheless, we record that the time evolution of the porosity has a qualitative analogue to the one obtained by neglecting p_L (see Figure 6). When the strain rate sensitivity, m , decreases, the initial part of both graphs become steeper. Indeed, for infinite slope, the material behavior would be perfectly plastic (this would correspond to $m = 0$).

The gap between the two curves is higher for lower values of the strain rate sensitivity, m , hence the Laplace pressure has more influence on the sintering process when the material tends towards the plastic behavior. This may be explained by the (Ashby) power law (for example, (12)), relating the equivalent strain rate w and the effective equivalent stress $\sigma(w)$. Indeed, it is evident from such an equation that, for lower values of the strain rate sensitivity, m , the effective equivalent strain rate is more sensitive to stress changes, and, in particular, to the difference between the stress evaluated by accounting for the Laplace

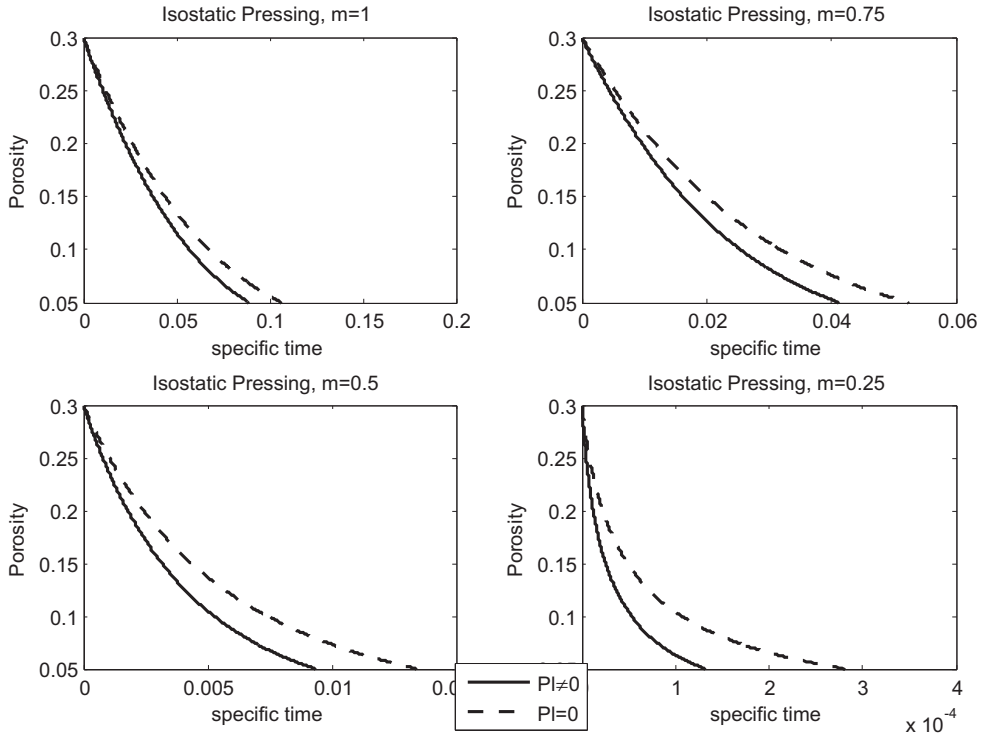


Figure 6. Isostatic pressing: evolution of porosity for $SEP = 10$.

pressure as a driving force of sintering or by neglecting it. For the sake of clarity, the Ashby relation (12) is displayed in Figure 7 for different values of the parameter m ; the plot highlights the change of w obtained by considering as the driving force $|\sigma - p_L|$ instead of $|\sigma|$, which is much more relevant for higher values of m .

Figure 8 is the analogue of Figure 6 for a lower value of external pressure, that is, $SEP = 1$. Here, the gap between the curves is remarkable because, in this case, the “sintering driving force” is basically the Laplace pressure, simply because it is higher than the externally imposed stress.

A comparison between the three different models for the normalized shear and bulk moduli φ and ψ , between the two different expressions for p_L (see (23) and (27)), is performed in the sequel. Figure 9 shows such a comparison for $SEP = 5$, for a material with linear-viscous behavior ($m = 1$).

The time-evolution diagrams shown in the left and right parts of Figure 9 are similar, because the values of the Laplace pressure given by (23) and (27) are compatible enough for porosities between 30% and 5% (see the inset in Figure 5). The differences among the curves relative to the various considered models are due to the corresponding expressions of the normalized bulk modulus ψ .

3.1. Influence of interstitial stress on industrial processes entailing isostatic pressing. A specific metallic alloy (aluminum-zinc-magnesium-copper) is examined in this section. This is motivated by its extensive use in industrial sintering processes. The main features of this material are listed in Table 1. For aluminum alloys, the average sintering time is thirty minutes and usually the applied external pressure is on the order of 100 MPa [Muhlburger and Paschen 1993; Schaffer et al. 2001; Gokce and Findik 2008].

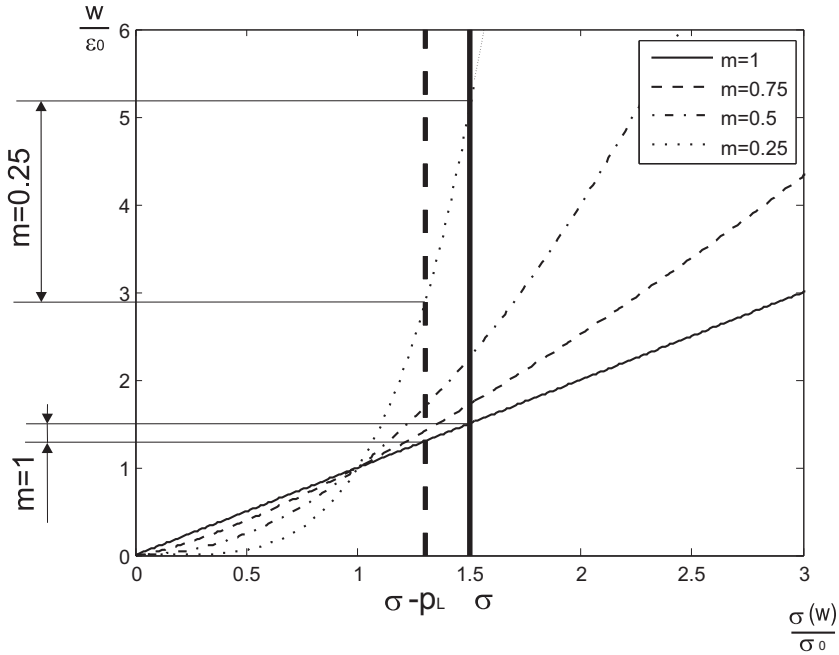


Figure 7. (Ashby) power law: sensitivity of the effective equivalent strain rate to the variation between σ and $|\sigma - p_L|$.

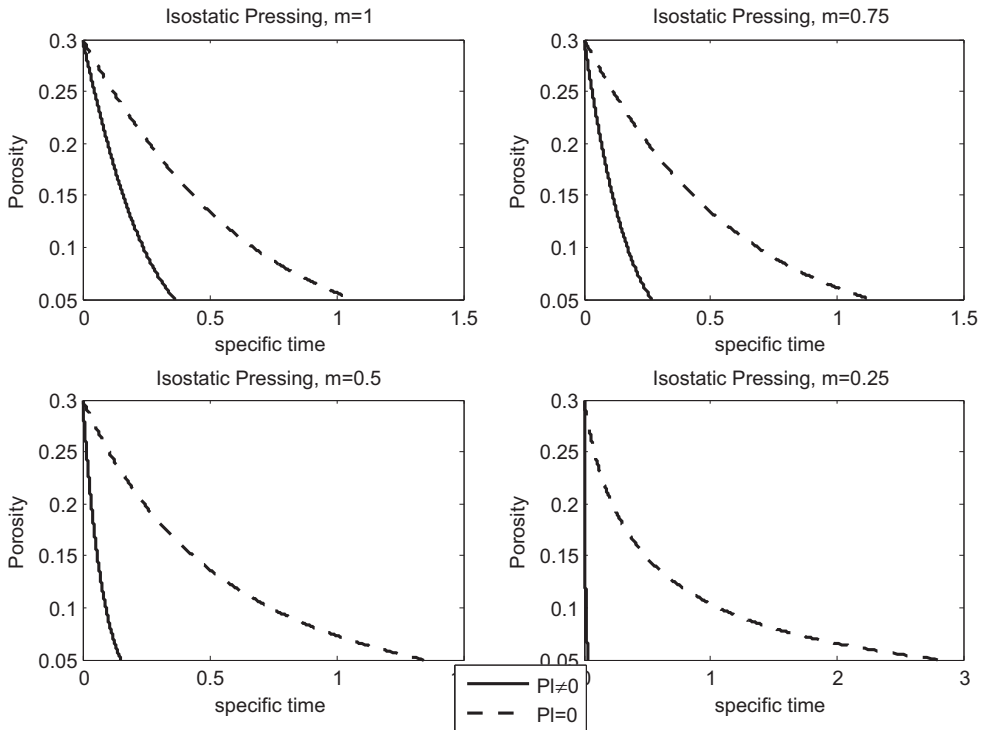


Figure 8. Isostatic pressing: evolution of porosity for $SEP = 1$.

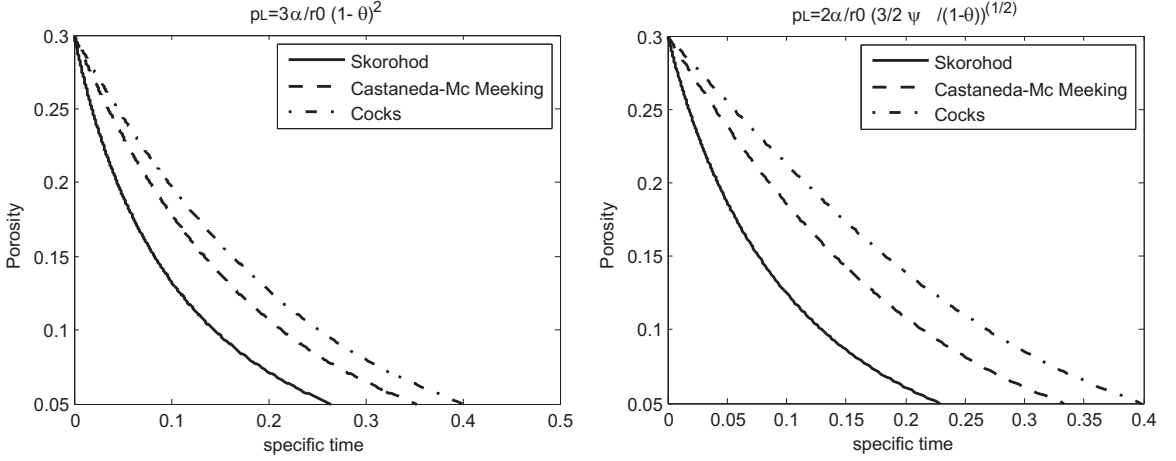


Figure 9. Isostatic pressing: evolution of porosity for $SEP = 5$, $m = 1$, for different models.

It may be shown that the important parameters influencing the Laplace pressure are the radius of the grains, r_0 , and the surface tension, α . Values of the powder grain size from 20 nm to $5 \mu\text{m}$ are taken into account here.

In the sequel, we shall examine the discrepancies in the estimates of the sintering times evaluated by either neglecting or accounting for the sintering stress p_L . Furthermore, we shall also calculate the residual porosity in both of the cases mentioned above.

3.1.1. Threshold external loading pressures and sintering times. Here we are interested in comparing the sintering times t and t_0 employed to reduce the porosity from 30% to 5% in cases in which the sintering driving force is taken to be either $|\sigma - p_L|$ or $|\sigma|$, respectively. We are also interested in calculating the values of the external pressure p^* for which the discrepancy between the sintering times, that is, $(t - t_0)/t$, attains the values 5%, 10%, and 15%. Obviously, whenever the external pressure is less than p^* , for a given value of discrepancy, for example 5%, an error greater than 5% occurs by neglecting the effect of the Laplace pressure.

Figures 10 and 11 show the threshold pressures for $5 \mu\text{m}$ and 50 nm powders (obtained by the Castañeda model). We see immediately that the effect of the Laplace pressure becomes more relevant for

Young's modulus	E	70.7 GPa
Poisson's ratio	ν	0.325
Surface tension	α	1.128 N/m
Activation energy	Q	14390 kJ
Melting temperature	T_m	659° C
Average particle radius	r_0	5–50 μm
Sintering temperature	T_s	100–350° C
Sintering pressure	P_b	600–610 MPa

Table 1. Characteristics of the considered aluminum-zinc-magnesium-copper alloy.

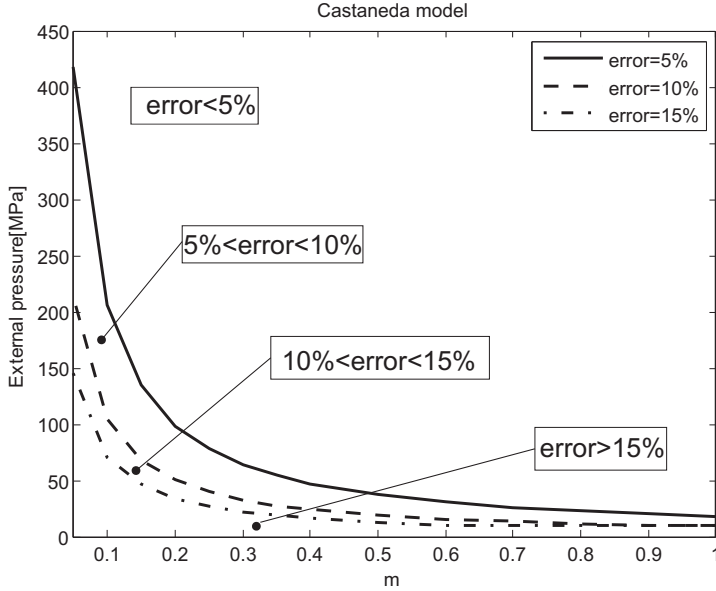


Figure 10. Threshold pressure p^* , for $5 \mu\text{m}$ powder.

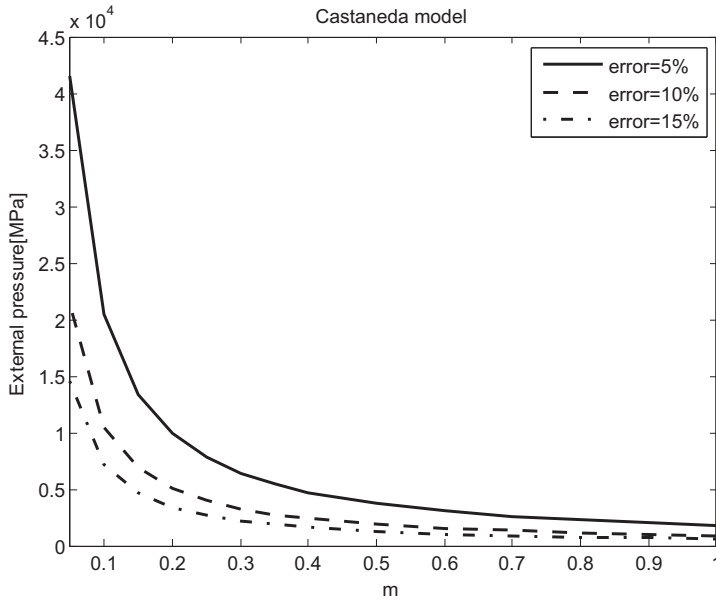


Figure 11. Threshold pressure p^* , for 50 nm powder.

lower values of the powder grain size. Hence, in this case the threshold pressures are comparable to those usually applied in industrial processes.

The threshold pressures evaluated by using the Cocks model do not exhibit meaningful differences with the results obtained by adopting the Castañeda model.

The results of these sections rely upon the model of the Laplace pressure based on the stochastic approach ((23), discussed in Section 2.3). Equation (27), instead derived by averaging the dissipation,

does not allow for evaluating p_L for different values of the strain rate sensitivity parameter m . However, the values of the threshold pressure obtained by using the latter model are in complete agreement with the ones obtained by using the former.

3.1.2. Residual porosity. The residual porosity is a fundamental feature of the material, because, among other reasons, it determines the mechanical properties of a sintered specimen.

A thirty-minute sintering process with external loading pressure of 100 MPa is now considered. Here we are interested in comparing the residual porosities θ_r and θ_{r0} after thirty minutes, when the sintering driving force is, respectively, taken to be either

- $|\sigma - p_L|$ or
- $|\sigma|$.

For the different values of powder grain size mentioned above, we are able to calculate the value of the strain rate sensitivity, m , that permits having a sintering reference time on the order of thirty minutes (30'). For the sake of convenience, without loss of generality, in the sequel a time range corresponding to a variation of $\pm 30\%$ of the reference time is considered.

Figure 12 shows the sintering time (that is, the time required to reduce the porosity from 30% to 5%) as a function of the strain rate sensitivity, m ; furthermore, the values of m corresponding to the real sintering times of $30' \pm 30\%$ are highlighted in the plot.

With such values of the parameter m , we may calculate the percentage error

$$E\% = \frac{\theta_r - \theta_{r0}}{\theta_r} 100[\%], \quad (30)$$

occurring when the Laplace pressure, p_L , is neglected. Figure 13 shows value of such an error as a function of the strain rate sensitivity, m , for grain sizes between 20 nm and 1 μm .

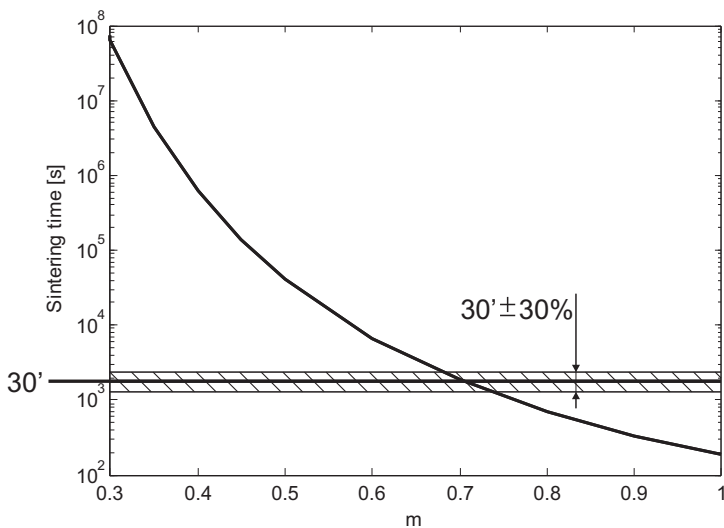


Figure 12. Sintering time as a function of the strain rate sensitivity, m .

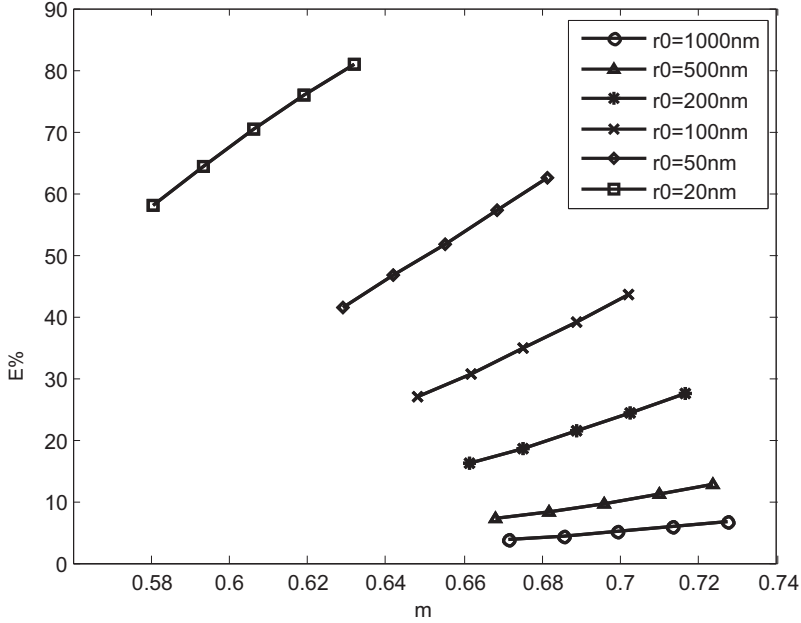


Figure 13. Errors $E\%$ on the residual porosity for different values of the grain size, r_0 .

For nanopowders (that is, for grain sizes less than $1\ \mu\text{m}$) the error becomes much higher than in the case of micropowders. In particular, for sizes on the order of $100\ \text{nm}$ an error of about 40% may occur, while for $20\ \text{nm}$ the error is on the order of 80% . For lower grain sizes, the gap between θ_r and $\theta_{r,0}$ is higher than for the previous cases.

The second parameter influencing the Laplace pressure is the surface tension α ; there are lots of uncertainties in the determination of its value [Kumikov and Khokonov 1983]. Hence, because of the lack of reliability, the sensitivity of the model to variations of α in the range of $\pm 50\%$ is analyzed. Figure 14 shows the error $E\%$ (defined by (30)) as a function of the surface tension α , for different values of the powder grain size. For increasing values of α , the Laplace pressure grows and hence the gap between θ_r and $\theta_{r,0}$ increases accordingly; this phenomenon turns out to be more relevant for lower powder grain sizes.

4. Effect of the gas pressure in pores on sintering processes entailing isostatic pressing

In this section the effect of the gas pressure in pores on sintering processes entailing isostatic pressing is studied through the comparison of results obtained by accounting for p_I or by neglecting it. Isostatic pressing processes that reduce the porosity from 30% to 5% are considered. The evolution of the pressure in the pores during sintering is given by (29) where, in the case of isostatic pressing, the external pressure p_0 is equal to the absolute value $|\sigma|$ of the applied stress.

Figure 15 shows, for $\text{SEP} = 10$, the absolute values of the *sintering driving forces*, that is, the stress due to the external load, the gas pressure in the pores, and the Laplace pressure. Figure 16 shows the values of the total sintering driving force, for different values of the SEP, in two cases:

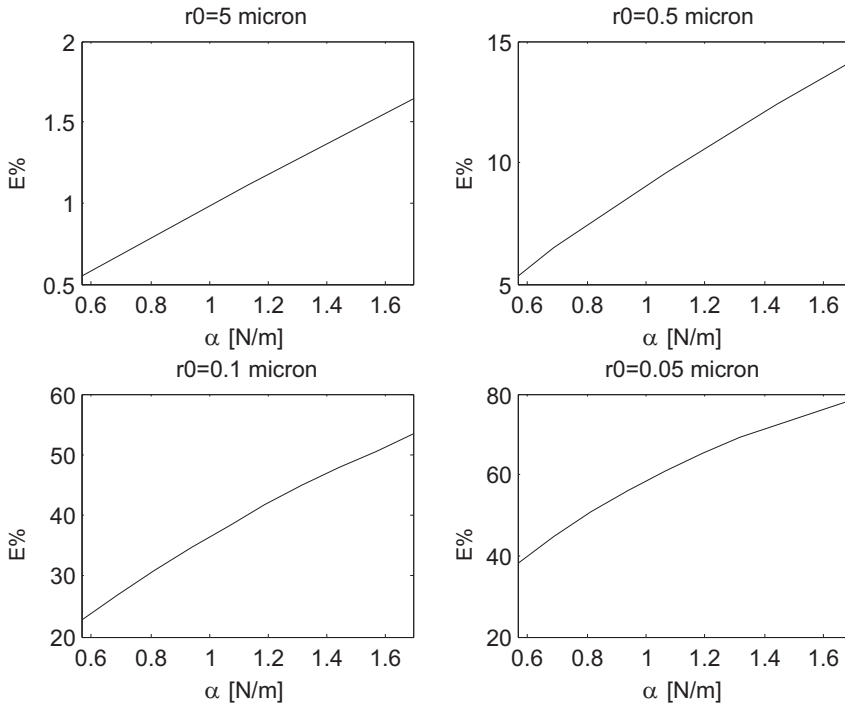


Figure 14. Errors $E\%$ on the residual porosity, for different values of the surface tension, α .

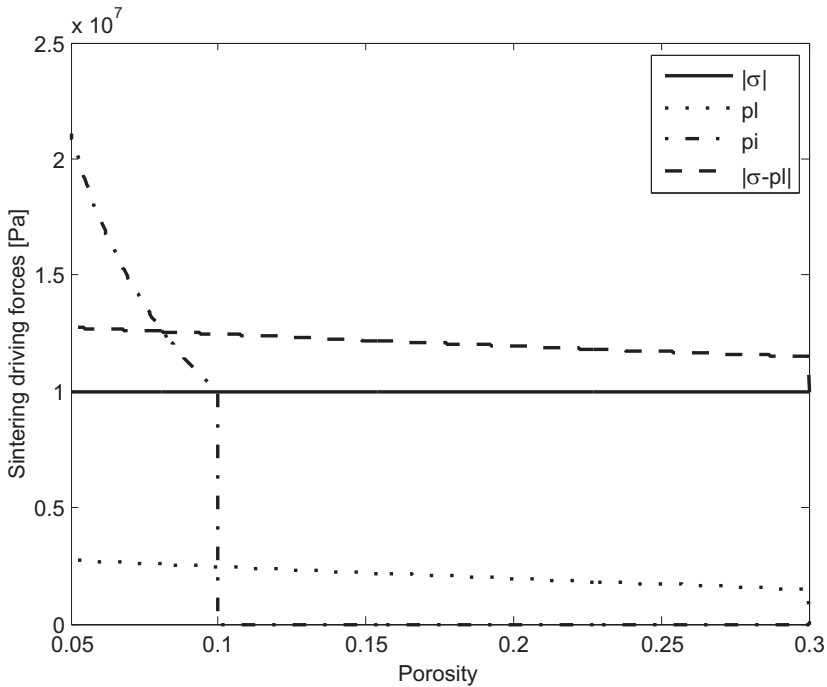


Figure 15. Sintering driving forces.

- accounting for the whole driving force (the dashed line) $\sigma - p_L + p_I$ and
- neglecting the gas pressure in the pores (the dotted line), that is, the driving force is considered to be $\sigma - p_L$.

The latter describes nonpressurized pores. Indeed, since no pressure could act against stresses caused by external loading (and Laplace pressure), the time decay of the porosity, in this case, would be faster than in reality. It is noticeable that, since $\sigma - p_L < 0$ and $p_I \geq 0$ during the whole sintering process (see (29)), the total driving force $\sigma - p_L + p_I$ may turn out to become null at a definite value of the porosity. Such a value will be denoted by θ^* and be given by the following condition:

$$|\sigma - p_L(\theta^*)| = p_I(\theta^*). \tag{31}$$

In the limiting case for which condition (31) holds, (21) yields $\dot{\theta} = 0$ and hence $\theta = \text{const}$. Thus, whenever such a condition is achieved the porosity remains constant at the limit value θ^* .

It is evident that the value of θ^* depends upon the external load and the choice of expression (23) or (27) for the Laplace pressure. Moreover, since $p_I = 0$ for $\theta > \theta_c$, condition (31) can be verified only in the third phase of sintering, when $p_I > 0$; it leads to $\theta^* < \theta_c$.

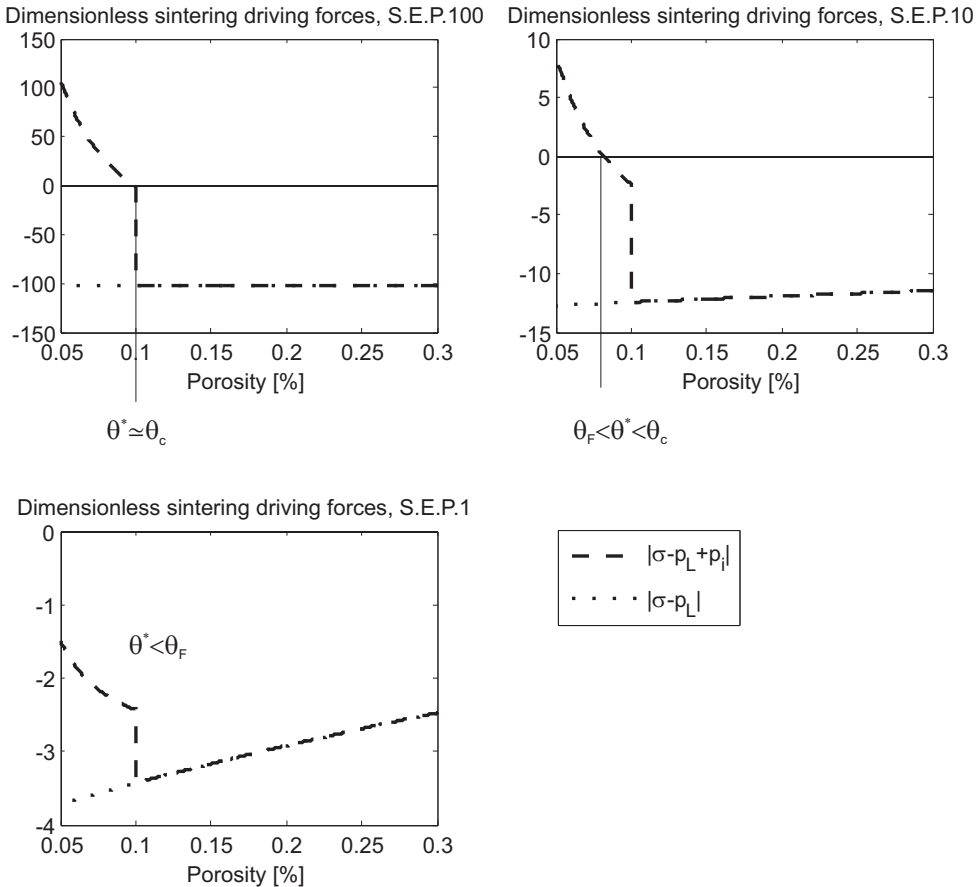


Figure 16. Dimensionless total sintering driving forces.

By denoting with θ_F the desired porosity at the end of the process and recalling that θ_c denotes the closure porosity, that is, the value of the porosity for which the pores becomes isolated, we may now distinguish two cases:

- Case in which $\theta_F < \theta^* < \theta_c$. Figure 17 shows the time evolution of the porosity, obtained by using the Castañeda–Duva–Crow model, for different values of the strain rate sensitivity, m , for $SEP = 10$, in two cases:
 - accounting for the gas pressure in the pores p_I (the continuous line), and
 - neglecting this pressure (the dashed line).

It is evident that, since $\theta > \theta_c$ (that is, during the first and second phases of sintering), the evolution of the porosity obviously is not affected by the presence of p_I , and hence the curves coincide. When the third phase begins, at porosity $\theta = \theta_c$, the dashed line moves away from the continuous one; as stated above, the sintering time obtained by accounting for the gas pressure in the pores is higher than the one obtained by neglecting it.

The fundamental result, in the case under examination, is that the desired final value of the porosity θ_F cannot be obtained; the value of the porosity at the end of the process is given by $\theta^* > \theta_F$. Moreover, whenever the condition (31) is achieved the rate of change of the porosity goes to zero; in the proximity of such a condition, the time-porosity graph presents an horizontal plateau.

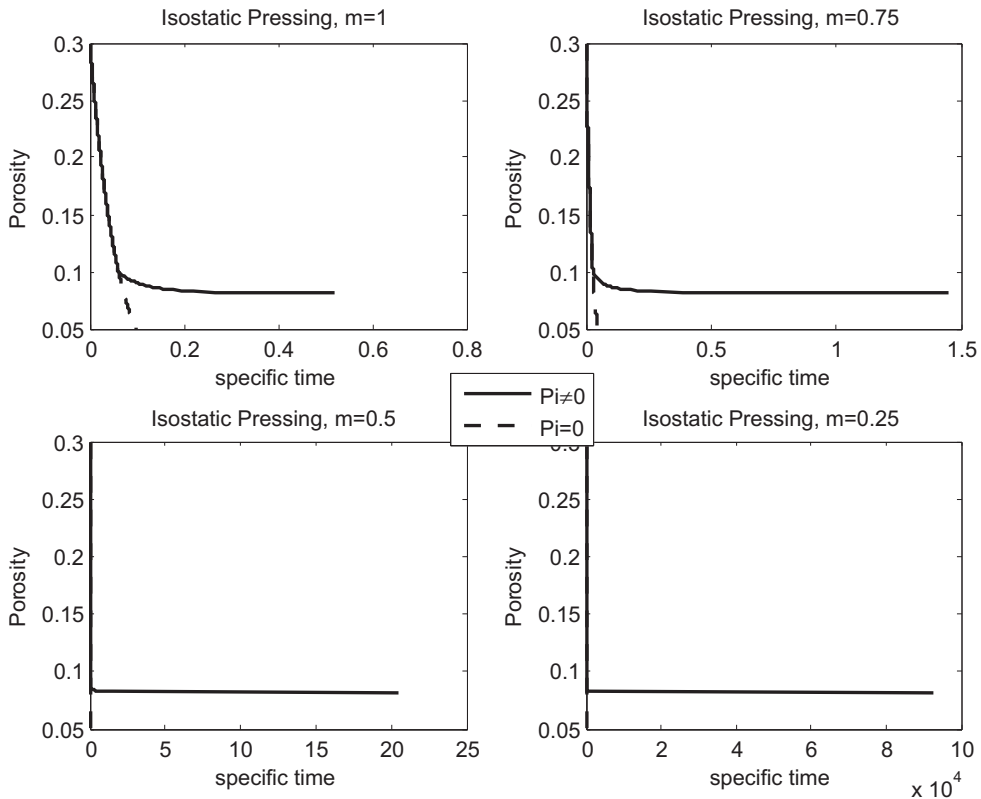


Figure 17. Isostatic pressing: evolution of porosity for $SEP = 10$.

This leads to a stretch of sintering times, which is evident from [Figure 17](#).

- *Case in which $\theta^* < \theta_F$.* [Figure 18](#) shows the time evolution of the porosity, obtained by using the Castañeda–Duva–Crow model, for different values of the strain rate sensitivity, m , for $SEP = 1$. It is evident from [Figure 16](#) that, for such a value of the SEP, the critical porosity θ^* is not achieved in the range of the considered porosities, that is, $\theta^* < \theta_F$. This allows for obtaining the desired porosity θ_F at the end of the process. The only effect of the gas pressure in the pores is to stretch the sintering times. This phenomenon will be studied in the following subsection.

In both cases, the gap between the two curves is higher for lower values of the strain rate sensitivity, m , and hence the presence of gas pressure in the pores has more influence on the sintering process whenever the material tends towards the plastic behavior. This may be explained by the (Ashby) power law (12), that indicates that for lower values of the parameter m , the effective equivalent strain rate is more sensitive to stress changes.

Comparison between the three different models for the normalized shear and bulk moduli φ and ψ and between the two different expressions for p_L (see (23) and (27)) is performed in the sequel. [Figure 19](#) shows such a comparison for $SEP = 1$ for a material with linear-viscous behavior ($m = 1$).

The time-evolution diagrams shown in the left and right portions of [Figure 19](#) are quite similar, because the value of the Laplace pressure given by (23) and (27) are compatible enough for porosities

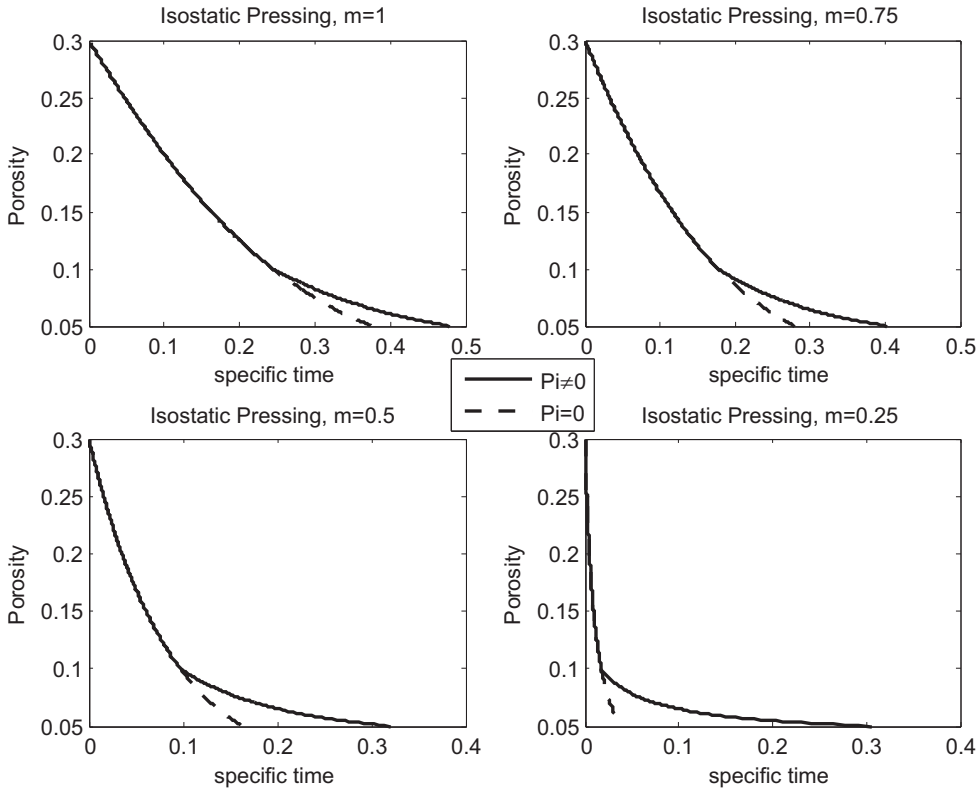


Figure 18. Isostatic pressing: evolution of porosity for $SEP = 1$.

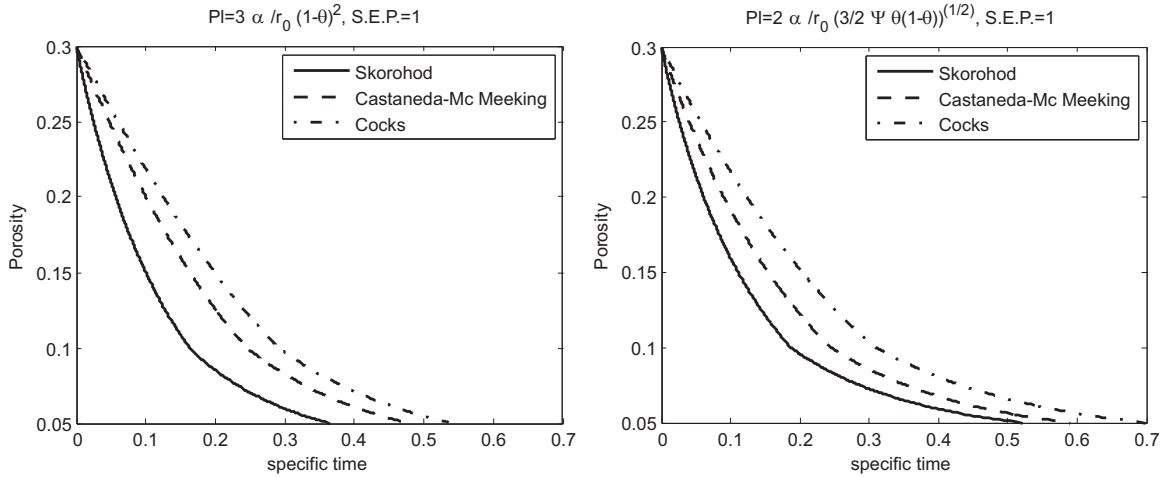


Figure 19. Isostatic pressing: evolution of porosity for SEP = 1.

between 30% and 5% (see the inset in Figure 5). The differences among the curves relative to the various considered models are due to the corresponding expressions of the normalized bulk modulus ψ .

Figure 20 shows such a comparison for SEP = 10 with $m = 1$. In this case as well, the left and right-hand graphs are similar. The differences among the curves relative to the various considered models are due to the corresponding expressions of the normalized bulk modulus ψ , leading, in the case of p_L given by (27), to slightly different values of the critical porosity θ^* .

4.1. Influence of the gas pressure in pores on industrial processes entailing isostatic pressing. Similarly to the analysis performed in Section 3.1, we are interested in determining if there exists a threshold for the external pressure under (or over) which the effect of the gas pressure in pores is negligible in a “real” industrial process. The same aluminum-zinc-magnesium-copper alloy presented in Section 3.1 is considered here.

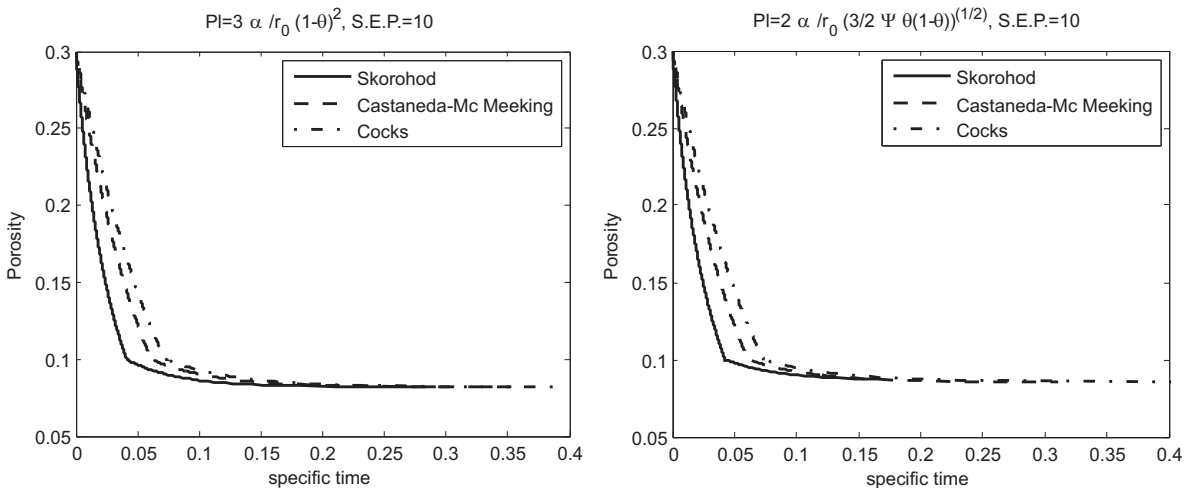


Figure 20. Isostatic pressing: evolution of porosity for SEP = 10.

As discussed above, in the case of isostatic pressing, the gas pressure in the pores at the beginning of the third phase of sintering (that is, at the closure porosity, θ_c) is equal to the external pressure. Hence, whenever the external pressure increases, the pressure in the pores also increases, acting “against” the sintering process and preventing the desired final porosity from being reached. [Figure 21](#) shows the final porosity that can be reached as a function of the applied external pressure for different values of the strain rate sensitivity, m , for both $5\ \mu\text{m}$ and $50\ \text{nm}$ powders.

Since the required final porosity can be reached only for low values of the external pressure (and, hence, of the gas pressure in the pores), there is no sense in looking for an external pressure threshold under which the effect of the gas pressure in the pores is negligible from the point of view of the sintering time, or the error on the evaluation of the residual porosity, similarly to [Sections 3.1.1](#) and [3.1.2](#).

5. Stability

5.1. Lower-order analysis. Here we may denote by $\theta^{(0)}(t)$ the fundamental solution of the evolution law [\(19\)](#) associated with a uniform distribution of the initial porosity. Following [\[Olevsky and Molinari 2006, §3.1.1\]](#) we assume that the perturbed solution has the form

$$\theta(t) = \theta^{(0)}(t) + \delta\theta(t) \exp(\lambda(t - t_0)), \quad (32)$$

where the magnitude of the perturbation $\delta\theta(t)$ is taken to be much smaller than that of $\theta^{(0)}(t)$ at all times. In [\[Olevsky and Molinari 2006, §3.1.1\]](#) a normalized perturbation growth rate with respect to the current rate of change of porosity is considered; this is done in order to have “first”-order information about the stability of the process. The quantity $\lambda = \delta\dot{\theta}/\delta\theta$ can be regarded as the perturbation growth rate. It is possible to calculate the quantity $\lambda/\dot{\theta}$ as a function of θ , θ_0 , m , p_L , and the external pressure. This can be done in the framework of the three different models considered in the previous sections.

Because, during sintering, shrinkage occurs monotonically ($\dot{\theta} \leq 0$), the problem is linearly stable if $\lambda < 0$, that is, $\lambda/\dot{\theta} > 0$, while it is linearly unstable if $\lambda > 0$, that is, $\lambda/\dot{\theta} < 0$. In [Figure 22](#) the quantity

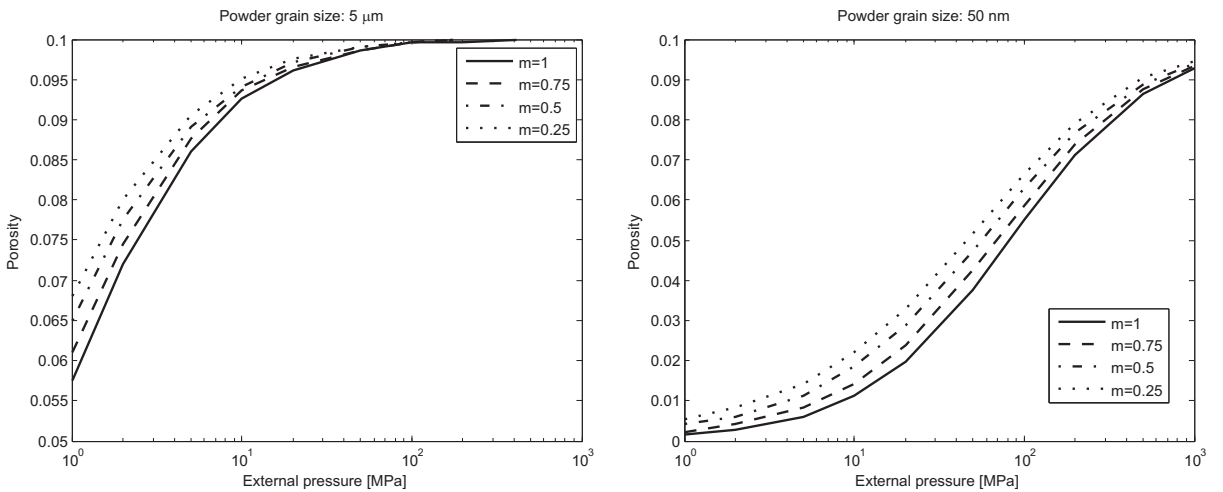


Figure 21. Final porosity as a function of applied external pressure, for $5\ \mu\text{m}$ powder.

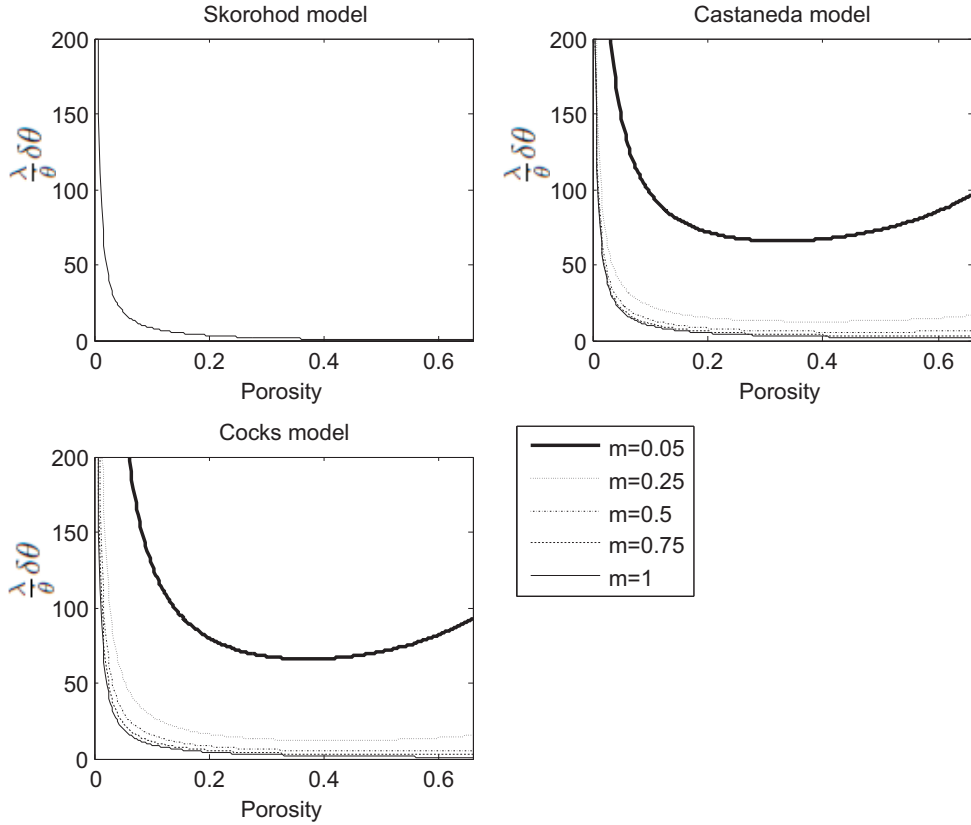


Figure 22. Normalized perturbation growth rate. Low order, $SEP = 10$.

$(\lambda/\dot{\theta})\delta\theta$ is plotted as a function of θ for different values of the strain rate sensitivity, m , with $SEP = 10$. It is evident from the graph that the process is always linearly stable. The value of the applied external pressure does not change the stability condition.

5.2. Higher-order analysis: Effect of the Laplace pressure. The former analysis was meant to explore the consequences of the perturbation of the porosity on the rate of change $\dot{\theta}$, evaluated by (19).

In the present context the stress σ is uncoupled from porosity, hence a more refined method of producing perturbations is needed. To this end, one may follow the procedure used in [Olevsky and Molinari 2006, §3.1.2] to account for perturbation of the actual porosity and, in our case, of the Laplace pressure. Note that the quantity p_{L0} (which can be written as a function of p_L and the porosity through (23) or (27)) is a material property and does not change during the sintering process.

Two differences may be highlighted between the stability analysis performed in the present work and the one introduced in [Olevsky and Molinari 2006]:

- Unlike in [Olevsky and Molinari 2006], here the high-order analysis entails a process with constant external pressure.
- The presence and the perturbation of the sintering stress p_L is considered here.

A perturbed solution is considered in the following form:

$$\theta(t) = \theta^{(0)}(t) + \delta\theta \exp(\lambda(t - t_0)), \quad p_L(t) = p_L^{(0)}(t) + \delta p_L \exp(\lambda(t - t_0)); \quad (33)$$

by substituting (33) in (19) and (23) (for the Laplace pressure derived by using stochastic approach), after linearization about the fundamental solution $(\theta^{(0)}(t), p_L^{(0)})$ we have

$$\begin{bmatrix} \frac{1}{\dot{\theta}} \frac{\partial f(\theta, \sigma, p_L)}{\partial \theta} - \frac{\lambda}{\dot{\theta}} & \frac{1}{\dot{\theta}} \frac{\partial f(\theta, \sigma, p_L)}{\partial p_L} \\ \frac{\partial p_{L0}(\theta, p_L)}{\partial \theta} & \frac{\partial p_{L0}(\theta, p_L)}{\partial p_L} \end{bmatrix}_{\theta^{(0)}(t), p_L^{(0)}(t)} \begin{bmatrix} \delta\theta \\ \delta p_L \end{bmatrix} = \begin{bmatrix} 0 \\ 0 \end{bmatrix}, \quad (34)$$

where

$$f(\theta, \sigma, p_L) = \dot{\varepsilon}_0 (1 - \theta)^{(3m-1)/2m} \left(\frac{|\sigma_z - p_L|}{A\sigma_0} \right)^{1/m} \psi^{-(1+m)/2m}, \quad (35)$$

and where the matrix in (34) is evaluated at $(\theta^{(0)}(t), p_L^{(0)}(t))$, as specified. Equation (34) has nontrivial solutions if and only if the determinant of the matrix is equal to zero. By imposing this condition, we obtain a characteristic first-order equation with respect to the normalized perturbation growth rate $\lambda/\dot{\theta}$. As in the lower-order case, the quantity $\lambda = \delta\dot{\theta}/\delta\theta$ can be regarded as the perturbation growth rate. Since, during sintering, shrinkage occurs monotonically ($\dot{\theta} \leq 0$), the problem is linearly stable if the quantity $\lambda/\dot{\theta}$ (the normalized perturbation growth rate) is negative, and linearly unstable if $\lambda/\dot{\theta} > 0$. This can be done in the framework of the three different models considered in the previous sections.

The root of (34) is shown in Figure 23 for the three principal cases defined in Section 2.1. It is evident that, since the normalized perturbation growth rate $\lambda/\dot{\theta}$ is negative for the whole porosity range, the sintering process is always stable. By carefully comparing Figure 22 to Figure 23 it can be detected that the effect of the Laplace pressure is to slightly increase the absolute value of $\lambda/\dot{\theta}$, that is, to increase the stability of the process.

Figure 23 shows the results obtained considering the Laplace pressure evaluated by using the stochastic approach, leading to expression (23) for the sintering stress. The results obtained by using the other methodology (which leads to p_L given by (27)) are very similar.

5.3. Higher-order analysis: Effect of the gas pressure in the pores. In this subsection, perturbations of the porosity evolution rate, Laplace pressure, and gas pressure in the pores, p_I , are introduced, in order to investigate the effect of p_I on the stability of the sintering process. Such perturbations are considered in the following form:

$$\begin{aligned} \theta(t) &= \theta^{(0)}(t) + \delta\theta \exp(\lambda(t - t_0)), \\ p_L(t) &= p_L^{(0)}(t) + \delta p_L \exp(\lambda(t - t_0)), \\ p_I(t) &= p_I^{(0)}(t) + \delta p_I \exp(\lambda(t - t_0)). \end{aligned} \quad (36)$$

The latter is substituted in the governing equations of the problem, namely (19), (29), and (23) (for the Laplace pressure derived by using stochastic approach) or (27) (for Laplace pressure obtained through dissipative approach). Note that the external pressure at the pore closure, p_0 , is a fixed parameter. After a linearization about the fundamental solution $(\theta^{(0)}(t), p_I^{(0)}, p_L^{(0)})$, the following set of equations can

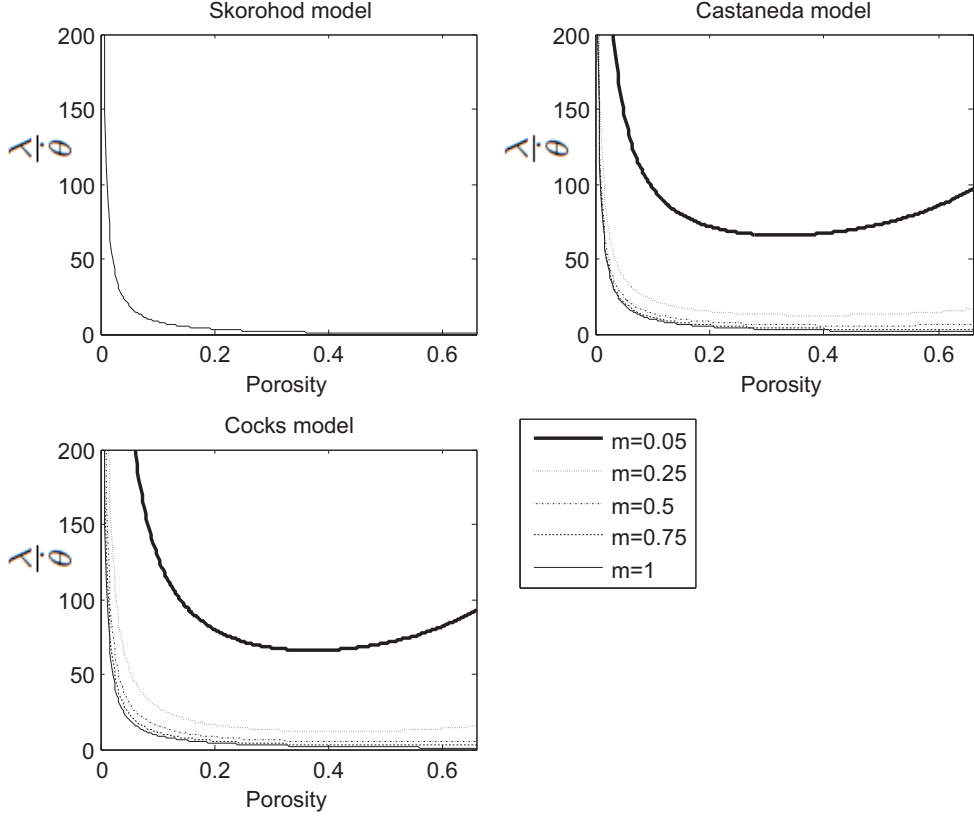


Figure 23. Normalized perturbation growth rate. High-order stability analysis, $SEP = 10$.

be obtained:

$$\begin{bmatrix} \frac{1}{\bar{\theta}} \frac{\partial f(\theta, \sigma, p_L)}{\partial \theta} - \frac{\lambda}{\bar{\theta}} & \frac{1}{\bar{\theta}} \frac{\partial f(\theta, \sigma, p_L)}{\partial p_L} & \frac{1}{\bar{\theta}} \frac{\partial f(\theta, \sigma, p_L)}{\partial p_I} \\ \frac{\partial p_{L0}(\theta, p_L)}{\partial \theta} & \frac{\partial p_{L0}(\theta, p_L)}{\partial p_L} & 0 \\ \frac{\partial p_0(\theta, p_I)}{\partial \theta} & 0 & \frac{\partial p_0(\theta, p_I)}{\partial p_I} \end{bmatrix}_{\theta^{(0)}(t), p_L^{(0)}(t), p_I^{(0)}(t)} \begin{bmatrix} \delta \theta \\ \delta p_L \\ \delta p_I \end{bmatrix} = \begin{bmatrix} 0 \\ 0 \\ 0 \end{bmatrix}. \quad (37)$$

As in the previous subsection, in order to obtain nontrivial solutions of (37), the determinant of the matrix has to be null. By imposing such a condition, a first-order equation with respect to the normalized perturbation growth rate $\lambda/\dot{\theta}$ is obtained. As in the previous cases, the problem is linearly stable if the quantity $\lambda/\dot{\theta}$ (normalized perturbation growth rate) is negative, and linearly unstable if $\lambda/\dot{\theta} > 0$. The normalized perturbation growth rate is plotted in Figure 24 as a function of the porosity, for different values of m and for the Skorohod, Castañeda–McMeeking, and Cocks models. Obviously, the presence of p_I influences just the third phase of the sintering process, for relative densities greater than 90%, that is, for $\theta < \theta_c = 0.1$. Moreover, the final porosity θ^* is here greater than zero, and depends upon the applied external pressure.

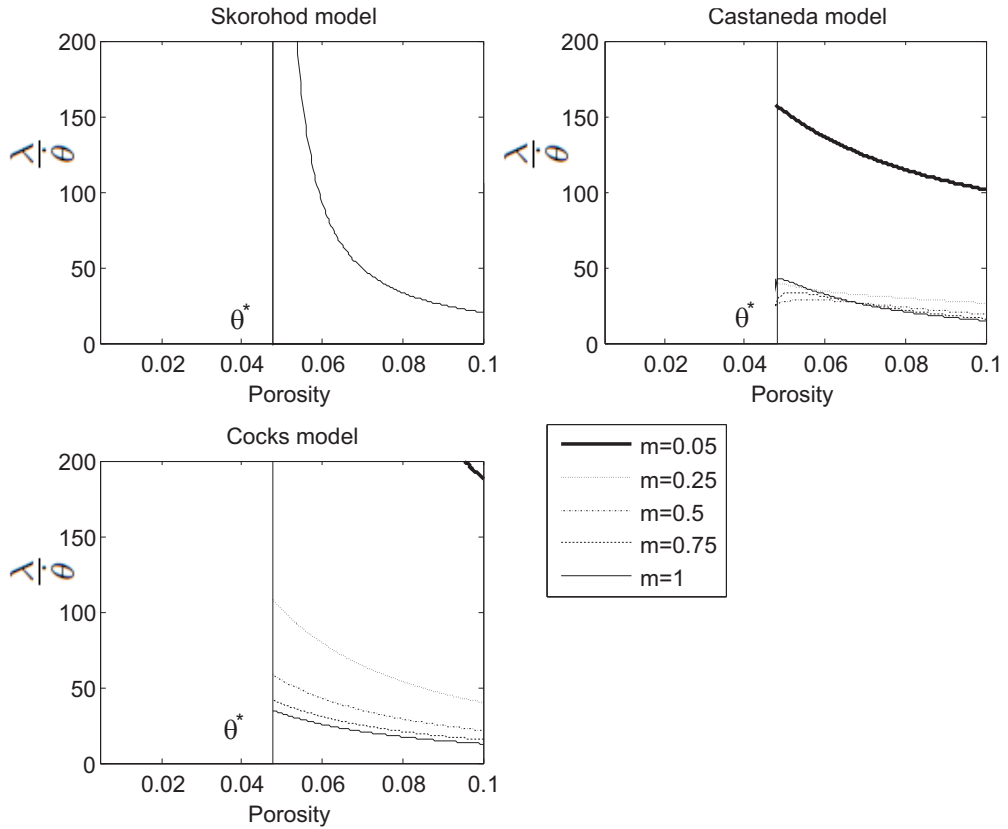


Figure 24. Normalized perturbation growth rate. High-order stability analysis, $SEP = 2$.

As it is evident from Figure 24, the effect of the gas pressure in the pores is to reduce the value of the normalized perturbation growth rate $\lambda/\dot{\theta}$, that is, to reduce the stability of the sintering process. Nevertheless, the process turns out to be stable.

Figure 24 shows the results obtained considering the Laplace pressure evaluated by using the stochastic approach, leading to the expression for the sintering stress (23). Results obtained by using the other methodology (which leads to (27) for p_L) are qualitatively very similar.

6. Conclusions

This work is focused on modeling the evolution of material properties during both hot isostatic pressing (HIP) and free sintering of axisymmetric samples. The effects of both the Laplace pressure, due to the surface tension at the interfaces between the matrix and pores, and the pressure exerted by the gas within the pores on the evolution of the porosity have been investigated for the first time in the literature for such samples. The stability of the process has also been studied.

The Laplace pressure acts in favor of closing the pores, thereby having a beneficial effect on the HIP process by reducing sintering times. Discrepancies in the estimates of such times and in the residual porosity, evaluated by either neglecting or accounting for the Laplace pressure, are studied. It is highlighted that this action cannot be neglected whenever the sintered material has a high strain rate

sensitivity and a small radius of its particles. Indeed, HIP of nanopowders turns out to be very sensitive to the Laplace pressure. This is particularly important for nanopowdered ceramics and nanoparticles of aluminum-zinc-magnesium-copper alloy, which are widely employed in industrial sintering processes.

The gas pressure acting within the pores strongly affects the sintering process only in its third (and final) phase in which, for porosity less than the closure porosity (which is usually on the order of 10%), the pores are basically isolated. During this phase, as the relative density increases the gas pressure in the closed pores also increases, acting “against” the sintering process. This in turn increases the sintering time and can prevent the HIP process from reaching the desired final porosity in the sample. Obviously, the higher the applied pressure the stronger this effect is. This confirms expectations, namely that the effects of the gas pressure must be accounted for whenever the desired final porosities are relatively small (precise evaluation giving information about the relationship between such gas pressure and the smallness of the desired porosity may be obtained through our model).

The stability of the process has been studied by perturbing the rate of change of the porosity and the Laplace pressure, as well as the gas pressure in the pores. While the effect of the former is to slightly increase the stability of the sintering process, the latter reduces the stability. Nevertheless, the process turns out to be stable.

Appendix: Free sintering

The case of free sintering corresponds to a condition frequently met in industrial processes. In these cases, there is no applied external pressure, so that the shrinkage is due only to the sintering stress, p_L .

In the case under examination, the stress and strain-rate tensors are purely hydrostatic. Thus, free sintering can be regarded as a particular case of isostatic pressing, with null external loading stress. The evolution law for the porosity may be obtained from (19), simply by substituting $\sigma = 0$:

$$\dot{\theta} = - \left(\frac{p_L - p_I}{\sigma_0 A} \right)^{1/m} \varepsilon_0 \psi^{-(1+m)/2m} (1 - \theta)^{(3m-1)/2m}. \quad (\text{A.1})$$

The introduction of the dimensionless specific time τ_L , defined by (20), yields the following normalization of (A.1):

$$\frac{\partial \theta}{\partial \tau_L} = (p_L - p_I)^{1/m} \psi^{-(1+m)/2m} (1 - \theta)^{(3m-1)/2m}. \quad (\text{A.2})$$

A.1 Effect of the Laplace pressure. Because for free sintering the gas pressure in the pores is neglected, the only force driving the process is the Laplace pressure, the choice of the approach used to derive its expression (stochastic or dissipation averaging; see Section 2.2) has a strong influence on the result. This issue may be studied in the sequel.

Sintering stress by using a stochastic approach ($p_L = (3\alpha/r_0)(1 - \theta)^2$, see Section 2.3(1)). By substituting (23) into (A.2), it may be written as follows:

$$\frac{\partial \theta}{\partial \tau_L} = \left(\frac{3\alpha}{r_0} \right)^{1/m} \psi^{-(1+m)/2m} (1 - \theta)^{3((m+1)/2m)}. \quad (\text{A.3})$$

In order to compare the evolution of the porosity for this case, for the three different models considered in Section 2.2 (Skorohod, Cocks, Castañeda–Duva–Crow, and McMeeking; the latter two models coincide

for isostatic pressing), Figure 25 shows the evolution of the porosity for different values of the strain rate sensitivity, m .

It is worth noting that the results obtained for the three considered models are fairly different. This is due to the different expressions for the normalized bulk modulus ψ . Figure 2 shows that the Cocks model, for $m = 1$, gives the highest values of ψ in the whole range of interesting porosities. For such values of ψ , (A.3) gives lower values of the rate of change of the porosity $\dot{\theta}$, corresponding to higher sintering times. Because the Skorohod model introduces smaller values of ψ , the sintering times obtained by adopting such a model are the shortest.

In Figure 25, the time evolution of the porosity, evaluated for the different models and for different values of the parameter m , is plotted. Whenever m decreases, Figure 2 shows that the values of the normalized bulk modulus ψ obtained by using the Castañeda model increase, while those coming from the Cocks model decrease. The same figure shows that, for lower values of m , the Castañeda model gives values of ψ lower than those obtained by using the Cocks expression for the same item. Hence, employment of the Cocks model gives sintering times lower than those obtained by using the approach of Castañeda. Also from Figure 25, note that when m tends to zero (ideal plastic behavior), the time-porosity graph has a steep knee.

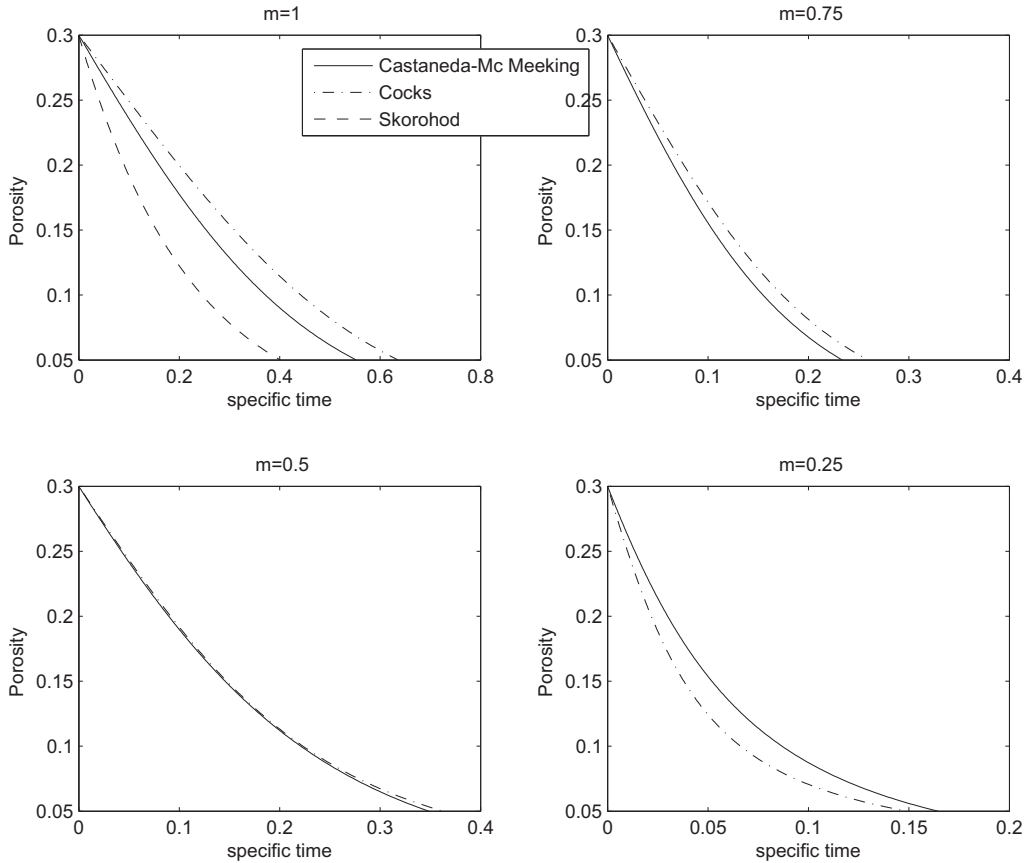


Figure 25. Free sintering evolution of porosity for different values of m , with $p_L = (3\alpha/r_0)(1 - \theta)^2$.

Sintering stress from dissipation averaging (that is, $p_L = (2\alpha/r_0)\sqrt{(3/2)\psi(\theta)\theta/(1-\theta)}$, see Section 2.3(2)). In this case, expression (A.1), which holds for $m = 1$ only, reduces to

$$\dot{\theta} = -\frac{\dot{\epsilon}_0}{\sigma_0 A} \frac{2\alpha}{r_0} \sqrt{\frac{3}{2} \frac{\theta(1-\theta)}{\psi(\theta)}}. \tag{A.4}$$

In the considered range of porosity, the resulting values of the Laplace pressure may be shown to be lower than those obtained by virtue of the expression derived by the stochastic approach (see Figure 5), and hence the sintering times are higher.

A.2 Effect of the gas pressure in the pores. In the case of free sintering, the stress due to the external (relative) pressure is $\sigma = 0$; the total driving force of the problem is thus given by the sum of a positive contribution, the Laplace pressure p_L , and the gas pressure in the pores, which gives a “negative” contribution.

Since the applied external pressure is equal to the standard atmospheric pressure, at the closure porosity θ_C , $p_I = 0$. Hence the gas pressure in the pores is usually negligible with respect to the interstitial pressure, p_L , and the condition (31) is not reached. More precisely, it can be attained for values of grain size not used in real sintering processes.

Figure 26 shows the evolution of the porosity for a free sintering process in two cases:

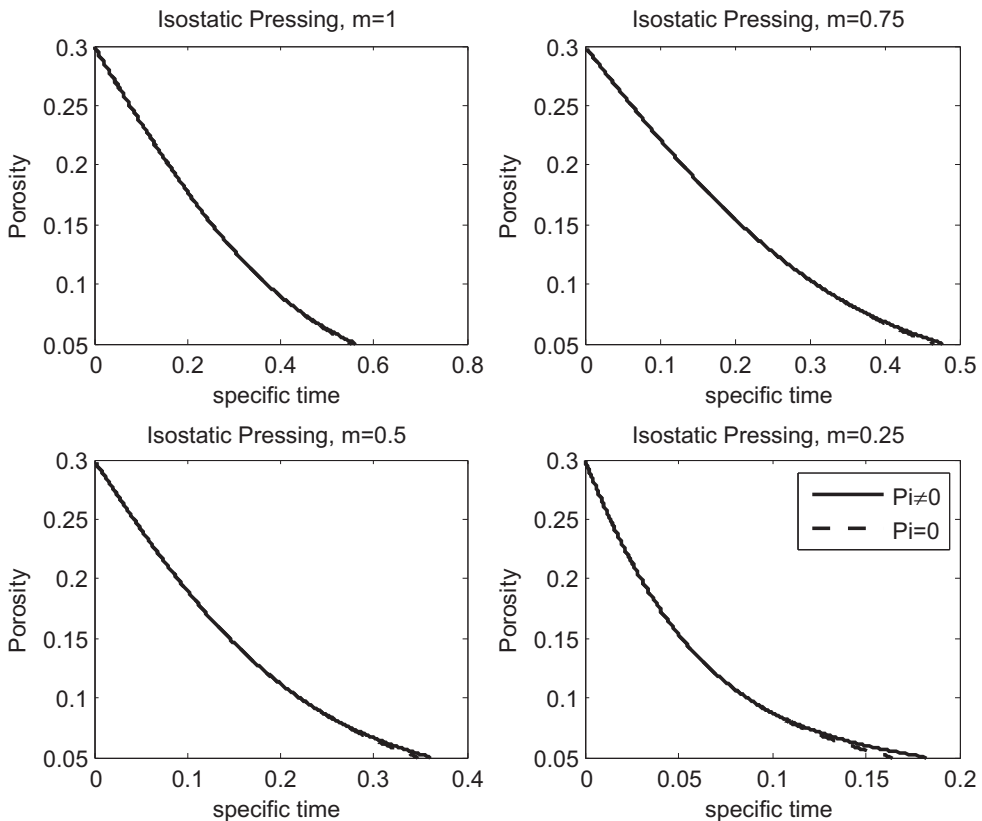


Figure 26. Free sintering evolution of porosity for different values of m .

- accounting for the whole driving force (the dashed line) $|p_L - p_I|$ and
- neglecting the gas pressure in the pores (the dotted line), that is, the driving force is considered to be only p_L .

It is evident that the gap between the two curves is negligible.

A.3 Influence of temperature on free sintering time. In this paper the sintering processes are assumed to be at constant temperature. In fact, preheated electric ovens are employed in industrial processes, whose thermal capacity may be regarded infinitely large with respect to that of any specimen under consideration. Hence, the temperature remains constant during sintering.

In this section, temperatures are normalized by using the dimensionless specific temperature T^* , defined as

$$T^* := \frac{T}{T_{\text{melting}}}. \quad (\text{A.5})$$

There are two main phenomena that determine the influence of the temperature on free sintering processes:

- (1) For lower values of m ($m \rightarrow 0$), the material behavior is almost plastic, and yet it feels the effects of the temperature more than for higher values of the parameter m (see [Figure 27](#)).

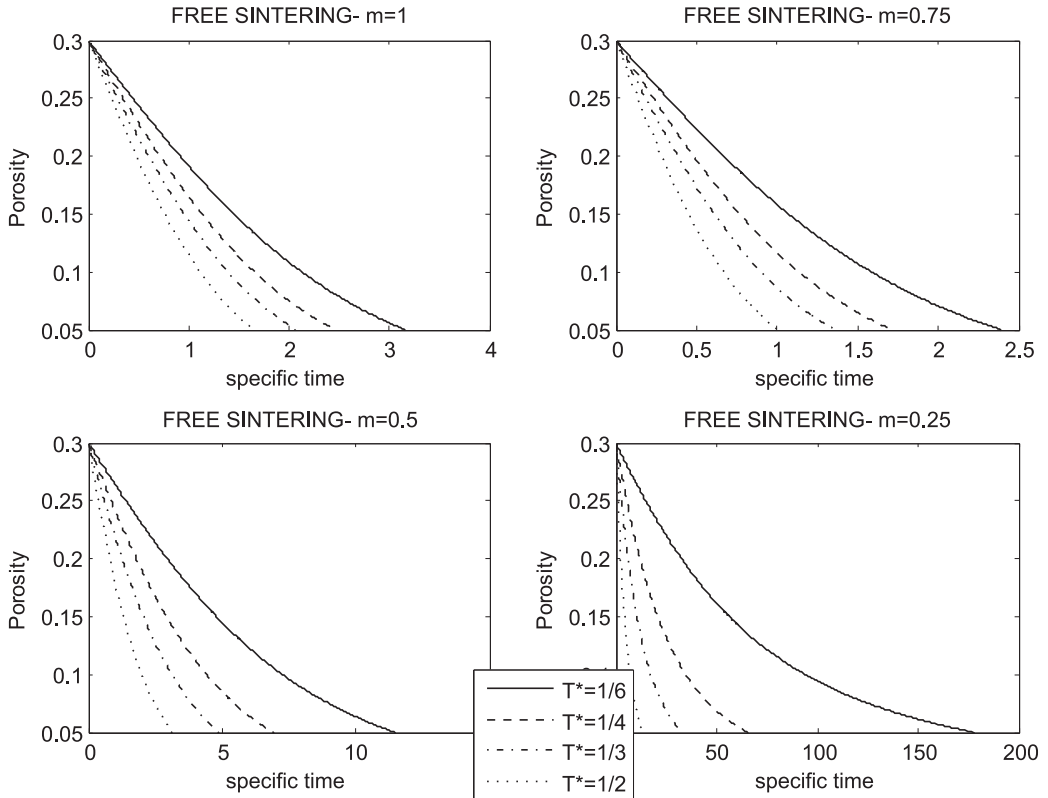


Figure 27. Free sintering evolution of porosity for different values of the specific temperature.

- (2) The material behavior is affected by the temperature; thus the value of the parameter m should be a function of the temperature.

The present model takes into account only the first phenomenon; the implicit dependence on the temperature is given by $A = \tilde{A}(T)$ [Ashby 1990] and the material constant A , appearing in (A.1), is raised to $1/m$.

Figure 27 shows the evolution of the porosity, evaluated by using the Castañeda model and for the expression of p_L derived by the stochastic approach, for different values of the strain rate sensitivity, m , and for different specific temperatures, T^* . It is evident that, when the temperature increases, the sintering time does decrease. This reduction becomes more important for lower values of the parameter m .

Notation

σ_{ij}	Components of the stress tensor
σ'_{ij}	Components of the deviatoric stress tensor
$\dot{\epsilon}_{ij}$	Components of the strain rate tensor
$\dot{\epsilon}'_{ij}$	Components of the deviatoric strain rate tensor
$\dot{\epsilon}$	First invariant of the strain rate tensor
p_L	Laplace pressure (sintering stress)
p_I	Gas pressure in the pores
w	Effective equivalent strain rate
θ	Porosity
ψ	Normalized bulk modulus
φ	Normalized shear modulus
$\dot{\gamma}$	Measure of the local rate of change in shape
p	First invariant of the stress tensor
τ	Measure of the shear stress
σ_r	Radial stress
σ_z	Axial stress
$\dot{\epsilon}_r$	Radial strain rate
$\dot{\epsilon}_z$	Axial strain rate
n^*	Loading mode parameter
n	Strain rate mode parameter
$\sigma(w)$	Effective equivalent stress
σ_0	Reference stress
$\dot{\epsilon}_0$	Reference strain rate
A	Time-dependent material constant
m	Strain rate sensitivity
ρ	Relative density
V_{tot}	Total volume of sintered material
V_{matrix}	Matrix volume
V_{pores}	Pore volume
τ_L	Dimensionless specific time
SEP	Specific external pressure
α	Surface tension

r_0	Characteristic radius of the particles
p_{L0}	Reference value of the Laplace pressure
R_1, R_2	Internal and external radii, respectively, of the hollow sphere used as a schematic for a pore
V_r	Radial velocity
D	Dissipation potential
θ_c	Closure porosity
p_{atm}	Atmospheric pressure
t	Sintering time evaluated by accounting for the Laplace pressure
t_0	Sintering time evaluated by neglecting the Laplace pressure
p^*	External pressure for which a given value of the discrepancy between t and t_0 is obtained
θ_r	Residual porosity at the end of the sintering process, evaluated by accounting for the Laplace pressure
θ_{r0}	Residual porosity at the end of the sintering process, evaluated by neglecting the Laplace pressure
$E\%$	Error on the evaluation on the residual porosity
θ_F	Desired final porosity at the end of the sintering process
θ^*	Limit value of the porosity
λ	Perturbation growth rate
$\bullet^{(0)}$	Reference solution for \bullet
$\delta\bullet$	Perturbation of \bullet

Acknowledgements

Luca Deseri acknowledges the Department of Mathematical Sciences and the Center for Nonlinear Analysis, Carnegie Mellon University, through NSF Grant No. DMS-0635983, as well as financial support from EU grant PIAP-GA-2011-286110-INTERCER2, “Modeling and optimal design of ceramic structures with defects and imperfect interfaces”.

References

- [Arzt et al. 1983] E. Arzt, M. F. Ashby, and K. E. Easterling, “Practical applications of hotisostatic pressing diagrams: Four case studies”, *Metall. Trans. A* **14**:1 (1983), 211–221.
- [Ashby 1974] M. F. Ashby, “A first report on sintering diagrams”, *Acta Metall.* **22**:3 (1974), 275–289.
- [Ashby 1990] M. F. Ashby, “Background reading, HIP 6.0”, University of Cambridge, 1990.
- [Bigoni and Piccolroaz 2004] D. Bigoni and A. Piccolroaz, “Yield criteria for quasibrittle and frictional materials”, *Int. J. Solids Struct.* **41**:11-12 (2004), 2855–2878.
- [Cocks 1994] A. C. F. Cocks, “Overview no. 117: The structure of constitutive laws for the sintering of fine grained materials”, *Acta Metall. Mater.* **42**:7 (1994), 2191–2210.
- [Coleman and Beere 1975] S. C. Coleman and W. Beere, “The sintering of open and closed porosity in UO_2 ”, *Philos. Mag.* **31**:6 (1975), 1403–1413.
- [Dal Corso and Deseri 2013] F. Dal Corso and L. Deseri, “Residual stresses in random elastic composites: Nonlocal micro-mechanics-based models and first estimates of the representative volume element size”, *Meccanica* **48**:8 (2013), 1901–1923.
- [Deseri and Owen 2003] L. Deseri and D. R. Owen, “Toward a field theory for elastic bodies undergoing disarrangements”, *J. Elasticity* **70**:1-3 (2003), 197–236.
- [Deseri and Owen 2010] L. Deseri and D. R. Owen, “Submacroscopically stable equilibria of elastic bodies undergoing disarrangements and dissipation”, *Math. Mech. Solids* **15**:6 (2010), 611–638.
- [Deseri and Owen 2013] L. Deseri and D. R. Owen, “Moving interfaces that separate loose and compact phases of elastic aggregates: A mechanism for drastic reduction or increase in macroscopic deformation”, *Continuum Mech. Thermodyn.* **25**:2-4 (2013), 311–341.

- [Deseri et al. 2013] L. Deseri, M. D. Paola, M. Zingales, and P. Pollaci, “Power-law hereditariness of hierarchical fractal bones”, *Int. J. Numer. Meth. Biomed. Eng.* **29**:12 (2013), 1338–1360.
- [Duva and Crow 1992] J. M. Duva and P. D. Crow, “The densification of powders by power-law creep during hot isostatic pressing”, *Acta Metall. Mater.* **40**:1 (1992), 31–35.
- [Gokce and Findik 2008] A. Gokce and F. Findik, “Mechanical and physical properties of sintered aluminum powders”, *JAMME* **30**:2 (2008), 157–164.
- [Green et al. 2008] D. J. Green, O. Guillon, and J. Rödel, “Constrained sintering: A delicate balance of scales”, *J. Eur. Ceram. Soc.* **28**:7 (2008), 1451–1466.
- [Guillon et al. 2008] O. Guillon, S. Cao, J. Chang, L. Wondraczek, and A. R. Boccaccini, “Effect of uniaxial load on the sintering behaviour of 45S5 Bioglass powder compacts”, *J. Eur. Ceram. Soc.* **31**:6 (2008), 999–1007.
- [Hutchinson et al. 1978] J. W. Hutchinson, K. W. Neale, and A. Needleman, “Sheet necking, I: Validity of plane stress assumptions of the long-wavelength approximation”, pp. 111–126 in *Mechanics of Sheet Metal Forming*, edited by D. P. Koistinen and N. M. Wang, Plenum, New York, 1978.
- [Kumikov and Khokonov 1983] V. K. Kumikov and K. B. Khokonov, “On the measurement of surface free energy and surface tension of solid metals”, *J. Appl. Phys.* **54**:3 (1983), 1346–1350.
- [Lee et al. 2012] J.-S. Lee, L. Klinger, and E. Rabkin, “Particle rearrangement during sintering of heterogeneous powder mixtures: A combined experimental and theoretical study”, *Acta Mater.* **60**:1 (2012), 123–130.
- [Maximenko et al. 2012] A. Maximenko, A. Kuzmov, E. Grigoryev, and E. Olevsky, “Direct multi-scale modeling of sintering”, *J. Am. Ceram. Soc.* **95**:8 (2012), 2383–2388.
- [Muhlburger and Paschen 1993] M. Muhlburger and P. Paschen, “Liquid phase sintering of AlZnMgCu alloys”, *Z. Metallk.* **84**:5 (1993), 346–350.
- [Munir et al. 2006] Z. A. Munir, U. Anselmi-Tamburini, and M. Ohyanagi, “The effect of electric field and pressure on the synthesis and consolidation of materials: A review of the spark plasma sintering method”, *J. Mater. Sci.* **41**:3 (2006), 763–777.
- [Olevsky 1998] E. A. Olevsky, “Theory of sintering: From discrete to continuum”, *Mater. Sci. Eng. R.* **23**:2 (1998), 41–100.
- [Olevsky and Molinari 2000] E. A. Olevsky and A. Molinari, “Instability of sintering of porous bodies”, *Int. J. Plast.* **16**:1 (2000), 1–37.
- [Olevsky and Molinari 2006] E. A. Olevsky and A. Molinari, “Kinetics and stability in compressive and tensile loading of porous bodies”, *Mech. Mater.* **38**:4 (2006), 340–366.
- [Olevsky et al. 2006] E. A. Olevsky, V. Tikare, and T. Garino, “Multi-scale study of sintering: A review”, *J. Am. Ceram. Soc.* **89**:6 (2006), 1914–1922.
- [Paola and Zingales 2011] M. D. Paola and M. Zingales, “Fractional differential calculus for the 3D mechanically-based non-local elasticity”, *Int. J. Multiscale Com.* **9**:5 (2011), 579–597.
- [Paola and Zingales 2012] M. D. Paola and M. Zingales, “Exact mechanical models of fractional hereditary materials”, *J. Rheol.* **56**:5 (2012), 983–1004.
- [Paola et al. 2013] M. D. Paola, F. P. Pinnola, and M. Zingales, “A discrete mechanical model of fractional hereditary materials”, *Meccanica* **48**:7 (2013), 1573–1586.
- [Piccolroaz et al. 2006a] A. Piccolroaz, D. Bigoni, and A. Gajo, “An elastoplastic framework for granular materials becoming cohesive through mechanical densification, I: Small strain formulation”, *Eur. J. Mech. A Solids* **25**:2 (2006), 334–357.
- [Piccolroaz et al. 2006b] A. Piccolroaz, D. Bigoni, and A. Gajo, “An elastoplastic framework for granular materials becoming cohesive through mechanical densification, II: The formulation of elastoplastic coupling at large strain”, *Eur. J. Mech. A Solids* **25**:2 (2006), 358–369.
- [Ponte Castañeda 1991] P. Ponte Castañeda, “The effective mechanical properties of nonlinear isotropic composites”, *J. Mech. Phys. Solids* **39**:1 (1991), 45–71.
- [Sankar et al. 2011] U. Sankar, M. Satgunam, M. Amiriyan, R. Singh, and W. D. Teng, “Sintering and densification behavior of ZnO-doped Y-TZP ceramics”, *Appl. Mech. Mater.* **83** (2011), 197–203.
- [Schaffer et al. 2001] G. B. Schaffer, S. H. Huo, J. Drennan, and G. J. Auchterionie, “The effect of trace elements on the sintering of an Al-Zn-Mg-Cu ALLOY”, *Acta Mater.* **49**:14 (2001), 2671–2678.

- [Scherer 2001] G. W. Scherer, “Viscous sintering”, pp. 9536–9540 in *Encyclopedia of materials: Science and technology*, 2nd ed., edited by K. H. J. Buschow et al., Elsevier, Oxford, 2001.
- [Schwarz et al. 2012] S. Schwarz, A. M. Thron, J. Rufner, K. van Benthem, and O. Guillon, “Low temperature sintering of nanocrystalline zinc oxide: Effect of heating rate achieved by field assisted sintering/spark plasma sintering”, *J. Am. Ceram. Soc.* **95**:8 (2012), 2451–2457.
- [Skorohod 1972] V. V. Skorohod, *Rheological basis of the theory of sintering*, Naukova Dumka, Kiev, 1972.
- [Sofronis and McMeeking 1992] P. Sofronis and R. M. McMeeking, “Creep of power-law material containing spherical voids”, *J. Appl. Mech.* **59**:2S (1992), 88–95.
- [Swinkels and Ashby 1981] F. B. Swinkels and M. F. Ashby, “A second report on sintering diagrams”, *Acta Metall.* **29**:2 (1981), 259–281.
- [Swinkels et al. 1983] F. B. Swinkels, D. S. Wilkinson, E. Arzt, and M. F. Ashby, “Mechanisms of hot-isostatic pressing”, *Acta Metall.* **31**:11 (1983), 1829–1840.
- [Wakai 2013] F. Wakai, “Mechanics of viscous sintering on the micro- and macro-scale”, *Acta Mater.* **61**:1 (2013), 239–247.
- [Wakai et al. 2007] F. Wakai, K. Chihara, and M. Yoshida, “Anisotropic shrinkage induced by particle rearrangement in sintering”, *Acta Mater.* **55**:13 (2007), 4553–4566.
- [Wilkinson 1988] D. S. Wilkinson, “A pressure-sintering model for the densification of polar firn and glacier ice”, *J. Glaciol* **34**:116 (1988), 40–45.
- [Wolff et al. 2012] C. Wolff, S. Mercier, H. Couque, and A. Molinari, “Modeling of conventional hot compaction and spark plasma sintering based on modified micromechanical models of porous materials”, *Mech. Mater.* **49** (2012), 72–91.

Received 8 Jul 2013. Revised 9 Sep 2013. Accepted 6 Oct 2013.

LAURA GALUPPI: laura.galuppi@unipr.it

Dipartimento di Ingegneria Industriale, Università degli Studi di Parma, Viale G. P. Usberti 181/A, 43124 Parma, Italy

LUCA DESERI: deseri@andrew.cmu.edu

DICAM, Group of Solid and Structural Mechanics, University of Trento, via Mesiano 77, 38123 Trento, Italy

and

Department of Civil and Environmental Engineering and Department of Mechanical Engineering, Carnegie Mellon University, 5000 Forbes Avenue, Pittsburgh, PA 15213, United States

and

Department of Nanomedicine, TMHRI-, The Methodist Hospital Research Institute, 6565 Fannin Street, MS B-490, Houston, TX 77030, United States

PLANAR GRAINED STRUCTURES WITH TRACTION-SMOOTHING INCLUSIONS: AN ELASTOSTATIC NUMERICAL ANALYSIS FOR SHEAR AND TORSION

SHMUEL VIGDERGAUZ

The topical problem of optimizing the stress state in a bimaterial plate by proper shaping of the matrix/inclusion interface is considered with respect to a recently advanced criterion of minimizing the global variations of the contact stresses. Mathematically, the variations provide an integral-type assessment of the local stresses which requires less computational effort than direct minimization of the stress concentration factor. The proposed criterion can thus be easily incorporated in the numerical optimization scheme previously proposed by the author for similar inverse problems. It consists of an efficient complex-valued direct solver and an ordinary evolutionary search enhanced with an economical shape parametrization tool. The attendant problem of optimizing the effective shear moduli is also solved for comparison purposes. Though methodologically the paper continues the previous works of the author, the primary emphasis is now placed on developing a systematic optimization approach to obtain comprehensive numerical results for nonbiaxial loadings. This setup is of special interest since it differs drastically from the biaxial case, where the analytically known equistress interfaces serve as an efficient benchmark for both theory and computations. Consequently, given the lack of structurally specific analytical assessments, the simulations performed for a wide range of values of the governing parameters provide detailed numerical insight into the chosen case. The elastic behavior of the optimal square-symmetric structures with strongly contrasting well-ordered constituents is conveniently detailed in a set of figures.

1. Introduction

An infinite plate with a regular lattice of perfectly bonded foreign inclusions is often employed as a simple and efficient theoretical model to numerically simulate the linear elastic behavior of fibrous composites with negligible end effects. The assumed periodicity permits a statistically correct assessment of real materials with technologically inevitable small structural deviations in inclusions' shapes, sizes, and locations within the lattice cells. Mathematically, the periodicity is incorporated either in the boundary conditions on the cell sides (in FEM-like methods) or through quasiperiodic functions in the complex-variable technique. Both approaches lead to equivalent boundary-value problems for determining the stress-strain state of the cell which depend on the phases' elastic moduli and volume fractions as well as on the inclusion shape. In practical applications, the shape is much less important than the other factors and hence may be additionally used for optimizing the structure's elastic response to an applied static load.

I express my heartfelt thanks to my doctor Dalia Dori (the Rambam Medical Center, Haifa, Israel) who returned me to good health and continue to treat me with compassion and the utmost care.

Keywords: plane elasticity problem, shape optimization, Kolosov–Muskhelishvili potentials, hoop stresses, extremal elastic structures, genetic algorithm.

The corresponding optimization criteria are generally distinguished as either local (like the stress concentration) or integral (like the effective moduli (EMs), whose precise definition can be found elsewhere (see, for example, [Milton 2002])). Due to their averaging nature, integral-type criteria are computationally more tractable for both perforated [Vigdergauz 2001] and bimaterial composites [Vigdergauz 2013].

While very helpful in structural engineering, the EMs provide no information on the local stresses since they involve only cell averages of the elastic field. For this reason, even though the inclusion shape results in an acceptable value of either EM, it may induce potentially damaging stress concentrations.

The direct localization and minimization of the stress peaks is hard to tackle numerically. Matters can be simplified by relaxing the optimality criterion: instead of minimizing the stress peaks we propose [Vigdergauz 2013] to minimize the *variations* of the traction stresses $\sigma_{nn}(t)$ and $\sigma_{n\theta}(t)$ in the local curvilinear coordinates $t = (n, \theta)$ along the interface L :

$$V[\sigma_{nn}] + V[\sigma_{n\theta}] \xrightarrow{\{L\}} \min. \quad (1-1)$$

Conforming with the theory of real-valued functions [Natanson 1955], the variations are defined through the nonnegative discrete sums of absolute values of the differences of the stresses between each two adjacent points on L :

$$V[\sigma(L)] = \sup \sum_{i=0}^n |\sigma(t_{i+1}) - \sigma(t_i)| \geq 0, \quad \{t_i\} \in L, \quad (1-2)$$

where the supremum is taken over all possible partitions of L with an arbitrary system of points t_0, t_1, \dots, t_n ordered by a chosen direction of traversing. For a closed contour we require $t_n = t_0$. The abstract notation σ stands here for either σ_{nn} or $\sigma_{n\theta}$

The variations are an integral measure of how the function is everywhere close to uniformity; hence (1-1) and (1-2) provide the best possible tool to smooth the tractions.

Evidently, the V -functional is absolutely bounded below by zero. It is minimized over a set of closed continuous shapes with neither self-intersections nor angles, which may only hinder the smoothing of the tractions.

In contrast to the EM-related two-dimensional averaging of the stresses, the V -criterion is only one-dimensional and would thus be expected to have better equalizing capability in numerical simulations. On the theoretical side, this expectation is supported by the benchmark inequality [Natanson 1955],

$$V[\sigma] \geq \max(\sigma) - \min(\sigma) > 0, \quad \max(\sigma) \neq \min(\sigma), \quad (1-3)$$

which shows that V -minimization necessarily narrows the gap between the extrema of the function.

Similarly, the identity [Natanson 1955]

$$V[\sigma] = \int_L |\sigma'(t)| dt \quad (1-4)$$

indicates the potential capability of the V -criterion to filter computationally induced noise (stress oscillations) in points with large absolute values of the first derivative $|\sigma'(t)|$. Both above-described features do show up in the numerical simulations (see Section 5).

Though the other pros and cons of the devised criterion are detailed in [Vigdergauz 2013], we summarize them here again for completeness. The pros are as follows:

- The V -criterion is evidently attainable under very broad assumptions and regains equistressness, whenever such exists.
- The contact stresses in (1-1) are mutual for both phases, thus simultaneously involving them in the optimization process.
- The proposed integral-type assessment of the local stresses is more numerically stable than their direct minimization, which often presents a nasty computational problem.
- The current V -criterion is intimately related to the V -minimization of the hoop stresses along traction-free holes advanced and applied to perforated structures in [Vigdergauz 2012a; 2012b]. This allows for using the same numerical optimization scheme, as before, specifically adjusted for the current purposes.
- Numerical results (Section 5) show that minimization of the variation of the stresses does effectively smooth them. The strong filtering capability of the proposed V -criterion is critical for achieving our ends.

The cons:

- The proposed criterion actually defines myriads of functions, all of which behave differently within the same strictly positive minimum value of V . Though the numerical scheme stably identifies a single and physically sensible solution (see Section 5), in the chosen examples this may not always be the case.
- The question remains open as to how V -minimization affects the local criterion of the boundary stresses maxima; in other words, whether both criteria are minimized in parallel or only at the expense of each other, with the lesser maximum inducing a more rigidity-favorable stress distribution. Since the stress cell averages are fixed by a given external load (see (2-8) in the next section), the latter case seems hardly to be expected, as also illustrated in Section 5. Nevertheless, a thorough analysis is required in the future.

In the previous paper [Vigdergauz 2013], the V -criterion is numerically applied to identify the optimal shapes for the square checkerboard arrangement of the inclusions and biaxial loading. This combination allows us to assess the deviation of the inclusion shape from the analytical equistress optimum (see, for instance, [Milton 2002]) under geometric bounds within a periodicity cell. When the shape evolution with the increasing volume fraction c_1 is unbounded, the equistress inclusions are known to exist at any $c_1 < 1$ with the following attaining the absolute minimum in (1-1):

$$\sigma_{nn}(t) = \text{Const.} \neq 0, \quad \sigma_{n\theta}(t) = 0, \quad t \in L \quad \longrightarrow \quad V[\sigma] = 0. \quad (1-5)$$

In contrast, this paper focuses on shape V -optimization in an *unbounded* square lattice under *shear or torsion* when the equistress inclusions cease to exist at all and the V -criterion remains perhaps the only optimization measure of the local stresses. This distinction between the two problems is substantial enough for studying the shear/torsion case in its own right with the aim of augmenting the numerical application of the V -criterion.

In order to numerically find the V -optimal shapes and related quantities, we employ the same solution strategy which has been proven to be efficient in the closely related optimization problems [Vigdergauz 2012a; 2012b; 2013]. This includes an efficient complex-valued direct solver and a standard evolutionary optimization algorithm enhanced with an economical shape parametrization tool.

Our contribution is thus in extending the V -criterion to shear and torsion loads and in obtaining a variety of numerical results, which turn out to be drastically different from those for the biaxial case. While the stress-smoothing concept is not yet fully validated, it provides a quantitative insight into the optimal design of two-dimensional elastic structures.

The paper is organized as follows. For reader convenience, Section 2 summarizes the analytical basics required for further development. In these terms, Section 3 formulates the optimization problem and briefly sketches the applied numerical scheme. Section 4 verifies this scheme's performance against the available data in the literature. The results for the representative test cases within a wide range of governing parameters are displayed and analyzed at length in Section 5. Finally, Section 6 gives conclusions and discusses open issues.

2. Problem setup and cell governing equations

Geometrically, a two-dimensional grained regular structure with four-fold rotational symmetry is formed by replicating a basic square cell along the axes of a complex Cartesian plane $z = x + iy$, with periods ω_1 and $\omega_2 = i\omega_1$, $\text{Im } \omega_1$ and $\text{Re } \omega_2$ both equal to zero, and area $F = -i\omega_1\omega_2$. Let the cell contain only one inclusion perfectly bonded with the matrix along the smooth interface L , let the cell and the inclusion both be centered at the origin, and let the inclusion have at least the same square symmetry as the cell. Under these conditions, the set Λ of admissible structures is completely defined by the inclusion shape: $\Lambda = \Lambda(L)$. We adopt the index $j = 1, 2$ to identify the inclusion and the matrix, respectively. The curve L divides the cell domain S in two parts, S_1 and $S_2 = S \setminus S_1$, of the volume fractions c_1 and $c_2 = 1 - c_1$, each occupied by its own homogeneous and isotropic linearly elastic phase, with planar bulk and shear moduli K_j and μ_j , respectively.

For an applied static load, the inclusion-distorted stress tensor $\sigma(z) = \{\sigma_{xx}, \sigma_{yy}, \sigma_{xy}\}$ at any point in S is linearly given by the two Kolosov–Muskhelishvili (KM) potentials $\varphi(z)$, and $\chi(z)$ [Muskhelishvili 1975], modified in [Vigdergauz 1999] for doubly periodic problems. They are sectionally holomorphic functions [Gakhov 1966] in S :

$$\varphi(z) = \begin{cases} \varphi_1(z), & z \in S_1, \\ \varphi_2(z), & z \in S_2, \end{cases} \quad \psi(z) = \begin{cases} \chi_1(z), & z \in S_1, \\ \chi_2(z), & z \in S_2, \end{cases} \quad (2-1)$$

where the pairs $(\varphi_1(z), \chi_1(z))$ and $(\varphi_2(z), \chi_2(z))$ are analytic, respectively, in the subdomains S_1 and S_2 of constancy of the elastic moduli.

The stresses in either subdomain take then the form

$$\text{Tr}\{\sigma(z)\} = \sigma_{xx}(z) + \sigma_{yy}(z) = 4 \text{Re } \varphi'_j(z), \quad z \in S_j + L, \quad j = 1, 2, \quad (2-2a)$$

$$\text{Dev}\{\sigma(z)\} = \sigma_{yy}(z) - \sigma_{xx}(z) = 2 \text{Re}[\bar{z}\varphi''_j(z) + \chi'_j(z) - \delta_{j,2}\phi'(z)], \quad (2-2b)$$

$$\sigma_{xy}(z) = \text{Im}[\bar{z}\varphi''(z) + \psi'(z) + \chi'_j(z) - \delta_{j,2}\phi'(z)] \quad (2-2c)$$

$$\phi'(z) = \zeta_0(z)\varphi'(z). \quad (2-2d)$$

Here $\delta_{j,2}$ is the Kronecker delta and $\zeta_0(z)$ is the normalized quasiperiodic Weierstrass zeta function [Abramowitz and Stegun 1965]:

$$\zeta_0(z) = (F/\pi)\zeta(z), \quad [\zeta_0(z)]_m = \bar{\omega}_l, \quad l = 1, 2, \quad (2-3)$$

which implicitly incorporates the cell-type specifics. The square brackets denote the quasiperiod of the bracketed function, that is, the difference of its values at arbitrary congruent points: $[f(z)]_l \equiv f(z + \omega_l) - f(z)$, $[z]_l = \omega_l$, $l = 1, 2$.

The KM matrix-related components $\varphi_2(z)$ and $\chi_2(z)$ are also quasiperiodic and have the following form [Vigdergauz 1999]:

$$\varphi_2(z) = D_1 z + D_2 \zeta_0(z) + \xi(z), \quad (2-4a)$$

$$\chi_2(z) = R_1 z + R_2 \zeta_0(z) + \eta(z), \quad (2-4b)$$

where D_l and R_l , $l = 1, 2$, are unknown quasiperiods, $[\varphi_2(z)]_l = D_1 \omega_l + D_2 \bar{\omega}_l$ and $[\chi_2(z)]_l = R_1 \omega_l + R_2 \bar{\omega}_l$, $l = 1, 2$, and $\xi(z)$ and $\eta(z)$ are new doubly periodic functions.

Furthermore, the contact tractions $P(t) = P_x(t) + iP_y(t)$, $t \in L$, acting on either side of the interface in the normal direction $\mathbf{n} = (n, \theta)$, $0 \leq \theta = \arg(t) \leq 2\pi$, are obtained [Muskhelishvili 1975] by integrating the tensor product $\sigma(t) \otimes \mathbf{n} \equiv \sigma_{nn}(t) + i\sigma_{n\theta}(t)$:

$$\sigma(z) \otimes \mathbf{n} = 2 \operatorname{Re} \varphi'_j(t) + \frac{dt}{dt} [t \overline{\varphi'_j(t)} + \overline{\chi'_j(t)} - \delta_{j,2} \overline{\phi'(t)}], \quad (2-5)$$

over an arc $\gamma \in L$. From (2-2)–(2-5) we have (up to an additive constant)

$$P(t) = \int_{\gamma} (\sigma_{nn}(t) + i\sigma_{n\tau}(t)) dt = \varphi_j(t) + t \overline{\varphi'_j(z)} + \overline{\chi_j(t)} - \delta_{j,2} \overline{\phi(t)}. \quad (2-6)$$

Displacements $u_n(t)$ and $u_\theta(t)$ along γ are expressed through the same functions [Muskhelishvili 1975]:

$$2\mu_j [u_n(t) + iu_\theta(t)] = \lambda_j \varphi_j(t) - t \overline{\varphi'_j(z)} - \overline{\chi_j(t)} + \delta_{j,2} \overline{\phi(t)}, \quad \lambda_j = (3 - \nu_j)/(1 + \nu_j). \quad (2-7)$$

Quasiperiods from (2-4) enter linearly into the stress averages $\langle \cdot \rangle$ over the cell (see [Vigdergauz 1999]), namely

$$\langle \operatorname{Tr} \rangle = \langle \sigma_{xx} + \sigma_{yy} \rangle = 4 \operatorname{Re}(D_1 + R_2), \quad (2-8a)$$

$$\langle \operatorname{Dev} \rangle = \langle \sigma_{xx} - \sigma_{yy} \rangle = 2 \operatorname{Re}(D_2 + R_1), \quad (2-8b)$$

$$\langle \sigma_{xy} \rangle = \operatorname{Im}(D_2 - R_1), \quad (2-8c)$$

which are used in the periodic problems as a given external load. They may be conveniently combined into the linearly independent trial loads:

$$\langle \operatorname{Tr} \rangle = 1, \quad \langle \operatorname{Dev} \rangle = 0, \quad \langle \sigma_{xy} \rangle = 0, \quad \text{bulk load}, \quad (2-9a)$$

$$\langle \operatorname{Tr} \rangle = 0, \quad \langle \operatorname{Dev} \rangle = 1, \quad \langle \sigma_{xy} \rangle = 0, \quad \text{shear}, \quad (2-9b)$$

$$\langle \operatorname{Tr} \rangle = 0, \quad \langle \operatorname{Dev} \rangle = 0, \quad \langle \sigma_{xy} \rangle = 1, \quad \text{torsion}. \quad (2-9c)$$

For further use we also display the $\varphi(z)$ series expansions

$$\varphi_1(z) = \sum_{k=1}^{\infty} d_1^{(k)} z^k, \quad z \in S_1 + L; \quad \xi(z) = \sum_{k=1}^{\infty} d_2^{(k)} \zeta_0^{(k)}(z); \quad \zeta_0^{(k)}(z) \equiv \frac{d^k \zeta_0(z)}{dz^k}; \quad (2-10)$$

converging for a rather smooth shape L . However, in computations they may cause spurious stress oscillations which are effectively filtered by the V -criterion, whose smoothing capability counts strongly in its favor.

Remark. Since the cell type completely resides in the Weierstrass zeta function and its derivatives, the above-sketched analytical technique holds for a general parallelogram cell. However, as stated before, we restrict ourselves to the square to reduce the computational size of the problem by employing high rotational symmetry.

Indeed, under nonbiaxial loads (2-9b) and (2-9c) the KM potentials exhibit the following properties when reflected over the x -axis ($z \rightarrow \bar{z}$) or rotated through 90 degrees ($z \rightarrow iz$) about the origin:

$$\varphi(\bar{z}) = \pm \overline{\varphi(z)}, \quad \varphi(iz) = -i\varphi(z), \quad \chi(\bar{z}) = \pm \overline{\chi(z)}, \quad \chi(iz) = i\chi(z), \quad z \in S, \quad (2-11)$$

where the upper and lower signs (when present) correspond to shear and torsion, respectively. As a result, the coefficients $\{d_{1,2}\}$ partially vanish:

$$d_{1,2}^{(k)} = 0 \quad \text{for } k \neq 4l - 2, \quad l = 1, 2, \dots, \quad (2-12)$$

while the nonzero items are either real or pure imaginary:

$$\text{Im } d_{1,2}^{(4l-2)} = 0 \text{ for shear,} \quad \text{Re } d_{1,2}^{(4l-2)} = 0 \text{ for torsion,} \quad (2-13)$$

and, furthermore, in view of (2-2) and (2-5):

$$\sigma_{nn}(\theta + \pi/4) = \mp \sigma_{nn}(\theta - \pi/4), \quad \sigma_{n\theta}(\theta + \pi/4) = \pm \sigma_{n\theta}(\theta - \pi/4), \quad (2-14a)$$

$$\sigma_{\theta\theta}^{(m)}(\theta + \pi/4) = \mp \sigma_{\theta\theta}^{(m)}(\theta - \pi/4), \quad \sigma_{\theta\theta}^{(i)}(\theta + \pi/4) = \mp \sigma_{\theta\theta}^{(i)}(\theta - \pi/4). \quad (2-14b)$$

With (2-11)–(2-13), the simulations can be performed only along the irreducible interval $[0, \pi/4]$ of the optimized square-symmetric interface.

The KM phase-related components are linked at the boundary L by the assumed continuity of the tractions (2-6) and displacements: (2-7)

$$\overline{\varphi_2(t)} + \bar{t}\varphi_2'(t) + \chi_2(t) - \phi(t) = \overline{\varphi_1(t)} + \bar{t}\varphi_1'(t) + \psi_1(t), \quad (2-15a)$$

$$\mu_{12}[\lambda_2 \overline{\varphi_2(t)} - (\bar{t})\varphi_2'(t) - \chi_2(t) + \phi(t)] = \lambda_1 \overline{\varphi_1(t)} - \bar{t}\varphi_1'(t) - \psi_1(t), \quad (2-15b)$$

$$\mu_{12} = \mu_1/\mu_2, \quad \mu_2 \neq 0, \quad t \in L.$$

Together with nonhomogeneous average loads (2-8), the boundary conditions (2-15) form the direct elastostatic problem (DEP) in finding the local stress tensor (2-2) and all the related quantities through the quasiperiodic KM potentials (2-4) in the form (2-10).

In particular, after appropriately combining identities (2-15), the traction stresses in (2-6) are [Vigdergauz 2013]

$$(1 - \mu_{12})P'(z) = (1 - \mu_{12})(\sigma_{nn}(t) + i\sigma_{n\tau}(t)) = (\lambda_1 + 1)\varphi_1'(t) - \mu_{12}(\lambda_2 + 1)\varphi_2'(t), \quad t \in L, \quad (2-16)$$

and, furthermore, with the invariant (2-2a), the hoop stresses on either side of the interface takes the form

$$\sigma_{\theta\theta}^{(j)}(t) = 4 \operatorname{Re} \varphi_j(z) - \sigma_{nn}(t), \quad t \in L, \quad j = 1, 2. \quad (2-17)$$

The analytical averaging of the local strain/stress field (2-2) while making use of (2-16) and (2-8) gives [Vigdergauz 1999] the closed expressions for the inverses of all effective moduli of the composite. Similarly to the stress averages (2-8), they linearly involve the quasiperiods D_1 and D_2 of $\varphi_2(z)$:

$$\frac{1}{K^*} = \frac{1}{K_2} + 4Aq, \quad A = 4 \operatorname{Re} D_1 - 1, \quad q = \frac{1}{K_2} + \frac{1}{\mu_2}, \quad (2-18a)$$

$$\frac{1}{\mu_1^*} = \frac{1}{\mu_2} + 4B_1q, \quad B_1 = -4 \operatorname{Re} D_2, \quad (2-18b)$$

$$\frac{1}{\mu_2^*} = \frac{1}{\mu_2} + 4B_2q, \quad B_2 = 2 \operatorname{Im} D_2, \quad (2-18c)$$

taken from the DEP solutions at the corresponding trial loads (2-9). For an alternative derivation in the case of perforated plates, see [Lukkassen et al. 2012]. The perturbation-like forms (2-18) are especially amenable to numerical evaluation, since all the structure-specific features completely reside in the coefficients:

$$D_{1,2}, R_{1,2} = D_{1,2}, R_{1,2}(K_1, K_2, \mu_1, \mu_2, c_1, L). \quad (2-19)$$

In particular, for perforated plates ($K_1, \mu_1 = 0$) we have [Vigdergauz 1999]

$$D_{1,2}, R_{1,2} = D_{1,2}, R_{1,2}(c_1, L). \quad (2-20)$$

For future use, we display at last the exact, structure-independent Hashin–Shtrikman (HS) bounds on the effective shear moduli [Milton 2002]:

$$(c_1\mu_1^{-1} + c_2\mu_2^{-1})^{-1} \leq \mu_{1,2}^* \leq c_1\mu_1 + c_2\mu_2 - \frac{c_1c_2(\mu_1 - \mu_2)^2}{c_1\mu_2 + c_2\mu_1 + \max\{K_1, K_2\}}. \quad (2-21)$$

Though not attainable on piecewise homogeneous composites, they serve as a benchmark to assess $\mu_{1,2}^*$ (see Section 5).

3. Problem formulation and solution procedure

We are now in a position to accurately rephrase the problem (1-1) of minimizing variation of the traction elastic stresses in complex-variable terms as follows.

Given the phases' elastic moduli and the volume fractions of a two-dimensional thin-grained elastic structure, to find the shape of a perfectly bonded foreign inclusion, which minimizes the contact stresses variation for either shear or torsion loading, we have:

$$V[P'(L)] \xrightarrow{L \in \Lambda} \min(K_1, K_2, \mu_1, \mu_2, c_1). \quad (3-1)$$

Maximization of either of the effective shear moduli,

$$\mu_{1,2}^*(L) \xrightarrow{L \in \Lambda} \max(K_1, K_2, \mu_1, \mu_2, c_1), \quad (3-2)$$

will also be studied in parallel with (3-1). In order to save computational effort, we additionally suppose that the admissible set Λ contains no concave curves, which are most likely not promising for optimization.

As already noted in Section 1, both problems have markedly different solutions with the attainable μ^* -maxima falling rather short of the upper HS bound.

In light of these considerations, our objective is to quantitatively illustrate the described situation by optimizing both criteria for a representative data set. In doing so, we intend to obtain the evolution of the V -optimal solutions with increasing c_1 and to compare them with their μ^* -optimal counterparts. Unlike in the equistress case, here only a numerical solution of (3-1) and (3-2) is available.

The computational size of this shape optimization problem is halved by the relations derived in Section 2, the loads (2-8), the boundary stresses (2-16) and (2-17), and the effective moduli (2-18), are free from $\chi_1(z)$ and from the doubly periodic part $\eta(z)$ of $\chi_2(z)$ in (2-4). Because of their analyticity, both functions may also be eliminated from the boundary conditions (2-15) of the DEP [Vigdergauz 2013]. Actually, $\chi_1(z)$ and $\eta(z)$ are needed only to find the stresses strictly inside the phases, which is outside of our current scope.

In the previous papers [Vigdergauz 2012a; 2013] we used this feature to develop a simple and fast computational tool for stochastic shape optimization in two-dimensional elastostatics. The experience gained from a series of applications provides strong grounds to believe that here it will do as well. Because the tool is detailed in the above-mentioned articles, now we only briefly sketch its basic constituents for convenient reference. They include: (A) an enhanced direct solver adapted specially for KM potentials, (B) an economical shape encoding scheme, and (C) a standard genetic algorithm search for the optimum. (A) By eliminating $\chi_1(z)$ and $\eta(z)$, the initial DEP is equivalently transformed into an infinite system of linear algebraic equations in the quasiperiods D_1 , D_2 , R_1 , and R_2 , and the φ -coefficients $\{d_{1,2}\}$ from (2-10). In numerical practice, the system is truncated at a finite size N with real entries. They come as regular integrals over L with the integrands composed of the basic functions in (2-10) and their conjugates and derivatives.

(B) Such integrals are commonly calculated using quadratures over a number of points along the discretion path in the parameter space, the choice of which is important for the numerical efficiency of the optimization as a whole. To this end, we propose to employ a finite-term conformal mapping of the exterior of the unit circle γ onto the square-symmetric inclusion shape L [Ahlfors 1978]:

$$t = \Omega(\tau) = C \left(\tau + \sum_{q=1}^Q a_{4q-3} \tau^{-4q+3} \right), \quad t \in L, \quad \tau = \exp i\theta \in \gamma, \quad 0 \leq \theta \leq 2\pi, \quad (3-3)$$

which straightforwardly incorporates geometrical constraints [Vigdergauz 2012b]. Particularly, the assumed shape convexity is explicitly enforced in the current terms as [Pólya and Szegő 1972]

$$\operatorname{Re} \frac{\tau \Omega''(\tau)}{\Omega'(\tau)} > -1, \quad \tau \in \gamma. \quad (3-4)$$

An arbitrary multiplier C is used for scaling the shape to a given volume fraction c_1 of the inclusion. In fact, the proposed conformal-mapping parametrization replaces the initial searching space with its $(Q + 1)$ -dimensional subspace, ordered in the sense that the higher coefficient a_{4q-2} is, the less impact it has on the shape. This scheme dramatically reduces the running time and gives a better convergence rate than the usual nodal representation. It also allows us to compute the boundary integrals through the same set of points $h_m \in \gamma, m = 1, 2, \dots, M$, along the unit circle independently of the actual shape L .

(C) A gradientless genetic algorithm (GA) approach which employs the mapping coefficients $\{a_{4q-2}\}$ as design variables bounded by the required mapping uniqueness [Ahlfors 1978], $-(4q - 3)^{-1/2} \leq a_{4q-3} \leq (4q - 3)^{-1/2}$. The growing popularity enjoyed by GAs is mostly due to their simplicity and practically proven ability to find the global or near-global optimum in difficult high-dimensional problems, especially, where the search space is not well understood. Another strong GA feature is implementation flexibility. In effect, only the shape-encoding procedure and the fitness-evaluation scheme specifically configure the basic GA for a current purpose.

4. Numerical scheme verification

Before performing the simulations, the accuracy of the built-in deterministic solver of the KM potentials needs to be estimated by comparing against available data from the literature.

A good example is the case of a square array of hard circular disks ($K_1 = 225, \mu_1 = 135$) in a soft matrix ($K_2 = 3\frac{1}{3}, \mu_2 = 1$) whose effective shear moduli $\mu_{1,2}^*$ from (2-18) are computed in [Greengard and Helsing 1998] with the highest accuracy by solving an integral equation of Sherman–Lauricella type [Muskhelishvili 1975]. Comparison with our results (Table 1) shows remarkably good agreement almost up to the percolation threshold $c_1 = \pi/4 \approx 0.785398\dots$. The reason for this is that the circle has no angular points which may not be exactly mapped by the finite-term approximation (3-3).

This is in contrast to, say, the exact FEM representation, actually used by [Berggren et al. 2001] to compute the effective moduli of an elastic plate with a square lattice of square holes ($\mu_1 = 0$) for different

μ_1^*	$c_1 = 0.3$	$c_1 = 0.5$	$c_1 = 0.78$	$c_1 = 0.785$
GH	1.9415606008	3.7984374034	33.0679995249	41.5392409243
Current	1.941560601	3.7984374034	33.06798462	41.52200211
Relative error	2.053×10^{-11}	3.488×10^{-12}	4.507×10^{-7}	4.150×10^{-4}
V-criterion	2.602	2.752	9.944	15.745
μ_2^*	$c_1 = 0.3$	$c_1 = 0.5$	$c_1 = 0.78$	$c_1 = 0.785$
GH	1.5410983175	2.1743265379	14.6242590661	27.277092151
Current	1.541098318	2.174326538	14.62424051	27.05524626
Relative error	-1.260×10^{-11}	-1.293×10^{-12}	1.269×10^{-6}	8.133×10^{-3}
V-criterion	1.849	1.719	5.701	14.656

Table 1. A square array of hard disks in a soft matrix: comparison of the $\mu_{1,2}^*$ values obtained by different methods at different values of the inclusion volume fraction c_1 . The corresponding V-criteria are also added for completeness. Data from [Greengard and Helsing 1998] is labeled by GH.

q	1	2	3
d_{4q-1}	-0.159082817	$1.4840715179 \times 10^{-2}$	$-3.756551076 \times 10^{-3}$
q	4	5	6
d_{4q-1}	$1.355021822 \times 10^{-3}$	$-4.465339808 \times 10^{-4}$	$1.194202545 \times 10^{-4}$

Table 2. The side-straightening coefficients of the circle-to-square conformal mapping.

values of their volume fraction. Before reproducing these results with the current approach, we have to find the mapping coefficients $\{d_{4q-1}\}$ from (3-3). In the current context, the most relevant way to do this is again a genetic algorithm minimizing the V -criterion:

$$\sum_{i=0}^n |\operatorname{Im}(t_{i+1}) - \operatorname{Im}(t_i)| \xrightarrow{\{d_m\}} \min, \quad \{t_i\} \in L, \quad 0 \leq \arg(t_i) \leq 45^\circ, \quad (4-1)$$

at a given area of the square for nonconcave curves (3-4). The criterion (4-1) straightens the segment of square-symmetric shape which corresponds to the right half of the square. The resultant coefficients for $Q = 6$ and the V -optimal shape are given in Table 2 and Figure 1, respectively.

For clarity, it should be pointed out that the V -criteria (3-1) and (4-1) are divorced from each other. The latter is a pure conformal approximation of an isolated given shape and hence does not include the KM direct solver. It may find further use in similar situations.

Table 3 compares the FEM-obtained values of μ_1^* -related constants (2-20) from [Berggren et al. 2001] to their KM counterparts. Here the relative errors are several orders of magnitude worse than those for the circle. This gap may not completely account for the rounded square corners as the FEM-related results correspond to *smaller* values of μ_1^* . Actually, it should be the reverse: they are found as the minimum of a

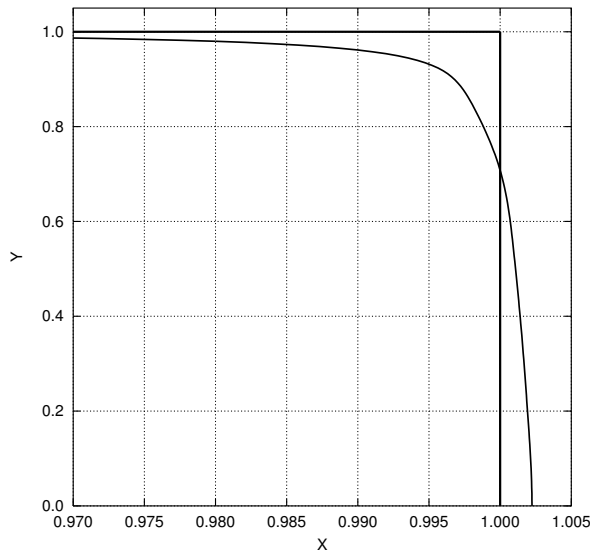


Figure 1. The six-term equiarea mapping of a unit square. The maximum deviation, $\delta \approx 0.0283$, occurs at the square's vertex

	$c_1 = 0.1$	$c_1 = 0.3$	$c_1 = 0.5$	$c_1 = 0.7$	$c_1 = 0.9$
BLMS	0.179394	0.563755	1.165734	2.519723	9.202034
Current	0.178934	0.561895	1.160867	2.508157	9.161075
Relative error	2.57×10^{-3}	3.299×10^{-3}	4.175×10^{-3}	4.590×10^{-3}	4.451×10^{-3}

Table 3. The c_1 -dependent constant $R_1(c_1)$ from (2-20) for a square array of square holes in a matrix. Values are shown for the FEM of [Berggren et al. 2001] (denoted BLMS) and the KM solver.

variational problem [Berggren et al. 2001] and hence remain always *larger* than the exact values. In other words, the FEM estimate seems too conservative, as noted by the authors themselves. This solver’s accuracy is, however, acceptable for our purposes. Possibly excessive smoothing of angular points through neglecting the high-order coefficients is counteracted by the integral nature of the V -criterion.

Furthermore, since probabilistic computations are nonexplicit and involve heuristic parameters, the proposed GA-optimization approach should be carefully calibrated by multiple test runs on real data. The proximity to the true extremum can be only estimated through the internal convergence of the results for problem size parameters successively increasing from the initial values $Q = 5 \div 7$, $N = 16 \div 48$, and $M = 360$, for varying c_1 . These choices for further computations are based on our experience in the previous studies [Vigdergauz 2012a; 2012b; 2013]. In the current simulations the V -optimum relative deviations induced by doubling each size remain typically less than 0.6%, providing an acceptable compromise between accuracy and computational cost. For eliminating GA-related stochastic noise, all output data were computed several times, randomly starting each optimization process and stopping the evolution after a rather large number of iterations, when the fitness is deemed to converge.

5. Numerical results

The conducted GA simulations aim to numerically find the optimum, by (3-1) and (3-2), in the representative interval of the inclusion volume fraction c_1 at given phases’ moduli. In order to make the results more conclusive, we present, for comparison, four distinctive cases, namely the interchanged pairs of soft inclusions/hard matrix and hard inclusion/soft matrix, each under either shear or torsion load. The local moduli values are borrowed from [Greengard and Helsing 1998], as given in the previous section. The graphed results show the c_1 -dependent evolution of the V - and $\mu_{1,2}^*$ -optimal inclusion shapes, the corresponding $\mu_{1,2}^*(c_1)$ values, and, finally, the stress distributions along the V -optimal interfaces. For correct comparison we kept the same GA parameter values for all observations.

Figure 2 presents the computed $V(c_1)$ -optima for the chosen cases. It is of interest that the hard inclusion demonstrates the decreasing dependence of V on c_1 . As we shall see below, this is primarily due to narrowing the interval (1-3) between the extrema of the case-dominating tangential tractions $\sigma_{n\theta}$ with increasing c_1 rather than due to smoothing.

Figure 3 shows the $\mu_1^*(c_1)$ and $\mu_2^*(c_1)$ maxima against their V -optimal counterparts and those of the circular inclusions, all within the HS bounds (2-21).

Essentially, even the $\mu_{1,2}^*$ maxima appear to be rather far from the upper HS bound. This is particularly true of the second modulus μ_2^* . Similar μ^* -optimization results have been obtained in [Vigdergauz 2001] for a more simple limiting case of a perforated structure ($\mu_1 = 0$). Furthermore, V -optimization

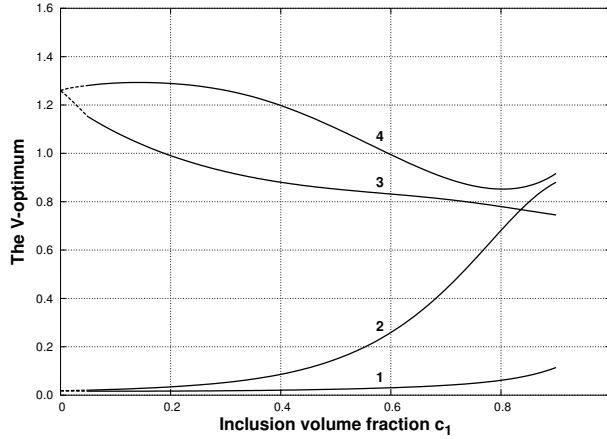


Figure 2. The $V(c_1)$ -optimum for the soft (1 and 2) and hard (3 and 4) inclusions under shear and torsion, respectively. The limiting values $V(0)$ (the dashed lines) are extrapolated from the computed interval $c \in [0.05; 0.9]$.

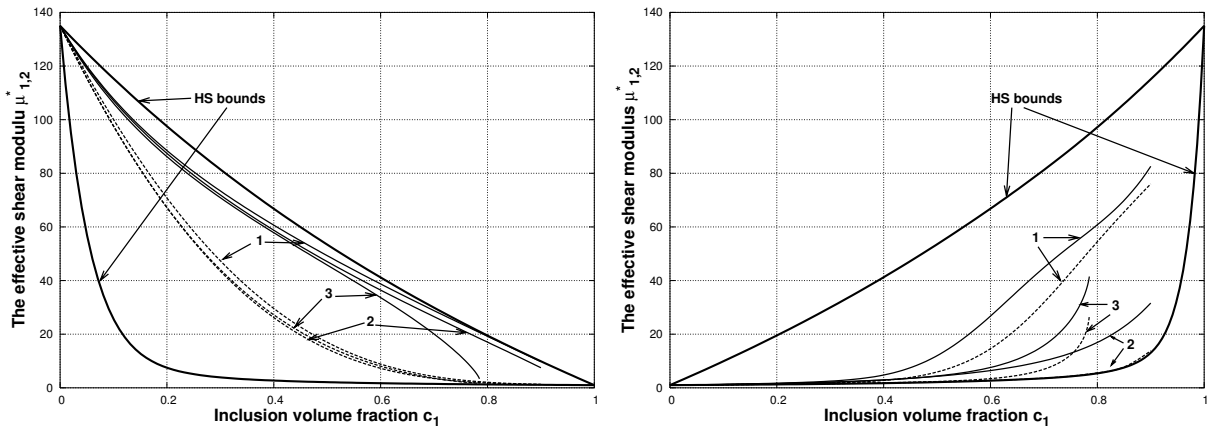


Figure 3. The soft (top) and hard (bottom) inclusions, for the effective shear moduli $\mu_1^*(c_1)$ and $\mu_2^*(c_1)$ (the dashed lines) within the HS bounds: optimum (1) and V -related values (2). The moduli for the circular inclusion (3) are also added for comparison.

is performed at the sacrifice of substantially decreased shear effective moduli, especially for the hard inclusion where the V -related modulus μ_2^* lies close to the HS lower bound. Moreover, in this case the V -related effective shear moduli are significantly less than even those for the circle (Figure 3, bottom). This is accounted for by affecting the V -performance of the inclusion shapes, as shown in Table 4. Since in both cases the tractions are monotone functions of the angle θ in the irreducible interval $[0, \pi/4]$ (see Figure 6 on page 101), V -optimization acts here by drastically diminishing their tangential components at the significant expense of much lower normal stresses, which enter into the criterion (1-2) with the same weight. Conceivably, the case-dependent weights for either component might improve the numerical sensitivity of the optimization scheme. This complication is, however, beyond the scope of this paper.

	V	μ_2^*	$\max(\sigma_{nn}(\theta))$	$\max(\sigma_{n\theta}(\theta))$
V-opt	0.801	4.342	0.373	0.634
Circle	1.205	6.654	0.190	1.544
Difference (%)	50.4	-53.2	49.0	-143.3

Table 4. The hard inclusion under torsion at $c_1 = 0.75$: comparison of the numerically obtained V -optimal values of K_e with those for the circular shape. The relative difference between each pair of counterparts with respect to the former is also added for convenience. Conforming with the symmetry relations (5-1b), $\min(\sigma_{nn}) = \min(\sigma_{n\theta}) = 0$.

Of special interest are the V and μ^* -optimal square-symmetric shapes compared in Figure 4 for discrete values of c_1 . In all instances, the μ^* -optimal inclusion shapes tend, as expected, to form nearly straight segments connecting distinct angular points. Their favorable role in maximizing the shear moduli

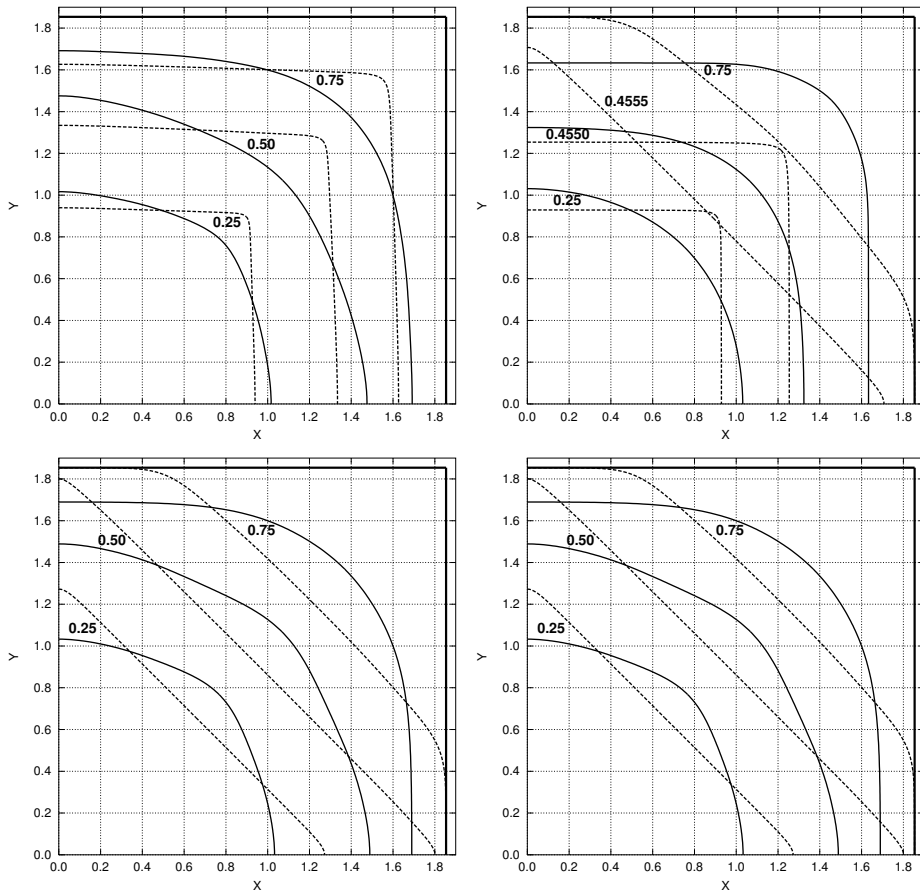


Figure 4. The soft (left) and the hard (right) inclusions under shear (the top two graphs) and torsion (the bottom two): evolution of the V - and μ^* -optimal (the dashed lines) shapes with increasing volume fraction c_1 .

was first numerically observed by Vigdergauz and Cherkayev [1986] and later analyzed in more depth [Cherkaev et al. 1998] for the simplest case of an isolated hole in a shear-loaded infinite plane. On the contrary, due to its smoothing nature, V -optimization rounds the inclusion shape. Furthermore, at any c_1 , the μ_1^* and μ_2^* -optimal soft inclusions differ from each other by rotation about the origin through 45° as caused by the different principal directions of the shear and torsion trial loads. For the μ^* -optimal holes this fact was indicated in [Vigdergauz 2001].

The μ_1^* -optimal hard inclusion behaves more complicatedly than the soft. It experiences a sudden rotation by 45° when evolving through the interval $c_1 \in [0.4550; 0.4555]$ (see the top right graph in Figure 4). This puzzling observation should be verified independently by other methods.

Finally, Figures 5 and 6 illustrate the angular distribution of the tractions and the induced hoop stresses along the irreducible part $0 \leq \theta \leq 45^\circ$ of the V -optimal interface. The symmetry relations (2-14) give the following locations of the distributions' zeros:

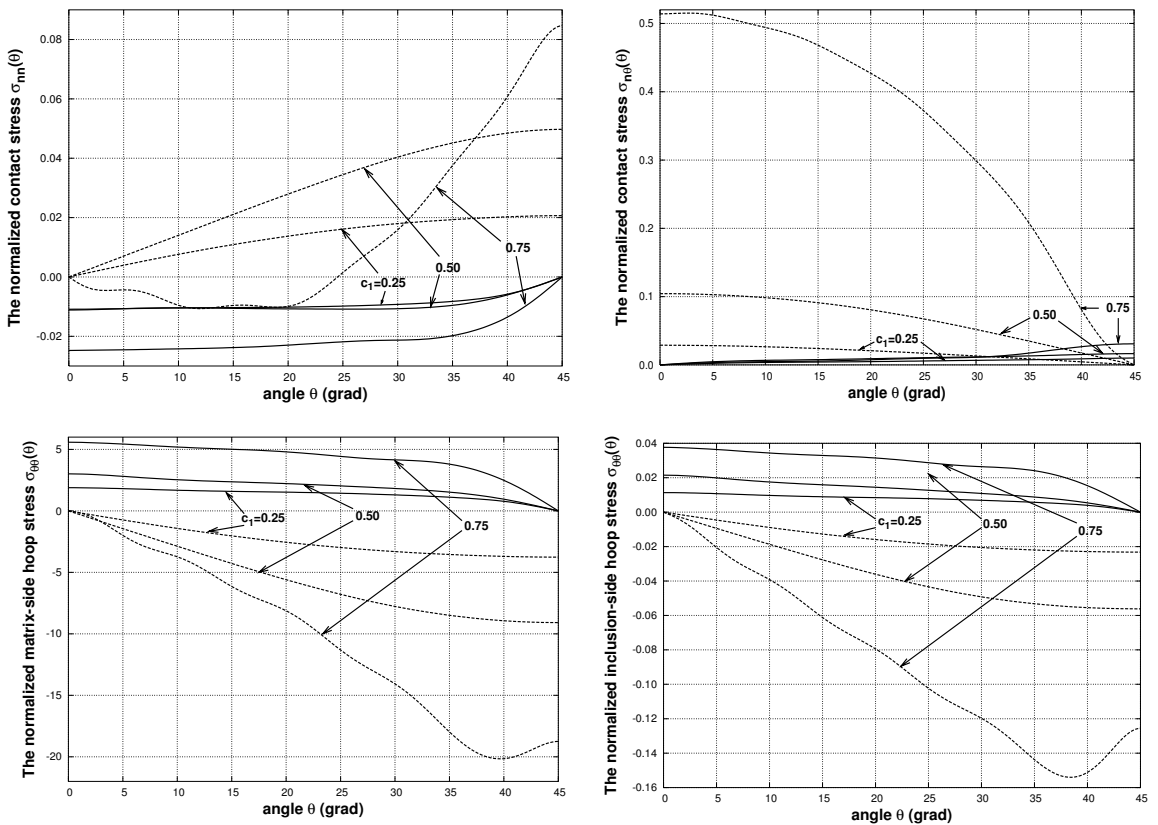


Figure 5. The boundary stresses for the V -optimal soft inclusion under shear and torsion (the dashed lines) for varying inclusion volume fraction c_1 : the normal contact traction (top left), tangential contact traction (top right), matrix-side hoop stress (bottom left), and inclusion-side hoop stress (bottom right).

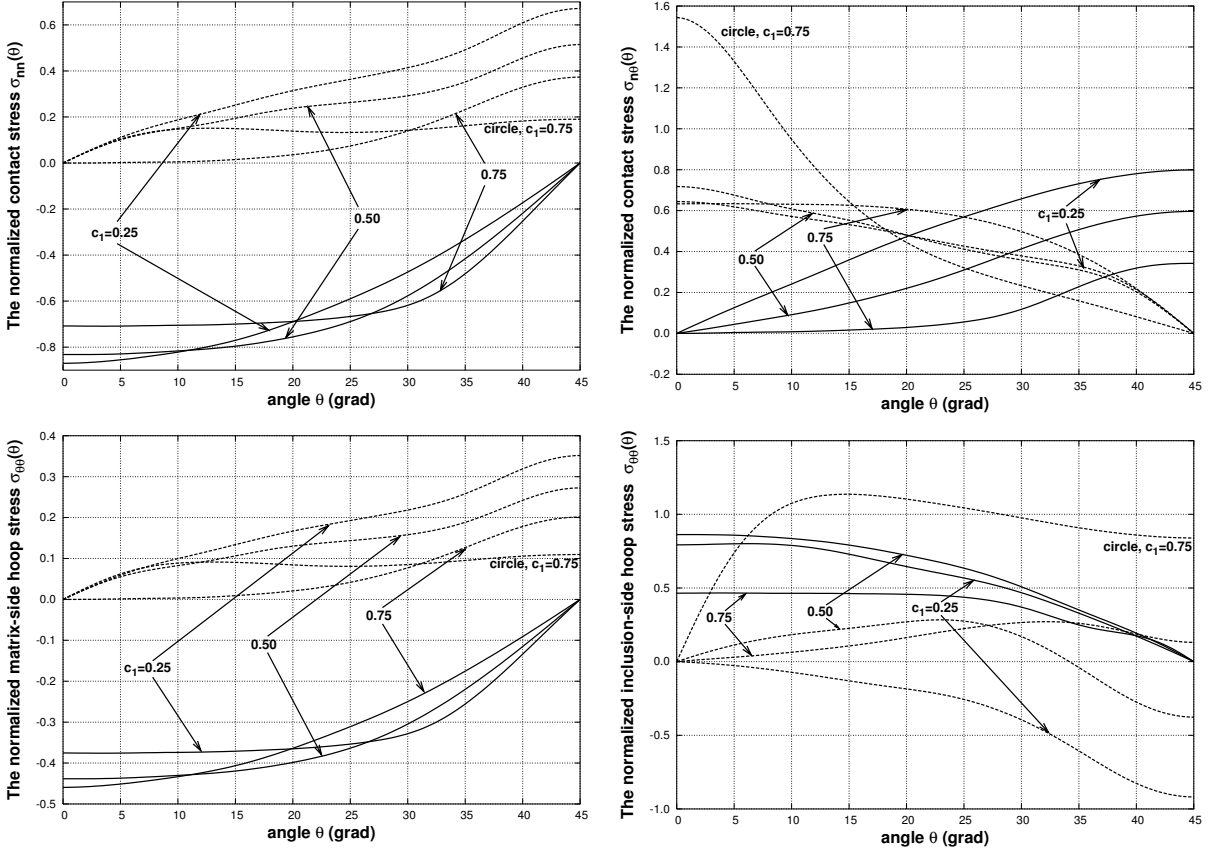


Figure 6. The boundary stresses for the V -optimal hard inclusion under shear and torsion (the dashed lines) with change in the inclusion volume fraction c_1 : the normal contact traction (top left), tangential contact traction (top right), matrix-side hoop stress (bottom left), and inclusion-side hoop stress (bottom right). Data for the circular hole at $c_1 = 0.75$ under torsion are also added for comparison.

$$\sigma_{nn}(\pi/4) = \sigma_{n\theta}(0) = \sigma_{\theta\theta}^{(m)}(\pi/4) = \sigma_{\theta\theta}^{(i)}(\pi/4) = 0 \quad \text{for shear,} \quad (5-1a)$$

$$\sigma_{nn}(0) = \sigma_{n\theta}(\pi/4) = \sigma_{\theta\theta}^{(m)}(0) = \sigma_{\theta\theta}^{(i)}(0) = 0 \quad \text{for torsion.} \quad (5-1b)$$

It should be borne in mind that the angle $\theta = \arctan(y/x) : t = x + iy \in L$ is measured in the physical plane rather than around the auxiliary unit circle γ . From these figures, one sees that none of the patterns show high-frequency oscillations. This is also true for the hoop stresses $\sigma_{\theta\theta}(\theta)$, which are not involved explicitly in the V -smoothing process.

In most cases, the boundary stresses are monotonic functions of the angle θ . The only exceptions are provided by the torsion for all stresses around the soft inclusion at $c_1 = 0.75$ and for the hard inclusion-side hoop stresses at any c_1 . Curiously the extremal values of the normal and tangential tractions around the hard inclusion under torsion and shear, respectively, decrease with increasing c_1 (see Figure 6). Both features are not V -specific since they also take place for the circle (not shown for better visibility).

6. Summary and future applications

The numerical V -optimization of the interface tractions is now extended to planar grained structures under shear and torsion loads. As explained in [Section 1](#), this loading case merits separate attention. The results obtained attest to the general applicability of the proposed V -criterion. Computationally, they are rather accurate, marking a sharp contrast with the biaxial mode, where the equistress principle permits one to simultaneously saturate the structurally independent HS upper K^* bound and the V -optimum by the same inclusions shapes. For clarity, we summarize the basic distinctions as follows.

- The V and μ^* -optimal inclusions significantly differ from each other in their shapes and orientations. The degree of dissimilarity depends on all the parameters involved: the load type, the relative inclusion rigidity, and its volume fraction.
- As a result, the corresponding shear moduli appear to be rather different, with the maximum being far from the upper HS bound. For bimaterial grained structures its unattainability was first proved by Allaire and Aubry [[1999](#)], if not earlier. Now some nontrivial quantitative characteristics of this phenomenon are also provided.
- Finally, the above-noted (see [Section 5](#)) dramatic rotation of the μ_1^* -optimal hard inclusion in passing the point $c_1 \approx 0.45525$ is well worth a further look and independent corroboration.

These observations stimulate similar investigations for V -optimal structures with badly ordered phases or with macroisotropy. In the latter case, it is of special interest to compare the numerical results with the corresponding phase-interchange analytical relations deduced by Gibiansky and Torquato [[1996](#)]. We hope to pursue both issues in further publications. It would also be interesting to study the V -criterion's performance for the weighted sums in (1-1), as mentioned in [Section 5](#). Due to the lack of analytical results, it would be prudent here to use a straightforward, numerical trial-and-error approach.

References

- [Abramowitz and Stegun 1965] M. Abramowitz and I. A. Stegun, *Handbook of mathematical functions, with formulas, graphs, and mathematical tables*, National Bureau of Standards Applied Mathematics Series **55**, Dover, New York, 1965.
- [Ahlfors 1978] L. V. Ahlfors, *Complex analysis*, 3rd ed., McGraw-Hill, New York, 1978.
- [Allaire and Aubry 1999] G. Allaire and S. Aubry, “On optimal microstructures for a plane shape optimization problem”, *Struct. Opt.* **17**:2-3 (1999), 86–94.
- [Berggren et al. 2001] S. A. Berggren, D. Lukkassen, A. Meidell, and L. Simula, “On stiffness properties of square honeycombs and other unidirectional composites”, *Compos. Part B-Eng.* **32**:6 (2001), 503–511.
- [Cherkaev et al. 1998] A. V. Cherkaev, Y. Grabovsky, A. B. Movchan, and S. K. Serkov, “The cavity of the optimal shape under the shear stresses”, *Int. J. Solids Struct.* **35**:33 (1998), 4391–4410.
- [Gakhov 1966] F. D. Gakhov, *Boundary value problems*, Pergamon, Oxford, 1966. Reprinted Dover, New York, 1990.
- [Gibiansky and Torquato 1996] L. V. Gibiansky and S. Torquato, “Phase-interchange relations for the elastic moduli of two-phase composites”, *Int. J. Eng. Sci.* **34**:7 (1996), 739–760.
- [Greengard and Helsing 1998] L. Greengard and J. Helsing, “On the numerical evaluation of elastostatic fields in locally isotropic two-dimensional composites”, *J. Mech. Phys. Solids* **46**:8 (1998), 1441–1462.
- [Lukkassen et al. 2012] D. Lukkassen, A. Meidell, and K. Pettersson, “An elementary proof of the Vigdergauz equations for a class of square symmetric structures”, preprint, 2012. [arXiv 1204.6419](https://arxiv.org/abs/1204.6419)
- [Milton 2002] G. W. Milton, *The theory of composites*, Cambridge Monographs on Applied and Computational Mathematics **6**, Cambridge University Press, 2002.

- [Muskhelishvili 1975] N. I. Muskhelishvili, *Some basic problems of the mathematical theory of elasticity*, 2nd ed., Noordhoff, Leyden, 1975.
- [Natanson 1955] I. P. Natanson, *Theory of functions of a real variable*, Frederick Ungar, New York, 1955.
- [Pólya and Szegő 1972] G. Pólya and G. Szegő, “Some geometrical aspects of complex variables, problem 108”, pp. 125–132 in *Problems and theorems in analysis, I: Series, integral calculus, theory of functions*, edited by G. Pólya and G. Szegő, Die Grundlehren der mathematischen Wissenschaften **193**, Springer, New York, 1972.
- [Vigdergauz 1999] S. Vigdergauz, “Complete elasticity solution to the stress problem in a planar grained structure”, *Math. Mech. Solids* **4**:4 (1999), 407–439.
- [Vigdergauz 2001] S. B. Vigdergauz, “The effective properties of a perforated elastic plate: Numerical optimization by genetic algorithm”, *Int. J. Solids Struct.* **38**:48–49 (2001), 8593–8616.
- [Vigdergauz 2012a] S. Vigdergauz, “Stress-smoothing holes in an elastic plate: From the square lattice to the checkerboard”, *Math. Mech. Solids* **17**:3 (2012), 289–299.
- [Vigdergauz 2012b] S. Vigdergauz, “Stress-smoothing holes in an elastic plate: The triangular checkerboard lattice of low symmetry”, *Math. Mech. Solids* **17**:6 (2012), 652–665.
- [Vigdergauz 2013] S. Vigdergauz, “A generalization of the equi-stress principle in optimizing the mechanical performance of two-dimensional grained composites”, *Math. Mech. Solids* **18**:4 (2013), 431–445.
- [Vigdergauz and Cherkayev 1986] S. B. Vigdergauz and A. V. Cherkayev, “A hole in a plate, optimal for its biaxial extension-compression”, *J. Appl. Math. Mech.* **50**:3 (1986), 401–404.

Received 15 Jul 2013. Revised 16 Oct 2013. Accepted 3 Dec 2013.

SHMUEL VIGDERGAUZ: vigd1805@013.net

Research and Development Division, The Israel Electric Corporation Ltd., P.O. Box 10, 1, Nativ-ha-Or, 31000 Haifa, Israel

CONTINUOUS CONTACT PROBLEM FOR TWO ELASTIC LAYERS RESTING ON AN ELASTIC HALF-INFINITE PLANE

ERDAL ÖNER AND AHMET BIRINCI

The continuous contact problem for two elastic layers resting on an elastic half-infinite plane and loaded by means of a rigid stamp is presented. The elastic layers have different heights and elastic constants. An external load is applied to the upper elastic layer by means of a rigid stamp. The problem is solved under the assumptions that all surfaces are frictionless, body forces of elastic layers are taken into account, and only compressive normal tractions can be transmitted through the interfaces. General expressions of stresses and displacements are obtained by using the fundamental equations of the theory of elasticity and the integral transform technique. Substituting the stress and the displacement expressions into the boundary conditions, the problem is reduced to a singular integral equation, in which the function of contact stresses under the rigid stamp is unknown. The integral equation is solved numerically by making use of the appropriate Gauss–Chebyshev integration formula for circular and rectangular stamp profiles. The contact stresses under the rigid stamp, contact areas, initial separation loads, and initial separation distances between the two elastic layers and the lower-layer elastic half-infinite plane are obtained numerically for various dimensionless quantities and shown in graphics and tables.

1. Introduction

Contact problems have been widely carried out in the literature. Their areas of application include pavements of highways and airfields, foundations, railway ballasts, foundation grillages, roller bearings, joints, and support elements (see, for example, [Garrido and Lorenzana 1998; Birinci and Erdöl 2001; Ozsahin 2007]). General methods for contact problems may be seen in [Hertz 1895; Galin 1961; Uffliand 1965]. Keer et al. [1972] analyzed the smooth receding contact problem between an elastic layer and a half-space formulated under the assumptions of plane stress, plane strain, and axisymmetric conditions. The plane smooth contact problem for an elastic layer lying on an elastic half-space with a compressive load applied to the layer through a frictionless rigid stamp was considered in [Ratwani and Erdogan 1973]. Civelek and Erdogan [1975] investigated the continuous and discontinuous contact problems between an elastic layer and a rigid half-plane for the case of a single load in tension. Geçit [1980] analyzed a tensionless contact without friction between an elastic layer and an elastic foundation. Geçit [1981] also studied the axisymmetric contact problem for an elastic layer and an elastic foundation. Çakıroğlu et al. [2001] analyzed the continuous and discontinuous contact problems of two elastic layers resting on an elastic semiinfinite plane. Dini and Nowell [2004] considered the problem of plane elastic contact between a thin strip and symmetric flat and rounded punches. El-Borgi et al. [2006] analyzed a receding contact plane problem between a functionally graded layer and a homogeneous substrate. The contact problem for multilayered composite structures was studied in [Ke and Wang 2006; 2007]. Kahya et al.

Keywords: continuous contact, elastic layer, integral equation, rigid stamp, theory of elasticity.

[2007] investigated a frictionless receding contact problem between an anisotropic elastic layer and an anisotropic elastic half-plane, when the two bodies were pressed together by means of a rigid circular stamp. A receding contact axisymmetric problem between a functionally graded layer and a homogeneous substrate was examined in [Rhimi et al. 2009]. Rhimi et al. [2011] studied a double receding contact axisymmetric problem between a functionally graded layer and a homogeneous substrate. A frictional contact problem for a rigid cylindrical stamp and an elastic layer resting on a half-plane was solved in [Çömez 2010]. Argatov and Mishuris [2010] examined an axisymmetric contact problem for a biphasic cartilage layer with allowance for tangential displacements on the contact surface. Chen et al. [2011] investigated the singular integral equation method for a contact problem of rigidly connected punches on an elastic half-plane. The contact problem for a layer was studied for the case when the elastic properties of the medium are arbitrary continuously differentiable functions of its thickness in Trubchik et al. [2011]. Adibnazari et al. [2012] investigated the contact of an asymmetrical rounded apex wedge with a half-plane. The two-dimensional contact problem of a rigid cylinder indenting an elastic half-space with surface tension was examined in [Long et al. 2012]. Aleksandrov [2012] solved the axisymmetric contact problem for a prestressed incompressible elastic layer. Chidlow et al. [2013] analyzed the two-dimensional solutions of both adhesive and nonadhesive contact problems involving functionally graded materials. Kumar and DasGupta [2012] studied the mechanics of contact of an inflated spherical nonlinear hyperelastic membrane pressed between two rigid plates. A quadratic boundary element formulation for continuously nonhomogeneous, isotropic, and linear elastic functionally graded material contact problems was carried out in Gun and Gao [2014]. Vollebregt [2014] presented a new solver, called BCCG+FAI, for solving elastic normal contact problems.

Although there is much research available in the literature related to contact problems of multiple layers and half-planes, there are not enough studies about initial separation loads and distances in contact mechanics. This paper aims to obtain initial separation loads and initial separation distances between two layers and a lower-layer elastic half-plane for a continuous contact problem. This paper also presents the contact stresses under the rigid stamp, and the contact areas.

2. General expressions for stresses and displacements

Figure 1 shows two elastic, homogeneous, isotropic layers with different elastic constants and heights, resting on an elastic half-infinite plane and subjected to a concentrated load with magnitude P by means of a rigid stamp. The thickness in the z direction is taken to be unit. Since $x = 0$ is the symmetry plane, it is sufficient to consider the problem in the region $0 \leq x < \infty$ only. For numerical calculations, two types of stamp profiles are used, circular and rectangular.

Consider a plane strain problem and let $\rho_1 g$ and $\rho_2 g$ be body forces acting vertically in the layers. The body force of the elastic half-infinite plane is neglected. The stress and the displacement components may be obtained as

$$u_i(x, y) = u_{ip}(x) + u_{ih}(x, y), \quad (1a)$$

$$v_i(x, y) = v_{ip}(y) + v_{ih}(x, y), \quad (1b)$$

$$\sigma_{ix}(x, y) = \sigma_{ixp}(y) + \sigma_{ixh}(x, y), \quad (2a)$$

$$\sigma_{iy}(x, y) = \sigma_{iyp}(y) + \sigma_{iyh}(x, y), \quad (2b)$$

$$\tau_{ixy}(x, y) = \tau_{ixyh}(x, y), \quad (2c)$$

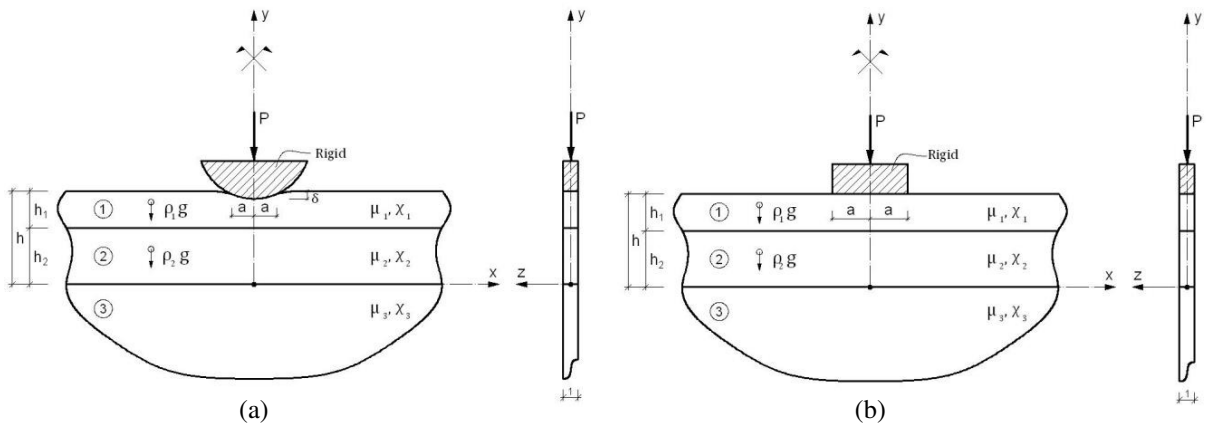


Figure 1. Geometry of the problem and loading condition. (a) Circular and (b) rectangular stamp cases.

where $i = 1, 2, 3$, the subscripts p and h refer to the particular part of the stress and the displacement components corresponding only to existing body forces, and the components of displacements and stresses for the layers and half-infinite plane without body forces, respectively. The particular part of the stress and the displacement components corresponding to ρ_1g and ρ_2g for the layers and the elastic half-infinite plane may be obtained as [Çakiroğlu 1990]

$$u_{1p}(x) = \left(\frac{3 - \chi_1}{8\mu_1} \right) \left(\frac{\rho_1gh_1}{2} \right) x, \quad (3a)$$

$$v_{1p}(y) = -\frac{\rho_1gy}{2\mu_1} \left[\frac{1 + \chi_1}{8} h_1 + \frac{\chi_1 - 1}{\chi_1 + 1} (h_2 + h - y) \right], \quad (3b)$$

$$u_{2p}(x) = \left(\frac{3 - \chi_2}{8\mu_2} \right) \left(\frac{\rho_2gh_2}{2} + \rho_1gh_1 \right) x, \quad (3c)$$

$$v_{2p}(y) = \frac{\chi_2 - 1}{\chi_2 + 1} \frac{\rho_2gy}{2\mu_2} (y - h_2) - \frac{1 + \chi_2}{8\mu_2} y \left(\rho_1gh_1 + \rho_2g \frac{h_2}{2} \right), \quad (3d)$$

$$u_{3p}(x) = \left(\frac{3 - \chi_3}{8\mu_3} \right) (\rho_2gh_2 + \rho_1gh_1) x, \quad (3e)$$

$$v_{3p}(y) = -\frac{1 + \chi_3}{8\mu_3} (\rho_1gh_1 + \rho_2gh_2) y, \quad (3f)$$

$$\sigma_{1xp}(y) = \frac{3 - \chi_1}{1 + \chi_1} \frac{\rho_1g}{2} (2y - h - h_2), \quad (3g)$$

$$\sigma_{1yp}(y) = \rho_1g(y - h), \quad (3h)$$

$$\sigma_{2xp}(y) = \frac{3 - \chi_2}{1 + \chi_2} \frac{\rho_2g}{2} (2y - h_2), \quad (3i)$$

$$\sigma_{2yp}(y) = -\rho_1gh_1 + \rho_2g(y - h_2), \quad (3j)$$

$$\sigma_{3yp}(y) = -(\rho_1gh_1 + \rho_2gh_2), \quad (3k)$$

$$\sigma_{3xp} = \tau_{1xyp} = \tau_{2xyp} = \tau_{3xyp} = 0, \quad (3l)$$

where $u = u(x, y)$ and $v = v(x, y)$ represent displacement components in the x and y directions, respectively; μ_i is the shear modulus, χ_i is an elastic constant, with $\chi_i = (3 - 4\nu_i)$ for plane strain, and ν_i is the Poisson's ratio ($i = 1, \dots, 3$). The subscripts 1, 2, and 3 refer to the upper layer, the lower layer, and the elastic half-infinite plane, respectively.

The components of the displacements and stresses for the layers and the half-infinite plane without body forces may be expressed as follows [Çakıroğlu 1990]:

$$u_{ih}(x, y) = \frac{2}{\pi} \int_0^\infty \{[A_i + B_i y]e^{-\alpha y} + [C_i + D_i y]e^{\alpha y}\} \sin(\alpha x) d\alpha, \quad (4a)$$

$$v_{ih}(x, y) = \frac{2}{\pi} \int_0^\infty \left\{ \left[A_i + B_i \left(\frac{\chi_i}{\alpha} + y \right) \right] e^{-\alpha y} + \left[-C_i + D_i \left(\frac{\chi_i}{\alpha} - y \right) \right] e^{\alpha y} \right\} \cos(\alpha x) d\alpha, \quad (4b)$$

$$\begin{aligned} \frac{1}{2\mu_i} \sigma_{ixh}(x, y) = \frac{2}{\pi} \int_0^\infty \left\{ \left[\alpha(A_i + B_i y) - \left(\frac{3 - \chi_i}{2} \right) B_i \right] e^{-\alpha y} \right. \\ \left. + \left[\alpha(C_i + D_i y) + \left(\frac{3 - \chi_i}{2} \right) D_i \right] e^{\alpha y} \right\} \cos(\alpha x) d\alpha, \end{aligned} \quad (4c)$$

$$\begin{aligned} \frac{1}{2\mu_i} \sigma_{iyh}(x, y) = \frac{2}{\pi} \int_0^\infty \left\{ - \left[\alpha(A_i + B_i y) + \left(\frac{1 + \chi_i}{2} \right) B_i \right] e^{-\alpha y} \right. \\ \left. + \left[-\alpha(C_i + D_i y) + \left(\frac{1 + \chi_i}{2} \right) D_i \right] e^{\alpha y} \right\} \cos(\alpha x) d\alpha, \end{aligned} \quad (4d)$$

$$\begin{aligned} \frac{1}{2\mu_i} \tau_{ixyh}(x, y) = \frac{2}{\pi} \int_0^\infty \left\{ - \left[\alpha(A_i + B_i y) + \left(\frac{\chi_i - 1}{2} \right) B_i \right] e^{-\alpha y} \right. \\ \left. + \left[\alpha(C_i + D_i y) - \left(\frac{\chi_i - 1}{2} \right) D_i \right] e^{\alpha y} \right\} \sin(\alpha x) d\alpha, \end{aligned} \quad (4e)$$

$$u_{3h}(x, y) = \frac{2}{\pi} \int_0^\infty \{[C_3 + D_3 y]e^{\alpha y}\} \sin(\alpha x) d\alpha, \quad (4f)$$

$$v_{3h}(x, y) = \frac{2}{\pi} \int_0^\infty \left\{ \left[-C_3 + D_3 \left(\frac{\chi_3}{\alpha} - y \right) \right] e^{\alpha y} \right\} \cos(\alpha x) d\alpha, \quad (4g)$$

$$\frac{1}{2\mu_3} \sigma_{3xh}(x, y) = \frac{2}{\pi} \int_0^\infty \left\{ \left[\alpha(C_3 + D_3 y) + \left(\frac{3 - \chi_3}{2} \right) D_3 \right] e^{\alpha y} \right\} \cos(\alpha x) d\alpha, \quad (4h)$$

$$\frac{1}{2\mu_3} \sigma_{3yh}(x, y) = \frac{2}{\pi} \int_0^\infty \left\{ \left[-\alpha(C_3 + D_3 y) + \left(\frac{1 + \chi_3}{2} \right) D_3 \right] e^{\alpha y} \right\} \cos(\alpha x) d\alpha, \quad (4i)$$

$$\frac{1}{2\mu_3} \tau_{3xyh}(x, y) = \frac{2}{\pi} \int_0^\infty \left\{ \left[\alpha(C_3 + D_3 y) - \left(\frac{\chi_3 - 1}{2} \right) D_3 \right] e^{\alpha y} \right\} \sin(\alpha x) d\alpha, \quad (4j)$$

where A_i, B_i, C_i, D_i ($i = 1, 2$) and C_3, D_3 are unknown coefficients which will be determined from the boundary conditions prescribed for $y = 0$, $y = h_2$, and $y = h$.

3. Boundary conditions and solution of the singular integral equation

The continuous contact problem for two elastic layers resting on an elastic half-infinite plane and subjected to a concentrated load with magnitude P by means of a rigid stamp will be investigated. The contact stresses under the rigid stamp, the contact areas, the distribution of the contact stresses between

the layers and the lower-layer half-infinite plane until the occurrence of the initial separation, the initial separation loads, and the initial separation distances will be examined.

The boundary conditions for the frictionless contact problem outlined above can be defined as follows:

$$\tau_{1xy}(x, h) = 0, \quad 0 \leq x < \infty, \quad (5a)$$

$$\sigma_{1y}(x, h) = \begin{cases} -p(x), & 0 \leq x < a, \\ 0, & a \leq x < \infty, \end{cases} \quad (5b)$$

$$\tau_{1xy}(x, h_2) = 0, \quad 0 \leq x < \infty, \quad (5c)$$

$$\tau_{2xy}(x, h_2) = 0, \quad 0 \leq x < \infty, \quad (5d)$$

$$\sigma_{1y}(x, h_2) = \sigma_{2y}(x, h_2), \quad 0 \leq x < \infty, \quad (5e)$$

$$\frac{\partial}{\partial x}[v_1(x, h_2) - v_2(x, h_2)] = 0, \quad 0 \leq x < \infty, \quad (5f)$$

$$\tau_{2xy}(x, 0) = 0, \quad 0 \leq x < \infty, \quad (5g)$$

$$\tau_{3xy}(x, 0) = 0, \quad 0 \leq x < \infty, \quad (5h)$$

$$\sigma_{2y}(x, 0) = \sigma_{3y}(x, 0), \quad 0 \leq x < \infty, \quad (5i)$$

$$\frac{\partial}{\partial x}[v_2(x, 0) - v_3(x, 0)] = 0, \quad 0 \leq x < \infty, \quad (5j)$$

$$\frac{\partial}{\partial x}[v_1(x, h)] = f(x), \quad 0 \leq x < a, \quad (5k)$$

where a is the half-width of the contact area between the rigid stamp and the upper layer, $p(x)$ is the unknown contact stress under the rigid stamp, and $f(x)$ is the derivative of the function $F(x)$ which characterizes profile of the rigid stamp. In the case of a circular stamp, $f(x)$ can be obtained as follows:

$$F(x) = h - \delta - [(R^2 - x^2)^{1/2} - R], \quad (6a)$$

$$f(x) = \frac{d}{dx}[F(x)] = -\frac{x}{(R^2 - x^2)^{1/2}}, \quad (6b)$$

where δ is the maximum displacement, which occurs on the layer under the stamp on the axis of symmetry ($x = 0$), and R is the radius of the rigid circular stamp.

In the case of rectangular stamp, because $F(x)$ is equal to a constant, $f(x)$ can be obtained as follows:

$$f(x) = \frac{d}{dx}[F(x)] = 0. \quad (6c)$$

Applying the boundary conditions (5a)–(5j) to the stress and displacement expressions, the coefficients A_i , B_i , C_i , D_i ($i = 1, 2$), C_3 , and D_3 can be determined in terms of the unknown contact stress $p(x)$; by substituting these coefficients into (5k), after some routine manipulations and using the symmetry condition $p(x) = p(-x)$, one may obtain the following singular integral equation for $p(x)$:

$$\int_{-a}^a \left[\frac{1}{t-x} + k(x, t) \right] p(t) dt = -\frac{4\pi\mu_1}{1+\chi_1} f(x), \quad -a < x < a, \quad (7)$$

where the kernel $k(x, t)$ is given by (A.1). The equilibrium condition of the problem may be expressed as

$$\int_{-a}^a p(t) dt = P. \quad (8)$$

In order to obtain the initial separation load and initial separation distance between the two elastic layers and the lower-layer half-infinite plane, the contact stresses $\sigma_{1y}(x, h_2)$ and $\sigma_{2y}(x, 0)$ need to be determined. Substituting the values of A_i , B_i , C_i , and D_i ($i = 1, 2$) as evaluated in terms of $p(x)$ into (2b) and after some algebraic manipulation, the contact stresses are obtained as follows:

$$\sigma_{1y}(x, h_2) = -\rho_1 g h_1 - \frac{1}{\pi h} \int_{-a}^a k_2^*(x, t) p(t) dt, \quad 0 \leq x < \infty, \quad (9a)$$

$$\sigma_{2y}(x, 0) = -\rho_1 g h_1 \left[1 + \frac{\rho_2 h_2}{\rho_1 h_1} \right] - \frac{\mu_2}{\mu_1} \frac{1}{\pi h} \int_{-a}^a k_3^*(x, t) p(t) dt, \quad 0 \leq x < \infty, \quad (9b)$$

where the kernels $k_2^*(x, t)$ and $k_3^*(x, t)$ are given by (A.2) and (A.3). In order to simplify the solution of the singular integral equation, the following dimensionless quantities are introduced:

$$x = as, \quad t = ar, \quad \phi(r) = \frac{p(ar)}{P/h}, \quad M(s) = \frac{m(as)}{P/h}, \quad m(as) = -\frac{4\pi\mu_1}{1 + \chi_1} f(as). \quad (10)$$

Substituting from (10), then (7), (8), (9a), and (9b) may be obtained as follows:

$$\int_{-1}^1 \left[\frac{1}{r-s} + N(s, r) \right] \phi(r) dr = M(s), \quad -1 < s < 1, \quad N(s, r) = ak(as, ar), \quad (11a)$$

$$\frac{a}{h} \int_{-1}^1 \phi(r) dr = 1, \quad (11b)$$

$$\frac{\sigma_{1y}(x, h_2)}{P/h} = -\frac{1}{\lambda} - \frac{1}{\pi} \frac{a}{h} \int_{-1}^1 k_2(x, ar) \Phi(r) dr, \quad 0 \leq x < \infty, \quad (11c)$$

$$\frac{\sigma_{2y}(x, 0)}{P/h} = -\frac{1}{\lambda} \left[1 + \frac{\rho_2 h_2}{\rho_1 h_1} \right] - \frac{\mu_2}{\mu_1} \frac{1}{\pi} \frac{a}{h} \int_{-1}^1 k_3(x, ar) \Phi(r) dr, \quad 0 \leq x < \infty, \quad (11d)$$

where λ is called the load factor, and defined as

$$\lambda = \frac{P}{\rho_1 g h h_1}. \quad (12)$$

3.1. Circular stamp case. The contact stress $p(x)$ vanishes at the ends because of the smooth contact at the end points, and therefore the index of the integral equation (11a) is -1 . Noting this, the solution of integral equation can be found as follows [Erdogan and Gupta 1972]:

$$\phi(r) = g(r)(1 - r^2)^{1/2}, \quad -1 < r < 1. \quad (13)$$

Using the appropriate Gauss–Chebyshev integration formula, (11a) and (11b) may be reduced to the following forms:

$$\sum_{i=1}^n (1 - r_i^2) \left[\frac{1}{r_i - s_j} + N(s_j, r_i) \right] g(r_i) = \frac{n+1}{\pi} M(s_j), \quad j = 1, \dots, n+1, \quad (14)$$

$$\frac{a}{h} \sum_{i=1}^n (1 - r_i^2) g(r_i) = \frac{n+1}{\pi},$$

where

$$r_i = \cos\left(\frac{i\pi}{n+1}\right), \quad i = 1, \dots, n, \quad (15a)$$

$$s_j = \cos\left(\frac{2j-1}{n+1} \frac{\pi}{2}\right), \quad j = 1, \dots, n+1. \quad (15b)$$

The extra equation in (14) corresponds to the consistency condition of the original integral equation in (11a). In this case, the $(n+1/2)$ -th equation in (14) is satisfied automatically. Hence, the equations in (14) constitute a system of $n+1$ equations for $n+1$ unknowns. Note that the system is highly nonlinear in a and an interpolation scheme is required to determine this unknown. Solving this system of equations and using (13), $\phi(r)$, the normalized contact stress distribution, and a half-width of the contact area are obtained. By using (13), substituting the results into (11c) and (11d) and using the Gauss integration formula, the contact stresses $\sigma_{1y}(x, h_2)$ and $\sigma_{2y}(x, 0)$ are determined. In order to be valid for the singular integral equation given in (11a), the contact stresses $\sigma_{1y}(x, h_2)$ and $\sigma_{2y}(x, 0)$ must be compressive everywhere and no sign changing is allowed. So, the critical load value can be calculated numerically by equating (11c) and (11d) to zero. Then λ_{cr} (the initial separation load) and x_{cr} (the initial separation distance) can be obtained.

3.2. Rectangular stamp case. Since the contact stress under the rigid stamp goes to infinity at the corners, that is, $g(\pm 1) \rightarrow \infty$, the index of the singular integral equation is $+1$. Assuming the solution of integral equation as [Erdogan and Gupta 1972]

$$\phi(r) = g(r)(1-r^2)^{-1/2}, \quad -1 < r < 1, \quad (16a)$$

and using the appropriate Gauss–Chebyshev integration formula, (11a) and (11b) may then be replaced by

$$\sum_{i=1}^n W_i \left(\frac{1}{r_i - s_j} + N(s_j, r_i) \right) g(r_i) = 0, \quad j = 1, \dots, n-1, \quad (16b)$$

$$\frac{a}{h} \sum_{i=1}^n W_i g(r_i) = 1, \quad (16c)$$

where

$$W_1 = W_n = \frac{\pi}{2n-2}, \quad W_i = \frac{\pi}{n-1}, \quad i = 2, \dots, n-1, \quad (16d)$$

$$r_i = \cos\left(\frac{i-1}{n-1}\pi\right), \quad i = 1, \dots, n, \quad (16e)$$

$$s_j = \cos\left(\frac{2j-1}{n-1} \frac{\pi}{2}\right), \quad j = 1, \dots, n-1. \quad (16f)$$

Equations (16b) and (16c) constitute n linear algebraic equations for n unknowns, $g(r_i)$, $i = 1, \dots, n$. Solution of these algebraic equations and use of (16a) gives the unknown contact stress function under the rigid stamp, $p(x)$. In order to obtain the initial separation load and distance in the case of a rectangular stamp, the same method as in the case of the circular stamp is followed.

4. Results and discussion

Some of the calculated results obtained from the solution of the continuous contact problem described in the previous sections for various dimensionless quantities such as R/h , $\mu_1/(P/h)$, μ_2/μ_1 , and μ_3/μ_2 are shown in Tables 1–5 and Figures 2–6. Table 1 and Figure 2 show the variation of the half-width of the contact area for a circular stamp with $\mu_1/(P/h)$ and R/h . As it can be seen in Table 1 and Figure 2, the half-width of the contact area a/h increases with increasing R/h , but decreases with increasing load ratio $\mu_1/(P/h)$. The variation of the contact stress under the rigid stamp for a rectangular stamp with μ_2/μ_1 is given in Figure 3. It may be observed in this figure that as μ_2/μ_1 increases, the normalized contact stress increases in the interior region of the rigid stamp and decreases in the region close to the corners. Figure 4 shows the variation of the contact stress distribution under a rigid circular stamp with μ_2/μ_1 . It appears that the maximum value of the contact stress is always at $x = 0$, and it increases with increasing μ_2/μ_1 .

In Figure 5, the contact stress distribution under the rectangular stamp is given. As expected, the contact stresses become infinite at the corners of the stamp. The normalized contact stress increases with decreasing (a/h) . Variation of the initial separation load λ_{cr} and the initial separation distance x_{cr} between the layers and the lower-layer half-infinite plane with μ_2/μ_1 for various values of μ_3/μ_2 in case

$\mu_1/(P/h)$	a/h						
	$R/h=10$	$R/h=50$	$R/h=100$	$R/h=250$	$R/h=500$	$R/h=750$	$R/h=1000$
10	0.6541	1.3043	1.7382	2.5392	3.3912	4.0241	4.5486
50	0.3069	0.6541	0.8861	1.3043	1.7382	2.0552	2.3149
100	0.21806	0.4762	0.6541	0.9747	1.3043	1.5433	1.7382
250	0.13815	0.3069	0.4287	0.6541	0.8861	1.0529	1.1883
500	0.0977	0.21806	0.3069	0.4762	0.6541	0.7822	0.8861
750	0.07978	0.17824	0.25142	0.39304	0.5442	0.6541	0.7429
1000	0.0691	0.15443	0.21806	0.3421	0.4762	0.5743	0.6541

Table 1. Variation of the half-width of the contact area for a circular stamp with $\mu_1/(P/h)$ and R/h ($\chi_1 = \chi_2 = \chi_3 = 2$, $h_2/h_1 = 1$, $\mu_2/\mu_1 = 2$, and $\mu_3/\mu_2 = 2$).

μ_2/μ_1	$\mu_3/\mu_2 = 0.5$		$\mu_3/\mu_2 = 1$		$\mu_3/\mu_2 = 2$	
	x_{cr}	λ_{cr}	x_{cr}	λ_{cr}	x_{cr}	λ_{cr}
0.1	4.10	166.95	3.31	118.343	2.80	83.5115
0.25	3.10	139.777	2.53	99.2449	2.17	69.8606
0.5	2.59	139.172	2.11	94.9923	1.82	64.8572
4	1.21	96.3381	1.16	55.4769	1.13	42.5852
10	1.04	43.3536	1.03	37.0934	1.02	33.6179
50	0.97	29.9315	0.97	29.1694	0.97	28.6559

Table 2. Variation of the initial separation load λ_{cr} and the initial separation distance x_{cr} between layers for a circular stamp with μ_2/μ_1 and μ_3/μ_2 ($\chi_1 = \chi_2 = \chi_3 = 2$, $h_2/h_1 = 1$, $R/h = 100$, $\mu_1/(P/h) = 500$, and $\rho_2/\rho_1 = 1$).

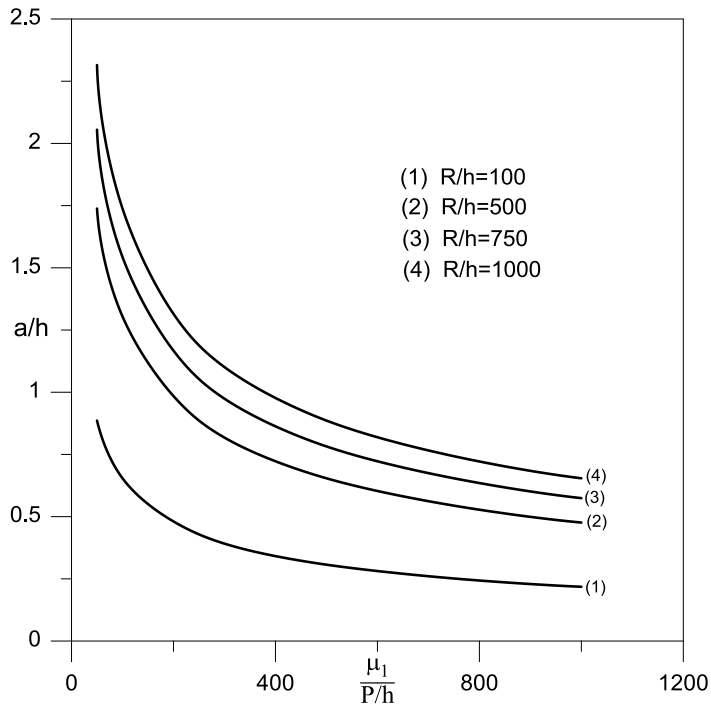


Figure 2. Variation of the half-width of the contact area for a circular stamp with $\mu_1/(P/h)$ ($\chi_1 = \chi_2 = \chi_3 = 2$, $h_2/h_1 = 1$, $\mu_2/\mu_1 = 2$, and $\mu_3/\mu_2 = 2$).

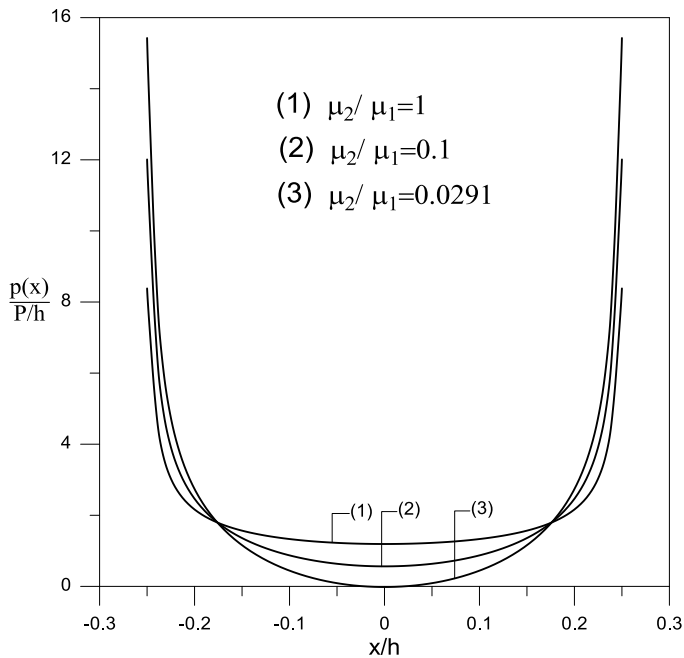


Figure 3. Variation of the contact stress distribution under the rigid stamp for a rectangular stamp with μ_2/μ_1 ($\chi_1 = \chi_2 = \chi_3 = 2$, $h_2/h_1 = 1$, $a/h = 0.7$, and $\mu_3/\mu_2 = 1$).

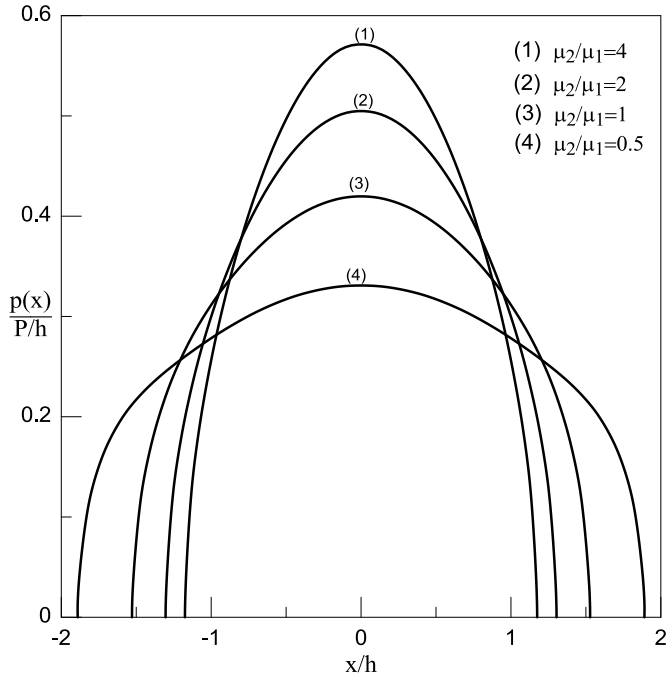


Figure 4. Variation of the contact stress distribution under the rigid stamp for a circular stamp with μ_2/μ_1 ($\chi_1 = \chi_2 = \chi_3 = 2$, $h_2/h_1 = 1$, $\mu_3/\mu_2 = 2$, $R/h = 500$, and $\mu_1(P/h) = 100$).

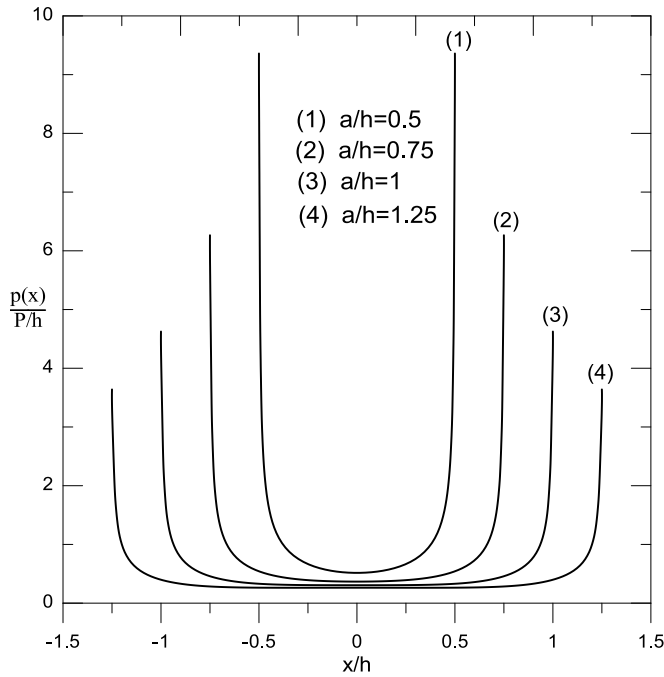


Figure 5. Variation of the contact stress distribution under the rigid stamp for a rectangular stamp with a/h ($\chi_1 = \chi_2 = \chi_3 = 2$, $h_2/h_1 = 1$, $\mu_3/\mu_2 = 1$, and $\mu_2/\mu_1 = 1$).

μ_2/μ_1	$\mu_3/\mu_2 = 0.5$		$\mu_3/\mu_2 = 1$		$\mu_3/\mu_2 = 2$	
	x_{cr}	λ_{cr}	x_{cr}	λ_{cr}	x_{cr}	λ_{cr}
0.1	4.11	306.572	3.32	219.487	2.81	156.831
0.25	3.11	229.880	2.55	167.793	2.19	121.864
0.5	2.61	195.927	2.15	142.534	1.86	103.65
4	1.92	150.064	1.58	102.83	1.40	73.6904
10	1.82	143.238	1.51	96.6480	1.34	69.1730
50	1.77	139.115	1.47	92.8876	1.30	67.53

Table 3. Variation of the initial separation load λ_{cr} and the initial separation distance x_{cr} between the lower layer and the elastic half-infinite plane for a circular stamp with μ_2/μ_1 and μ_3/μ_2 ($\chi_1 = \chi_2 = \chi_3 = 2$, $h_2/h_1 = 1$, $R/h = 100$, $\mu_1/(P/h) = 500$, and $\rho_2/\rho_1 = 1$).

μ_2/μ_1	$\mu_3/\mu_2 = 0.5$		$\mu_3/\mu_2 = 1$		$\mu_3/\mu_2 = 2$	
	x_{cr}	λ_{cr}	x_{cr}	λ_{cr}	x_{cr}	λ_{cr}
0.1	3.76	91.2134	3.64	76.8386	3.16	35.5079
0.25	3.44	87.0030	2.91	63.6723	2.56	32.8831
0.5	2.98	80.4193	2.50	54.4106	2.22	32.6244
1	2.57	70.5130	2.15	46.2382	1.94	32.5297
4	1.67	49.8831	1.61	32.118	1.58	26.0751
10	1.51	27.9614	1.50	24.2309	1.49	22.3332

Table 4. Variation of the initial separation load λ_{cr} and the initial separation distance x_{cr} between layers for a rectangular stamp with μ_2/μ_1 and μ_3/μ_2 ($\chi_1 = \chi_2 = \chi_3 = 2$, $h_2/h_1 = 1$, $a/h = 0.7$, and $\rho_2/\rho_1 = 1$).

μ_2/μ_1	$\mu_3/\mu_2 = 0.5$		$\mu_3/\mu_2 = 1$		$\mu_3/\mu_2 = 2$	
	x_{cr}	λ_{cr}	x_{cr}	λ_{cr}	x_{cr}	λ_{cr}
0.1	3.86	96.1742	3.65	86.8571	3.17	66.6502
0.25	3.47	93.7733	2.93	73.7035	2.59	57.2691
0.5	2.99	84.9483	2.55	66.6905	2.27	52.1141
1	2.65	78.6212	2.28	61.3007	2.05	48.06
4	2.29	70.7674	1.99	54.4808	1.82	43.0774
10	2.19	68.2357	1.91	52.4519	1.76	41.6836

Table 5. Variation of the initial separation load λ_{cr} and the initial separation distance x_{cr} between the lower layer and the elastic half-infinite plane for a rectangular stamp with μ_2/μ_1 and μ_3/μ_2 ($\chi_1 = \chi_2 = \chi_3 = 2$, $h_2/h_1 = 1$, $a/h = 0.7$, and $\rho_2/\rho_1 = 1$).

of a circular stamp is given in Tables 2 and 3. As it can be seen in these tables, the initial separation load and distance between the layers and the lower-layer half-infinite plane decrease with increasing μ_2/μ_1 and μ_3/μ_2 .

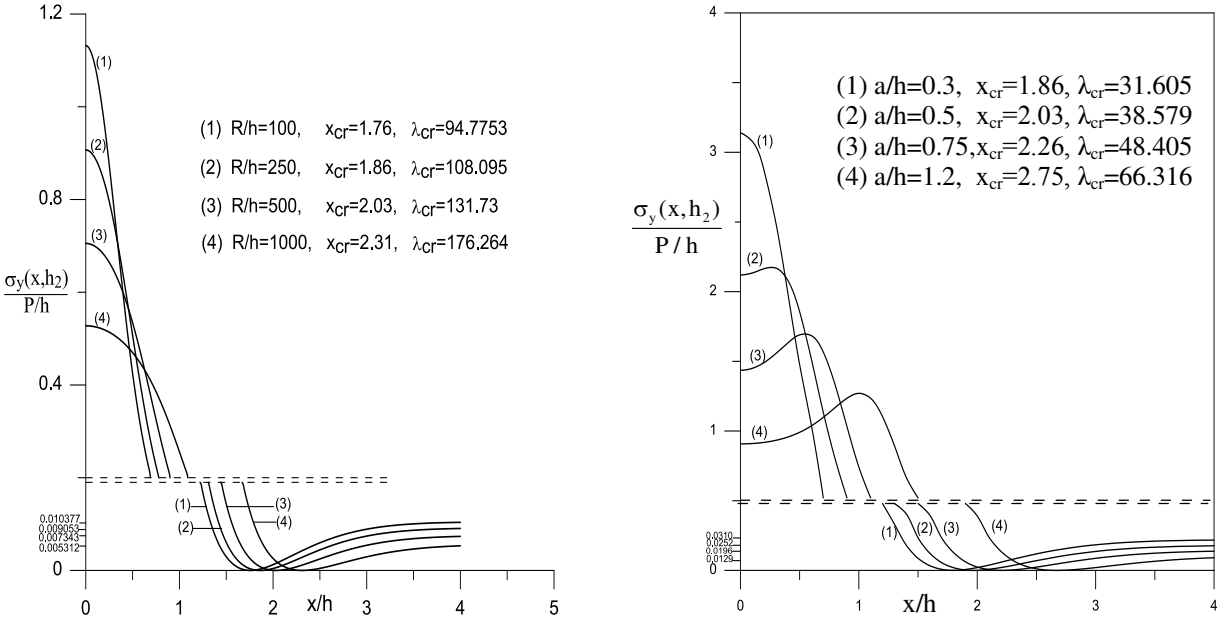


Figure 6. Variation of the contact stress distribution between two elastic layers. Left: variation with R/h for a circular stamp with $\chi_1 = \chi_2 = \chi_3 = 2$, $\mu_1/(P/h) = 500$, $h_2/h_1 = 1$, $\mu_2/\mu_1 = 2$, $\mu_3/\mu_2 = 2$, and $\rho_2/\rho_1 = 1$. Right: Variation with a/h for a rectangular stamp with $\chi_1 = \chi_2 = \chi_3 = 2$, $h_2/h_1 = 1$, $\mu_2/\mu_1 = 1$, $\mu_3/\mu_2 = 1$, and $\rho_2/\rho_1 = 1$.

Figure 6, left, shows the variation of the initial separation load and the initial separation distance between layers for a circular stamp with R/h . It appears that the initial separation load and the initial separation distance increase with increasing R/h . The variation of the initial separation load and the initial separation distance between layers for a rectangular stamp with a/h is shown in Figure 6, right. It appears that the initial separation load and the initial separation distance increase with increasing a/h . In Tables 4 and 5, variations of the initial separation load and distance between the two elastic layers and the lower-layer elastic half-infinite plane for a rectangular stamp with μ_3/μ_2 and μ_2/μ_1 are given. As it can be seen in Tables 4 and 5, the initial separation load and distance decrease with increasing μ_3/μ_2 and μ_2/μ_1 .

5. Conclusions

This paper considers the continuous contact problem for two elastic layers resting on an elastic half-infinite plane. The results presented in this paper show that the elastic properties of the layers and intensity of the applied load have considerable effect on the contact stress distribution, the contact areas, the initial separation load, the and the initial separation distance. Additionally, the rigid stamp width (in the rectangular stamp case) and the radius of the rigid stamp (in the circular stamp case) play a very important role in the contact stress distribution, contact areas, initial separation load, and initial separation distance.

Appendix

Expressions of the kernels $k(x, t)$, $k_2^*(x, t)$, and $k_3^*(x, t)$ appearing in (7), (9a), and (9b) are given as follows:

$$k(x, t) = \frac{1}{h} \int_0^\infty \left\{ \frac{1}{\Delta^{**}} \left[e^{-5z-4z\xi} (-4z^2\xi^2 e^{z+2z\xi} (m_1(1+\chi_1)(e^{4z} - 2e^{2z+2z\xi} + e^{4z\xi}) \right. \right. \\ + 4e^{2z+2z\xi} (1+\chi_2))(1+\chi_3) - 4z\xi(1+\chi_2)e^{z+2z\xi} (m_2(-m_1(1+\chi_1)(e^{4z} - 2e^{2z+2z\xi} + e^{4z\xi}) \\ + (1+\chi_2)e^{2z}(1-2e^{2z\xi} + e^{4z\xi})) + (-e^{2z} + e^{4z\xi} - e^{4z} + e^{2z+4z\xi} - 4ze^{2z+2z\xi})(1+\chi_3) \\ + e^z(m_1(1+\chi_1)(e^{4z} - 2e^{2z+2z\xi} + e^{4z\xi}))(m_2(1+\chi_2)(-1 + e^{4z\xi}) \\ + (1+\chi_3)(1-2e^{2z\xi} + e^{4z\xi})) + (1+\chi_2)(e^{4z} - e^{4z\xi} + 4ze^{2z+2z\xi})(m_2(1+\chi_2)(1-2e^{2z\xi} + e^{4z\xi}) \\ \left. \left. + (1+\chi_3)(-1 + e^{4z\xi})) \right) \right] - 1 \right\} \sin \left[(t-x) \frac{z}{h} \right] dz, \quad (\text{A.1})$$

$$k_2^*(x, t) = \int_0^\infty \frac{2}{\Delta^{**}} \left[-m_1(1+\chi_1)e^{-4z-5z\xi} (-4(e^{z+6z\xi} + e^{3z+4z\xi})z^3\xi^3(1+\chi_3) \right. \\ + e^{z+2z\xi}(e^{2z\xi}(-1+z) + e^{2z}(1+z))(-m_2(1+\chi_2)(-1 + e^{4z\xi} - (1+\chi_3)(1-2e^{2z\xi} + e^{4z\xi})) \\ + e^{z+2z\xi}z\xi(-e^{2z} + e^{2z\xi} - e^{6z\xi} - e^{2z+4z\xi} + 4(z-1)e^{4z\xi} + 4(z+1)e^{2z}e^{2z\xi}))m_2(1+\chi_2) \\ + (1-2e^{2z\xi} + e^{4z\xi})(e^{2z} + e^{2z\xi})(1+\chi_3)) + 4z^2\xi^2e^{z+4z\xi}(m_2(1+\chi_2)(e^{2z} + e^{2z\xi}) \\ \left. \left. + (e^{2z\xi}(z-1) + e^{2z}(z+1))(1+\chi_3)) \right) \right] \cos \left[\frac{z}{h}(t-x) \right] dz, \quad (\text{A.2})$$

$$k_3^*(x, t) = \int_0^\infty \frac{4}{\Delta^{**}} \left[-e^{-3z-2z\xi} (-1 + e^{2z\xi} + z\xi(1 + e^{2z\xi}))((1-z)e^{2z\xi} \right. \\ \left. - (1+z)e^{2z} + z\xi(e^{2z+2z\xi}))m_2(1+\chi_1)(1+\chi_2) \right] \cos \left[\frac{z}{h}(t-x) \right] dz, \quad (\text{A.3})$$

where

$$\Delta^{**} = e^{-4z-4z\xi} \left[16e^{2z+4z\xi} z^3\xi^3 (- (1+\chi_2) + m_1(1+\chi_1))(1+\chi_3) - (-e^{4z} + e^{4z\xi} - 4ze^{2z+2z\xi}) \right. \\ \times m_1(1+\chi_1)((-1 + e^{4z\xi})m_2(1+\chi_2) + (1-2e^{2z\xi} + e^{4z\xi})(1+\chi_3)) + (e^{4z} + e^{4z\xi} - 2e^{2z+2z\xi}) \\ \times (1+2z^2)(1+\chi_2)((1-2e^{2z\xi} + e^{4z\xi})m_2(1+\chi_2) + (-1 + e^{4z\xi})(1+\chi_3)) \\ - 4z^2(e^{2z+4z\xi}(1+\chi_2)((1-2e^{2z\xi} + e^{4z\xi})m_2(1+\chi_2) + (-1 + e^{4z\xi} - 8ze^{2z\xi})(1+\chi_3)) \\ - m_1(1+\chi_1)(-4e^{2z+4z\xi}m_2(1+\chi_2) + (e^{6z\xi} - e^{4z+2z\xi} - 4ze^{2z+4z\xi})(1+\chi_3)) \\ - 4z\xi e^{2z\xi}(m_1(1+\chi_1)((-e^{4z} + e^{4z\xi} - e^{2z} - 4ze^{2z+2z\xi} + e^{2z+4z\xi})m_2(1+\chi_2) \\ + (e^{2z}(1-2e^{2z\xi} + e^{4z\xi})(1+\chi_3)) - (1+\chi_2)(2e^{2z}(1-2e^{2z\xi} + e^{4z\xi})m_2z(1+\chi_2) \\ \left. \left. + (e^{4z} + e^{4z\xi} - 2ze^{2z} + 2ze^{2z+4z} - 2e^{2z+2z\xi}(1+2z^2\xi^2))(1+\chi_3))) \right] \right].$$

References

- [Adibnazari et al. 2012] S. Adibnazari, F. Sharafbafi, and P. Ghanati, "Contact of an asymmetrical rounded apex wedge with a half plane", *Int. J. Eng. Sci.* **50**:1 (2012), 192–197.

- [Aleksandrov 2012] V. M. Aleksandrov, “Axisymmetric contact problems for a prestressed incompressible elastic layer”, *J. Appl. Math. Mech.* **76**:1 (2012), 170–174.
- [Argatov and Mishuris 2010] I. I. Argatov and G. S. Mishuris, “Axisymmetric contact problem for a biphasic cartilage layer with allowance for tangential displacements on the contact surface”, *Eur. J. Mech. A Solids* **29**:6 (2010), 1051–1064.
- [Birinci and Erdöl 2001] A. Birinci and R. Erdöl, “Continuous and discontinuous contact problem for a layered composite resting on simple supports”, *Struct. Eng. Mech.* **12**:1 (2001), 17–34.
- [Çakıroğlu 1990] F. L. Çakıroğlu, *The frictionless contact problem for two elastic layers resting on an elastic half-plane*, Ph.D. thesis, Civil Engineering Department, Karadeniz Technical University, Trabzon, Turkey, 1990. in Turkish.
- [Çakıroğlu et al. 2001] F. L. Çakıroğlu, M. Çakıroğlu, and R. Erdöl, “Contact problems for two elastic layers resting on elastic half-plane”, *J. Eng. Mech. (ASCE)* **127**:2 (2001), 113–118.
- [Chen et al. 2011] Y. Z. Chen, X. Y. Lin, and Z. X. Wang, “Singular integral equation method for contact problem for rigidly connected punches on elastic half-plane”, *Appl. Math. Comput.* **217**:12 (2011), 5680–5694.
- [Chidlow et al. 2013] S. J. Chidlow, W. W. F. Chong, and M. Teodorescu, “On the two-dimensional solution of both adhesive and non-adhesive contact problems involving functionally graded materials”, *Eur. J. Mech. A Solids* **39** (2013), 86–103.
- [Civelek and Erdogan 1975] M. B. Civelek and F. Erdogan, “The frictionless contact problem for an elastic layer under gravity”, *J. Appl. Mech.* **42**:1 (1975), 136–140.
- [Çömez 2010] I. Çömez, “Frictional contact problem for a rigid cylindrical stamp and an elastic layer resting on a half plane”, *Int. J. Solids Struct.* **47**:7–8 (2010), 1090–1097.
- [Dini and Nowell 2004] D. Dini and D. Nowell, “Flat and rounded fretting contact problems incorporating elastic layers”, *Int. J. Mech. Sci.* **46**:11 (2004), 1635–1657.
- [El-Borgi et al. 2006] S. El-Borgi, R. Abdelmoula, and L. Keer, “A receding contact plane problem between a functionally graded layer and a homogeneous substrate”, *Int. J. Solids Struct.* **43**:3–4 (2006), 658–674.
- [Erdogan and Gupta 1972] F. Erdogan and G. D. Gupta, “On the numerical solution of singular integral equations”, *Quart. Appl. Math.* **29** (1972), 525–534.
- [Galın 1961] L. A. Galın, *Contact problems in the theory of elasticity*, North Carolina State College Translation Series, Raleigh, 1961.
- [Garrido and Lorenzana 1998] J. A. Garrido and A. Lorenzana, “Receding contact problem involving large displacements using the BEM”, *Eng. Anal. Bound. Elem.* **21**:4 (1998), 295–303.
- [Geçit 1980] M. R. Geçit, “A tensionless contact without friction between an elastic layer and an elastic foundation”, *Int. J. Solids Struct.* **16**:5 (1980), 387–396.
- [Geçit 1981] M. R. Geçit, “Axisymmetric contact problem for an elastic layer and elastic foundation”, *Int. J. Eng. Sci.* **19**:6 (1981), 747–755.
- [Gun and Gao 2014] H. Gun and X.-W. Gao, “Analysis of frictional contact problems for functionally graded materials using BEM”, *Eng. Anal. Bound. Elem.* **38** (2014), 1–7.
- [Hertz 1895] H. Hertz, *Gesammelte werke*, Johannes Ambrosius Barth, Leipzig, 1895.
- [Kahya et al. 2007] V. Kahya, T. S. Ozsahin, A. Birinci, and R. Erdöl, “A receding contact problem for an anisotropic elastic medium consisting of a layer and a half plane”, *Int. J. Solids Struct.* **44**:17 (2007), 5695–5710.
- [Ke and Wang 2006] L.-L. Ke and Y.-S. Wang, “Two-dimensional contact mechanics of functionally graded materials with arbitrary spatial variations of material properties”, *Int. J. Solids Struct.* **43**:18–19 (2006), 5779–5798.
- [Ke and Wang 2007] L.-L. Ke and Y.-S. Wang, “Two-dimensional sliding frictional contact of functionally graded materials”, *Eur. J. Mech. A Solids* **26**:1 (2007), 171–188.
- [Keer et al. 1972] L. M. Keer, J. Dundurs, and K. C. Tsai, “Problems involving of a receding contact between a layer and a half space”, *J. Appl. Mech. (ASME)* **39**:4 (1972), 1115–1120.
- [Kumar and DasGupta 2012] N. Kumar and A. DasGupta, “On the contact problem of an inflated spherical hyperelastic membrane”, *Int. J. Nonlinear Mech.* **57** (2012), 130–139.
- [Long et al. 2012] J. M. Long, G. F. Wang, X. Q. Feng, and S. W. Yu, “Two-dimensional Hertzian contact problem with surface tension”, *Int. J. Solids Struct.* **49**:13 (2012), 1588–1594.

- [Ozsahin 2007] T. S. Ozsahin, “Frictionless contact problem for a layer on an elastic half plane loaded by means of two dissimilar rigid punches”, *Struct. Eng. Mech.* **25**:4 (2007), 383–403.
- [Ratwani and Erdogan 1973] M. Ratwani and F. Erdogan, “On the plane contact problem for a frictionless elastic layer”, *Int. J. Solids Struct.* **9**:8 (1973), 921–936.
- [Rhim i et al. 2009] M. Rhimi, S. El-Borgi, W. Ben Said, and F. Ben Jemaa, “A receding contact axisymmetric problem between a functionally graded layer and a homogeneous substrate”, *Int. J. Solids Struct.* **46**:20 (2009), 3633–3642.
- [Rhim i et al. 2011] M. Rhimi, S. El-Borgi, and N. Lajnef, “A double receding contact axisymmetric problem between a functionally graded layer and a homogeneous substrate”, *Mechanics of Materials* **43**:12 (2011), 787–798.
- [Trubchik et al. 2011] I. S. Trubchik, L. N. Evich, and B. I. Mitrin, “The analytical solution of the contact problem for the functionally graded layer of complicate structure”, *Procedia Engineering* **10** (2011), 1754–1759.
- [Uffliand 1965] I. S. Uffliand, *Survey articles on the applications of integral transforms in the theory of elasticity*, North Carolina State Collage Translation Series, Raleigh, 1965.
- [Vollebregt 2014] E. A. H. Vollebregt, “A new solver for the elastic normal contact problem using conjugate gradients, deflation, and an FFT-based preconditioner”, *J. Comput. Phys.* **257** (2014), 333–351.

Received 14 Aug 2013. Revised 6 Dec 2013. Accepted 22 Dec 2013.

ERDAL ÖNER: eoner@bayburt.edu.tr

Department of Civil Engineering, Bayburt University, 69000 Bayburt, Turkey

AHMET BIRINCI: birinci@ktu.edu.tr

Department of Civil Engineering, Karadeniz Technical University, 61080 Trabzon, Turkey

SUBMISSION GUIDELINES

ORIGINALITY

Authors may submit manuscripts in PDF format online at the Submissions page. Submission of a manuscript acknowledges that the manuscript is original and has neither previously, nor simultaneously, in whole or in part, been submitted elsewhere. Information regarding the preparation of manuscripts is provided below. Correspondence by email is requested for convenience and speed. For further information, write to contact@msp.org.

LANGUAGE

Manuscripts must be in English. A brief abstract of about 150 words or less must be included. The abstract should be self-contained and not make any reference to the bibliography. Also required are keywords and subject classification for the article, and, for each author, postal address, affiliation (if appropriate), and email address if available. A home-page URL is optional.

FORMAT

Authors can use their preferred manuscript-preparation software, including for example Microsoft Word or any variant of $\text{T}_{\text{E}}\text{X}$. The journal itself is produced in $\text{L}^{\text{A}}\text{T}_{\text{E}}\text{X}$, so accepted articles prepared using other software will be converted to $\text{L}^{\text{A}}\text{T}_{\text{E}}\text{X}$ at production time. Authors wishing to prepare their document in $\text{L}^{\text{A}}\text{T}_{\text{E}}\text{X}$ can follow the example file at www.jomms.net (but the use of other class files is acceptable). At submission time only a PDF file is required. After acceptance, authors must submit all source material (see especially Figures below).

REFERENCES

Bibliographical references should be complete, including article titles and page ranges. All references in the bibliography should be cited in the text. The use of $\text{BibT}_{\text{E}}\text{X}$ is preferred but not required. Tags will be converted to the house format (see a current issue for examples); however, for submission you may use the format of your choice. Links will be provided to all literature with known web locations; authors can supply their own links in addition to those provided by the editorial process.

FIGURES

Figures must be of publication quality. After acceptance, you will need to submit the original source files in vector format for all diagrams and graphs in your manuscript: vector EPS or vector PDF files are the most useful. (EPS stands for Encapsulated PostScript.)

Most drawing and graphing packages—Mathematica, Adobe Illustrator, Corel Draw, MATLAB, etc.—allow the user to save files in one of these formats. Make sure that what you’re saving is vector graphics and not a bitmap. If you need help, please write to graphics@msp.org with as many details as you can about how your graphics were generated.

Please also include the original data for any plots. This is particularly important if you are unable to save Excel-generated plots in vector format. Saving them as bitmaps is not useful; please send the Excel (.xls) spreadsheets instead. Bundle your figure files into a single archive (using zip, tar, rar or other format of your choice) and upload on the link you been given at acceptance time.

Each figure should be captioned and numbered so that it can float. Small figures occupying no more than three lines of vertical space can be kept in the text (“the curve looks like this:”). It is acceptable to submit a manuscript with all figures at the end, if their placement is specified in the text by means of comments such as “Place Figure 1 here”. The same considerations apply to tables.

WHITE SPACE

Forced line breaks or page breaks should not be inserted in the document. There is no point in your trying to optimize line and page breaks in the original manuscript. The manuscript will be reformatted to use the journal’s preferred fonts and layout.

PROOFS

Page proofs will be made available to authors (or to the designated corresponding author) at a Web site in PDF format. Failure to acknowledge the receipt of proofs or to return corrections within the requested deadline may cause publication to be postponed.

Improved thermoelastic coefficients of a novel short fuzzy fiber-reinforced composite with wavy carbon nanotubes	SHAILESH I. KUNDALWAL and MANAS C. RAY	1
Moment Lyapunov exponents and stochastic stability of coupled viscoelastic systems driven by white noise	JIAN DENG, WEI-CHAU XIE and MAHESH D. PANDEY	27
Combined effects of interstitial and Laplace pressure in hot isostatic pressing of cylindrical specimens	LAURA GALUPPI and LUCA DESERI	51
Planar grained structures with traction-smoothing inclusions: an elastostatic numerical analysis for shear and torsion	SHMUEL VIGDERGAUZ	87
Continuous contact problem for two elastic layers resting on an elastic half-infinite plane	ERDAL ÖNER and AHMET BIRINCI	105